MICRO & NANO TECHNOLOGIES

Fabrication and Design of Resonant Microdevices

Behraad Bahreyni

William

FABRICATION AND DESIGN OF RESONANT MICRODEVICES

MICRO & NANO TECHNOLOGIES

Series Editor: Jeremy Ramsden
Professor of Nanotechnology
Microsystems and Nanotechnology Centre, Department of Materials
Cranfield University, United Kingdom

The aim of this book series is to disseminate the latest developments in small scale technologies with a particular emphasis on accessible and practical content. These books will appeal to engineers from industry, academia and government sectors.

For more information about the book series and new book proposals please contact the Publisher, Dr. Nigel Hollingworth at nhollingworth@williamandrew.com.

http://www.williamandrew.com/MNT

FABRICATION AND DESIGN OF RESONANT MICRODEVICES

Behraad Bahreyni
Department of Engineering Science,
Simon Fraser University, BC, Canada

William Andrew
Norwich, NY, USA

ISBN: 978-0-8155-1577-7

Library of Congress Cataloging-in-Publication Data

Bahreyni, Behraad.
Fabrication and design of resonant microdevices / Behraad Bahreyni.
p. cm. -- (Micro & nano technologies ; 3)
Includes bibliographical references and index.
ISBN 978-0-8155-1577-7
1. Microelectromechanical systems--Design and construction. 2. Microfabrication. 3. Resonance. I. Title.
TK7875.B35 2008
621--dc22

2008017717

Printed in the United States of America

This book is printed on acid-free paper.

10 9 8 7 6 5 4 3 2 1

Published by:
William Andrew Inc.
13 Eaton Avenue
Norwich, NY 13815
1-800-932-7045
www.williamandrew.com

NOTICE
To the best of our knowledge the information in this publication is accurate; however the Publisher does not assume any responsibility or liability for the accuracy or completeness of, or consequences arising from, such information. This book is intended for informational purposes only. Mention of trade names or commercial products does not constitute endorsement or recommendation for their use by the Publisher. Final determination of the suitability of any information or product for any use, and the manner of that use, is the sole responsibility of the user. Anyone intending to rely upon any recommendation of materials or procedures mentioned in this publication should be independently satisfied as to such suitability, and must meet all applicable safety and health standards.

To my father, mother, and wife for their love and support

Contents

Series Editor's Preface

The headlong rush towards ever greater degrees of miniaturization constantly renders many industrial processes and even entire technological sectors obsolete. This is perhaps most prominent in the manufacture of integrated circuits used in information processors, where Moore's law, initially put forward as a forecast, has achieved the status of not merely a remarkably accurate empirical summary of a long-observed trend, but that of an apparent fiat with dictatorial powers. There are, of course, strong technical and commercial reasons for this being so. Processing power increases with the number of components in a circuit, and if those components can be made smaller and closer together, the system operates more rapidly. And, one may note that even the smallest commercially available components are still much greater than the size of the minimum physical object required to encode one bit of information, hence miniaturization will certainly continue.

In the field of microelectromechanical systems (MEMS), however, other considerations prevail. These systems process information embodied in real physical quantities such as inertial mass and electrical capacitance. Performance generally scales unfavourably with diminishing size, hence the present range of their sizes probably represents the optimal endpoint of a compromise between adequate performance and acceptable cost. The latter depends not only on the direct costs of making the device (system) itself, but also on the indirect costs of incorporating a device of a given size into a larger system. In automotive applications, for example—in terms of the number of units manufactured (volume) perhaps the largest sector—size and weight are at a premium, and sensorization of a motor vehicle, which effectively means enhancing its capabilities by embedding many performance-monitoring sensors in it, is only practically possible if the sensors, and the equally important actuators, are of micrometer dimensions, but further reduction of size is neither necessary nor desirable (because of performance degradation). Incidentally, performance also includes important safety features—the almost universal provision of airbags, for example, is dependent, *inter alia*, on the availability of miniature accelerometers to actuate their release.

Therefore, further development in MEMS will take place through more ingenious and better design, and the selection of new materials. To do this successfully, a thorough grounding in the fundamentals of the field is

required. Perhaps the most fundamental concept pervading MEMS is resonance. Bahreyni's book, focusing on resonant microdevices, comprehensively provides that grounding. It will be of interest to engineers intending to specialize in MEMS, and will also serve as a reference work for practitioners, who may wish to refresh their knowledge of some area of the field. Finally, it will be of interest to all engineers and scientists with an intelligent and lively interest in the acquisition of new knowledge. MEMS are nowadays so ubiquitous in our society that it is surely useful for all of us to be more familiar with them.

Jeremy Ramsden
Cranfield University, United Kingdom
March 2008

Acknowledgments

One may not be able to finish a task like writing a book if it were not for the support and help of the people around the author, including those who had a share in educating the person. For this reason, I am thankful to all of my past teachers for providing me the basis to attempt this daring task. In particular, I would like to thank Dr Bijan Rashidian, who motivated me to research on micromachined devices and Dr Cyrus Shafai who showed me how to fabricate such devices. I would also like to thank Dr Ashwin Seshia for providing me with the opportunity to work on various projects.

My publisher, Dr Nigel Hollingworth, played a major role in conceiving this book. He patiently worked with me from the beginning until the work on the book was finished. I thank him for all his understanding.

I have been blessed with the support and love from my parents, Behrooz and Masoumeh, my sister, Behnaz, and my brothers, Behzad and Behiad, throughout my life. In particular, I am grateful for the guidance, encouragement, and selfless love of my parents. Last but not least, I would like to express my gratitude to my wife, Solmaz. Much of the time I spent on this book was taken from the time we should have spent together.

Behraad Bahreyni
May 2008

1 Introduction

Microengineering refers to the practice and technology of making three dimensional structures and devices with dimensions on the order of less than a micrometre to a few millimetres. Micromachining is the name for the techniques used to produce the structures and moving parts of microengineered devices.

Microelectromechanical Systems (MEMS) contain tiny mechanical elements that are often produced with microfabrication techniques. The biggest advantage here is not necessarily that the system can be miniaturised but it is the mass-production of thousands of mechanical devices with the aid of techniques that have been used to fabricate complex microchips. As a result, the price of individual components can be reduced significantly, as has happened with integrated circuits.

A microsystem may be constructed from parts produced using different technologies on different substrates connected together (i.e., a *hybrid* system). Alternatively, all components of a system could be constructed on a single substrate using one technology (i.e., a *monolithic* system). Hybrid systems have the advantage that the most appropriate technologies for each component can be selected to optimise the system performance. This will often lead to a shorter development time since microfabrication techniques for each component may already exist and compromises will not have to be made for compatibility. Monolithic devices on the other hand, are more compact than hybrid devices and can be more reliable (e.g., fewer interconnections that can go wrong). Moreover, once the fabrication process has been developed, monolithic devices can be manufactured more cheaply since less assembly is required.

1.1 Resonance

Resonance is a dynamic behaviour that is observed when certain systems are excited properly. In general, these systems exhibit an amplified response to their input when the frequency of the excitation is equal to the resonant frequency(ies) of the system, thanks to a more efficient transfer of the energy from the excitation source to the structure. The damping of the excitation energy is an important issue when considering the dynamic behaviour of a system whether the resonant response is desired or should be avoided. Familiar examples of resonant response of mechanical systems include vibrations of guitar strings when stroked, oscillations of a mass attached to a spring after an initial displacement, generation of sound waves when rubbing the edge of a wine glass, and movements of a clock pendulum. In case of large scale mechanical structures, it is generally desired to avoid resonance as it often causes accelerated fatigue and eventually failure of the structure. Destruction of the bridge at Tacoma Narrows in November 1940 due to wind is an

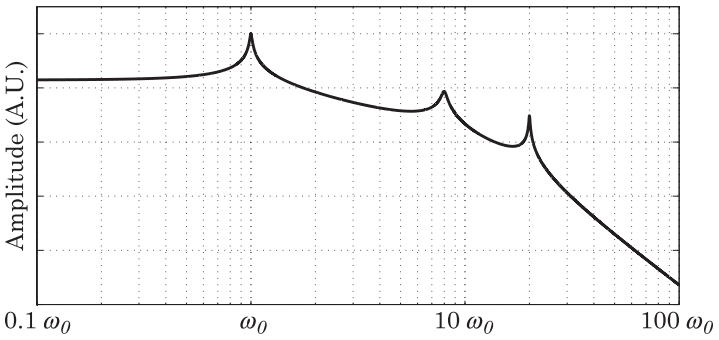

Figure 1.1 Amplitude response of a system with multiple resonant frequencies.

infamous example of destructive effects of resonance at large scales. To avoid such disasters, the structural designers try to damp the resonant response of the system by including proper energy dissipating mechanisms in the design. Common examples of resonance electrical systems include RLC circuits and microwave cavities. Unwanted electrical resonance is the cause of ringing in the step response of electrical systems and in some cases may lead to instabilities.

1.2 Frequency and Time Response of Resonators

An example of the amplitude response of an underdamped system (to be defined shortly) with multiple resonant frequencies is shown in Fig. 1.1. The resonance behaviour of a system around its resonant frequency can in most cases be approximated as the response of an underdamped second order system. An ideal resonance behaviour produces a peak in amplitude response and a $-180°$ phase shift in phase response around the resonant frequency of the system. The amount of damping in the system determines how sharp these transitions are. Both the amplitude and phase response of a system can be used to analyse the system behaviour around resonance.

Let us consider a simple mass-damper-spring system as an example. Assume that x is the displacement of the mass due to excitation force F applied to the mass (see Fig. 1.2). Using Newton's laws of motion, the differential equation describing the system response is:

$$M\frac{d^2x}{dt^2} + \zeta\frac{dx}{dt} + Kx = F \tag{1.1}$$

where M, ζ, and K are the mass, damping coefficient, and spring constant, respectively. The system transfer function is:

$$H(s) = \frac{\mathcal{X}(s)}{\mathcal{F}(s)} = \frac{1}{Ms^2 + \zeta s + K} \tag{1.2}$$

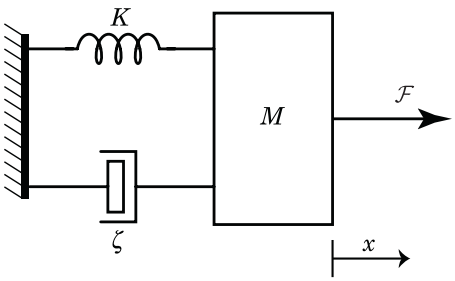

Figure 1.2 A mass-spring-damper system.

where $\mathcal{F}(s)$ and $\mathcal{X}(s)$ are the Laplace transforms of the $F(t)$ and $x(t)$, respectively. The *natural frequencies* of the system, or system poles, are the roots of the denominator of the system transfer function[1]:

$$p_{1,2} = \frac{-\zeta \pm \sqrt{\zeta^2 - 4MK}}{2M}. \tag{1.3}$$

There are three possible scenarios for physical systems depending on the values of M, ζ, and K:

(a) $\zeta^2 - 4MK > 0$: The system poles are two negative real numbers and the system is said to be *overdamped*;
(b) $\zeta^2 - 4MK = 0$: The system poles are equal to each other and are negative real numbers. The system is called *criticallydamped*;
(c) $\zeta^2 - 4MK < 0$: The system poles are complex conjugates with negative real parts and the system is *underdamped*.

Resonant devices are underdamped systems, and therefore, only this case is considered here. Two important parameters are often used when addressing the performance of a second order resonant device [2]: *resonant frequency* and *quality factor*. *Resonant frequency*, ω_r, is the frequency at which the system output reaches a maximum for a constant drive signal amplitude. *Quality factor* is a measure of the amount of losses during resonator operation and is defined as:

$$Q = 2\pi \frac{\text{Average stored energy}}{\text{Energy loss per cycle}}. \tag{1.4}$$

The relationship between the resonant frequency and the undamped natural frequency (i.e., imaginary part of system poles for $\zeta = 0$), ω_0, of a second order

[1] Natural frequencies are also the eigenvalues of the characteristic equation of the system.
[2] Or for a higher order device when its operation is approximated as that of a second order device over a limited bandwidth.

system is:

$$\omega_r = \omega_0 \sqrt{1 - \frac{1}{2Q^2}}. \tag{1.5}$$

Most micromachined resonators have large quality factors. Therefore, the resonant frequencies of these devices are nearly identical to their undamped natural frequencies and are often used interchangeably in literature.

The undamped natural frequency of a second order mass-spring system is given by $\omega_0 = \sqrt{K/M}$. The quality factor of such a second order mechanical resonator is given by:

$$Q = \frac{M\omega_0}{\zeta} = \frac{K}{\zeta\omega_0}. \tag{1.6}$$

The system transfer function can now be rewritten in a more general way as:

$$H(s) = \frac{\mathcal{X}(s)}{\mathcal{F}(s)} = \frac{\mathcal{A}}{s^2 + \frac{\omega_0}{Q}s + \omega_0^2} \tag{1.7}$$

where $\mathcal{A} = 1/M = \omega_0/\zeta Q$ is a constant.

The frequency response of the system can be found by setting $s = j\omega$ in Eq. (1.7):

$$\begin{aligned} H(j\omega) &= \frac{\mathcal{A}}{\omega_0^2 - \omega^2 + \frac{\omega_0}{Q}j\omega} \\ \Rightarrow |H(j\omega)| &= \frac{\mathcal{A}}{\sqrt{(\omega_0^2 - \omega^2)^2 + \left(\frac{\omega_0}{Q}\omega\right)^2}} \\ \angle H(j\omega) &= \arctan \frac{\frac{\omega_0}{Q}\omega}{\omega^2 - \omega_0^2}. \end{aligned} \tag{1.8}$$

Fig. 1.3 illustrates the frequency responses of two systems with similar natural frequencies of $\omega_0 = 1000$ rad/sec but with different quality factors of 5 and 25.

It is instructive to investigate the system behaviour at two important frequencies: $\omega = 0$ and $\omega = \omega_0$. At very low frequencies as ω approaches 0, it follows from the above relationships that $|H(j\omega)| \approx \mathcal{A}/\omega_0^2 = 1/K$ and $\angle H(j\omega) \approx 0$. On the other hand, at resonance where $\omega = \omega_0$, one can see that $|H(j\omega)| = Q\mathcal{A}/\omega_0^2 = Q/K$and $\angle H(j\omega) = -90°$. The fact that a resonator has an amplified response at its resonant frequency is the main reason for their adaptation as frequency selectors or sensitive sensing elements.

The quality factor of a resonator can be estimated using the amplitude or phase response of the device versus frequency:

$$Q = \frac{f_0}{\Delta f_{-3\text{ dB}}} = \frac{\omega_0}{2}\frac{d}{d\omega}\angle H(j\omega) \tag{1.9}$$

where $\Delta f_{-3\text{ dB}}$ is the bandwidth around the resonant frequency of the device where the signal amplitude drops by -3 dB and $\angle H(j\omega)$ is the argument (i.e., phase) of the transfer function of the resonator. It can also be shown that the resonant frequency is the geometrical mean of -3 dB frequencies[3].

We can use the system transfer function from Eq. (1.7) to find the step response of the system[4]:

$$\begin{aligned} x(t) &= \frac{\mathcal{A}}{\omega_0^2}\left(1 - e^{-\frac{\omega_0 t}{2Q}}\cos\left(\omega_0 t\sqrt{1-\frac{1}{4Q^2}}\right)\right. \\ &\quad \left. - \frac{e^{-\frac{\omega_0 t}{2Q}}}{\sqrt{1-\frac{1}{4Q^2}}}\sin\left(\omega_0 t\sqrt{1-\frac{1}{4Q^2}}\right)\right) \\ &\approx \frac{\mathcal{A}}{\omega_0^2}\left(1 - (\cos\omega_0 t + \sin\omega_0 t)\, e^{-\frac{\omega_0 t}{2Q}}\right). \end{aligned}$$

As examples, the step response of one of resonators with output spectrum of Fig. 1.3 is shown in Fig. 1.4. The resonant frequency can be measured by calculating the period of the decaying sinusoidal wave. The quality factor of the resonators can be estimated from the time response as well: the amplitude of vibrations drops by a factor of e^{-1} (i.e., 37%) from its maximum value after Q/π cycles.

1.3 Micromachining and Scaling

Scaling affects the performance of micromachined devices in various ways. For example, if all of the dimensions of a beam are shrunk by a constant factor, its spring constant decreases by the same factor while its mass reduces by the cube of that factor. Consequently, the deflections of the beam under its own weight becomes far smaller, even relative to the shrunk dimensions. Another aftermath of scaling in case of a beam is the increase in its resonant frequency by as much as the scaling factor. Scaling affects many of the other aspects of a

[3] a is the geometrical mean of b and c if $a = \sqrt{b\,c}$.

[4] The step function is defined as a piecewise linear function such that $u(t) = 1$ for $t \geq 0$ and $u(t) = 0$ for $t < 0$. *Step response* is the system response to a step input.

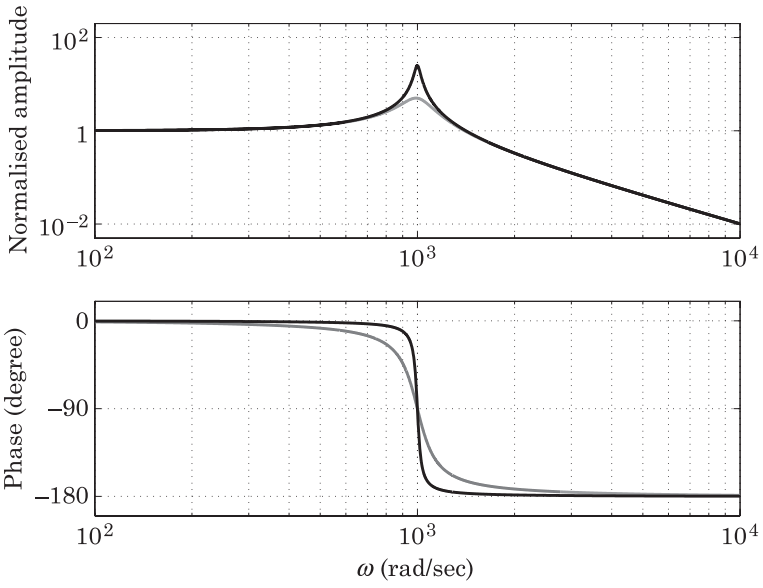

Figure 1.3 Amplitude and phase responses of two resonators with quality factors of 5 and 25 and identical resonant frequencies of $\omega_0 = 1000$ rad/sec.

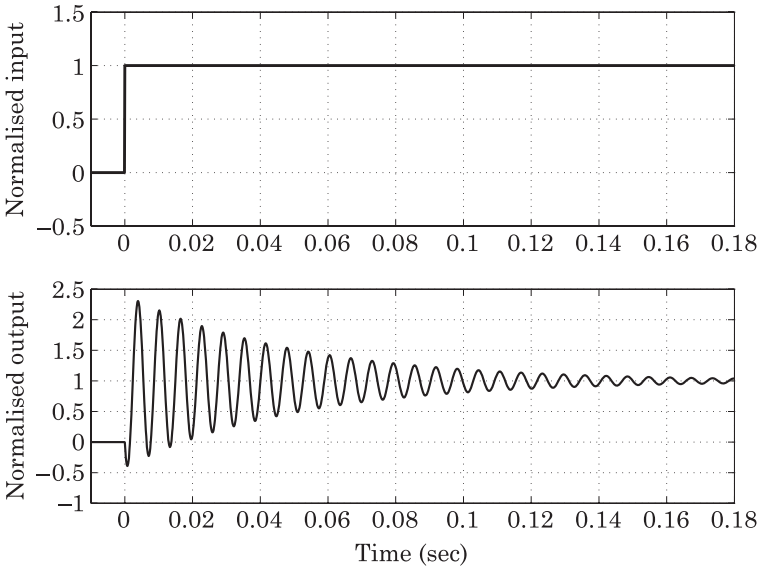

Figure 1.4 The step response of a resonator with a Q of 25 and resonant frequency of $\omega_0 = 1000$ rad/sec.

device behaviour, its interaction with surroundings, and its response to point, surface, and body forces. As a result of these scaling effects, micromachined devices behave differently from their large scale counterparts [1–3]. For example,

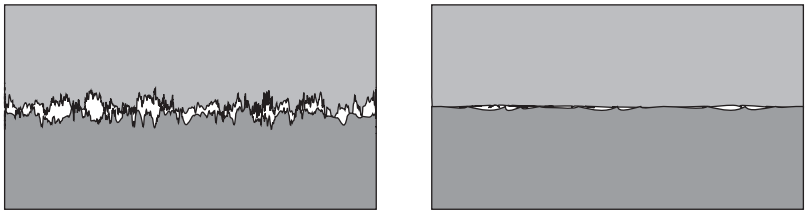

Figure 1.5 Illustrating the difference between the effective contact area between two rough (left) and smooth (right) surfaces.

Table 1.1 The Effect of Scaling by a Factor of α

Property	Scaling factor
Linear dimension	α
Area	α^2
Volume	α^3
Mass	α^3
Inertia	α^3
Electrostatic energy	α^3
Electrostatic force	α^2
Magnetic energy	α^5
Magnetic force	α^5
Coulomb force	α^{-2}
Areal defect density	α^{-2}
Deflection under own weight	α^2
Resonant frequency	α^{-1}

friction is often assumed to be proportional to the surface area between two objects which are rubbing past each other. However, due to the roughness of the surfaces, the actual contact area between two macro-scale objects is typically orders of magnitude smaller than their geometric areas (see Fig. 1.5). Micromachined structures and films, on the other hand, usually have very smooth surfaces, which translates into about a 1:1 ratio between the geometric and contact areas between two touching structures. Consequently, the friction forces are considerably larger compared to what might be expected from large-scale calculations. In fact, friction is an important cause of device failure for micromachined devices. Table 1.1 summarises some of the device and physical properties which are affected by scaling.

Failure of resonant systems is often a result of imperfections (i.e., defects) in the structural materials. Micromachined devices are significantly less prone to these imperfections thanks to their small dimensions and the random scatter of such defects across the bulk of the material. Nevertheless, a material defect can prevent the resonator from operating, cause permanent failure of

a micromachined resonator after a number of cycles, or damp the resonator response to unacceptable levels.

References

1. M. Elwenspoek and R. Wiegerink, *Mechanical microsensors*, Springer-Verlag, Berlin, Germany, 2001.
2. M.J. Madou, *Fundamentals of microfabrication: the science of miniaturization*, 2nd edn., CRC Press, Boca Raton, USA, 2002.
3. S.D. Senturia, *Microsystem design*, Kluwer Academic Publishers, Boston, USA, 2000.

2 Microfabrication

Dimensions of micromachined devices generally fall in the 100 nm to 10 mm range. Although some micromachined structures could be produced by precision machining techniques, the associated cost and low throughput of precision machining techniques prohibits commercial applications of such techniques. Instead, fabrication of MEMS mainly relies on the technologies inherited from microelectronic processing. Although microelectronic fabrication steps are generally expensive, the final cost of each device can be low thanks to the batch processing of a large number of devices at the same time. Micromachining differs from microelectronic processes in many aspects as the processing steps are tailored to satisfy the requirements for fabrication of mechanical devices. While in microelectronic processing the emphasis is on electrical properties of the films, the primary aim of micromachining is to obtain films with desired mechanical properties. For instance, precise doping of films is a common step in microelectronics to form different junctions while in micromachining doping is often used to reduce the resistance of the films for better electrical conduction or as an etch-stop technique to define the dimensions of a device. As another example, the etch depth in micromachining is often larger than what is needed for microelectronics. Most microfabrication techniques are about crafting a 3-dimensional structure from a 2-dimensional top view of the device. This chapter overviews the major micromachining techniques as a quick reference. The interested reader is encouraged to refer to the numerous sources on details, mechanisms, and recipes for micromachining steps [1–4].

A microfabrication process flow generally includes:

- deposition or growth of a film of a material with desired material, mechanical, and electrical properties;
- a lithography step to transfer the desired patterns to the underlying substrate or film;
- selective removal of the films through physical or chemical processes.

Other possible steps in a micromachining process include planarisation to reduce the roughness and the height differences across the wafer, a doping step to adjust electrical properties or for film thickness adjustments, and bonding of wafers and substrates to other substrates.

2.1 Material Selection

The first step when designing a process flow for fabrication of a micromachined device is to choose the structural and other materials which

are to be used in the process flow. Some of the properties of materials that are commonly used in MEMS fabrication are listed in Table 2.1. Traditionally, silicon and polysilicon have been used most often as the structural materials for MEMS. This was initially due to the wealth of existing knowledge on processing of silicon samples from microelectronic fabrication. Luckily for the micromachining engineers, silicon has several favourable mechanical properties in addition to its superb electrical specifications that have made it the material of choice for microelectronics. Nevertheless, there are numerous cases where other materials offer significant advantages over silicon. Examples include applications where a piezoelectric material is needed or when the devices are designed to work in harsh environments.

Silicon is a brittle material with a Young's modulus and tensile yield strength that approach metals such as stainless steel. Polysilicon has similar mechanical properties as silicon. However, a polysilicon film is made of tightly packed grains of crystalline silicon. In some applications, this might lead to long term variations in material properties and even failure due to the change in the morphology of the grains especially under continuous thermal and mechanical loads [5,6]. Furthermore, devices made from single crystalline silicon generally have less internal stresses and less internal damping than those made from polysilicon films. The smaller internal friction in single crystalline silicon can lead to a larger quality factor for resonators made from single crystalline layers than the ones made from polysilicon films [7].

Another widely-used material in MEMS fabrication is silicon dioxide (SiO_2). Although not used as the main structural layer for MEMS, amorphous SiO_2 films are frequently used for electrical isolation of the layers and also as masking and sacrificial layers during the device fabrication. These amorphous SiO_2 films can be deposited on various substrates or grown on top of a silicon substrate. Amorphous SiO_2 is also used as glass substrate for fabrication of MEMS devices especially for microfluidic and BioMEMS applications were an insulating transparent substrate is desired [12]. Crystalline SiO_2 is commonly known as quartz. Quartz exhibits piezoelectric properties which can be used for both actuation and sensing applications. Oscillators based on quartz resonators have widespread applications where precise reference signal sources are needed. The piezoelectric property of quartz has made it a viable material for sensory applications [13,14]. Quartz substrates have low losses at high frequencies and have been employed for RF MEMS applications [15,16].

Silicon nitride, Si_3N_4, is the other frequently used dielectric in micromachining. Si_3N_4 is chemically more stable than SiO_2, making it a suitable mask layer for etching. While SiO_2 can either be deposited or grown from a silicon substrate, Si_3N_4 is only deposited due to is extremely slow growth rate. By choosing the deposition parameters properly, it is possible to alter the mechanical properties of Si_3N_4 films, most notably, the amount of internal stresses in grown films.

Mechanical devices made of silicon can operate at up to 600 °C and the silicon electronic devices can function at temperatures as high as 250 °C. However,

Table 2.1 Properties of Materials Commonly Used in Fabrication of MEMS Resonators at 300 K. Applications nomenclature: 1: Structural; 2: Transduction; 3: Sacrificial; 4: Dielectric; 5: Coating; 6: Electrical routing; and 7: Etch mask.

Material	Young's modulus (GPa)	Mass density (kg m^{-3})	Electrical resistivity (Ω m)	Thermal conductivity (W m^{-1} K^{-1})	Thermal expansion coefficient (ppm K^{-1})	Typical applications	References
Silicon	165.6	2330	varies	156	2.616	1, 3, 7	[8]
SiC	448	3200	varies	500	4.2	1, 5	[9]
SiO_2	73	2200	–	1.4	0.55	3, 4, 7	[10]
Si_3N_4	385	3100	–	19	0.8	3, 4, 7	[10]
Quartz	72.4	2203	–	1.38	0.5	1, 2	[11]
AlN	345	3260	–	67	4	2	[11]
Al	70.3	2710	2.73×10^{-8}	237	23.2	1, 6	[11]
Ni	221	8900	7.16×10^{-8}	90.4	13.5	1, 6, 7	[11]
Cu	132	8940	1.73×10^{-8}	398.1	16.12	1, 6	[11]
Au	77.2	19300	2.249×10^{-8}	315	14.2	6	[11]

there are several applications which require the devices to operate at higher temperatures. Silicon carbide (SiC) is an alternative material for making devices that operate at such high temperatures. Compared to silicon, SiC also has a larger Young's modulus and is more chemically inert, making it a candidate for the structural layer for the devices that operate in harsh environments [9,17]. SiC has also been used for coating of other MEMS devices for increased wear resistance. On the other hand, the same advantages of SiC over silicon bring up challenges in deposition and etching of SiC films. Nevertheless, numerous SiC devices have been demonstrated for various sensory applications [18].

Lead zirconate titanate or PZT (Pb $Zr_xTi_{1-x}O_3$) is another material with piezoelectric properties. PZT films have been mostly used for actuation purposes because of the large coupling factor between the applied electric field and the mechanical deformation of the PZT films [19]. However, the piezoelectric properties of PZT have also been employed for power generation and sensory applications [20–22]. Other piezoelectric materials that are used for fabrication of MEMS are zinc oxide (ZnO) and aluminium nitride (AlN)[23,24]. AlN is specially an attractive material for fabrication of piezoelectric MEMS as its deposition and processing are compatible with CMOS processes. This can potentially lead to integration of the MEMS with signal processing electronics on the same chip [25].

A number of different metals are used in fabrication of MEMS. Aluminium and gold are the two metals are primarily used for their low resistance to route signals around the chip and also for reflective coatings on micromirrors [26,27]. Metals such as aluminium, titanium, and nickel have also been used as the structural material for MEMS [28]. Nickel is of particular importance since low-stress films as thick as several hundreds of microns can be electroplated relatively easily [29,30]. Nickel and its alloys also exhibit ferromagnetic properties and have been used in certain magnetic actuator applications [31].

2.2 Lithography

Lithography is the process of transferring a mask pattern onto a substrate. The required steps are (see Fig. 2.1):

(i) the substrate is coated with a photosensitive material, known as *photoresist*;
(ii) the patterns on the mask are *aligned* with features which already exist on the wafer;
(iii) a light source with proper wavelength (usually UV) is used to *expose* the photoresist;
(iv) the exposed photoresist is immersed in, or sprayed with, a *developing* solution to remove the extra photoresist as defined by the mask patterns.

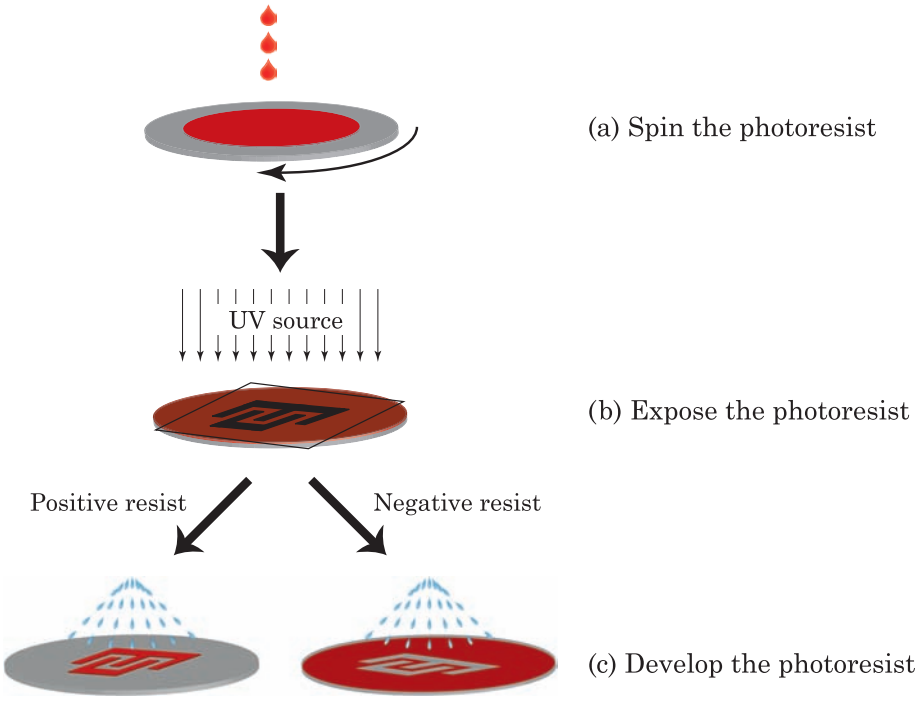

Figure 2.1 Typical lithography steps (excluding the alignment).

There are two types of photoresist that one can use to transfer the mask pattern onto the substrate. If the exposed photoresist changes chemically such that it dissolves in the developer, it is called to be a *positive* resist. On the other hand, a *negative* resists becomes more chemically stable when exposed. If one uses a positive resist, the image on wafer after developing will be a positive image of the mask pattern while the opposite happens with a negative resist. Positive resists are typically better suited for high resolution pattern transfer in typical lithography systems with UV light sources [1,2].

In order to have a thin uniform photoresist layer on a wafer, a certain amount of photoresist is poured at the centre of the wafer and the wafer is spun to high speeds (on the order of thousands of rpm). Generally, a thermal treatment of the coated wafer, known as soft-baking, is necessary to rid of the solvents in the resist and to make the photoresist more chemically stable. Some surface treatment might be necessary before spinning the photoresist to promote the adhesion of photoresist to the substrate (especially for positive resists). On a silicon substrate, this can be done by coating the substrate surface with a very thin layer of hexamethyldisilazane (HMDS) or other primers such as trichlorophenylsilane (TCPS) or bistrimethylsilacetamide (BSA).

To assure proper construction of the devices, it is necessary that the different layers are aligned to each other as precisely as possible. This is generally done by trying to match the mask patterns with existing features on the wafer while

looking through the mask. Alignment marks are placed on each mask to assist with the alignment of different layers. After aligning the features on the mask and the wafer, the photoresist is exposed to the light through the mask. This can be done in three ways:

(i) the mask and the wafer can be pressed together during the exposure period (*contact printing*);
(ii) the mask is kept at a small distance from the substrate (*proximity printing*);
(iii) mask patterns are scaled using a system of lenses and the final image is projected onto the substrate (*projection printing*).

For proximity and contact printing, the minimum possible feature size (MFS) for a light source with wavelength λ_s is given by:

$$MFS_c = \frac{3}{2}\sqrt{\lambda_s \left(s_{ms} + \frac{d_{PR}}{2}\right)} \tag{2.1}$$

where d_{PR} is the thickness of the photoresist layer and s_{ms} is the separation between the mask and the substrate (0 for contact printing). For projection printing, the minimum feature size is given by:

$$MFS_p = k_1 \frac{\lambda_s}{NA} \tag{2.2}$$

where k_1 is an experimentally determined parameter depending on photoresist properties, process conditions, and mask aligner optics and NA is the numerical aperture of the lenses used for collimating the light (a number between 0 and 1). A NA of one indicates that all of the input light is collected by the lens, which is obviously an ideal case [2].

It is obvious from Eqs. (2.1) and (2.2) that a smaller wavelength results in a better lithography resolution. The wavelengths for typical light sources are in ultraviolet (UV) range (436 nm and 365 nm commonly referred to as *g-line* and *i-line*, respectively), deep ultraviolet (DUV) range (248 nm and 193 nm), and extreme ultraviolet (EUV) range (5–100 nm). As the wavelengths get shorter, it becomes increasingly more difficult to have a light source with enough output energy, find the proper photoresist, and make the required optical elements for the mask aligner. Therefore, it is generally intended to push the limits of a currently working optical setup by different techniques such as immersion lithography (to increase the NA) and phase-shift masks (to reduce the diffraction effects) [2]. Typical lithography systems for MEMS fabrication use g-line or i-line light sources for device dimensions and gaps on the order of μm.

X-rays have also been used for high-resolution lithography [32]. A challenge with using X-rays is the generation of beams with enough energy to expose the

resist. Moreover, designing optical elements for X-rays is not straightforward as X-rays penetrate most materials, which also bring up a challenge in making masks for X-ray lithography systems. However, X-ray lithography has been successfully used to fabricate electronic chips or MEMS and is also being studied for future generation lithography systems [33].

Electron and ion beams can also be used to directly draw the desired patterns on photoresist. Due to their shorter wavelengths, e-beam or ion-beam lithography systems are capable of producing features as small as a few nanometres on photoresist [34,35]. However, due to the sequential nature of their operation, the throughput of these systems is much less than the conventional systems that expose the chip area or even the whole wafer surface in one shot. Moreover, both ions and electrons are charged particles, and therefore, the exposure has to be performed under vacuum. For these reasons, e-beam and ion-beam lithography are currently used only for research or for low volume production (e.g., making masks).

Another technique to print small features on the substrates is nano-imprinting [36,37]. A probe similar to what is used in atomic force microscopy (AFM) is used to transfer the desired pattern onto the substrate. This can be done by physically scratching the surface, local oxidation, or material deposition by controlling the position of the tip of the probe. This technique is capable of producing nanometre scale features. However, since the patterns are drawn on the substrate, nano-imprinting is a slow process.

2.3 Film Growth and Deposition

In order to fabricate a micromachined device, it is often required to work with thin films. These films can be deposited by employing various physical and chemical techniques or can be grown using the substrate material. Depending on application, numerous factors should be taken into account when deciding on the method and parameters for deposition or growth of these films including:

- type of the film (i.e., metal, dielectric, or semiconductor);
- mechanical properties (e.g., the stresses in the film);
- electrical properties (e.g., electrical resistance);
- thermal properties (e.g., thermal conductivity);
- optical properties (e.g., reflectivity in the bandwidth of interest);
- film quality (e.g., the tolerable amount of defects);
- film thickness uniformity across the wafer;
- the required thermal budget to deposit or grow the film;
- other properties (e.g., ferromagnetism and chemical sensitivity);
- deposition/growth rate and cost.

As will be seen later, many films can be deposited in different ways and it is up to the device designer to choose the right technique for his/her particular application. The following sections provide a brief introduction to the commonly used techniques for growing/depositing films for MEMS applications.

2.3.1 Thermal Oxidation

Thermal oxidation can be employed to grow a silicon dioxide (SiO_2) film on a silicon substrate or maybe a polysilicon film. In fact, one of the reasons that silicon replaced germanium in microelectronics was the existence of a stable oxide for silicon that could be easily grown from the substrate. Silicon oxidises if it is kept in an oxygen rich environment at elevated temperatures. The required oxygen can be supplied by a flow of O_2, which results in formation of SiO_2 according to:

$$Si + O_2 \rightarrow SiO_2.$$

This is called *dry oxidation* as opposed to *wet oxidation* where the required oxygen is supplied by water vapour instead of oxygen:

$$Si + 2H_2O \rightarrow SiO_2 + 2H_2.$$

Since the silicon required for formation of the SiO_2 film is from the substrate, the growth rate slows down as the film gets thicker. For the same reason, the growth rate for wet oxidation is higher than dry oxidation since the smaller H_2O molecules more easily penetrate the SiO_2 film than O_2 molecules. However, it takes a very long time to grow silicon dioxide films which are more than a few microns thick even if wet oxidation is employed.

The thickness of the film, x_0, can be predicted using the Deal–Grove model [2,4,38]:

$$x_0^2 + Ax_0 = B(t + \tau) \tag{2.3}$$

where A and B are generally determined through measurements, t is the oxidation time, and τ is a parameter that accounts for the initial rapid growth of thin films for dry oxidation. Values of these parameters for typical oxidation temperatures are given in Table 2.2 [38].

Obviously, growing an SiO_2 film is feasible only if the underlying substrate is silicon and if the required high temperatures do not harm the structures that might already be on the wafer. One might also need to consider the change in the doping profiles and the internal stresses in films due to the high temperature processing of the wafers.

2.3.2 Physical Vapour Deposition

A seemingly straightforward process to coat a substrate with a thin film is to force the atoms of the target material to leave a source and settle on the substrate. Such techniques are referred to as physical vapour deposition (PVD) as no chemical reactions are involved.

Table 2.2 Coefficients for the Deal–Grove Model for Oxidation of Silicon

Temperature (°C)	Dry oxidation			Wet oxidation		
	A (μm)	B (μm^2/hr)	τ (hr)	A (μm)	B (μm^2/hr)	τ (hr)
800	0.370	0.0011	9	–	–	–
920	0.235	0.0049	1.4	0.50	0.24	0
1000	0.162	0.0117	0.37	0.226	0.34	0
1100	0.090	0.027	0.076	0.11	0.60	0
1200	0.040	0.045	0.027	0.05	0.85	0

2.3.2.1 Evaporation

One common technique, especially used for deposition of metallic films, is to evaporate the target material and hold the substrate at a given distance from the target [4,39,40]. To reduce the undesirable effects of present contaminants in the ambient, the whole process is performed under vacuum at low pressures (i.e., in the μTorr range and below).

The *mean free path* is the average distance that a particle travels between collisions with other particles. The value of the mean free path can be calculated from [2]:

$$\lambda = \frac{K_B T}{\sqrt{2}\pi d^2 P_{env}} \tag{2.4}$$

where K_B is Boltzmann's constant (1.3806×10^{-23} J K^{-1}), T is the ambient temperature in kelvin, P_{env} is the pressure, and d is the diameter of gas molecules. A consequence of operation under high vacuum is that the molecules that leave the melt of the target material have long mean free paths. For example, the mean free path of gas molecules at atmospheric pressure is about 60 nm but can be as long as several metres inside an evaporation chamber. This means that the molecules that leave the melt, which can be assumed as a point source of the target material, travel in straight lines until they hit the substrate and settle on it. As a result, evaporated films have poor step coverage, which can actually be used to the advantage of the process flow designer in some cases.

Two techniques are often employed to melt the target materials. In the simpler case, the required amount of the target material is placed inside metallic containers which are made of materials whose melting points are much higher than the target material (e.g., tungsten). Large currents are passed through the container so that through Joule heating the target material eventually melts. A schematic of such a system is shown in Fig. 2.2. In some cases, pieces of the target material are put inside a crucible which is heated by passing a current through the metallic coil wrapped around it. It is obviously difficult to evaporate materials with high melting temperatures using the above technique. Moreover,

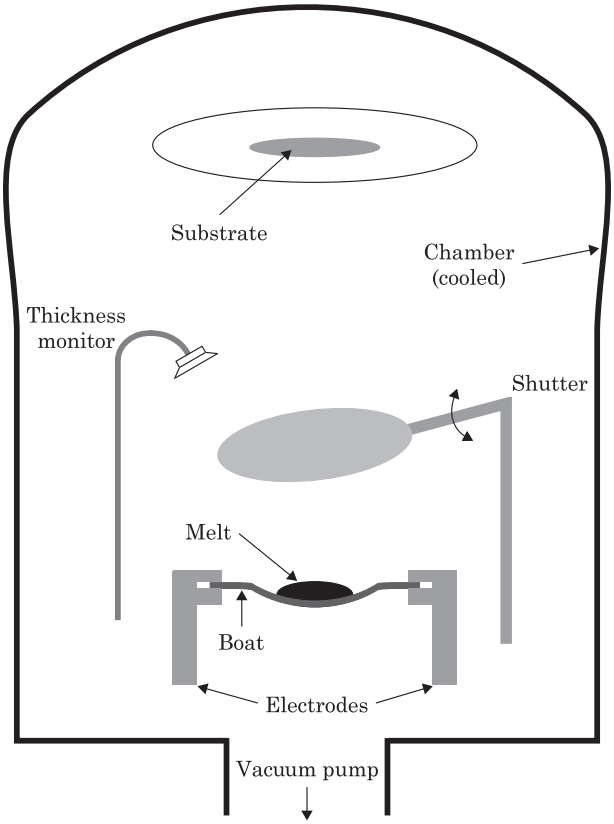

Figure 2.2 Schematic of a thermal evaporator.

since the boat or the coil are heated at least as much as the melt, they might introduce contamination that can affect the quality of the deposited film. The problem of raising the temperature can be circumvented through inductive heating of the target material in the crucible, but the problem of contamination from the crucible remains.

The second heating technique to avoid contamination from the containers is by locally heating the target material with a high power electron beam. The high energy electrons that bombard the target metal and heat it up, also radiate X-rays. This might be undesirable in some applications especially if electronic devices already exist on the substrate.

The deposition rate and the thickness of the evaporated film are usually monitored with the aid of a crystal oscillator (see Fig. 2.2). During the process, the evaporated material settles on the surface of the crystal and modifies its resonant frequency, which is then detected by monitoring the output of an oscillator circuit around the crystal resonator. This, in fact, is an example of using a resonator for sensing applications.

In addition to being able to evaporate and pattern a film at a later step, evaporation is used as part of a common technique for patterning metal structures, called *lift-off*.

2.3.2.2 Sputtering

Sputtering is another method for coating a substrate with a thin film of a target material in a physical manner (i.e., without chemical reactions). The surface of the target is bombarded with a flow of relatively heavy ions to knock off atoms at the surface of the target material which then settle on the surface of the substrate and gradually form a film of the material. The ion flow needed for bombardment of the target is produced with the aid of a plasma at pressures on the order of a few mTorrs. Argon is often chosen because of its high atomic mass and the fact that, as a noble gas, it does not react with the target or substrate. Xenon has also been used for physical sputtering of materials. The required plasma can be generated by applying a large DC voltage (from about 500 V to few kilovolts) between two electrodes spaced apart from each other by 5–10 cm. For a large enough electric field, the free electrons in the gas between the electrodes accelerate towards the anode (i.e., the electrode connected to the higher voltage) and collide with gas molecules in their path, resulting in release of a large number of excited atoms, high energy electrons, and positive ions. This phenomenon is known as *gas breakdown*. When the excited atoms return to their relaxed state, they emit the excess energy in form of photons, which gives a plasma its characteristic glow (see Fig. 2.3). The plasma is sustained by continuous generation of these energised particles. The plasma colour and intensity can be used to calculate and monitor the deposition rate in a sputtering system [39]. The generated positive ions bombard the cathode, transfer part of their momentum to the atoms at the surface of the cathode, and may knock them off if they have enough energy. Some of these atoms settle on the surface of the substrate and form the film.

If the target is made of, or covered with, an insulating material, the energised particles in plasma cause accumulation of charge on the surface of the target, opposing the DC field across the plasma, and eventually extinguishing the plasma. This can be avoided by using an alternating field, usually with a frequency of 13.56 MHz, to ignite and sustain the plasma. The heavy ions cannot respond to such a high frequency and it is the electrons that travel between the electrodes, leaving both electrodes with a net negative charge. However, the electric potential on each electrode is proportional to their areas, and therefore, one of the electrodes can be made to sit at a higher electric potential (by modifying their relative areas), causing the positive ions to travel toward the electrode with a smaller area; i.e., the target as the substrate is often placed on a metallic tray with a large surface area [2,39,40].

To increase the sputtering rate, one needs to improve the ionisation rate of the gas molecules. A large DC magnetic field can be used to force the electrons

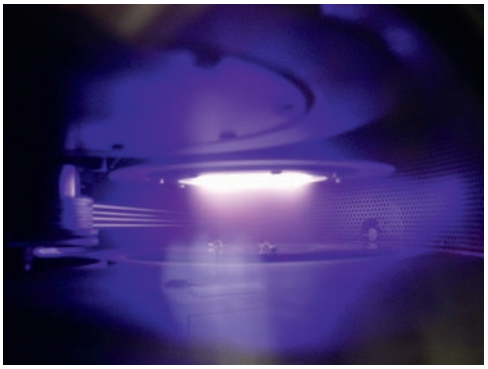

Figure 2.3 The generated plasma in a sputtering system.

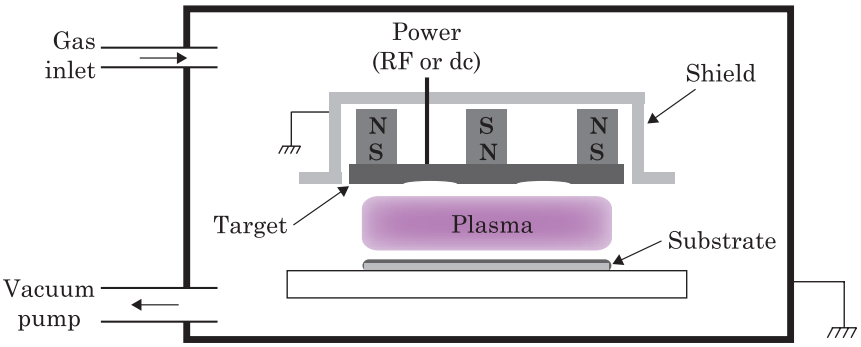

Figure 2.4 A simple magnetron sputtering system.

into orbitary motion in the proximity of the target, and hence, increase the chance of producing ions. The increased ion density also allows for starting and sustaining the plasma at lower pressures to lower the level of contaminants. Fig. 2.4 illustrates the assembly of a simple sputtering system.

Since sputtering is performed at relatively higher pressures compared to evaporation, the mean free path of particles is considerably shorter (on the order of millimetres or less). Consequently, atoms of the target material undergo several collisions before settling on the surface of the sample, which is often a few centimetres away from the target. This results in improved step coverage for sputtered films. Sputtering offers many advantages over evaporation, partly due to the larger number of process variables that can be modified (e.g., pressure, power, temperature, bias, etc.). The thickness, uniformity, and stress in deposited films can be controlled more easily in sputtering than evaporation. Furthermore, a wide variety of materials, including many metals and dielectrics, can be sputtered while evaporation is generally limited to metals. Sputtering also allows for simultaneous or layer-by-layer deposition of several materials, and thereby, formation of alloys. However, the evaporated films can potentially

Figure 2.5 Lift-off processing steps: (a) spinning and patterning of the photoresist layer; (b) evaporation of the metal thin film; and (c) removal of the photoresist layer and excess metal.

be purer as they are deposited under high vacuum conditions. Moreover, the chance for the sample to get hot is higher for sputtering than evaporation.

It is possible to use non-inert gases in sputtering processes. Nitrogen and oxygen have been used for reactive sputtering; i.e., their energised atoms in plasma react with the target material and the substrate is coated with the reaction byproduct. This technique is often used for sputtering of aluminium nitride (AlN) films for piezoelectric transducers [41,42].

2.3.3 Lift-off

Lift-off is a technique to deposit a thin patterned metal layer on a substrate [2,43]. The surface of the substrate is covered with photoresist with the negative image of the desired final pattern, either by using a positive mask and a negative resist or vice versa. The coated substrate is transferred to an evaporation system and a thin metal film is evaporated on the photoresist and the exposed substrate. Thanks to the poor sidewall coverage in evaporation processes, the photoresist remains exposed on sidewalls and the deposited metal film will be discontinuous. The final step in lift-off is to remove the photoresist by dissolving it in a solvent, which at the same time causes removal of the portion of the metal film which was deposited on the photoresist layer. These steps are illustrated in Fig. 2.5.

It should be noted that as a consequence of using evaporation to deposit the metal layer, the sidewall coverage in lift-off process is poor and having steep sidewalls on the surface of the chip may result in discontinuities along the signal path. Thereby, lift-off is often used when the wafer surface is relatively smooth.

2.3.4 Chemical Vapour Deposition

Chemical vapour deposition (CVD) is a versatile and flexible technology to deposit a variety of different materials including dielectrics, semiconductors, and metals [2–4,40,44–47]. As the name suggests, the process involves chemical reactions. Although the process can happen in a liquid environment, the CVD process in micromachining and microelectronics is often performed in a gaseous ambient, offering better control over process parameters and reducing contamination.

The steps in a CVD process are [2,4]:

- the precursor gases are transferred to the surface of the substrate, where they usually react with each other and produce a range of daughter molecules;
- the gas molecules are adsorbed at the surface;
- with the surface acting as a catalysor, the molecules react with each other, resulting in the deposition of the desired film material;
- the reaction byproducts are desorbed from the surface and transported away from it.

A typical CVD system is schematically illustrated in Fig. 2.6.

Depending on the target film, different gases are combined under controlled conditions and made to react with each other. The deposited film is usually the byproduct of the reaction between the different gas molecules although in some cases, the deposited film is from the decomposition of a single gas. For example, a polysilicon film can be deposited from silane according to:

$$\mathrm{SiH}_4^g \longrightarrow \mathrm{Si}^s + 2\mathrm{H}_2^g$$

where the superscripts ^{g} and ^{s} indicate that the material is in gaseous or solid form. The solid byproducts of a reaction can be produced in the gaseous environment above the surface and then fall onto the surface. However, in order to have a high quality film, it is important that the solid byproducts be produced on the surface of the wafer and not in the gaseous media.

The CVD processes can be categorised based on the pressure inside the chamber during the process. Until the 1960's, the CVD was performed at atmospheric pressures (APCVD) at elevated temperatures in the range of 700 to 1250 °C. After introduction in early 1970's, low pressure CVD (LPCVD) systems replaced APCVD ones in most applications. In an LPCVD chamber, the reactions occur at pressures in the 100's of mTorr range. The advantages of LPCVD over APCVD films include better uniformity, lower processing temperatures, and less dependence on gas dynamics inside the chamber.

In order for the mixed gases to react with each other, they need to be activated by supplying additional energy. In APCVD and LPCVD systems, this extra energy is provided thermally, requiring high temperatures for deposition

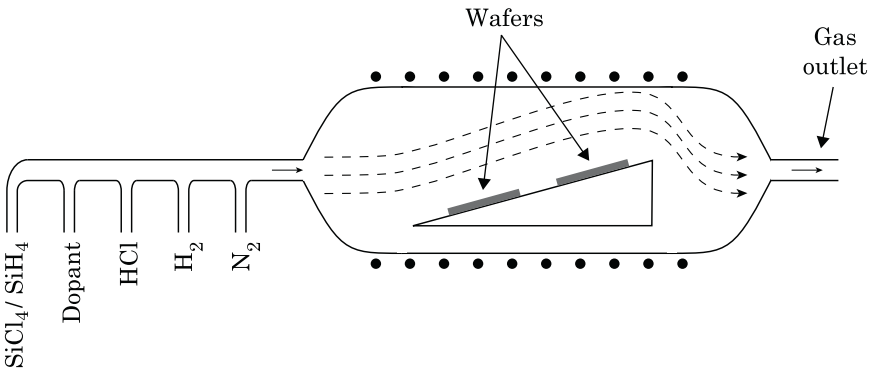

Figure 2.6 A typical polysilicon CVD system with heater elements around the chamber and gas inlets.

of films. However, such high temperatures are difficult to design around. For example, aluminium forms an alloy with silicon at about 650 °C, which is unacceptable in microelectronic processes. On the other hand, high processing temperatures also modify the doping profiles, which in most cases is undesirable. For these reasons, another form of CVD processes, known as plasma enhanced CVD (PECVD), was developed where the activation energy was provided by a plasma. It became evident from the early days of using CVD in microelectronic processes that the surface of the substrate had to be clean and contamination-free in order to have a high quality film with good adhesion to the bottom layers. Another advantage of PECVD over LPCVD and APCVD systems is the possibility of cleaning the surface through removing (i.e., etching) a thin layer from the surface before the deposition process.

While depositing a film, it is possible to add dopants carriers to the precursor gases to modify the electrical properties of the film. Mechanical properties of the deposited films are also influenced by the process parameters such as pressure and temperature. It is also possible to fine tune the mechanical/electrical properties of the films by depositing sandwiches of different layers. For example, one can alternate layers with internal tensile and compressive stresses in them in order to obtain a composite structure that is effectively stress-free. As another example, it is common to deposit a polysilicon film followed by a silicon dioxide layer that is highly doped with phosphors. Annealing these films will result in the diffusion of dopants into the polysilicon film and lowering its resistance.

A particular case of polysilicon CVD has been of great importance in microelectronics. If the surface of a silicon wafer is such that the crystalline structure is exposed (i.e., there is no native oxide or any other film or contamination on the surface), the atoms in the deposited film align themselves with the orientation of the atoms from the substrate, leading to the growth of a single crystalline silicon film. This process is called *epitaxy*. An epitaxial film is of high enough quality to be used for fabrication of electronics devices. It is possible to have an abrupt pn junction by adding proper dopants to the

deposited film that is grown on top of a substrate with the opposite type of doping. In fact, the transistors in bipolar processes with junction isolation used to be fabricated from an epitaxial layer [48]. In order to assure a clean substrate surface, a chlorine based chemistry is used to deposit the epitaxial silicon film:

$$\mathrm{SiCl}_4^g + 2\mathrm{H}_2^g \longrightarrow \mathrm{Si}^s + 4\mathrm{HCl}^g.$$

By modifying the ratio of $SiCl_4$ to H_2, one can vary the deposition rate and even switch between deposition and etching, an essential step to clean the substrate [44,48]. In CMOS processes, epitaxial layers have been used to prevent latch-up.

2.3.5 Electroplating

Electroplating, or electrodeposition, is a metal deposition technique that has been used at industrial scale since the early nineteenth century. It is possible to electroplate metallic layers as thick as several hundred microns with acceptable quality and internal stress levels. In a typical electroplating setup (see Fig. 2.7), the wafer is connected to the negative pole (i.e., *cathode*) of a voltage source while an electrode made of the target material is connected to the positive pole (i.e., *anode*). The electrode and the wafer are then immersed into a solution, known as *electrolyte*, which contains ions of the target metal. The electrolyte is a solution of one or more metal salts and sometimes organic agents. If the surface of the wafer is covered with a conductive layer, the positively charged ions in the solution move towards the wafer and settle on it, closing the electric circuit. In order to selectively deposit the metal, it is required to use a negative mask to cover the areas which should not have the metal layer deposited on them. The masking layer also acts as a mould as long as the thickness of the deposited film is less than the sidewall height of the mask layer. During the process atoms from anode replace the ions that have settled on the wafer, and therefore, as long as the solution volume is kept constant, its chemical properties should not change.

The processing steps for electroplating a metal layer are:

(i) a seed layer, typically a thin layer of sputtered or evaporated metal, is deposited on the wafer for electrical conduction;
(ii) a mould layer (e.g., photoresist) is deposited and patterned to selectively expose the seed layer;
(iii) the metal film is deposited in the electroplating setup as discussed above;
(iv) the mould layer is removed;
(v) the seed layer is removed from areas not covered by the deposited metal.

Parameters that control the film properties, especially the density and internal stress, are the plating current and temperature.

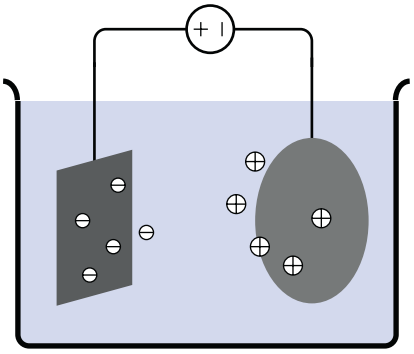

Figure 2.7 An electroplating bath.

When plating with a DC source, the deposition rate becomes diffusion limited; i.e., the maximum plating rate will depend on the density of ions in a boundary layer around the cathode surface and the speed that the ions penetrate through this region. One can reduce the thickness of this boundary layer by using a pulse voltage source and switching the direction of the plating current for a portion of each cycle[1]. Using a pulse source increases the limit for plating current due to the reduced thickness of the diffusion layer and the improved nucleation rate, leading to higher deposition rates in pulse plating. The plating frequency is usually between 100 Hz to 10 kHz with duty cycles in the 10 to 30% range. The duty cycle and plating frequency can also be fine tuned to adjust the deposited film parameters, such as reflectivity, stress, and density.

Nickel, copper, gold, and some ferromagnetic alloys are layers which are electroplated in micromachining more often than other materials [49–55]. Copper is usually plated in a pulse plating set-up while nickel is DC plated. Electrodeposition of nickel structures, in particular, is a common technique for fabrication of tall metallic structures thanks to the low stress levels in plated nickel films.

LIGA is probably the best known method of fabricating high aspect ratio structures. LIGA is an acronym derived from the German words Lithografie, Galvanik, Abformung, which mean lithography, electroforming, and injection moulding [33,56]. In a standard LIGA process, high intensity, low divergence, hard X-rays, usually produced by a synchrotron, are used as the exposure source to pattern a thick PMMA (polymethylmethacrylate) layer as the X-ray resist. Thicknesses of several hundreds of microns and aspect ratios of greater than 100 to 1 have been achieved for structures made in LIGA or LIGA like processes [57]. By means of subsequent replication processes, such resist relieves may be transformed into complementary relief structures [58].

[1]The average or the DC value of the waveform should still be negative in order to have a net amount of plating on the wafer.

Table 2.3 Common Etchants in Micromachining

Target	Etchant	Etch type	Typical etch rate
Si	KOH	wet/anisotropic	1.4 μm/min
Si	TMAH	wet/anisotropic	1 μm/min
Si	XeF_2	dry/isotropic	0.5–5 μm/min
Si	$SF_6 + O_2$	dry/anisotropic	0.8–1.5 μm/min
Si	$CF_4 + O_2$	dry/anisotropic	0.1 μm/min
Si	$SF_6 + C_4F_8$	dry/DRIE	0.5–3 μm/min
SiO_2	HF	wet/isotropic	0.02–0.23 μm/min
SiO_2	CHF_3	dry/anisotropic	0.07–0.2 μm/min
Si_3N_4	H_3PO_4	wet/isotropic	4.5 nm/min
Si_3N_4	$SF_6 + O_2$	dry/anisotropic	0.15–0.2 μm/min
Al	$BCl_3 + Cl_2$	dry/anisotropic	0.5 μm/min
Ti	HF	wet/isotropic	0.2–1.1 μm/min
Photoresist	O_2	dry/isotropic	0.2–0.5 μm/min

2.4 Etching

Etching is a very critical step in microfabrication. In most cases, a lithography step is followed by the selective etching of films or substrates to produce the required patterns and structures. Consequently, an important factor is the *selectivity* of the etch; i.e., the relative removal rate of the target material to that of the masking layer or other structures. Since the etched profiles can be as deep as several hundred microns, proper choice of masking materials and their thicknesses is critically important to avoid unwanted removal of the features on the substrate. The most commonly used materials for mask layers when etching polysilicon or crystalline silicon are silicon dioxide and silicon nitride. Metal films have also been used as masking layers in dry etching processes.

Etching techniques can be categorised according to the resulting profiles. If the etch proceeds without a directional preference, it is called *isotropic*. If certain directions are etched at different rates than the others because of the structure of the substrate or the process variables, the etch is called to be *anisotropic*. The etching processes can also be divided into two groups based on whether they are performed in a liquid media (*wet etching*) or in a gaseous environment (*dry etching*). General references on etching recipes and techniques for microfabrication applications are [1,10,59–61]. Table 2.3 summarises some of the common etching chemistries and the target materials in microfabrication of MEMS.

2.4.1 Wet Etching

In the early days of microelectronic processing, almost all of the etching steps included dipping of the sample in a liquid solution which selectively reacted with

the desired material. Wet etching is a purely chemical process during which the etchant molecules need to move to the surface of the sample, react with the substrate material, and the reaction by-products have to be removed to allow for the etch to proceed. However, controlling the wet etching process is not simple and there is a higher chance of contamination for the processed samples.

In special cases, wet etching can be anisotropic; i.e., the etch proceeds faster along certain crystallographic directions than the others. A well-known example is etching of single crystal silicon substrates in alkali solutions such as potassium hydroxide (KOH). KOH etches (100) planes about 400 times faster than (111) planes [10]. Consequently, etching holes on <100> silicon wafers in KOH (or similar alkali solutions) produces sidewall angles of 54.74°, which is the angle between (100) and (111) planes. Tetramethyl ammonium hydroxide (TMAH) is another popular anisotropic wet etchant of silicon. The advantages of TMAH over KOH are its better compatibility with IC processes and better etch selectivity between silicon and SiO_2 or Si_3N_4.

Another important wet etchant is hydrofluoric acid (HF) which is used to etch SiO_2[1]. Although being a dangerous substance whose handling demands extreme levels of care, its selectivity to silicon has led to its application in many micromachining processes. Diluted or buffered HF solutions are often used to remove sacrificial oxide at the end of a fabrication process and release the moving parts of the device.

The etch depth in wet processes can be controlled using a variety techniques. The straightforward method is to etch trough the thickness of the whole film and stop at the interface of the next thin film layer. The etch rate of some substrates in certain chemicals depends on the doping levels at different regions, which can be employed to stop the etching process and define patterns. Lastly, sometimes the etch is bias dependent and can be stopped at biased *pn* junctions [1,62].

2.4.2 Vapour Phase Etching

Certain gases may directly attack the substrate material without external energy sources. However, to control the etching process, the reactions need to be contained in chambers, usually at defined pressures.

Xenon difluoride (XeF_2) is an example of such gases that can be used to etch silicon [63,64]. XeF_2 is a white crystalline solid with a sublimation pressure of about 4 Torr. XeF_2 is extremely selective to silicon; i.e., it etches other materials with negligible rates. Since no external energy sources are required to start and maintain the etch, the processing systems are relatively simple and inexpensive. A XeF_2 etching system is typically composed of a vacuum chamber, a container for XeF_2 crystals, and often an expansion chamber to let the solid XeF_2 sublime and the gas reach operating pressures. Properties of XeF_2 make it a suitable candidate to release microfabricated structures by etching sacrificial or bulk silicon. Bromine trifluoride is another gas with properties similar to XeF_2 but is more toxic than XeF_2 and seldom used [65].

HF vapour can be used to etch SiO_2 films in a similar manner using custom made or commercially available systems [66,67]. Using a vapour HF system is safer than dealing with liquid HF as the chemicals are contained inside a reaction chamber.

2.4.3 Ion Milling

Ion milling is at the other extreme of processes for etching of a substrate where the material removal is purely due to its physical bombardment. In such a process, ions of inert gases (usually argon) are accelerated towards the substrate where they eject the molecules from the surface of the substrate. This is very similar to what happens in a sputtering system where the target is bombarded with atoms of an inert gas. The main difference is in the ion energies and the resulting directionality of the process. The etching pressure is often around 1 mTorr or below.

Ion milling, due to its physical nature, can be used to pattern a wide variety of materials, even those for which a proper chemical etchant is not available. However, this also causes processing issues as the masking layers are also etched in this process with poor selectivity [2,68]. The other disadvantage of ion milling, especially when using large-diameter wafers, is its low throughput due to the limitations on the diameter of the ion beam. On the other hand, focused ion beams (FIB) are frequently used and can cut trenches as narrow as 20 nm if required [69,70]. Such beams can also be used to cut through the substrate to prepare samples for taking cross-sectional images [71].

2.4.4 Reactive Ion Etching

While the isotropic nature of vapour phase etching makes it suitable for releasing fabricated microstructures, the lack of control on etched profiles hinders their application for patterning of the structures. As an example, it is often needed that the sidewalls of the microdevices be smooth and vertical (or close to vertical), which is generally unachievable with isotropic etchants. On the other hand, throughput and selectivity issues of ion milling make it unsuited for many processes. A compromise can be reached by combining both physical and chemical etching processes: the etchant molecules can be electrically charged and accelerated toward the substrate in order to add anisotropy to gas phase etching, hence the name reactive ion etching (RIE). This procedure etches the substrate preferentially in the direction of the trajectory of the etchant ions. The etchant molecules can be ionised with the aid of a plasma. Similar to sputtering, an external electrical field energises the free electrons inside a chamber, which then ionise the etchant molecules upon colliding with them. Typically, the etching pressures inside an RIE chamber are between 5 to 500 mTorr [72].

To make the etch more directional, it is desired to perform the etch at low pressures (5–20 mTorr). At these pressures, the mean free path of the ions is relatively large and it is hoped that the accelerated ions will hit the substrate before colliding with other gas molecules. However, in a low pressure environment, there are fewer radicals, and therefore, the etch rates are relatively small (e.g., 0.1 μm/min or less). To increase the etch rate and maintain the directionality of the etch, a magnetic field may be employed. As with the sputtering systems, this external magnetic field mainly affects the light and agile electrons by forcing them to have a circular path inside the plasma. These energised electrons travel a much longer distance inside the plasma and the probability of their collision with inactivated molecules significantly improves. Consequently, the number of radicals in the plasma increases, and so does the etch rate. The required magnetic field is usually produced by a coil around the plasma volume, and hence the name *inductively coupled plasma* (ICP) (see Fig. 2.8). As an example, ICP sources produce plasma densities on the order of 5×10^{11} cm^{-3}, compared with densities of $0.5–5.0 \times 10^{10}$ cm^{-3} without an ICP source. Due to the increase in the number of radicals, it is possible to maintain the plasma at pressures as low as 1 mTorr. Another advantage of RIE with ICP is that the etching can be performed with smaller RF powers, and hence, it is a less aggressive etch than the normal RIE for applications where damage to the substrate or the mask is a concern.

Most materials that are used in typical microfabrication processes can be etched in a reactive ion etching chamber with proper gas chemistry. It should be noted that the masking layers are also bombarded with ions during the etch process. Consequently, the selectivity of the etch to typical masking layers (e.g., photoresist, SiO_2, and polysilicon) is worse than what is possible in most wet etching and vapour phase etching processes.

A research scale RIE system which uses an ICP source for higher plasma density is shown in Fig. 2.9. Refer to Table 2.3 for a summary of some of the etch chemistries which are often used in microfabrication processes.

2.4.5 Deep Reactive Ion Etching

Silicon is readily etched in an environment with fluorine radicals (as in XeF_2 etching). Therefore, it is the acceleration of the ions towards the substrate which gives the RIE its directionality. While RIE provides almost vertical sidewalls for etch depths of 2–3 μm, the directionality of the etch worsens as one tries to etch deeper into a silicon substrate. On the other hand, in microfluidic applications, it is sometimes required to etch 100's of microns into the substrate or even etch through the wafer (e.g., 0.5–1 mm). For fabrication of microdevices, vertical sidewalls are often required with structural thicknesses as high as 10–20 μm, which is very difficult to achieve in RIE systems. There are two deep reactive ion etching (DRIE) techniques that offer more directionality than the simple RIE

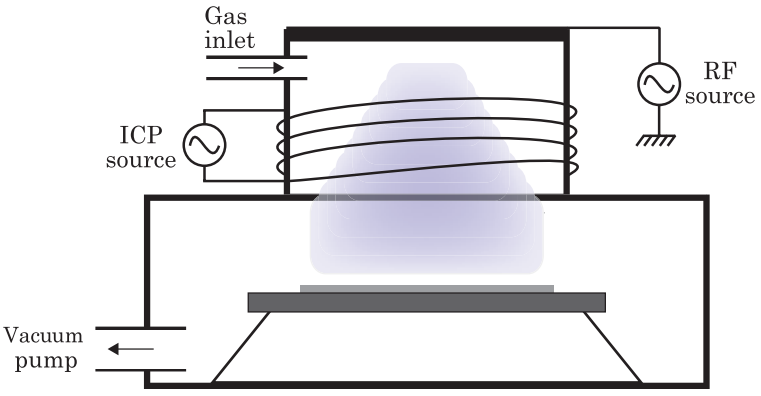

Figure 2.8 An RIE system with the ICP source.

Figure 2.9 An RIE system. *Courtesy of Oxford Instruments.*

process: Bosch process and cryogenic etch [73]. A common masking material for etching of silicon is a film of grown/deposited SiO_2 for both processes.

2.4.5.1 The Bosch process

The Bosch process relies on alternative etch and deposition cycles [73,74]. The etch step is similar to RIE of silicon with SF_6. However, after a fixed period of etching, SF_6 is pumped out and C_4F_8 is introduced into the chamber. During

Figure 2.10 Subsequent etch and deposition cycles in a DRIE process and the resulting scallop-like edges on sidewalls.

the deposition step, C_4F_8 breaks into CF_2 and other Teflon-like longer polymer chains which coats everywhere on the substrate, including the sidewalls. The ion bombardment in the subsequent RIE step removes the deposited material from the bottoms of the etched regions but the sidewalls are passivated with a few nanometres of the deposited layer. The deposition and etch cycles are repeated until the desired etch depth is achieved as illustrated in Fig. 2.10. The etch rate and profile can be modified by changing the efficiencies of the deposition and etch steps or by adjusting the ratio of the time for each of the two steps. The deposition and etch cycles can be as short as 3 seconds, but are usually around 10 seconds. Therefore, it is required to choose fast mass flow controllers for the gas lines and a fast vacuum pump to be able to switch between the gas chemistries quickly and efficiently. Inductive coupling is employed to increase the plasma density at the operating pressures (10–50 mTorr). Typical etch rates are on the order of 0.5–5 μm/min.

Due to the alternating deposition and etch steps in Bosch process, the sidewalls of etched structures exhibit a roughness on the order of 2–5 nm (see Fig. 2.10). Moreover, the sidewalls may have a positive or negative slope, depending on the mask openings and etch parameters. The etch depth in Bosch process also depends on the width of the mask opening. Buried etch stop layers, for example as with silicon-on-insulator wafers, should be used if the accurate etch depth is important. Fig. 2.11 illustrates an example of the depth and the aspect ratios which can be obtained with a Bosch process.

2.4.5.2 Cryogenic etching

In cryogenic DRIE, the wafer is placed on a cryogenically cooled chuck and is held at −170 °C to −100 °C during the process. The cold environment reduces the isotropic etching due to chemical reactions but the etch due to ion bombardment proceeds while the sidewalls of the etched profiles are protected by a deposited film of the etching byproducts [75,76]. The combination of these effects results in almost vertical sidewalls without the scallop-like features on the sidewalls of the structures etched in the Bosch process. However, Bosch process in general offers higher aspect ratios and depth, particularly when etching silicon.

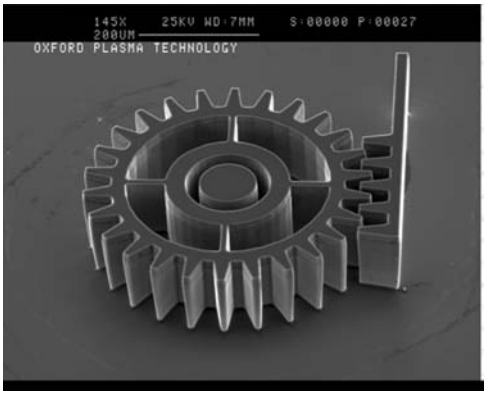

Figure 2.11 A gear etched using Bosch process. *Courtesy of Oxford Instruments.*

2.5 Doping

One of the main reasons for the widespread use of semiconductors in microelectronics is that their electrical properties can be modified in a controlled way by adding minute amounts of specific impurities to them. *Doping* is the process of adding such impurities known as *dopants*, to the bulk or a film of the semiconducting material. The concept of doping is explained in the simplest form by looking at a two dimensional (2D) model of atoms and their covalent bonds in crystalline silicon. In its pure form, each atom in a perfect crystal with covalent bonds shares its outmost electrons with the neighbouring atoms, and therefore, the electrons are relatively tightly bound to their locations at low temperatures (Fig. 2.12-a). As a result, a semiconductor behaves almost as an electrical insulator at low temperatures. As one raises the temperature, some of these electrons gain enough energy to break free from these bonds and the resistivity of the crystal drops with temperature. However, the resistivity of pure semiconductors remains high at typical operational temperatures of most devices (e.g., -40 °C to 140 °C).

If a silicon atom is replaced with an atom with an extra electron in its outmost shell, this extra electron is loosely bonded to its original location. At elevated temperatures, such electrons can hop between neighbour silicon atoms in our simple 2-D model (Fig. 2.12-b). This mobile negative charge reduces the resistivity of the bulk of the semiconductor. A piece of semiconductor with extra free electrons is called to be n type. A similar case happens when the dopant atom lacks one electron in its outmost shell compared to the silicon atom; i.e., when it has 3 electrons in its outmost shell. In this case, electrons from the neighbour silicon atoms can hop into this empty spot, and in turn, leave a positively charged ion behind. The whole process is similar to having a mobile positive charge, known as a *hole*, in the lattice (Fig. 2.12-c). A piece of semiconductor with more holes than electrons is called to be p type. Phosphorous and arsenic from the fifth group in periodic table of elements are

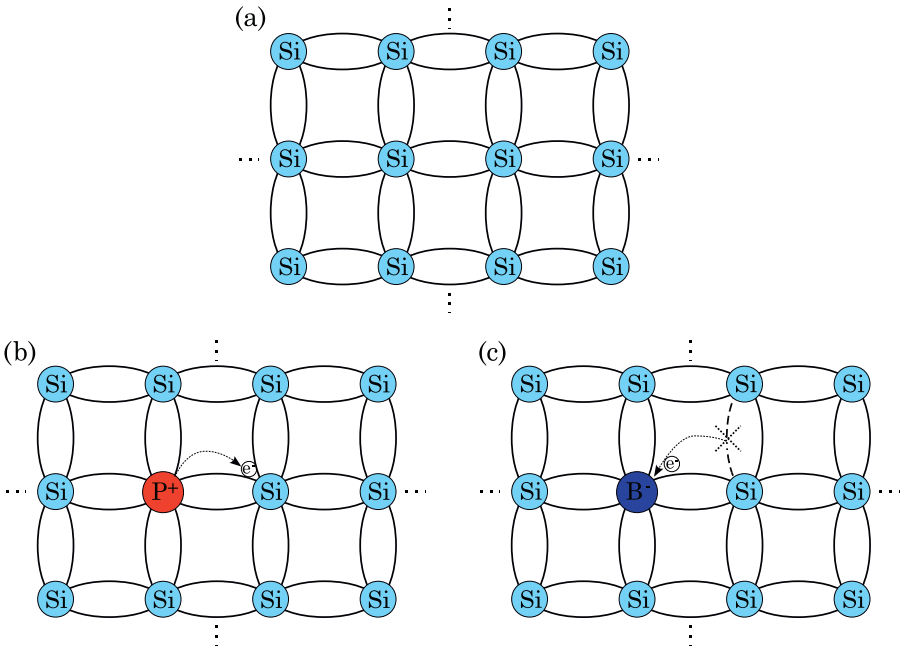

Figure 2.12 The 2-D model of an undoped silicon crystal (a) and addition of n-dopants (b) and p-dopants (c) to the crystal.

typical n-type dopants of silicon while boron and aluminium, from the third group in periodic table, are the typical p-dopants for silicon.

Diffusion theory states that matter flows in a direction to reduce the concentration gradients. Diffusion was the technique that was originally used to dope semiconductor wafers [2–4]. The wafers are placed inside a furnace between 800 °C and 1200 °C and a gas containing the desired dopant is passed over the wafers. The depth and level of doping are determined by the relative gas pressure and the doping time. Areas of the wafer that need not be doped can be protected with a masking layer, such as SiO_2 or Si_3N_4. All early processes in microelectronics employed this technique to fabricate electronic devices.

An alternative technique which has been employed for cases where the exact level of doping or depth are not too critical is to cover the wafer surface with a paste containing the dopants and place the wafer in a rapid thermal annealing system. Dopant atoms penetrate the silicon wafer much like the case where a gas was used for doping. This technique is frequently employed to crudely adjust the resistivity of a wafer and for the fabrication of inexpensive solar cells.

The high temperatures that are needed for diffusion can be incompatible with other processing steps. Moreover, diffusion is more or less an isotropic process; i.e., the dopant atoms diffuse sideways under the mask openings almost as much as they penetrate into the bulk. For these reasons, a technique similar to RIE

Figure 2.13 Doping profiles after diffusion (a) and ion implantation (b).

has been developed: the dopant ions are accelerated towards the substrate which then penetrate into the substrate due to their momentum [2,4]. The wafer is often tilted slightly to avoid deep penetration of the dopants into the substrate through the crystalline structure. However, this physical process damages the crystal structure and a thermal treatment step is required to anneal the crystal. The thermal treatment also activates the implanted dopants by letting them fit into the crystal structure. The doping level can be set by adjusting the ion dose and time.

A significant advantage of ion implantation over diffusion is the control over the doping profile and depth besides the doping level. The doping depth can be controlled by choosing the energy of the ions and the dopants can be implanted anywhere from just under the surface up to as much as few micrometres deep into the bulk. Sample doping profiles after diffusion and ion implantation are shown in Fig. 2.13. In addition to the obvious advantages of doping depth control in microelectronics, this technique can also be employed to form an insulating layer inside the bulk of a silicon wafer if oxygen atoms are implanted beneath the surface.

2.6 Bonding

Fabrication of several complicated mechanical devices requires not only the machining of individual components but also the assembly of components. In micromachining, bonding techniques are used to assemble individual micromachined parts to form a complete structure. Entire wafers or individual dies can be bonded together [77–81].

Several bonding processes have been developed for different applications. Silicon direct bonding is used to bond a pair of silicon wafers together directly. This technique is often called *fusion bonding* as the two wafers are pressed together at elevated temperatures (typically 800 °C and above) until they bond

Figure 2.14 Schematic of an anodic bonding setup.

to each other. Cleanness of the surface of the wafers and their smoothness are the important parameters to insure a high quality bond [82,83]. Fusion bonding can be used on bare or oxidised wafers. A primary application of silicon fusion bonding is in the fabrication of silicon-on-insulator (SOI) wafers, where a wafer bonding and thinning process is used to produce a bulk-quality layer of single-crystal silicon over a thin film of thermally grown silicon dioxide.

A bonding technique that can be performed at much lower temperatures is bonding of a glass substrate to a silicon wafer. This process is called *anodic bonding*, as a large positive DC voltage (i.e., 400–1000 V) is applied to the silicon wafer (i.e., anode) while the silicon and the glass substrates are held together at about 450 °C (see Fig. 2.14). Under such conditions, the ions in the glass substrate, especially sodium ions, will become mobile and move away from the glass–silicon interface. The fixed negative charge that is left behind at the interface contributes to a space charge layer in close proximity to the silicon substrate and most of the applied potential will appear across this layer. The produced electric field pulls the surfaces together and initiates the bonding process, usually from the touching point of the probe and the glass substrate. Compared to fusion bonding, anodic bonding is more tolerant of surface roughness and contamination. Besides the fabrication of micromachined structures, anodic bonding has been frequently used for wafer level packaging of fabricated devices. If required, two glass wafers can also be anodically bonded to each other. In this case, however, a thin silicon film is usually deposited on the glass substrate that is connected to the anode [1,84].

Sometimes the alloy of two materials has a lower melting point than either of the original materials. The melting point of the alloy of these materials is called the *eutectic* point. This property can be exploited to bond two substrates to each other through a process called *eutectic bonding* for the process. Each of the substrates is coated with one of the two materials. The wafers are then brought into contact and heated so that diffusion causes the two materials to mix with each other at the surface. When a thin layer of the alloy is formed, it melts and produces a permanent seal after cooling. Materials that have been used for eutectic bonding for MEMS applications include Au–Sn with a eutectic point of 363 °C and Sn–Pb with a eutectic point of 183 °C [85,86].

Figure 2.15 Fabrication of SOI wafers through bonding: two oxidised wafers are bonded together and the desired device layer thickness is achieved through thinning the top wafer.

2.6.1 Silicon-On-Insulator Wafers

It is often needed that different segments of a microfabricated device to be kept electrically isolated from each other; e.g., the electrodes of a capacitive transducer. Furthermore, the final step in most processes is to release the structure by etching a sacrificial layer. Therefore, MEMS are often made from an electrically conductive structural layer above an insulating layer. On the other hand, the required thickness for the structural layers for MEMS often falls in the 1–50 μm range. While it is possible to deposit structural layers through typical CVD or PVD processes, obtaining films thicker than a few micrometres is challenging partly due to difficulty in controlling the quality and internal stresses during deposition processes.

A technique that can considerably simplify the processing step, especially in cases where a single structural layer is needed, is to use silicon-on-insulator (SOI) wafers where a layer of SiO_2 is sandwiched between a relatively thin layer of single crystalline silicon and a handle wafer. The SOI wafers are generally fabricated in two ways: either oxygen atoms are implanted and activated at a certain depth into a silicon wafer or two oxidised wafers are bonded to each other. In the implantation technique, known as *separation by implantation of oxygen* (SIMOX), high energy oxygen atoms are implanted at depths of 100–1500 nm below the wafer surface. These atoms are then activated in a high temperature furnace and after reacting with the silicon atoms, form a *buried* silicon oxide layer which electrically isolates the top silicon layer from the wafer bulk [8,87]. Due to the practical restrictions on the implantation depth of the oxygen atoms, the thickness of the top silicon layer for SOI wafers that are fabricated with this method is limited to a few hundred nanometres. Moreover, making SOI wafers thorough SIMOX for large wafers (i.e., larger than 200 mm) is a slow process because of the limitations on the ion dose and ion beam diameter. Consequently, most SOI wafers for MEMS fabrication are made through bonding (see Fig. 2.15). The top wafer is thinned down in order to have the desired thickness for the silicon layer which will be used as the structural layer, also referred to as the *device layer*. The thickness of the *buried oxide* layer can also be controlled by setting the initial oxide thickness on the wafers before bonding.

The existence of an isolated device layer simplifies the process flow in many cases and the use of SOI wafers in micromachining has been growing, especially

since the thickness of the device layer on an SOI wafer can be much thicker than the deposited films (up to several hundred micrometres compared to few microns) [88]. A simple MEMS fabrication process with SOI wafers can be as follows:

- a metal is deposited on areas to improve electrical conduction where needed or on the bond pad sites;
- the device layer is etched, often in an RIE or DRIE process;
- the structure is released by etching the buried oxide layer through the openings in the device layer.

The simple fabrication process, low (or controlled) internal stress in the device layer, and possibility of having structural layers as thick as a full wafer have made SOI wafers a popular substrate in MEMS fabrication. SOI wafers are also used in microelectronics for different reasons. In microelectronics, SOI wafers have thin device and buried oxide layers (on the order of 100's of nanometres or less). Having a thin device layer allows for fabrication of devices with reduced leakage and parasitic capacitance, leading to better device performance.

2.7 Planarisation

Subsequent etch and deposition steps increase the surface roughness of a substrate. However, many applications require smooth surfaces at the end or during the process; e.g., bonding. A rough surface can also jeopardise the resolution and yield of a lithography step. In such cases, a polishing step is performed to reduce the surface roughness. An abrasive chemical slurry is poured onto the surface of the substrate while a polishing pad is pressed against the substrate and moved in a rotary motion. The process is often called chemical-mechanical-polishing (CMP). To enhance the uniformity across the wafer, dummy structures are used to slow down the thinning process where the existing layers have a faster removal rate than the rest of the wafer. The other solution to the non-uniform removal rate is to cover the whole wafer with a thick film and then thin it down to the required thickness.

2.8 Bulk vs Surface Micromachining

The terms *bulk* and *surface* micromachining are used frequently to refer to different techniques for fabrication of MEMS. Bulk micromachining refers to the case where the structure is carved from the substrate. This is generally done by etching the substrate and releasing the etched structures. A doping or metallisation step might also be required to reduce the resistance of the signal paths. Surface micromachining, on the other hand, refers to fabrication of microstructures from deposited films. Consequently, the thickness of the

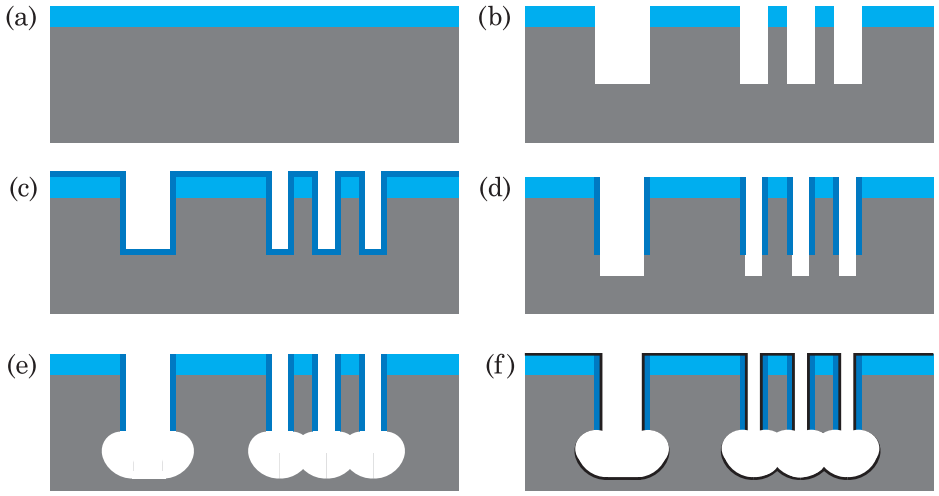

Figure 2.16 Steps of SCREAM process.

structures made in surface micromachining processes is often limited to a few micrometres. However, surface micromachining is a more flexible technique as one can have several released layers and may choose from different materials for different device layers. One important issue in surface micromachining is controlling the internal stresses of the deposited films if a planar structure is desired at the end of the process.

2.9 Examples of Process Flows

Examples of three micromachining processes are given below to illustrate the application of methods studied so far for fabrication of MEMS. As an example of a bulk micromachining process, the steps of SCREAM (single crystal reactive etching and metallisation) process are explained. MicraGEM (Micralyne generalised MEMS process) from Micralyne Inc. is another a bulk micromachining process that employs SOI wafers and silicon to glass bonding to fabricate MEMS. Finally, MUMPs (multi-user MEMS process) is an example of a standard surface micromachining process which has been available to MEMS researchers for almost a decade.

2.9.1 SCREAM

SCREAM (single crystal reactive etching and metallisation) is a fairly simple process flow which can be easily expanded to meet the requirements of various applications [89–91]. The fabrication steps as illustrated in Fig. 2.16, are:

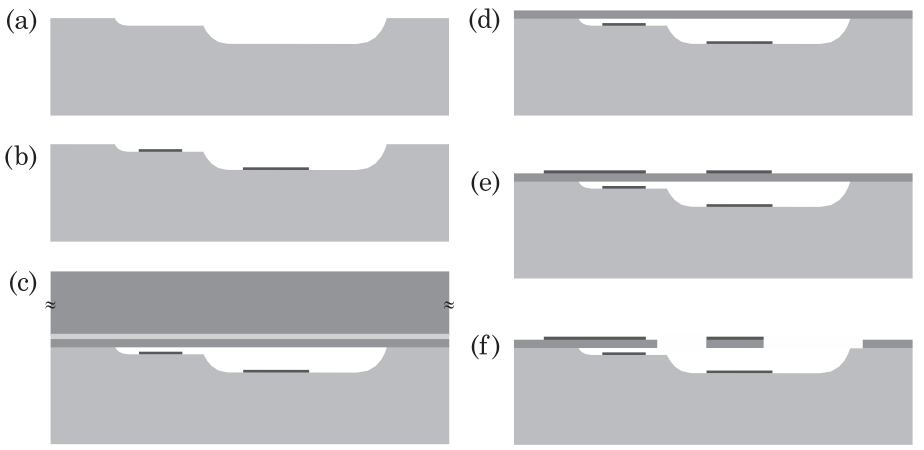

Figure 2.17 MicraGEM process flow.

(a) the substrate is coated with a relatively thick dielectric (e.g., thermal oxide);
(b) the dielectric layer and the underlying substrate are etched in an RIE (or DRIE) step as deeply as required for the final structure thickness;
(c) a thin layer of a dielectric film is conformally deposited on the etched substrate such that it covers the sidewalls of the etched cavities;
(d) the deposited dielectric film is etched in an RIE step. This removes the dielectric film from the bottom of the cavities and the surface of the substrate but not the film on the sidewalls;
(e) an isotropic gas phase etchant is used to etch the bottom of the cavities and undercut the protected sidewalls until the desired segments of the structures are released. This step might be preceded by an RIE step to etch the bottom of the cavities before introducing the isotropic etchant;
(f) a metal film is sputtered for electrical connection to the device.

The SCREAM process can be tweaked to be compatible with CMOS processes which allows the fabrication of the MEMS and signal processing electronics on the same chip [92]. A similar process can also be employed for fabrication of buried channels for microfluidic applications [93].

2.9.2 MicraGEM

MicraGEM (Micralyne generalised MEMS process) is a commercially available technology from Micralyne Inc. [94]. The process steps for fabrication of devices in MicraGEM technology are illustrated in Fig. 2.17 and are:

(a) a Pyrex substrate with a thickness of 525 μm is isotropically etched in two subsequent steps to depths of 2 μm and 10 μm, respectively;

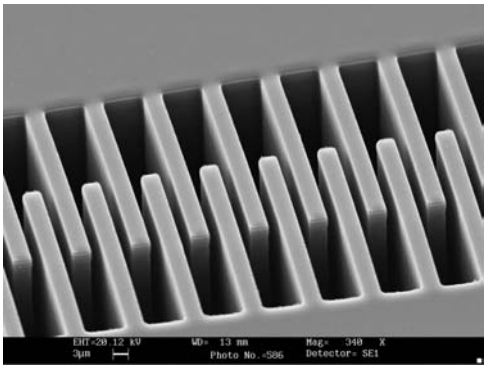

Figure 2.18 A comb drive fabricated in MicraGEM process. *Courtesy of Micralyne Inc.*

(b) bottom metal electrodes are patterned inside the etched cavities;
(c) an SOI wafer is anodically bonded to the Pyrex substrate;
(d) handle wafer and buried oxide layers are etched away in a wet process;
(e) the top metal layer is deposited (750 Å of gold on top of 100 Å of chrome) and patterned;
(f) the silicon layer (device layer of the original SOI wafer) is patterned and etched in a DRIE system.

MicraGEM is a bulk micromachining process and the structures made in this process do not suffer from pre-existing stresses. The device layer of the SOI wafers used in this technology is 10 µm thick, which translates into 10 µm tall devices. The lithographic resolution of MicraGEM process is 2 µm. A comb structure fabricated in MicraGEM process is shown in Fig. 2.18.

2.9.3 MUMPs

The MUMPs (multi-user MEMS process) is a three-layer polysilicon surface micromachining process derived from the research conducted at the University of California, Berkeley in the late 1980's and early 1990's [95]. The process has been modified to make it more versatile for average MEMS designers [96,97].

The process starts by depositing an insulating nitride layer (*Nitride* in Fig. 2.19) on heavily doped 100 mm silicon wafers by LPCVD. The following layers are deposited and patterned in subsequent steps:

(a) a 500 nm LPCVD polysilicon film (*Poly0*);
(b) a 2 µm LPCVD phosphosilicate glass (PSG) sacrificial layer (*1st Oxide*);
(c) a 2 µm LPCVD structural polysilicon film (*Poly1*);
(d) a 750 nm LPCVD phosphosilicate glass sacrificial layer (*2nd Oxide*);

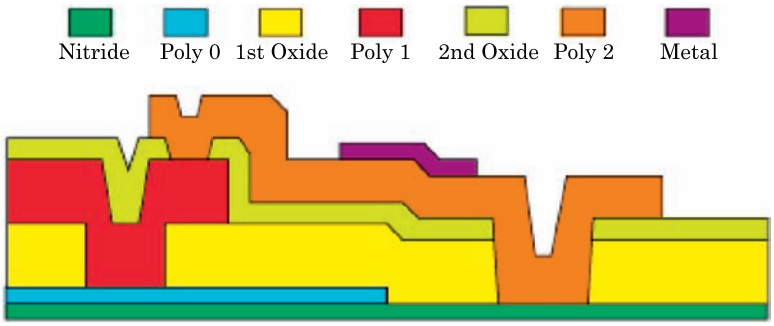

Figure 2.19 Cross section of layers in MUMPs technology.

(e) a 1.5 μm LPCVD polysilicon film (*Poly2*);
(f) a 500 nm metal film (*Metal*).

The last process step is the removal of sacrificial oxide layers. A critical-point drying process is used to avoid stiction of the released devices to the substrate. If needed, one can add dimples (through partially removing some of the 1st Oxide) to the bottom of the structures to reduce the possibility of stiction.

Released structures fabricated in MUMPs can be either 2 μm or 1.5 μm thick depending on the polysilicon layer that they are made from. It is also possible, although not officially supported, to remove the oxide layer between the polysilicon layers during the process to obtain a 3.5 μm thick structural layer. The lithographical resolution in MUMPs is 2 μm, setting the minimum line widths and gaps to the same amount.

References

1. M.J. Madou, *Fundamentals of microfabrication: the science of miniaturization*, 2nd edn., CRC Press, Boca Raton, USA, 2002.
2. S.A. Campbell, *The science and engineering of microelectronic fabrication*, 2nd edn., Oxford University Press, New York, USA, 2001.
3. G.E. McGuire, Ed., *Semiconductor materials and process technology handbook*, Noyes Publications, Park Ridge, USA, 1988.
4. G.S. May and S.M. Sze, *Fundamentals of semiconductor fabrication*, Wiley, New York, USA, 2004.
5. S. Allameh, P. Shrotriya, A. Butterwick and S.B.W. Soboyejo, "Surface topography evolution and fatigue fracture in polysilicon MEMS structures", *IEEE Journal of Microelectromechanical Systems*, Vol. 12, no. 3, pp. 313–324, June 2003.
6. L. Chu, L. Que, A. Oliver and Y. Gianchandani, "Lifetime studies of electrothermal bent-beam actuators in single crystal silicon and polysilicon", *IEEE Journal of Microelectromechanical Systems*, Vol. 15, no. 3, pp. 498–506, June 2006.
7. S. Pourkamali, A. Hashimura, R. Abdolvand, G. K. Ho, A. Erbil and F. Ayazi, "High-Q single crystal silicon HARPSS capacitive beam resonators with self-aligned sub-100-nm transduction gaps", *IEEE Journal of Microelectromechanical Systems*, Vol. 12, no. 4, pp. 487–496, August 2003.

8. R. Hull, Ed., *Properties of crystalline silicon*, Institution of Electrical Engineers, London, United Kingdom, 1999.
9. M. Mehregany, C. Zorman, N. Rajan and C.H. Wu, "Silicon carbide MEMS for harsh environments", *Proceedings of the IEEE*, Vol. 86, no. 8, pp. 1594–1609, August 1998.
10. K. Petersen, "Silicon as a mechanical material", *Proceedings of the IEEE*, Vol. 70, no. 5, pp. 420–457, May 1982.
11. J.A. King, Ed., *Materials handbook for hybrid microelectronics*, Artech House, Norwood, USA, 1988.
12. T. Ichiki, M. Watanabe, Y. Sugiyama and Y. Horiike, "Microfluidic mixer devices fabricated using high-aspect-ratio glass micromachining technology", in *Digest of papers of the international microprocesses and nanotechnology conference*, November 2002, pp. 292–293.
13. A.A. Kosterev, F.K. Tittel, D.V. Serebryakov, A.L. Malinovsky and I.V. Morozov, "Applications of quartz tuning forks in spectroscopic gas sensing", *Review of Scientific Instruments*, Vol. 76, no. 4, 2005. pp. 043 105:–1–9.
14. A. Madni and L. Costlow, "Common design techniques for quartz rate sensors for both automotive and aerospace/defense market applications", *Proceedings of IEEE sensors conference*, Orlando, USA, vol. 2, June 2002, pp. 1597–1602.
15. J. Rizk and G. Rebeiz, "W-band CPW RF MEMS circuits on quartz substrates", *IEEE Transactions on Microwave Theory and Techniques*, Vol. 51, no. 7, pp. 1857–1862, July 2003.
16. C. won Jung, M. jer Lee, G. Li and F.D. Flaviis, "Reconfigurable scan-beam single-arm spiral antenna integrated with RF-MEMS switches", *IEEE Transactions on Antennas and Propagation*, Vol. 54, no. 2, pp. 455–463, February 2006.
17. R. Wang, W. Ko and D. Young, "Silicon-carbide MESFET-based 400 °C MEMS sensing and data telemetry", *IEEE Sensors Journal*, Vol. 5, no. 6, pp. 1389–1394, December 2005.
18. D. Gao, M. Wijesundara, C. Carraro, R. Howe and R. Maboudian, "Recent progress toward a manufacturable polycrystalline SiC surface micromachining technology", *IEEE Sensors Journal*, Vol. 4, no. 4, pp. 441–448, August 2004.
19. N. Tagawa, K.-I. Kitamura and A. Mori, "Design and fabrication of MEMS-based active slider using double-layered composite PZT thin film in hard disk drives", *IEEE Transactions on Magnetics*, Vol. 39, no. 2, pp. 926–931, March 2003.
20. Z. Wang, W. Zhu, H. Zhu, J. Miao, C. Chao, C. Zhao and O.K. Tan, "Fabrication and characterization of piezoelectric micromachined ultrasonic transducers with thick composite PZT films", *IEEE Transactions on Ultrasonics, Ferroelectrics and Frequency Control*, Vol. 52, no. 12, pp. 2289–2297, December 2005.
21. L.-P. Wang, K. Deng, L. Zou, R. Wolf, R. Davis and S. Trolier-McKinstry, "Microelectromechanical systems (MEMS) accelerometers using lead zirconate titanate thick films", *IEEE Electron Device Letters*, Vol. 23, no. 4, pp. 182–184, April 2002.
22. S. Platt, S. Farritor and H. Haider, "On low-frequency electric power generation with PZT ceramics", *IEEE/ASME Transactions on Mechatronics*, Vol. 10, no. 2, pp. 240–252, April 2005.
23. S. Trolier-McKinstry and P. Muralt, "Thin film piezoelectrics for MEMS", *Journal of Electroceramics*, Vol. 12, no. 1–2, pp. 7–17, January 2004.
24. Y. Yu, T.-L. Ren and L.-T. Liu, "High quality silicon-based AlN thin films for MEMS application", *Journal of Integrated Ferroelectrics*, Vol. 69, pp. 367–374, 2005.
25. M. Hara, J. Kuypers, T. Abe and M. Esashi, "Surface micromachined AlN thin film 2 GHz resonator for CMOS integration", *Sensors and Actuators A: Physical*, Vol. 117, no. 2, pp. 211–216, January 2005.
26. P.V. Kessel, L. Hornbeck, R. Meier and M. Douglass, "A MEMS-based projection display", *Proceedings of the IEEE*, Vol. 86, no. 8, pp. 1687–1704, August 1998.

27. T. Chan and J.E. Ford, "Retroreflecting optical modulator using an MEMS deformable micromirror array", *Journal of Lightwave Technology*, Vol. 24, no. 1, pp. 516–525, January 2006.
28. M.F. Aimi, "Bulk titanium microelectromechanical systems, Ph.D. dissertation", University of California, Santa Barbara, USA, June 2005.
29. W. Dai, C. Oropeza, K. Lian and W. Wang, "Experiment design and UV-LIGA microfabrication technology to study the fracture toughness of Ni microstructures", *Journal of Microsystem Technologies*, Vol. 12, no. 4, pp. 306–314, March 2006.
30. Z. Zhou, Y. Zhou, C. Yang, J. Chen, G. Ding, W. Ding, M. Wang and Y. Zhang, "The evaluation of Young's modulus and residual stress of nickel films by microbridge testings", *Journal of Measurement Science and Technology*, Vol. 15, no. 12, pp. 2389–2394, December 2004.
31. J.W. Judy, "Batch-fabricated ferromagnetic microactuators with silicon flexures", Ph.D. dissertation, Department of Electrical Engineering and Computer Sciences, University of California, Berkeley, USA, 1996.
32. M. Peckerar and J. Maldonado, "X-ray lithography-an overview", *Proceedings of the IEEE*, Vol. 81, no. 9, pp. 1249–1274, September 1993.
33. H. Guckel, "High-aspect-ratio micromachining via deep X-ray lithography", *Proceedings of the IEEE*, Vol. 86, no. 8, pp. 1586–1593, August 1998.
34. R. Fontana, J. Katine, M. Rooks, R. Viswanathan, J. Lille, S. MacDonald, E. Kratschmer, C. Tsang, S. Nguyen, N. Robertson and P. Kasiraj, "E-beam writing: a next-generation lithography approach for thin-film head critical features", *IEEE Transactions on Magnetics*, Vol. 38, no. 1, pp. 95–100, January 2002.
35. J. Lee, R. Kubena and G. Hagen, "Submicrometer silicon MOSFET's fabricated using focused ion-beam lithography", *IEEE Transactions on Electron Devices*, Vol. 33, no. 2, pp. 310–311, February 1986.
36. G. Luo, G. Xie, Y. Zhang, G. Zhang, Y. Zhang, P. Carlberg, T. Zhu and Z. Liu, "Scanning probe lithography for nanoimprinting mould fabrication", *Journal of Nanotechnology*, Vol. 17, no. 12, pp. 3018–3022, June 2006.
37. D. Wachenschwanz, W. Jiang, E. Roddick, A. Homola, P. Dorsey, B. Harper, D. Treves and C. Bajorek, "Design of a manufacturable discrete track recording medium", *IEEE Transactions on Magnetics*, Vol. 41, no. 2, pp. 670–675, February 2005.
38. B.E. Deal and A.S. Grove, "General relationship for the thermal oxidation of silicon", *Journal of Applied Physics*, Vol. 36, no. 12, pp. 3770–3778, December 1965.
39. D.M. Mattox, Ed., *Handbook of physical vapor deposition (PVD) processing*, Noyes publications, Westwood, USA, 1998.
40. K. Seshan, Ed., *Handbook of thin-film deposition processes and techniques*, 2nd edn., Noyes Publications / William Andrew Publishing, Norwich, USA, 2002.
41. C. Wu, W. Chiu and H. Kao, "Textured and smooth AlN films prepared by Helicon sputtering system", *Electronics Letters*, Vol. 37, no. 4, pp. 253–255, February 2001.
42. L. Callaghan, V. Lughi, N. MacDonald and D. Clarke, "Beam-supported AlN thin film bulk acoustic resonators", *IEEE Transactions on Ultrasonics, Ferroelectrics and Frequency Control*, Vol. 53, no. 5, pp. 1001–1007, May 2006.
43. D. Banks, *Microengineering, MEMS, and interfacing: a practical guide*, CRC Press, Boca Raton, USA, 2006.
44. P. van Zant, *Microchip fabrication: a practical guide to semiconductor processing*, 5th edn., McGraw-Hill, New York, USA, 2004.
45. W. O'Mara, R. Herring and L. Hunt, Eds., *Handbook of semiconductor silicon technology*, Noyes Publications, Park Ridge, USA, 1990.
46. R.F. Bunshah, Ed., *Handbook of deposition technologies for films and coatings: science, technology and applications*, 2nd edn., Noyes Publications, Park Ridge, USA, 1990.
47. H.O. Pierson, *Handbook of chemical vapor deposition (CVD): principles, technology, and applications*, 2nd edn., Noyes Publications, Norwich, USA, 1999.

48. D.J. Hamilton and W.G. Howard, *Basic integrated circuit engineering*, McGraw-Hill, New York, USA, 1975.
49. W.-L. Huang, Z. Ren and C.-C. Nguyen, "Nickel vibrating micromechanical disk resonator with solid dielectric capacitive-transducer gap", *Proceedings of the IEEE international frequency control symposium and exposition*, June 2006, pp. 839–847.
50. C. Tsou, S.-L. Huang, H. Li and T. Lai, "Electroplated nickel micromachined probes with out-of-plane predeformation for IC chip testing", *Journal of Micromechanics and Microengineering*, Vol. 16, no. 10, pp. 2197–2202, October 2006.
51. P. Dixit, L. Xu, J. Miao, J.H. Pang and R. Preisser, "Mechanical and microstructural characterization of high aspect ratio through-wafer electroplated copper interconnects", *Journal of Micromechanics and Microengineering*, Vol. 17, no. 9, pp. 1749–1757, September 2007.
52. F.E. Rasmussen, J. Ravnkilde, P. Tang, O. Hansen and S. Bouwstra, "Electroplating and characterization of cobalt-nickel-iron and nickel-iron for magnetic microsystems applications", *Sensors and Actuators A: Physical*, Vol. 92, no. 1–3, pp. 242–248, August 2001.
53. S. Guan and B. Nelson, "Magnetic composite electroplating for depositing micromagnets", *IEEE Journal of Microelectromechanical Systems*, Vol. 15, no. 2, pp. 330–337, April 2006.
54. A. Frazier and M. Allen, "Metallic microstructures fabricated using photosensitive polyimide electroplating molds", *IEEE Journal of Microelectromechanical Systems*, Vol. 2, no. 2, pp. 87–94, June 1993.
55. N.V. Myung, D.-Y. Park, B.-Y. Yoo and P.T.A. Sumodjo, "Development of electroplated magnetic materials for MEMS", *Journal of magnetism and magnetic materials*, Vol. 265, no. 2, pp. 189–198, September 2003.
56. E. Becker, W. Ehrfield, P. Hagmann, A. Maner and D. Münchmeyer, "Fabrication of microstructures with high aspect ratios and great structural heights by synchrotron radiation lithography, galvanoforming, and plastic moulding (LIGA process)", *Journal of Microelectronic Engineering*, Vol. 4, no. 1, pp. 35–56, May 1986.
57. M. McCormick, E. Chowanietz and A. Lees, "Microengineering design and manufacture using the LIGA process", *Engineering Science and Education Journal*, Vol. 3, no. 6, pp. 255–262, December 1994.
58. L.-W. Pan and L. Lin, "Batch transfer of LIGA microstructures by selective electroplating and bonding", *IEEE Journal of Microelectromechanical Systems*, Vol. 10, no. 1, pp. 25–32, March 2001.
59. K. Williams and R. Muller, "Etch rates for micromachining processing", *IEEE Journal of Microelectromechanical Systems*, Vol. 5, no. 4, pp. 256–269, December 1996.
60. K. Williams, K. Gupta and M. Wasilik, "Etch rates for micromachining processing-part II", *IEEE Journal of Microelectromechanical Systems*, Vol. 12, no. 6, pp. 761–778, December 2003.
61. M. Elwenspoek and H. Jansen, *Silicon micromachining*, ser. Cambridge studies in semiconductor physics and microelectronic engineering, Vol. 7, Cambridge University Press, Cambridge, United Kingdom, 1998.
62. G.T.A. Kovacs, *Micromachined transducers sourcebook*, McGraw-Hill, Boston, USA, 1998.
63. P. Chu, J. Chen, R. Yeh, G. Lin, J. Haung, B. Warneke and K. Pister, "Controlled pulsed-etching with xenon difluoride", *Digest of technical papers of the international conference on solid state sensors and actuators, transducers 97*, Chicago, USA, June 1997, pp. 665–668.
64. B. Bahreyni, "Deep etching of silicon with XeF_2", Master's thesis, Department of Electrical and Computer Engineering, University of Manitoba, Canada, 2001.
65. X. Wang, X. Yang, K. Walsh and Y. Tai, Gas-phase etching with bromine trifluoride, *Digest of technical papers of the international conference on solid state sensors and actuators, transducers 97*, Chicago, USA, vol. 2, June 1997, pp. 1505–1508.

66. Y.-I. Lee, K.-H. Park, J. Lee, C.-S. Lee, H. Yoo, C.-J. Kim and Y.-S. Yoon, "Dry release for surface micromachining with HF vapor-phase etching", *IEEE Journal of Microelectromechanical Systems*, Vol. 6, no. 3, pp. 226–233, September 1997.
67. A. Witvrouw, B. Du Bois, P. De Moor, A. Verbist, C.A. Van Hoof, H. Bender and C. Baert, "Comparison between wet HF etching and vapor HF etching for sacrificial oxide removal", Jean Michel Karam and John A. Yasaitis, Eds., *Proceedings of SPIE: Micromachining and Microfabrication Process Technology VI,* vol. 4174, SPIE, Santa Clara, USA, pp. 130–141, 2000.
68. P. Docker, P. Kinnell and M. Ward, "A dry single-step process for the manufacture of released MEMS structures", *Journal of Micromechanics and Microengineering*, Vol. 13, no. 5, pp. 790–794, September 2003.
69. S. Reyntjens and R. Puers, "A review of focused ion beam applications in microsystem technology", *Journal of Micromechanics and Microengineering*, Vol. 11, no. 4, pp. 287–300, July 2001.
70. J. Melngailis, "Focused ion beam technology and applications", *Journal of Vacuum Science & Technology B: Microelectronics and Nanometer Structures*, Vol. 5, no. 2, pp. 469–495, March 1987.
71. T. Ishitani and T. Yaguchi, "Cross-sectional sample preparation by focused ion beam: A review of ion-sample interaction", *Microscopy Research and Technique*, Vol. 35, no. 4, pp. 320–333, November 1996.
72. H. Jansen, H. Gardeniers, M. de Boer, M. Elwenspoek and J. Fluitman, "A survey on the reactive ion etching of silicon in microtechnology", *Journal of Micromechanics and Microengineering*, Vol. 6, no. 1, pp. 14–28, March 1996.
73. M.J. Walker, "Comparison of bosch and cryogenic processes for patterning high-aspect-ratio features in silicon", U.F.W. Behringer and D.G. Uttamchandani, Eds., *Proceedings of SPIE*, vol. 4407, no. 1. The International Society for Optical Engineering, April 2001, pp. 89–99.
74. F. Lärmer and A. Schilp, "Verfahren zum anisotropen ätzen von silicium (method for anisotropically etching silicon)", German Patent 4 241 045.2, 1994.
75. S. Aachboun, P. Ranson, C. Hilbert and M. Boufnichel, "Cryogenic etching of deep narrow trenches in silicon", *Journal of Vacuum Science Technology*, Vol. 18, pp. 1848–1852, July 2000.
76. M.W. Pruessner, W.S. Rabinovich, T.H. Stievater, D. Park and J.W. Baldwin, "Cryogenic etch process development for profile control of high aspect-ratio submicron silicon trenches", *Journal of Vacuum Science & Technology B: Microelectronics and Nanometer Structures*, Vol. 25, no. 1, pp. 21–28, January 2007.
77. C. Fung, P. Cheung, W. Ko and D. Fleming, Eds., *Micromachining and micropackaging of transducers*, Elsevier Science Publishers B. V., Amsterdam, The Netherlands, 1985.
78. A. Hanneborg, Silicon wafer bonding techniques for assembly of micromechanical elements, *Proceedings of the 4th IEEE micro electro mechanical systems conference, MEMS '91*, Nara, Japan, January 1991, pp. 92–98.
79. M. Alexe and U. Gösele, Eds., *Wafer bonding: applications and technology*, ser. Springer Series in Materials Science, Vol. 75, Springer-Verlag, Berlin, Germany, 2004.
80. Q.-Y. Tong and U. Gösele, *Semiconductor wafer bonding: science and technology*, John Wiley & Sons, New York, USA, 1998.
81. M. Schmidt, "Wafer-to-wafer bonding for microstructure formation", *Proceedings of the IEEE*, Vol. 86, no. 8, pp. 1575–1585, August 1998.
82. A.A. Ayón, X. Zhang, K.T. Turner, D. Choi, B. Miller, S.F. Nagle and S.M. Spearing, "Characterization of silicon wafer bonding for power MEMS applications", *Sensors and Actuators A: Physical*, Vol. 103, no. 1–2, pp. 1–8, January 2003.
83. Z. Liu and D.L. DeVoe, "Micromechanism fabrication using silicon fusion bonding", *Journal of Robotics and Computer-Integrated Manufacturing*, Vol. 17, no. 1–2, pp. 131–137, February 2001.

84. J. Wei, S. Nai, C. Wong, Z. Sun and L.C. Lee, "Low temperature glass-to-glass wafer bonding", *IEEE Transactions on Advanced Packaging*, Vol. 26, no. 3, pp. 289–294, August 2003.
85. C. Lee, W.-F. Huang and J.-S. Shie, "Wafer bonding by low-temperature soldering", *Sensors and Actuators A: Physical*, Vol. 85, no. 1–3, pp. 330–334, August 2000.
86. Y. Cheng, L. Lin and K. Najafi, "Localized silicon fusion and eutectic bonding for MEMS fabrication and packaging", *IEEE Journal of Microelectromechanical Systems*, Vol. 9, no. 1, pp. 3–8, March 2000.
87. S. Bengtsson, "Wafer bonding and smartcut for formation of silicon-on-insulator materials", *Proceedings of the 5th international conference on solid-state and integrated circuit technology*, Beijing, China, October 1998, pp. 745–748.
88. J.M. Noworolski, E. Klaassen, J. Logan, K. Petersen and N.I. Maluf, "Fabrication of SOI wafers with buried cavities using silicon fusion bonding and electrochemical etchback", *Sensors and Actuators A: Physical*, Vol. 54, no. 1-3, pp. 709–713, June 1996.
89. K.A. Shaw, Z.L. Zhang and N.C. MacDonald, "SCREAM I: a single mask, single-crystal silicon, reactive ion etching process for microelectromechanical structures", *Sensors and Actuators A: Physical*, Vol. 40, pp. 63–70, 1994.
90. N.C. MacDonald, "SCREAM microelectromechanical systems", *Journal of Microelectronic Engineering*, Vol. 32, pp. 49–73, 1996.
91. C.S.B. Lee, S. Han and N.C. MacDonald, "Multiple depth, single crystal silicon microactuators for large displacement fabricated by deep reactive ion etching", *Technical digest of solid state sensor and actuator workshop*, Hilton Head Island, USA, June 1998, pp. 45–50.
92. H. Xie, L. Erdmann, X. Zhu, K.J. Gabriel and G.K. Fedder, "Post-CMOS processing for high-aspect-ratio integrated silicon microstructures", *IEEE Journal of Microelectromechanical Systems*, Vol. 11, no. 2, pp. 93–102, April 2002.
93. M.J. de Boer, R.W. Tjerkstra, J.W. Berenschot, H.V. Jansen, G.J. Burger, J.G.E. Gardeniers, M. Elwenspoek and A. van den Berg, "Micromachining of buried micro channels in silicon", *IEEE Journal of Microelectromechanical Systems*, Vol. 9, pp. 94–103, 2000.
94. *MicraGEM: Standardized MEMS Manufacturing Process*, Micralyne Inc., 1911 94 Street, Edmonton, Alberta, Canada T6N 1E6, February 2006.
95. W.C. Tang, "Electrostatic comb drive for resonant sensor and actuator applications", Ph.D. dissertation, Department of Electrical Engineering and Computer Sciences, University of California, Berkeley, USA, 1992.
96. D.A. Koester, R. Mahadevan, B. Hardy and K.W. Markus, *MUMPs design handbook*, 7th edn., Cronos Integrated Microsystems, 3026 Cornwallis Rd. Research Triangle Park, NC 27709, 2001.
97. MEMSCAP Inc., 4021 Stirrup Creek Drive, Suite 120, Durham, NC 27703, USA. [Online]. Available:http://www.memscap.com.

3 Transduction Mechanisms

A transducer is a device that converts one physical quantity to another. The change in the resistance of some materials upon the application of stress to them is one example (piezoresistive effect) and deformation of a piezoelectric crystal under an applied electric field is another. During the operation of a resonant device, the resonator body has to be brought and kept under constant vibrations by means of some actuating force. The initial responsibility of the actuating mechanism is to excite the mechanical body such that the energy in the system builds up and sufficiently large vibration amplitudes are achieved. During the steady state operation, the actuating force provides enough energy in proper form and frequency to compensate for various damping mechanisms in the system to keep the vibrations amplitude constant.

To be able to detect and control resonance, a sensing mechanism has to be included in the resonator design. As with actuation, several transduction mechanisms exist. However, opting for a transduction mechanism is usually a matter of technological availability and the designer might not be free to choose the method that he/she prefers.

This chapter discusses the main actuation and sensing techniques which are used for micromachined transducers. For a resonant transducer with electrical input and outputs, the excitation is a function of an electrical quantity while the output electrical quantity is often a function of the velocity of the resonator body. We assume that the behaviour of the resonator can be modelled as that of a lumped second order mass–spring system as discussed in Chapter 1. In many cases, we can also assume a linear, or linearised, relationship between the input electrical signal, $\mathcal{X}_i$, and the force that is applied to the resonator[1]:

$$\mathcal{F}_{in} = \eta_i \mathcal{X}_i \tag{3.1}$$

where $\mathcal{X}_i$ is either the input current or voltage. We also assume that the output electrical quantity from the resonator has a linear, or linearised, correspondence to the velocity vector of the resonator body:

$$\mathcal{X}_o = \eta_o \dot{\vec{u}} \tag{3.2}$$

where $\mathcal{X}_o$ can be either the output current or voltage, depending on the transduction mechanism.

[1] The excitation can also be a moment, a pressure, or a shear stress.

For harmonic excitations at frequency ω, Eq. (1.1) can be solved in conjunction with Eqs. (3.1) and (3.2), yielding:

$$\mathcal{X}_o = \eta_i \eta_o \frac{j\omega}{K - M\omega^2 + j\omega\zeta} \mathcal{X}_i. \tag{3.3}$$

At resonance (i.e., $\omega = \omega_0$), the relationship between the input and output electrical signals is:

$$\begin{aligned} \mathcal{X}_o &= \frac{\eta_i \eta_o}{\zeta} \mathcal{X}_i \\ &= \frac{\eta_i \eta_o Q}{\sqrt{KM}} \mathcal{X}_i. \end{aligned} \tag{3.4}$$

It can be seen that in order to have a strong signal at the output of the resonator one must:

- maximise the electromechanical coupling factor at the input, η_i;
- maximise the electromechanical coupling factor at the output, η_o;
- minimise damping (or increase the Q), ζ.

We discuss the transduction factors in this chapter and overview the damping mechanisms later.

3.1 Electrostatic Transduction

Electrostatic forces exist between structures which are either charged independently from each other or proportionally (e.g., the electrodes of a capacitor charged by applying a voltage between them). The magnitude of these forces depends on the voltage difference between the objects, their geometry, and the distance and medium between them. Electrostatic analysis of a capacitor consisting of two parallel plates separated by a dielectric medium is relatively straightforward. If a capacitor is charged so that a voltage difference of V_B appears between its electrodes, the exerted attractive electrostatic force on the electrodes, $\mathcal{F}_V$, is found from:

$$\begin{aligned} \mathcal{F}_V = \nabla W_e &= \frac{1}{2} \nabla (C V_B^2) \\ &= \frac{V_B^2}{2} \nabla C \end{aligned} \tag{3.5}$$

where W_e is the stored potential energy on the capacitor and ∇C is the gradient of the changes in capacitance[2]. It should be noted that the analysis to find the

[2]In Cartesian coordinates, operator ∇ is defined as $\nabla = \vec{a}_x \frac{\partial}{\partial x} + \vec{a}_y \frac{\partial}{\partial y} + \vec{a}_z \frac{\partial}{\partial z}$, where $\vec{a}_x$, $\vec{a}_y$, and $\vec{a}_z$ are the unit vectors along each of the axes.

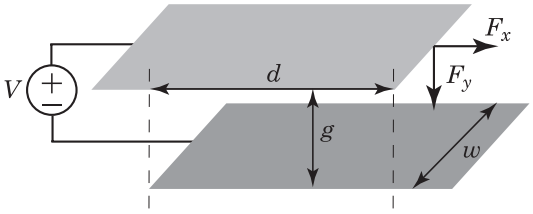

Figure 3.1 Electrostatic forces on two parallel plates.

electric field distribution, and consequently, the forces between micromachined structures assumes a static field distributions everywhere. This is because the electric field generally stabilises throughout the device at much shorter times than the mechanical response time of the structure.

Two special cases are of more importance for electrostatic actuation: (1) plates moving parallel to each other and (2) plates moving orthogonal to each other. Ignoring fringing fields, the capacitance of a parallel plate capacitor is found from $C = \varepsilon A g^{-1}$, where ε is the permittivity of the dielectric (for air $\varepsilon \approx \varepsilon_0 = 8.854 \times 10^{-12}$ F m^{-1}), A is the effective area of the plates, and g is the gap between the plates. Using Eq. (3.5), for force components along x and y axes, as shown in Fig. 3.1, we have:

$$\mathcal{F}_x = \frac{1}{2}V^2 \frac{\partial}{\partial x}\left(\varepsilon \frac{(d+x)w}{g}\right) = \varepsilon \frac{w}{2g}V^2 \tag{3.6}$$

$$\mathcal{F}_y = \frac{1}{2}V^2 \frac{\partial}{\partial y}\left(\varepsilon \frac{wd}{g-y}\right) = \varepsilon \frac{wd}{2(g-y)^2}V^2 \tag{3.7}$$

where w and d are the width and length of segments of the plates interacting with each other and x and y are the amounts of displacements along x and y axes, respectively. Eqs. (3.6) and (3.7) hold if the gap between the electrodes is small compared to their lateral dimensions (i.e., $g \ll d$ and $g \ll w$).

The thickness of the structural and sacrificial layers used for fabrication of micromachined devices is typically on the order of micrometres. This is an advantage for moving structures which are stacked on top of each other since the gap between them can be made small (see Eq. (3.7)). However, the electrostatic force between two neighbouring structures, which are to move laterally, is directly proportional to the thickness of the structural layers. The small thickness of these structures adversely affects the practical amount of obtainable electrostatic forces, as the lateral gaps between micromachined structures is often set by lithography. To have a larger interacting area, interdigitated fingers, as shown in Fig. 3.2, can be used to increase the capacitance between laterally moving structures. Interdigitated fingers can also be used when capacitive sensing is the method of choice in sensory applications.

A regular comb-drive consists of at least one set of comb fingers as shown in Fig. 3.2 and some sort of mechanical restoring force or stabilising mechanism

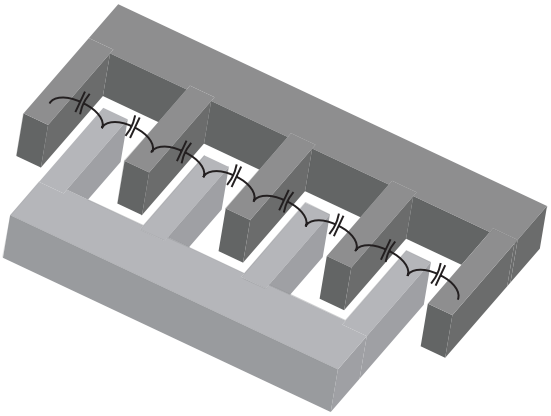

Figure 3.2 Interdigitating fingers for increased capacitance (the capacitances between the two sets of fingers are explicitly shown).

and a second set of comb fingers anchored to the substrate. The comb structure, in its basic or modified form, has been used in many different applications such as actuators [1–3], microsensors [4,5], mechanical filters [6,7], and oscillators [8,9].

Parallel plate capacitors are also used in micromachined devices for actuation purposes [10–12]. However, the minimum distance between the structures made from the same layer in common micromachining processes is usually set by the lithography limits (on the order of a micrometre). Consequently, the achievable amount of force for lateral movements is generally less than interdigitated structures (see Eq. (3.7)). To circumvent this problem, novel fabrication techniques are proposed to either increase the thickness of structural layers [13,14] or to reduce the gap between microstructures below the lithography limits [15,16]. On the other hand, parallel plate electrostatic transducers can be effectively used for out-of-plane actuation and sensing as small vertical gaps can be produced relatively easily by controlling the thickness of the sacrificial layers.

One application area where parallel plate electrostatic actuators are exclusively used is for bulk mode resonators [17,18]. The operation of these resonators is based on the change in geometry of pieces of structural material due to excitation of various resonant modes. Actuating electrodes are placed at proper locations to excite the desired mode of the resonator. The complexity of the mode shapes of these resonators in almost all cases dictates the exclusive use of parallel plate capacitive interfaces.

A biased capacitor can also be used for electrostatic sensing. The electrical charge on a capacitor is:

$$Q = CV_s \tag{3.8}$$

where V_s is the voltage between the capacitor electrodes. If the capacitance changes, for example due to the displacement of the electrodes, the charge on the capacitor changes with time, resulting in a current flow:

$$\begin{aligned} i_{\text{out}} &= \frac{\partial Q}{\partial t} = \frac{\partial (CV_s)}{\partial t} \\ &= \frac{\partial C}{\partial t} V_s + C \frac{\partial V_s}{\partial t}. \end{aligned} \tag{3.9}$$

The sense electrodes of micromachined resonators are often biased with a purely DC voltage, and therefore, the last term in the above equation vanishes:

$$i_{\text{out}} = \nabla C \cdot \frac{\partial \vec{u}}{\partial t} V_s \tag{3.10}$$

where $\vec{u}$ is the vector for the relative displacement of the electrodes. This equation is the basis for capacitive (i.e., electrostatic) sensing. From Eq. (3.2), it can be seen that $\eta_o = \nabla C V_s$.

An example of a resonator which uses electrostatic actuation and sensing is illustrated in Fig. 3.3. In this configuration, the AC voltage $v_a \sin \omega_a t$ is used to drive the structure under resonance. The DC voltage source V_{sh} is used to bias the shuttle of the resonator hence putting the same bias voltage across both ports of the resonator. The electrostatic force is given by:

$$\begin{aligned} \mathcal{F}_{\text{es}} &= \frac{1}{2} \left(\frac{\partial C}{\partial x} \right) \left((v_a \sin \omega_a t - V_{sh})^2 - V_{sh}^2 \right) \\ &= \frac{1}{2} \left(\frac{\partial C}{\partial x} \right) \left(\frac{v_a^2}{2} - 2 v_a V_{sh} \sin \omega_a t - \frac{v_a^2}{2} \cos 2\omega_a t \right) \end{aligned} \tag{3.11}$$

where $\partial C / \partial x$ is the rate of change in the capacitances of the input or output ports. Typically, the applied DC bias voltage is much larger than the actuation signal (i.e., $V_{sh} \gg v_a$) which lets us ignore the nonlinear term in Eq. (3.11). Since $\mathcal{X}_i = v_a \sin \omega t$, it can be seen that:

$$\eta_{ie} = \frac{\partial C_i}{\partial x} V_{\text{Sh}}. \tag{3.12}$$

The output signal from a biased electrostatic transducer is a current (i.e., $\mathcal{X}_o = i_{\text{out}}$) that can be found from:

$$i_{\text{out}} = \frac{\partial \left(C(-V_{sh}) \right)}{\partial t} = -V_{sh} \frac{\partial C}{\partial x} \frac{\partial x}{\partial t} \tag{3.13}$$

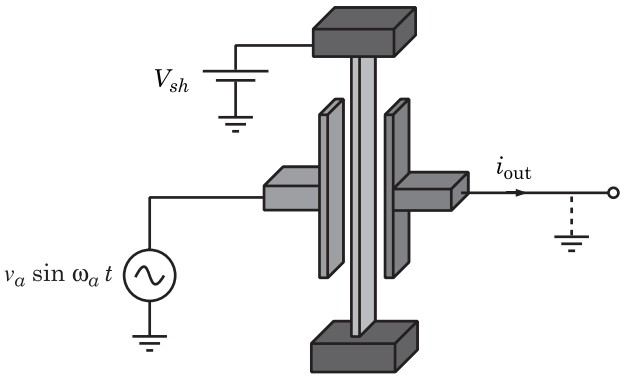

Figure 3.3 Schematic of an electrostatic resonator with drive and bias voltage sources.

and therefore,

$$\eta_{oe} = \frac{\partial C_o}{\partial x} V_{sh}. \tag{3.14}$$

A concept that is often used when discussing parallel plate electrostatic transducers is the *electrostatic spring constant*. To illustrate this concept, let us look at the Taylor series expansion of Eq. (3.7) which gives the electrostatic force between the electrodes of a parallel plate electrostatic actuator:

$$\mathcal{F}_y \approx -\frac{\varepsilon A V^2}{2g^2} + \frac{\varepsilon A V^2}{g^3} y - \frac{3\varepsilon A V^2}{2g^4} y^2 + \cdots \tag{3.15}$$

indicating that, as expected, the electrostatic attractive force becomes larger when the plates move toward each other. Ignoring the DC component (i.e., the first term) and high order nonlinear terms (i.e., third term and beyond), it can be seen that about any given distance $y \ll g$, the electrostatic force is proportional to the amount of displacement disturbances at that point. This behaviour is similar to that of a spring and can mathematically be modelled as one. However, unlike the reaction of a typical spring that opposes the applied force, the reaction of an electrostatic spring is in the same direction as the original force; i.e., the value of the electrostatic spring is negative. The magnitude of this negative spring constant increases with the voltage between the electrodes. At some point, the value of the electrostatic spring constant becomes larger than that of the mechanical restoring spring and the system becomes unstable and the moving electrode collapses on the fixed one. This phenomenon, known as *pull-in*, often leads to failure, either because of the short-circuit current through the electrodes or the stiction of the two electrodes [19]. For a simple parallel plate capacitor with an initial gap g_0 between the electrodes and a mechanical restoring spring constant of K_m the value of the

pull-in voltage is given by:

$$V_{PI} = \sqrt{\frac{8K_m g_0^3}{27\varepsilon A_{\text{eff}}}} \tag{3.16}$$

where A_{eff} is the effective area of the electrodes and ε is the dielectric constant of the medium between them.

Electrostatic transduction is a popular actuation method for microresonators for the following reasons:

- the steady state power requirements for electrostatic actuators are almost zero. This is due to the fact that there is no DC current flow through the comb capacitors. The AC current is also small due to the small sizes of the capacitors;
- electrostatic actuators are easy to fabricate, either for lateral or normal displacements;
- they can be made of various materials which are already available in micromachining processes such as silicon, polysilicon, and metals;
- they can be integrated with electronics with low contamination risk and moderate processing difficulties;
- the same structure that is used for actuation can be used for capacitive sensing.

A drawback of using electrostatic actuators is the large voltages they require for operation, which itself is a consequence of the small values of the capacitance gradients. Furthermore, micromachined electrostatic actuators are controlled by applying different voltages to the electrodes rather than directly putting a certain amount of charge on electrodes. As a result, the force between two electrodes is always attractive and micromachined electrostatic actuators can only be used to *pull* and not *push*.

3.2 Piezoelectric Transduction

Piezoelectricity refers to a phenomenon where an electric field develops a mechanical strain inside a dielectric material *and* an applied mechanical strain results in electric polarisation across the material. The electric polarisation manifests itself as an electric charge which can be sensed as a measure of the applied stress as illustrated in Fig. 3.4 [20,21]. The cause of the piezoelectricity is the change in the alignment of the polarisation domains inside the dielectric by the external field. Ferroelectric materials can be treated to exhibit the piezoelectricity through a process known as *poling*. Poling refers to heating the material above a certain temperature (known as *Curie temperature*) and exposing it to a large electric field to align the randomly oriented dipoles inside

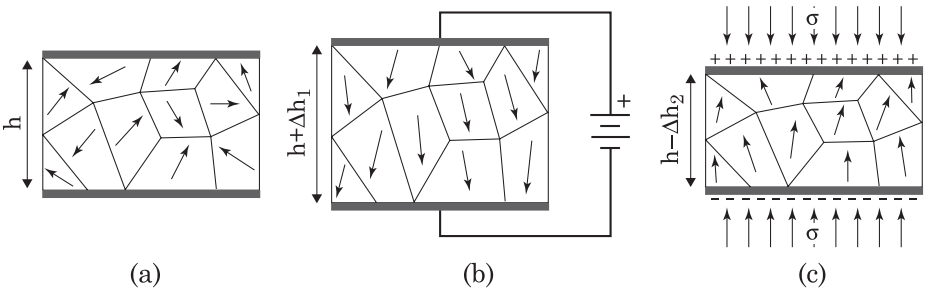

Figure 3.4 Illustration of piezoelectricity: (a) relaxed state; (b) the change of dimension upon application of an external field; and (c) appearance of electric charge under stress.

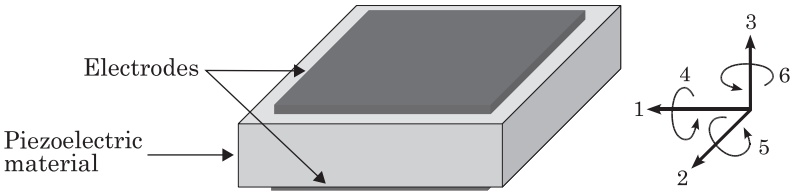

Figure 3.5 Indexing conventions for normal and shear components of the strains and stresses inside a piezoelectric material as well as the directions of the fields.

the material. The material will remain polarised after the heat is reduced and the external field is removed [22].

In electromagnetics, the effect of internal electric moments is modelled by adding a second term to the relationship between the electric field $\vec{\mathcal{E}}$ and electric displacement $\vec{\mathcal{D}}$:

$$\vec{\mathcal{D}} = \varepsilon\vec{\mathcal{E}} + \vec{P} \tag{3.17}$$

where $\vec{P}$ is the polarisation vector. Equations which relate the electric field to mechanical stress are [23–25]:

$$\begin{aligned} \sigma_P &= c^E_{PQ}\epsilon_Q - d_{Pq}\mathcal{E}_q \\ \mathcal{D}_p &= d_{pQ}\epsilon_Q + \varepsilon^{\epsilon}_{pq}\mathcal{E}_q \end{aligned} \tag{3.18}$$

where d_{Pq} are the piezoelectric stress coefficients (in C m^{-2}), c^E_{PQ} are the elastic coefficients of the solid (in Pa), σ_P are elements of the stress tensor, ϵ_Q are the elements of the strain tensor, $\mathcal{E}_q$ are elements of the electric field vector, $\mathcal{D}_p$ are elements of the electric displacement vector, and $\varepsilon^{\epsilon}_{pq}$ are the permittivity constants. The indices p, q, P, and Q are numbers between 1 and 6 and are defined as illustrated in Fig. 3.5.

Eq. (3.18) can be used to analyse piezoelectric sensors as well as piezoelectric actuators. The induced charge is small and difficult to measure due to the

leakage currents and parasitics. Consequently, piezoelectric sensing is most effective when the applied stress is cyclical. Examples for this case are piezoelectric resonators where a periodic signal is applied to a set of electrodes to bring the crystal under resonance while the crystal vibrations are picked up by a second set of electrodes. Such crystals have widespread applications in precision oscillators and high-Q passive filers for RF applications [21,26–29].

For large scale actuators, one or more layers of piezoelectric materials are sandwiched between electrode or dielectric layers. For micromachining applications, however, a single layer of a piezoelectric film is usually deposited and patterned on top of an electrode, followed by a top electrode layer. However, most piezoelectric materials are brittle, often exhibit higher internal damping factors than silicon, and typically suffer from large internal stresses after their deposition. One solution is to deposit (or *glue*) a layer of piezoelectric material on top of the main resonator body which can be a relatively thick silicon structure [30–33]. Doing so, one simultaneously benefits from the large transduction factors between the electrical and mechanical domains and the higher intrinsic quality factor of silicon compared to typical piezoelectric films. In these cases, it is often the d_{31} piezoelectric coefficient that transforms the input electric voltage into a mechanical moment which then deflects the structure underneath the piezoelectric film.

Piezoelectric actuators are used where good control over the produced displacements are required such as in precision tuning and scanning probe microscopy [34–37]. A day-to-day application for piezoelectric actuators is pushing the ink droplets out of the nozzles on inkjet printer heads [38,39]. Another familiar application is where the piezoelectric property of a material is used for both actuation and sensing in resonant devices for timing, filtering, or sensing applications [40,41].

Common piezoelectric materials are quartz (i.e., the crystalline form of SiO_2), lead zirconate titanate (PZT), aluminium nitride (AlN), zinc oxide (ZnO), barium titanate, lead zirconate, and lead titanate [32,42–44]. None of these materials are used in a typical microelectronic processing facility due to contamination concerns, which means that dedicated processing equipment should be used to work with piezoelectric materials. With some reservations, AlN may be deposited on electronic chips to fabricate piezoelectric devices, but the piezoelectric coefficient of AlN is small compared to PZT or quartz. Although quartz wafers can be used in typical processes, their efficient operation needs special packaging which makes their integration with electronics very difficult.

3.3 Magnetic Transduction

Magnetic fields can be employed for actuation at micro-scale. Lorentz force is the commonly used mechanism for magnetic actuators without magnetic

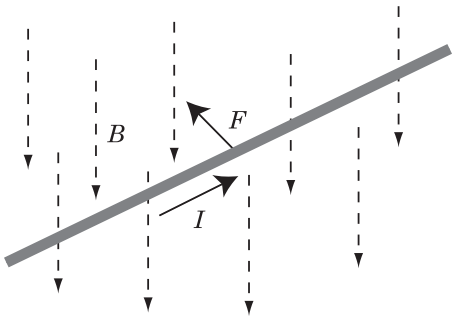

Figure 3.6 Lorentz force on a current carrying conductor in a magnetic field, B.

materials. The Lorentz force exerted on current carrying conductors in a magnetic field is given by:

$$\vec{\mathcal{F}}_l = I\vec{L} \times \vec{B} \tag{3.19}$$

where I is the current through the conductor, $\vec{L}$ is a vector whose magnitude is the interacting length of the conductor with magnetic field and its direction is the same as the current in the conductor, and $\vec{B}$ is the magnetic flux density (see Fig. 3.6). It can be seen that

$$|\eta_{im}| = |\vec{L} \times \vec{B}|. \tag{3.20}$$

Lorentz force has been used for actuation of microstructures with the aid of a magnetic field produced externally. Relatively large currents are needed to produce large enough forces due to the limited range of external magnetic field that can be produced (generally less than 1 T) and the small dimensions of micromachined devices. Consequently, the resistivity of the actuating arms should be made small, through doping or proper choice of structural material, to avoid large voltage drops across them [45,46]. It is also possible to use multiple parallel conductors or coils for increased force [47].

When a conductor moves through a magnetic field, a voltage appears across it. This phenomenon is described through Faraday's law:

$$\text{emf} = -N\frac{d\Phi}{dt} \tag{3.21}$$

where Φ is the magnetic flux. For a single straight wire of length L moving at speed $\dot{\vec{u}}$ inside a magnetic field $\vec{B}$, the induced voltage is found from:

$$\text{emf} = L\vec{B} \times \dot{\vec{u}}. \tag{3.22}$$

This induced voltage can be used for sensing the movements of a conductor. The maximum output transduction coefficient is given by:

$$\eta_{om} = L|\vec{B}|. \tag{3.23}$$

Inside an externally applied magnetic field, the force on current carrying conductor can be used for actuating the resonator and the induced voltage on a moving conductor provides the signal for sensing the movements of the resonator body [48,49].

Iron, nickel, cobalt and some of the rare earth elements and their alloys exhibit a phenomenon known as *ferromagnetism*. If a piece of these materials is put inside a small magnetic field, the magnetic domains inside it align themselves with the field and the material is magnetised. This increases the magnetic field inside the material by a large factor, known as the *relative permeability* of the material, which can be in the range of few hundreds to few hundreds of thousands. The force that a magnetic field exerts on a magnetised material can also be used for actuation purposes [50–54]. In many cases, the required field is produced by an external permanent magnet or coil, which limits the flexibility of this actuation method.

Ferromagnetic materials deform in presence of a magnetic field, changing their length slightly in the direction of the applied field. This phenomena is called *magnetostriction* and can be used for sense or actuation applications [55,56].

3.4 Thermal Actuation

Temperature variations affect the operation of the micromachined devices in two ways: (1) the dimensions of the structure change or a stress may develop inside the rigid segments of the structure; and (2) the material properties change as a function of temperature. Most of the mechanical and electrical properties of the materials are temperature dependent, including the Young's modulus, electrical resistivity, specific heat, thermal expansion coefficient, relative permittivity, and thermal conductivity.

Most materials expand when heated up. The thermal expansion coefficients of most materials are on the order of parts per million (ppm). Thermal actuation is not a common actuation mechanism at large scales due to the small displacements and the large amounts of required power for heating up the structures. However, thermal expansion of properly designed beams or layers has been employed in micromachined devices for actuation purposes. The large surface-to-volume ratio of micromachined devices means that these structures heat up and cool down rather quickly, with time constants on the order of milliseconds or less, while their heat storage capability is negligible. As a result, it is possible to use thermal actuators for resonator applications with operating frequencies on the order of several kilo hertz or even larger [57,58].

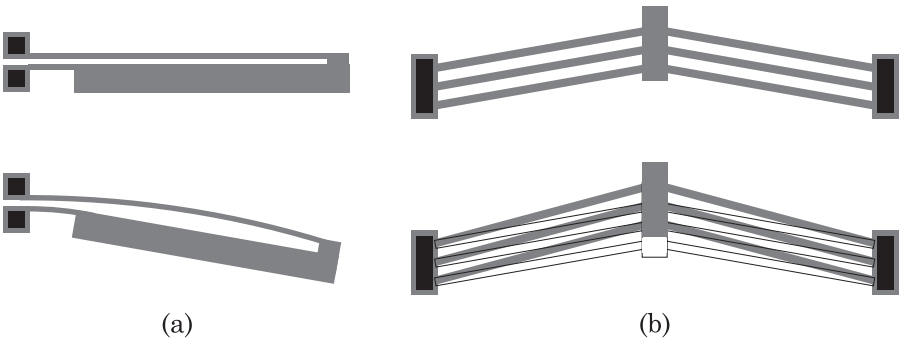

Figure 3.7 Thermal actuators.

Joule heating is usually employed to heat up the structure but other techniques, such as induction with RF signals may also be employed [59,60]. When a current is passed through a resistor R, the dissipated power, which is converted to heat, is calculated from:

$$P = \hat{I}^2 R = \frac{\hat{V}^2}{R} \tag{3.24}$$

where $\hat{I}$ and $\hat{V}$ are the root mean square (rms) values of the current through the resistor and the voltage across it, respectively.

The generated heat causes an increase in the physical dimensions of the structure which can be employed for actuation purposes. Two of such actuators are shown in Fig. 3.7. The two arms of the structure shown in Fig. 3.7 (a), have different resistances since a portion of one of the arms is made wider than the other one [61,62]. When a current is passed through the beams of this structures, the long narrow arm becomes hotter and extends further than the other arm. Since both beams are joined at their ends, the difference in the extensions of the two beams causes the structure to bend towards the wider beam as illustrated. Several of these actuators can be used in parallel to increase the output force [63].

Operation of the second device illustrated in Fig. 3.7 (b) is also fairly straightforward [64]. When a current is passed through the beams, all of them extend by the same amount and push the central beam of the device forward. The amount of shuttle movement depends on the length of beam extensions as well as angle between the two groups of them to the left and right of the shuttle. These actuators are used to exert relatively large forces along straight paths [58,65].

Heat transfer mechanisms should be studied to investigate the efficiency of electro-thermal actuators or the dynamic response of the microstructures. The heat is exchanged between a structure and its surrounding environment or the neighbouring structures through *conduction*, *convection*, and *radiation*[66–68].

Thermal conduction is often the main heat transfer mechanism in micromachined resonators and refers to the case where the thermal energy is transferred to the neighbouring structures or to the ambient gas through the transfer of energy between the molecules. The temperature distribution due to thermal conduction can be found by solving the heat equation:

$$\nabla^2 T = \frac{1}{\kappa}\left(\rho_m \mathcal{C}_p \frac{\partial T}{\partial t} - q_{\text{gen}}\right) \tag{3.25}$$

where T is the temperature (in kelvin), κ is the thermal conductivity of the material (in W m^{-1} K^{-1}), q_{gen} is the produced heat per volume (in W m^{-1} K^{-1}), ρ_m is the mass density (in kg m^{-3}), $\mathcal{C}_p$ is the heat capacity (in J kg^{-1} K^{-1}), and t is time (in sec).

Convection refers to heat transfer with the mass of a fluid (gas or liquid). Convection can be free or forced. Heat transfer through convection is usually negligible for micromachined devices that operate in a gas ambient or under vacuum because the thermal conductivity of structural materials for micromachined devices (e.g., silicon or metals) is orders of magnitude larger than that of the environment surrounding them.

Radiation may become the dominant heat transfer mechanism at high temperatures (e.g., several hundred degrees Celsius). This usually does not occur in microresonator applications.

3.5 Piezoresistive Sensing

Consider a resistor of length L and cross sectional area of A which is made of a material with resistivity ρ. The resistance of this resistor is given by:

$$R = \rho \frac{L}{A}. \tag{3.26}$$

If a mechanical strain ϵ_l is longitudinally applied to this resistor, it can be seen that:

$$\begin{aligned} dR &= d\rho \frac{L}{A} + dL \frac{\rho}{A} - dA \frac{\rho L}{A^2} \\ \rightarrow \frac{dR}{R} &= \frac{d\rho}{\rho} + \frac{dL}{L} - \frac{dA}{A}. \end{aligned} \tag{3.27}$$

Gauge factor is defined as the normalised change in resistance for a small applied strain; i.e., $GF = (dR/R)/\epsilon_l$. If the material is electrically and statically isotropic (i.e., its resistivity, Young's modulus, and Poisson's ratio are the same

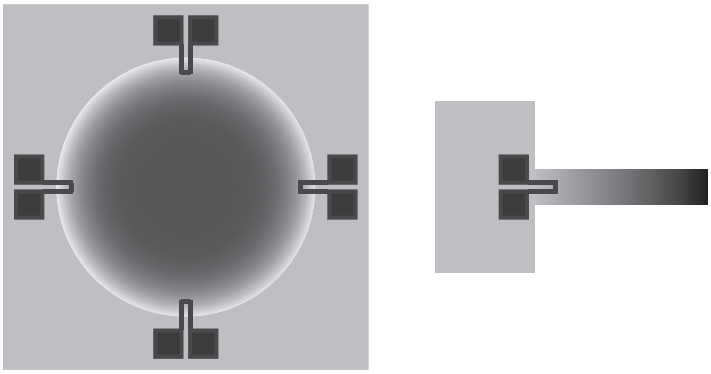

Figure 3.8 Placement of piezoresistors around a circular membrane and edge of a cantilever to detect their deflections relative to the substrate.

along different axes), the gauge factor can be calculated from Eq. (3.27):

$$GF = \frac{d\rho/\rho}{\epsilon_l} + (1 + 2\nu) \tag{3.28}$$

where ν is the Poisson's ratio of the material. In most materials, such as metals, the change in the resistivity due to stress is negligible compared to the geometrical effects and the gauge factor of resistors made from these materials is typically between 1.5–2[3]. For piezoresistive materials, however, the change in the resistivity of the material, ρ, is more dominant than the geometrical effects. Most semiconductor materials are piezoresistive, whose gauge factors, as expected, is a function of doping level. For example, the gauge factor for silicon piezoresistors can vary from -24 for an n-doped resistor to $+26$ for a p-doped resistor [69,70]. The large gauge factor of semiconductor resistors is a result of the changes in the band structure of the material under stress [71].

Piezoresistors are often placed at locations where the amount of developed strain is large to improve the sensitivity of measurements. For simple beam and plate structures, the locations where the moving structure is anchored to the substrate usually undergo the maximum stress during the device operation, and therefore, piezoresistors are often placed at these corners (see Fig. 3.8). It is important to note that the resistivity of semiconductor resistors is also a strong function of temperature and proper temperature compensation techniques are required to assure accurate measurements across the operating temperature range of the device. A simple Wheatstone bridge, such as the one shown in Fig. 3.9 can be used to compensate for such non-idealities to the first order by using resistors with similar temperature drift properties in the reference branch as those in the measurement branch [72,73]. To increase the sensitivity of the

[3]The Poisson's ratio for most isotropic materials, including metals, is around 0.3.

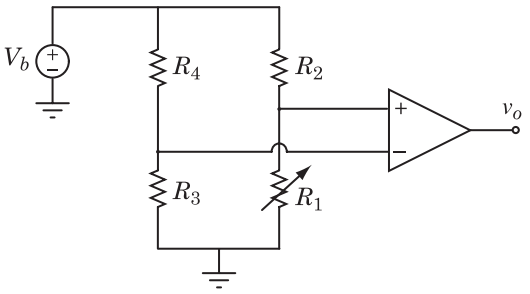

Figure 3.9 A simple Wheatstone bridge to monitor the changes in R_1. The bridge is balanced if $R_1/R_2 = R_3/R_4$.

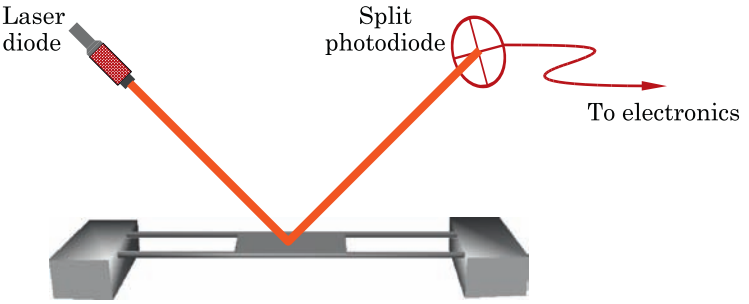

Figure 3.10 Schematic of a laser beam bounce setup for detection of out of plane movements.

bridge, R_4 may also be chosen to be a sensing piezoresistor or R_2 can be a piezoresistor which is placed at a location where the strain changes oppositely to where R_1 is located.

Silicon piezoresistors are usually either patterned from a thin layer of polysilicon which is deposited on top of a dielectric layer or from ion-implanted regions which are electrically isolated from the rest of the structure through reverse biased pn junctions. Using implanted piezoresistors makes the fabrication process simpler at the cost of having a leakage current through the junctions and the added parasitic capacitances.

3.6 Optical Sensing

Silicon is a reflective material as are many other materials used in semiconductor device fabrication (e.g., metals). Optical means may be used to sense the displacement or deformation of micro-engineered structures, especially when the displacements are normal to the resonator plane. The most common setup for optical sensing of movements is shown in Fig. 3.10 . In this configuration, a laser beam is aimed at the top of the moving structure and the

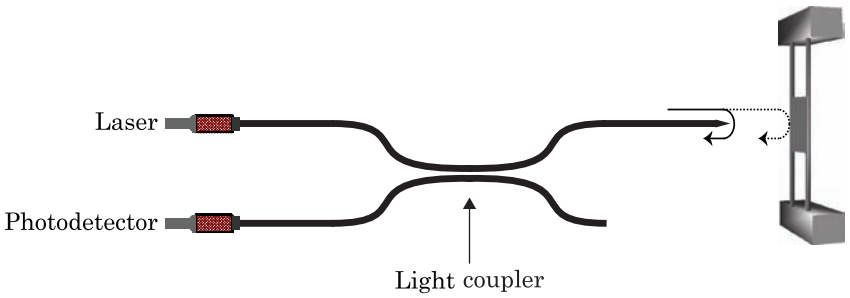

Figure 3.11 A fibre optic interferometer.

reflected beam is centred on a split photodiode. Out of plane deflections of the resonator body result in the movement of the laser spot on the photodiode, and therefore, modulate the output current of the photosensor. This is the setup that has been used in scanning probe microscopy (SPM) with sub-angstroms resolutions.

The other choice for optical sensing is an optical interferometer. A laser beam is directed at the surface to be monitored in such a way that interference fringes build up. By analysing these fringes and their changes with time, the amount of displacement or deformation may be detected and quantified. This technique is often used for monitoring the static or dynamic deflections of a structure under an external load. Different types of interferometers can be used for this purpose, including Michelson, Fabry–Perot, and Mach–Zehnder interferometers [74]. Fibre optic interferometers, as illustrated in Fig. 3.11, are particularly suited for experiments with micromachined devices where the laser beam is directed through the tip of an optical fibre toward the structure under test [75]. A portion of the beam is reflected back inside the fibre due to the discontinuity in the index of refraction at the interface of the fibre and air (or vacuum). Part of the light that has left the fibre is reflected back from the surface of the device under test and enters the fibre after twice travelling the distance between the tip of the fibre and device surface. These two reflected light beams combine with each other inside the fibre and form standing light waves which can be detected using a coupler and a photosensor.

By employing optical methods to detect displacements, one can avoid many of the challenges of electrical sensing techniques such as electromagnetic interference and electrical parasitics. Consequently, optical techniques can typically provide sensitivities and resolutions that are superior than other techniques to measure the relative displacements of an object without much effort. However, it is generally difficult to integrate the required optical apparatus with micromachined devices, partly due to packaging and alignment challenges. Nevertheless, these techniques have successfully been employed in laboratories to detect sub-angstroms displacements.

3.7 Other Techniques

Several other techniques have been employed for sensing and actuation at micro- and nano-scales. For example, chemical reactions with thin films or the bulk of a material are employed in chemical sensors. In case of resonant chemical sensors, it is often a change in the mass of the structure that causes a shift in the resonant frequency of the structure [76,77].

If the distance between two objects at different potentials becomes too small, the electrons can *tunnel* through the gap between the objects, resulting in a current. This current is exponentially proportional to the distance between the structures, and therefore, can be employed as a very sensitive method of measuring the relative displacements of two objects [78–81]. Electron tunnelling was the first phenomena which was used in a scanning probe microscope to analyse the surface properties of solids [82,83].

Hydraulic actuation and combustion have been used at micro-scales with the motivation that the energy density in fuel is large and these machines could produce power for mobile applications. However, actuation at micro-scales using combustion and hydraulic has so far proven to be inefficient due to inadequate sealing techniques, wearing of the components, and loss of the thermal energy to the surroundings [84–86]. Furthermore, micro-turbines are generally made of complicated structures with complex fabrication processes requiring the bonding of as many as six wafers together [87]. Finally, the operation frequency for these actuation mechanisms is much too small for most resonator applications.

Electrostriction refers to a property of dielectrics where the physical dimensions of the material change in response to the square (and even orders) of the applied electric field. While electrostriction is a property of all materials, it is too small in most cases to be used for actuation purposes [88–91]. Nevertheless, electrostriction in some materials, including polymers like polyvinylidene fluoride (PVDF), is large enough to be used for actuation at micro-scales [34,92].

References

1. R. Legtenberg, A.W. Groeneveld and M. Elwenspoek, "Comb-drive actuators for large displacements", *Journal of Micromechanics and Microengineering*, Vol. 6, no. 3, pp. 320–329, September 1996.
2. D.A. Horsley, N. Wongkomet, R. Horowitz and A.P. Pisano, "Precision positioning using a microfabricated electrostatic actuator", *IEEE Transactions on Magnetics*, Vol. 35, no. 2, pp. 993–999, March 1999.
3. M.A. Rosa, S. Dimitrijev and H.B. Harrison, "Enhanced electrostatic force generation capability of angled comb finger design used in electrostatic comb-drive actuators", *IEE Electronics Letters*, Vol. 34, no. 18, pp. 1787–1788, September 1998.
4. W.O. Davis, "Mechanical analysis and design of vibratory micromachined gyroscopes", Ph.D. dissertation, Department of Mechanical Engineering, University of California, Berkeley, USA, 2001.

5. N. Yazdi, F. Ayazi and K. Najafi, "Micromachined inertial sensors", *Proceedings of the IEEE*, Vol. 86, no. 8, pp. 1640–1659, August 1998.
6. L. Lin, R.T. Howe and A.P. Pisano, "Microelectromechanical filters for signal processing", *IEEE Journal of Microelectromechanical Systems*, Vol. 7, no. 3, pp. 286–294, September 1998.
7. C.T.-C. Nguyen, "Frequency-selective MEMS for miniaturized low-power communication devices", *IEEE Transactions on Microwave Theory and Techniques*, Vol. 47, no. 8, pp. 1486–1503, August 1999.
8. C.T.-C. Nguyen, "Micromechanical resonators for oscillators and filters", *Proceedings of the IEEE ultrasonics symposium*, Ann Arbor, USA, Vol. 1, November 1995, pp. 489–499.
9. C.T.-C. Nguyen and R.T. Howe, "An integrated CMOS micromechanical resonator high-Q oscillator", *IEEE Journal of Solid-State Circuits*, Vol. 34, no. 4, pp. 440–455, April 1999.
10. T.A.W. Roessig, "Integrated MEMS tuning fork oscillators for sensor applications", Ph.D. dissertation, Department of Mechanical Engineering, University of California, Berkeley, USA, 1998.
11. P.B. Chu and S.J. Pister, "Analysis of closed-loop control of parallel-plate electrostatic microgrippers", *Proceedings of the IEEE international conference on robotics and automation*, San Diego, USA, Vol. 1, May 1994, pp. 820–825.
12. M.S.-C. Lu, "Parallel-plate micro servo for probe-based data storage", Ph.D. dissertation, Electrical and Computer Engineering, Carnegie Mellon University, Pittsburgh, USA, 2002.
13. K.A. Shaw, Z.L. Zhang and N.C. MacDonald, "SCREAM I: a single mask, single-crystal silicon process for microelectromechanical structures", *Proceedings of the 6th IEEE micro electro mechanical systems conference, MEMS '93*, Atlanta, USA, February 1993, pp. 155–160.
14. J.W. Weigold, W.H. Juan and S.W. Pang, "Etching and boron diffusion of high aspect ratio Si trenches for released resonators", *Journal of Vacuum Science and Technology, B*, Vol. 15, no. 2, pp. 267–272, March 1997.
15. F. Ayazi and K. Najafi, "High aspect-ratio combined poly and single-crystal silicon (HARPSS) MEMS technology", *IEEE Journal of Microelectromechanical Systems*, Vol. 9, no. 3, pp. 288–294, September 2000.
16. S. Pourkamali, A. Hashimura, R. Abdolvand, G.K. Ho, A. Erbil and F. Ayazi, "High-Q single crystal silicon HARPSS capacitive beam resonators with self-aligned sub-100-nm transduction gaps", *IEEE Journal of Microelectromechanical Systems*, Vol. 12, no. 4, pp. 487–496, August 2003.
17. Z. Hao, S. Pourkamali and F. Ayazi, "VHF single-crystal silicon elliptic bulk-mode capacitive disk resonators; part I: Design and modeling", *IEEE Journal of Microelectromechanical Systems*, Vol. 13, no. 6, pp. 1043–1053, December 2004.
18. V. Kaajakari, T. Mattila, A. Oja, J. Kiihamäki and H. Seppä, "Square-extensional mode single-crystal silicon micromechanical resonator for low-phase-noise oscillator applications", *IEEE Electron Device Letters*, Vol. 25, no. 4, pp. 173–175, April 2004.
19. S. Pamidighantam, R. Puers, K. Baert and H. Tilmans, "Pull-in voltage analysis of electrostatically actuated beam structures with fixed-fixed and fixed-free end conditions", *Journal of Micromechanics and Microengineering*, Vol. 12, no. 4, pp. 458–464, July 2002.
20. J.G. Korvink and O. Paul, Eds., *MEMS: A practical guide to design, analysis, and applications*, William Andrew Publishing, Norwich, USA, 2006.
21. E. Akdogan, M. Allahverdi and A. Safari, "Piezoelectric composites for sensor and actuator applications", *IEEE Transactions on Ultrasonics, Ferroelectrics and Frequency Control*, Vol. 52, no. 5, pp. 746–775, May 2005.
22. T. Granzow, A.B. Kounga, E. Aulbach and J. Rödel, "Electromechanical poling of piezoelectrics", *Applied Physics Letters*, Vol. 88, no. 25, pp. 252 907:1–252 907:3, June 2006.

23. M. Weinberg, "Working equations for piezoelectric actuators and sensors", *IEEE Journal of Microelectromechanical Systems*, Vol. 8, no. 4, pp. 529–533, December 1999.
24. D. Ballantine, R. White, S. Martin, A. Ricco, G. Frye, E. Zellars and H. Wohltjen, *Acoustic wave sensors - theory, design, and physico-chemical applications*, Academic Press, San Diego, USA, 1997.
25. T. Ikeda, *Fundamentals of piezoelectricity*, Oxford University Press, New York, USA, 1990.
26. R. Kubena, F. Stratton, D. Chang, R. Joyce, T. Hsu, M. Lim and R. Closkey, "MEMS-based quartz oscillators and filters for on-chip integration", *Proceedings of the 2005 IEEE international frequency control symposium and exposition*, August 2005, pp. 122–127.
27. R.J. Matthys, *Crystal oscillator circuits*, Krieger Publishing Company, Malabar, USA, April 1991.
28. W.-K. Chen, Ed., *The circuits and filters handbook*, 2nd edn., CRC Press, Boca Raton, USA, 2002.
29. R. Aigner, S. Marksteiner, L. Elbrecht and W. Nessler, "RF-filters in mobile phone applications", *Digest of Technical Papers of the International Conference on Solid State Sensors and Actuators, Transducers '03*, Boston, USA, Vol. 1, June 2003, pp. 891–894.
30. G. Piazza, P.J. Stephanou and A.P. Pisano, "Single-chip multiple-frequency ALN MEMS filters based on contour-mode piezoelectric resonators", *IEEE Journal of Microelectromechanical Systems*, Vol. 16, no. 2, pp. 319–328, April 2007.
31. G. Piazza, R. Abdolvand, G.K. Ho and F. Ayazi, "Voltage-tunable piezoelectrically-transduced single-crystal silicon micromechanical resonators", *Sensors and Actuators A: Physical*, Vol. 111, no. 1, pp. 71–78, March 2004.
32. N. Tagawa, K.-I. Kitamura and A. Mori, "Design and fabrication of MEMS-based active slider using double-layered composite PZT thin film in hard disk drives", *IEEE Transactions on Magnetics*, Vol. 39, no. 2, pp. 926–931, March 2003.
33. D.L. DeVoe, "Piezoelectric thin film micromechanical beam resonators", *Sensors and Actuators A: Physical*, Vol. 88, no. 3, pp. 263–272, January 2001.
34. K. Uchino, "Piezoelectric and electrostrictive actuators", *Proceedings of the sixth IEEE international symposium on applications of ferroelectrics*, Bethlehem, USA, June 1986, pp. 610–618.
35. C.-Y. Lee and E.S. Kim, "Piezoelectrically actuated tunable capacitor", *IEEE Journal of Microelectromechanical Systems*, Vol. 15, no. 4, pp. 745–755, August 2006.
36. S. Akamine, T. Albrecht, M. Zdeblick and C. Quate, "Microfabricated scanning tunneling microscope", *IEEE Electron Device Letters*, Vol. 10, no. 11, pp. 490–492, November 1989.
37. N. Tamer and M. Dahleh, "Feedback control of piezoelectric tube scanners", *Proceedings of the 33rd IEEE conference on decision and control*, Vol. 2, Lake Buena Vista, USA, December 1994, pp. 1826 –1831.
38. J. Brünahl and A.M. Grishin, "Piezoelectric shear mode drop-on-demand inkjet actuator", *Sensors and Actuators A: Physical*, Vol. 101, no. 3, pp. 371–382, October 2002.
39. P.-H. Chen, H.-Y. Peng, H.-Y. Liu, S.L. Chang, T.I. Wu and C.-H. Cheng, "Pressure response and droplet ejection of a piezoelectric inkjet printhead", *International Journal of Mechanical Sciences*, Vol. 41, no. 2, pp. 235–248, February 1999.
40. L. Callaghan, V. Lughi, N. MacDonald and D. Clarke, "Beam-supported AlN thin film bulk acoustic resonators", *IEEE Transactions on Ultrasonics, Ferroelectrics and Frequency Control*, Vol. 53, no. 5, pp. 1001–1007, May 2006.
41. Z. Wang, W. Zhu, H. Zhu, J. Miao, C. Chao, C. Zhao and O.K. Tan, "Fabrication and characterization of piezoelectric micromachined ultrasonic transducers with thick composite PZT films", *IEEE Transactions on Ultrasonics, Ferroelectrics and Frequency Control*, Vol. 52, no. 12, pp. 2289–2297, December 2005.
42. H. Toshiyoshi, H. Fujita and T. Ueda, "A piezoelectrically operated optical chopper by quartz micromachining", *IEEE Journal of Microelectromechanical Systems*, Vol. 4, no. 1, pp. 3–9, March 1995.

43. Y. Yu, T.-L. Ren and L.-T. Liu, "High quality silicon-based AlN thin films for MEMS application", *Journal of Integrated Ferroelectrics*, Vol. 69, pp. 367–374, 2005.
44. Z.Y. Cheng, T.-B. Xu, Q. Zhang, R. Meyer Jr., D. Van Tol and J. Hughes, "Design, fabrication, and performance of a flextensional transducer based on electrostrictive polyvinylidene fluoride-trifluoroethylene copolymer", *IEEE Transactions on Ultrasonics, Ferroelectrics and Frequency Control*, Vol. 49, no. 9, pp. 1312–1320, September 2002.
45. D.S. Greywall, "Micromechanical RF filters excited by the lorentz force", *Journal of Micromechanics and Microengineering*, Vol. 9, no. 1, pp. 78–84, March 1999.
46. J.S. Ko, M.L. Lee, D.-S. Lee, C.A. Choi and Y.T. Kim, "Development and application of a laterally driven electromagnetic microactuator", *Applied physics letters*, Vol. 81, no. 3, pp. 547–549, July 2002.
47. C. Liu, "Development of surface micromachined magnetic actuators using electroplated permalloy", *Journal of Mechatronics*, Vol. 8, no. 5, pp. 613–633, August 1998.
48. K. Ikeda, H. Kuwayama, T. Kobayashi, T. Watanabe, T. Nishikawa, T. Yoshida and K. Harada, "Silicon pressure sensor integrates resonant strain gauge on diaphragm", *Sensors and Actuators A: Physical*, Vol. 21, no. 1–3, pp. 146–150, February 1990.
49. X.M.H Huang, X.L. Feng, C.A. Zorman, M. Mehregany and M.L. Roukes, "VHF, UHF and microwave frequency nanomechanical resonators", *New Journal of Physics*, Vol. 7, p. 247, 2005.
50. C. Liu and Y.W. Yi, "Micromachined magnetic actuators using electroplated permalloy", *IEEE Transactions on Magnetics*, Vol. 35, no. 3, pp. 1976–1985, May 1999.
51. M. Capanu, J.G. Boyd and P.J. Hesketh, "Design, fabrication, and testing of a bistable electromagnetically actuated microvalve", *IEEE Journal of Microelectromechanical Systems*, Vol. 9, no. 2, pp. 181–189, June 2000.
52. J.W. Judy, R.S. Muller and H.H. Zappe, "Magnetic microactuation of polysilicon flexure structures", *IEEE Journal of Microelectromechanical Systems*, Vol. 4, no. 4, pp. 162–169, December 1995.
53. I. Seok Son and A. Lal, "A remotely actuated magnetic actuator for microsurgery with piezoresistive feedback", *The 2nd Annual International IEEE-EMB Special Topic Conference on Microtechnologies in Medicine & Biology*, Madison, USA, May 2002, pp. 332–336.
54. M. Prasciolu, A. Carpentiero, R. Kumar, D. Cojoc, S. Cabrini, L. Businaro, F. Romanato, E.D. Fabrizio, D. Recchia and G. Parmigiani, "Electromagnetically actuated surface micromachined free standing torsion beam micromirror made by electroplated nickel", *Japanese Journal of Applied Physics*, Vol. 43, no. 1, pp. 418–423, January 2004.
55. T. Bourouina, A. Garnier and H. Fujita, "Magnetostrictive microactuators and application to two-dimensional optical scanners", *Japanese Journal of Applied Physics*, Vol. 41, no. 3A, pp. 1608–1613, March 2002.
56. A. Ludwig and E. Quandt, "Giant magnetostrictive thin films for applications in microelectromechanical systems", *Journal of Applied Physics*, Vol. 87, no. 9, pp. 4691–4695, May 2000.
57. M. Aikele, K. Bauer, W. Ficker, F. Neubauer, U. Prechtel, J. Schalk and H. Seidel, "Resonant accelerometer with self-test", *Sensors and Actuators A: Physical*, Vol. 92, no. 1–3, pp. 161–167, August 2001.
58. B. Bahreyni, G. Wijeweera, C. Shafai and A. Rajapakse, "Analysis and design of a micromachined electric field sensor", *IEEE Journal of Microelectromechanical Systems*, Vol. 17, no. 1, pp. 31–36, February 2008.
59. C.C. Barrona, J.H. Comtoisa and M.A. Michalicek, "Electrothermal actuators fabricated in four-level planarized surface micromachined polycrystalline silicon", *Sensors and Actuators A: Physical*, Vol. 70, no. 1–2, pp. 23–31, October 1998.
60. B. Rashidian and M.G. Allen, "Electrothermal microactuators based on dielectric loss heating", *Proceedings of the 6th IEEE micro electro mechanical systems conference, MEMS '93*, Atlanta, USA, February 1993, pp. 24–29.

61. Q.-A. Huang and N.K.S. Lee, "Analysis and design of polysilicon thermal flexure actuator", *Journal of Micromechanics and Microengineering*, Vol. 9, pp. 64–70, 1999.
62. P. Lerch, C.K. Slimane, B. Romanowic and P. Renaud, "Modelization and characterization of asymmetrical thermal micro-actuators", *Journal of Micromechanics and Microengineering*, Vol. 6, pp. 134–137, 1996.
63. J.H. Comtois, M.A. Michalicek and C.C. Barron, "Electrothermal actuators fabricated in four-level planarized surface micromachined polycrystalline silicon", *Sensors and Actuators A: Physical*, Vol. 70, no. 1–2, pp. 23–31, October 1998.
64. L. Que, J.-S. Park and Y.B. Gianchandani, "Bent-beam electrothermal actuatorspart i: Single beam and cascaded devices", *IEEE Journal of Microelectromechanical Systems*, Vol. 10, no. 2, pp. 247–254, June 2001.
65. X. Chen, C. Peng, H. Tao, C. Ye, Q. Bai, S. Chen and S. Xia, "Thermally driven micro-electrostatic fieldmeter", *Sensors and Actuators A: Physical*, Vol. 132, no. 2, pp. 677–682, November 2006.
66. R. Hickey, D. Sameoto, T. Hubbard and M. Kujath, "Time and frequency response of two-arm micromachined thermal actuators", *Journal of Micromechanics and Microengineering*, Vol. 13, pp. 40–46, 2003.
67. L.C. Thomas, *Fundamentals of heat transfer*, Prentice-Hall, Englewood Cliffs, USA, 1980.
68. F. Incropera and D. DeWitt, *Fundamentals of heat and mass transfer*, 4th edn., Wiley, New York, USA, 1996.
69. B. Bahreyni, F. Najafi and C. Shafai, "Piezoresistive sensing with twin-beam structures in standard MEMS foundry processes", *Sensors and Actuators A: Physical*, Vol. 127, no. 2, pp. 325–331, March 2006.
70. V.A. Gridchin, V.M. Lubimsky and M.P. Sarina, "Piezoresistive properties of polysilicon films", *Sensors and Actuators A: Physical*, Vol. 49, no. 1–2, pp. 67–72, June 1995.
71. S.M. Sze, *Semiconductor devices: physics and technology*, John Wiley, New York, USA, 1985.
72. L.K. Baxter, *Capacitive sensors: design and applications*, Wiley-IEEE Press, New York, USA, 1997.
73. T. Polak and C. Pande, *Engineering measurements: methods and intrinsic errors*, Professional Engineering Publishing, London, United Kingdom, 1999.
74. S. Martellucci, A.N. Chester and A.G. Mignani, Eds., *Optical sensors and microsystems: new concepts, materials, technologies*, Kluwer Academic Publishers, New York, USA, 2002.
75. A. Lewin, A. Kersey and D. Jackson, "Non-contact surface vibration analysis using a monomode fibre optic interferometer incorporating an open air path", *Journal of Physics E: Scientific Instruments*, Vol. 18, no. 7, pp. 604–608, July 1985.
76. R. Howe and R. Muller, "Resonant-microbridge vapor sensor", *IEEE Transactions on Electron Devices*, Vol. 33, no. 4, pp. 499–506, April 1986.
77. I. Voiculescu, M. Zaghloul, R. McGill, E. Houser and G. Fedder, "Electrostatically actuated resonant microcantilever beam in CMOS technology for the detection of chemical weapons", *IEEE Sensors Journal*, Vol. 5, no. 4, pp. 641–647, August 2005.
78. J.A. Harley and T.W. Kenny, "A high-stiffness axial resonant probe for atomic force microscopy", *IEEE Journal of Microelectromechanical Systems*, Vol. 10, no. 3, pp. 434–441, September 2001.
79. H.K. Rockstad, T. Tang, J. Reynolds, T. Kenny, W. Kaiser and T.B. Gabrielson, "A miniature, high-sensitivity, electron tunneling accelerometer", *Sensors and Actuators A: Physical*, Vol. 53, no. 1–3, pp. 227–231, May 1996.
80. H. Dong, Y. Jia, Y. Hao and S. Shen, "A novel out-of-plane MEMS tunneling accelerometer", *Sensors and Actuators A: Physical*, Vol. 120, no. 2, pp. 360–364, May 2005.
81. D. DiLella, L. Whitman, R. Colton, T. Kenny, W. Kaiser, E. Vote, J. Podosek and L. Miller, "A micromachined magnetic-field sensor based on an electron tunneling

displacement transducer", *Sensors and Actuators A: Physical*, Vol. 86, no. 1–2, pp. 8–20, October 2000.
82. G. Binnig, H. Rohrer, C. Gerber and E. Weibel, "Tunneling through a controllable vacuum gap", *Applied Physics Letters*, Vol. 40, no. 2, pp. 178–180, January 1982.
83. G. Binnig and H. Rohrer, "Scanning tunneling microscopy", *Journal of Surface Science*, Vol. 126, no. 1–3, pp. 236–244, March 1983.
84. A. London, A. Epstein and J. Kerrebrock, "High-pressure bipropellant microrocket engine", *Journal of Propulsion and Power*, Vol. 17, no. 4, pp. 780–787, July–August 2001.
85. C. Lee, K. Jiang, P. Jin and P. Prewett, "Design and fabrication of a micro Wankel engine using MEMS technology", *Journal of Microelectronic Engineering*, Vol. 73–74, no. 1, pp. 529–534, June 2004.
86. D.H. Lee, D.E. Park, J.B. Yoon, S. Kwon and E. Yoon, "Fabrication and test of a MEMS combustor and reciprocating device", *Journal of Micromechanics and Microengineering*, Vol. 12, no. 1, pp. 26–34, 2002.
87. A.H. Epstein, S.D. Senturia, I.A. Waitz, J.H. Lang, S.A. Jacobson, F.F. Ehrich, M.A. Schmidt, G.K. Ananthasuresh, M.S. Spearing, K.S. Breuer and S.F. Nagle, "Microturbomachinery", USA Patent 5 932 940, 1999.
88. A.F. Devonshire, "Theory of ferroelectrics", *Advances in Physics*, Vol. 3, no. 10, pp. 85–130, April 1954.
89. H. Kay, "Electrostriction", *Journal of Reports on Progress in Physics*, Vol. 18, pp. 230–250, 1955.
90. R. Newnham, V. Sundar, R. Yimnirun, J. Su and Q. Zhang, "Electrostriction: Nonlinear electromechanical coupling in solid dielectrics", *Journal of Physical Chemistry B*, Vol. 101, no. 48, November 1997. pp. 10 141–10 150.
91. E. Fukada, "History and recent progress in piezoelectric polymers", *IEEE Transactions on Ultrasonics, Ferroelectrics and Frequency Control*, Vol. 47, no. 6, pp. 1277–1290, November 2000.
92. S.M. Pilgrim, "Electrostrictive ceramics for low-frequency active transducers", *IEEE Transactions on Ultrasonics, Ferroelectrics and Frequency Control*, Vol. 47, no. 4, pp. 861–876, July 2000.

4 Modelling of Statics

Micromachined devices are continuous three-dimensional systems whose operation often involves multiple physical domains, such as electrostatic, magnetic, statical, thermal, electromechanical, thermoelastic, and electrical. A model is a mathematical representation of the system which can be used to analyse and predict the system response under different conditions. The steps to make a micromachined device are design, fabrication, and test. Having proper models is important in all of these steps. A proper device model is needed in the design step to choose proper device dimensions and estimate the signal levels to and from the device. Quite often, the micromachined system is needed to interact with other systems (e.g., inside a feedback loop) and the developed model might be used within the larger model of the whole system. Development of proper models for fabrication steps, especially the etch and deposition steps, allows for process optimisation and easy tailoring of the process variables for a specific application. However, these processing steps involve rather complicated phenomena, often at the molecular or atomic levels, and simple models do not exist for many of them and one has to resort to numerical simulations. Modelling of the fabrication processes is not covered in this book and the interested reader should refer to the literature on this topic [1–4]. A device model is also useful when testing strategies are developed, for example, to take advantage of nonlinear behaviour of a device under test.

It is usually possible to develop physical models based on the structure and the employed actuation and sense mechanisms for a micromachined resonator. Often, a principal model is developed to investigate the response of the system to the main stimulus but other models can be studied to investigate the response of the system to disturbances.

While the main reason for static modelling of a system is to investigate the response of the system under static conditions, its results can also be used for the dynamic analysis of the structure; for instance, the magnitude of a resonator response at the resonant frequency is about Q times the static response where Q is the quality factor. Most resonant devices can be approximated as mass–spring systems. Knowing the structural materials and the dimensions of the device, the mass of the different parts of the resonator can be easily estimated. Calculation of the spring constants in a system, however, can be more involved. It should also be noted that the dynamic behaviour of the system depends on its effective mass and spring constants that can be different from the values which are simply evaluated from geometrical calculations.

If the displacement vector inside a material is given by $\vec{u}$, the strain vector is defined as:

$$\vec{\epsilon} = \nabla \vec{u}. \tag{4.1}$$

The general relationship between the strain and stress tensors for a linear elastic solid is given by [5–7]:

$$\begin{aligned}
\sigma_{11} &= c_{1111}\epsilon_{11} + c_{1112}\epsilon_{12} + \cdots + c_{1133}\epsilon_{33} \\
\sigma_{12} &= c_{1211}\epsilon_{11} + c_{1212}\epsilon_{12} + \cdots + c_{1233}\epsilon_{33} \\
&\vdots \qquad\qquad \vdots \\
\sigma_{33} &= c_{3311}\epsilon_{11} + c_{3312}\epsilon_{12} + \cdots + c_{3333}\epsilon_{33}
\end{aligned} \tag{4.2}$$

where the indices 1 to 3 represent the orientation along the corresponding axes; e.g., σ_{11} is the compressional stress along the x-axis while ϵ_{23} is the shear strain between axes y and z (i.e., plane yz). The above system of equations can be written as:

$$\sigma_{ij} = \sum_{k=1}^{3}\sum_{l=1}^{3} c_{ijkl}\epsilon_{kl} \tag{4.3}$$

where σ_{ij} and ϵ_{ij} are elements of second-order tensors (i.e., matrices) and c_{ijkl} are elements of the fourth order *elasticity tensor*. The number of coefficients in Eq. (4.2) can be reduced from 81 to 21 with assumptions of symmetry and homogeneousness. For a transversely isotropic solid, such as silicon, the number of unknowns reduces further to only five. The stress strain relationships for silicon are completely defined with three independent coefficients, due to the symmetric structure of the silicon crystal [8]:

$$\begin{bmatrix} \sigma_1 \\ \sigma_2 \\ \sigma_3 \\ \tau_4 \\ \tau_5 \\ \tau_6 \end{bmatrix} = \begin{bmatrix} c_{11} & c_{12} & c_{12} & 0 & 0 & 0 \\ c_{12} & c_{11} & c_{12} & 0 & 0 & 0 \\ c_{12} & c_{12} & c_{11} & 0 & 0 & 0 \\ 0 & 0 & 0 & c_{44} & 0 & 0 \\ 0 & 0 & 0 & 0 & c_{44} & 0 \\ 0 & 0 & 0 & 0 & 0 & c_{44} \end{bmatrix} \begin{bmatrix} \epsilon_1 \\ \epsilon_2 \\ \epsilon_3 \\ \gamma_4 \\ \gamma_5 \\ \gamma_6 \end{bmatrix} \tag{4.4}$$

or

$$\begin{bmatrix} \epsilon_1 \\ \epsilon_2 \\ \epsilon_3 \\ \gamma_4 \\ \gamma_5 \\ \gamma_6 \end{bmatrix} = \begin{bmatrix} s_{11} & s_{12} & s_{12} & 0 & 0 & 0 \\ s_{12} & s_{11} & s_{12} & 0 & 0 & 0 \\ s_{12} & s_{12} & s_{11} & 0 & 0 & 0 \\ 0 & 0 & 0 & s_{44} & 0 & 0 \\ 0 & 0 & 0 & 0 & s_{44} & 0 \\ 0 & 0 & 0 & 0 & 0 & s_{44} \end{bmatrix} \begin{bmatrix} \sigma_1 \\ \sigma_2 \\ \sigma_3 \\ \tau_4 \\ \tau_5 \\ \tau_6 \end{bmatrix} \tag{4.5}$$

where the axes indices are similar to what is illustrated in Fig. 3.5 and we have used the common symbols τ and γ for shear stresses and strains. In this case, the elasticity and stiffness coefficients are related to each other

Table 4.1 Elastic Constants of Silicon at 298 K and Their Temperature Coefficients

	Elastic constant (GPa)	Temperature coefficient ($\times 10^{-6}$ K^{-1})
c_{11}	165.64	−75
c_{12}	63.94	−24.5
c_{44}	79.51	−55.5

according to:

$$\begin{aligned} s_{11} &= \frac{c_{11}+c_{12}}{(c_{11}-c_{12})(c_{11}+2c_{12})} \\ s_{12} &= \frac{-c_{12}}{(c_{11}-c_{12})(c_{11}+2c_{12})} \\ s_{44} &= \frac{1}{c_{44}}. \end{aligned} \tag{4.6}$$

The values for elastic coefficients of silicon at 298 K and their temperature coefficients are listed in Table 4.1 [8,9].

For an isotropic, i.e., a material whose mechanical properties are independent of orientation, the number of required constants reduces to only two:

$$\begin{aligned} c_{ii} &= E\frac{1-\nu}{(1+\nu)(1-2\nu)} && \text{for } i = 1,2,3 \\ c_{jj} &= E\frac{1}{1+\nu} && \text{for } j = 4,5,6 \\ c_{mn} &= E\frac{\nu}{(1+\nu)(1-2\nu)} && \text{for } mn = \{12,21,23,32,13,31\} \end{aligned}$$

with other elastic constants equal to zero. Parameters E and ν are called *Young's modulus* and *Poisson's ratio*, respectively.

For the sake of simplicity, we assume that the structural material for the devices that we study in this and the next chapter are homogeneous and isotropic.

4.1 Beams under Longitudinal Stress

Dimensions of structures change under mechanical stress. Consider a straight beam of length L along the x-axis, subjected to axial stress σ_x, that is made of an isotropic homogeneous material (see Fig. 4.1). The mechanical strain along the x-direction is found from:

$$\epsilon_x = \frac{\Delta L}{L} \tag{4.7}$$

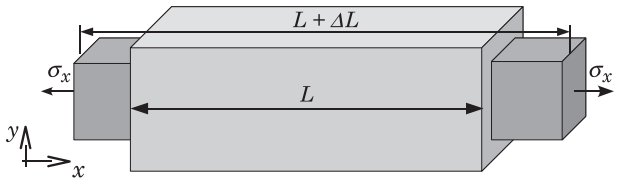

Figure 4.1 A straight beam under an axial stress.

where ΔL is the amount of beam elongation. Hook's law relates the stress and strain to each other:

$$\sigma = E\epsilon \tag{4.8}$$

where E is the *Young's modulus* of the material (also known as the elastic modulus) where σ and ϵ are vectors. Often, a material is anisotropic[1], meaning that the coefficients relating stress and strain are different along different orientations. In such cases, E is given by a matrix (see previous section).

In addition to the change in length, the cross sectional dimensions of the beam change under an axial strain. For a slab of an isotropic material with initial length, width, and height of L, W, and h, respectively, we have:

$$\begin{aligned} L' &= (1+\epsilon_x)L \\ W' &= (1-\nu\epsilon_x)W \\ h' &= (1-\nu\epsilon_x)h \end{aligned} \tag{4.9}$$

where L', W', and h' are the dimensions under the axial strain ϵ_x.

It can be seen that if an axial force $\mathcal{T}$ is applied to a straight beam, the resultant strain is found from:

$$\mathcal{T} = \sigma A = EA\epsilon \tag{4.10}$$

where A is the cross-sectional area of the beam. Remembering that $\epsilon = \Delta L/L$, the longitudinal spring constant of a beam under axial stress can be found from:

$$k_l = \frac{\mathcal{T}}{\Delta L} = E\frac{A}{L}. \tag{4.11}$$

[1]Most crystalline materials, including silicon, are electrically and mechanically anisotropic.

4.2 Bending of Beams

One of the basic spring structures for micromachined devices is a slender beam; i.e., a beam whose length is much larger than its width and thickness. For small deflections, the behaviour of these beams is studied using Euler's beam theory [10,11]. Euler's theory assumes that the beam cross-section is constant along its axis, the beam is loaded in its plane of symmetry, the material is isotropic, and the plane sections of the beam remain plane after bending. These assumptions are often valid for the beam springs of micromachined devices. The differential equation to find the static beam deflections is [10,12]:

$$\frac{\mathcal{M}}{E\mathcal{I}} = \frac{\partial^2 \psi}{\partial x^2}\left[1 + \left(\frac{\partial \psi}{\partial x}\right)^2\right]^{-\frac{3}{2}} \tag{4.12}$$

where $\psi(x)$ is the deflection of the beam in y-direction, E is the Young's modulus of elasticity, and $\mathcal{M}$ is the applied moment. Parameter $\mathcal{I}$ is the second moment of inertia.

For small deflections relative to the length of the beam $\left(\frac{\partial \psi}{\partial x}\right)^2 \ll 1$, and therefore, this term can be ignored. Differentiating Eq. (4.12), it can be seen:

$$E\mathcal{I}\frac{\partial^2 \psi}{\partial x^2} = \mathcal{M} \tag{4.13}$$

$$E\mathcal{I}\frac{\partial^3 \psi}{\partial x^3} = \mathcal{V} \tag{4.14}$$

$$E\mathcal{I}\frac{\partial^4 \psi}{\partial x^4} = \mathcal{N} \tag{4.15}$$

where $\mathcal{V}$ is the shearing force and $\mathcal{N}$ is the distributed load along the length of the beam. Each of the above equations with proper boundary conditions may be used to calculate the deflection of a beam, depending on types of loads on a beam. One can use the Dirac's impulse function to solve the problem when the load is applied to a point rather than being distributed along the length of the beam [13–15]. Typical beam boundary conditions are summarised in Table 4.2.

The value of $\mathcal{I}$ for a beam along the x-axis with deflections in xy-plane is given by [11]:

$$\mathcal{I} = \int_A r^2 dA. \tag{4.16}$$

For a beam with rectangular cross section of thickness h and width W the moment of inertia is found to be:

$$\mathcal{I} = \int_{-\frac{h}{2}}^{\frac{h}{2}} \int_{-\frac{W}{2}}^{\frac{W}{2}} r^2 ds dr = \frac{hW^3}{12}. \tag{4.17}$$

Table 4.2 Typical Beam Boundary Conditions at the Ends of a Straight Beam

Boundary condition	Drawing symbol	ψ	$\dot{\psi}$	$\ddot{\psi}$	$\dddot{\psi}$
Free		*Unknown*	*Unknown*	*0*	*0*
Guided		*Unknown*	*0*	*Unknown*	*Unknown*
Pinned		*0*	*Unknown*	*0*	*0*
Clamped		*0*	*0*	*Unknown*	*Unknown*

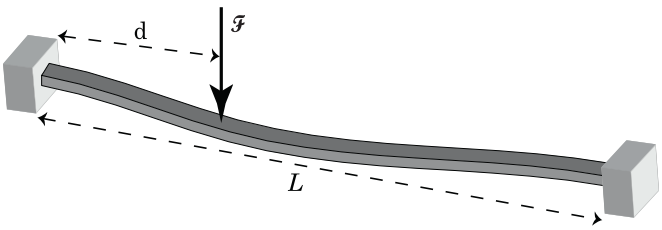

Figure 4.2 Schematic of a slender beam under a shear force.

For example, deflections of the beam illustrated in Fig. 4.2 can be found from solving Eq. (4.15):

$$E\mathcal{I}\frac{\partial^4\psi}{\partial x^4} = \mathcal{F}\delta(x-d) \tag{4.18}$$

with boundary conditions $\psi(0) = \psi(L) = 0$ and $\dot{\psi}(0) = \dot{\psi}(L) = 0$. The solution is:

$$\psi(x) = \begin{cases} \dfrac{\mathcal{F}}{6E\mathcal{I}}\left(\dfrac{d^2(3L-2d)x^3}{L^3} - \dfrac{3d^2(L-d)x^2}{L^2} - (x-d)^3\right) & \text{for } x \geq d \\ \dfrac{\mathcal{F}(L-d)^2}{6E\mathcal{I}L^3}\left((L+2d)x^3 - 3dLx^2\right) & \text{for } x < d. \end{cases} \tag{4.19}$$

The spring constant for the case where the force is applied to the centre of the beam (i.e., $d = L/2$) is found from:

$$k_b = \frac{\mathcal{F}}{\psi(\frac{L}{2})} = \frac{192E\mathcal{I}}{L^3} = \frac{16EhW^3}{L^3}. \tag{4.20}$$

Table 4.3 Static Deflection Equations and Spring Constants for Typical Beam Structures of Length L under Distributed and Point Loads in Typical Situations. The deflection equation for the clamped–clamped beam in the last row is valid for $x < L/2$.

Boundary conditions	Load	Deflection equation	Spring constant
Clamped-Free	$\mathcal{F}\delta(x-L)$	$\frac{\mathcal{F}x^2}{6E\mathcal{I}}(x-3L)$	$\frac{3E\mathcal{I}}{L^3}$
Clamped-Free	$\frac{\mathcal{F}}{L}$	$\frac{\mathcal{F}x^2}{24E\mathcal{I}L}\left(x^2-4Lx+6L^2x\right)$	$\frac{8E\mathcal{I}}{L^3}$
Clamped-Guided	$\mathcal{F}\delta(x-L)$	$\frac{\mathcal{F}x^2}{12E\mathcal{I}}(3L-2x)$	$\frac{12E\mathcal{I}}{L^3}$
Clamped-Clamped	$\frac{\mathcal{F}}{L}$	$\frac{\mathcal{F}x^2}{24E\mathcal{I}L}(x-L)^2$	$\frac{384E\mathcal{I}}{L^3}$
Clamped-Clamped	$\mathcal{F}\delta(x-\frac{L}{2})$	$\frac{\mathcal{F}x^2}{48E\mathcal{I}}(3L-4x)$	$\frac{192E\mathcal{I}}{L^3}$

Table 4.3 summarises the deflection equations and spring constants for straight beams under typical conditions. In case of having a distributed force $\mathcal{F}/L$, the spring constant in this table is found from dividing the total force acting on the beam by the maximum resultant deflections; i.e., $\mathcal{F}/\psi_{\max}$.

4.2.1 Spring Constant of a Beam under Axial Stress

The design of many resonant sensors is based on the shift in the resonant frequency of the sensor structure due to the change in the spring constant of the beams under an applied axial stress or its effective mass. This effect has also been used for fine tuning of spring constants in other applications [16,17]. An analytic model for the spring constant of a guided beam under axial stress is derived below.

The differential equation for static bending of a beam under axial stress is [10,18]:

$$E\mathcal{I}\frac{\partial^4\psi}{\partial x^4}-\mathcal{P}\frac{\partial^2\psi}{\partial x^2}=\mathcal{F} \tag{4.21}$$

where $\mathcal{P}$ is the applied axial force (positive for a tensile force) and $\mathcal{F}$ is the load distributed along the beam (see Fig. 4.3). This equation is generally solved numerically. Approximate solutions have also been derived for this equation (e.g., by using power series) and can be found in literature [10,13,19,20]. An exact solution can be obtained for this equation for a beam-spring by applying

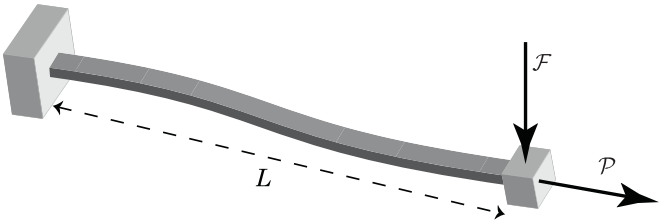

Figure 4.3 Schematic of a slender beam under a shear force and axial stress.

the clamped-guided boundary conditions [21]:

$$\psi(x) = \frac{\mathcal{F}}{E\mathcal{I}\gamma^3}\left((\cosh(\gamma x) - 1)\tanh\left(\frac{\gamma L}{2}\right) - \sinh(\gamma x) + \gamma x\right) \tag{4.22}$$

where $\gamma^2 = \mathcal{P}/E\mathcal{I}$. The spring constant for a guided beam under axial stress is:

$$k_b(\mathcal{P}) = \frac{\mathcal{F}}{\psi_{\max}} = \frac{E\mathcal{I}\gamma^3}{\gamma L - 2\tanh\frac{\gamma L}{2}}. \tag{4.23}$$

It must be noted that there are limits to the amount of axial stress that can be applied to a beam. The structure deforms permanently if the applied tensile stress is larger than the *yield strength* of the structural material and too much tensile stress, i.e., above the *ultimate tensile strength* of the material, leads to rupture and permanent failure[2]. On the other hand, a large compressive force results in the buckling of the beam. The buckling limit for a slender beam of length L can be found from Euler's beam theory [18,22]:

$$\mathcal{P}_{cr} = -\chi\frac{E\mathcal{I}}{L^2} \tag{4.24}$$

where χ is a constant depending on the boundary conditions at supports. It can be shown that $\chi = \pi^2$ for a pinned–pinned beam and $\chi = 4\pi^2$ for a clamped–clamped beam [18].

4.3 Deflections of Plates

A plate that is fixed at its edges is seldom used as a resonator, partly because of its large surface area and clamping regions that lead to low quality factors

[2]The ultimate tensile stress of silicon is on the order of few GPa, depending on the crystallographic direction and fabrication techniques.

compared to beam-based structures. However, a plate can be considered as a two dimensional extension of a beam and its static analysis is needed for a more accurate three dimensional study of the structures.

The deflections of a plate of thickness h are given by [23–26]:

$$\mathcal{D}\nabla^4\psi(x,y) = p(x,y) \tag{4.25}$$

where $p(x,y)$ is the distributed load on the surface of the plate and $\mathcal{D}$ is the plate flexural rigidity given by:

$$\mathcal{D} = \frac{Eh^3}{12(1-\nu^2)}. \tag{4.26}$$

Operator $\nabla^4 = \nabla^2\nabla^2$ is known as *biharmonic* operator. The biharmonic operator in Cartesian coordinates is given by:

$$\nabla^4 = \left(\frac{\partial^4}{\partial x^4} + 2\frac{\partial^4}{\partial x^2\partial y^2} + \frac{\partial^4}{\partial y^4}\right).$$

References

1. C. Ho, J. Plummer, S. Hansen and R. Dutton, "VLSI process modeling–SUPREM III", *IEEE Transactions on Electron Devices*, Vol. 30, no. 11, pp. 1438–1453, November 1983.
2. I. Brodie and J.J. Muray, *The physics of micro/nano-fabrication*, Plenum Press, New York, USA, 1992.
3. R. Nassar and W. Dai, Eds., *Modeling of microfabrication systems*, "ser. Microtechnology and MEMS", Springer Verlag, Berlin, Germany, 2003.
4. B. El-Kareh, *Fundamentals of semiconductor processing technologies*, Kluwer Academic Publishers, Norwell, USA, 1994.
5. W.M. Lai, D. Rubin and E. Krempl, *Introduction to continuum mechanics*, Butterworth-Heinemann Ltd, Oxford, United Kingdom, 1993.
6. E. Hearn, *Mechanics of materials 2*, 3rd edn., Butterworth-Heinemann, Oxford, United Kingdom, 1997.
7. T. Megson, *Structural and stress analysis*, Butterworth-Heinemann, Oxford, United Kingdom, 1996.
8. R. Hull, Ed., *Properties of crystalline silicon*, Institution of Electrical Engineers, London, United Kingdom, 1999.
9. H.J. McSkimin and J.P. Andreatch, "Elastic moduli of silicon vs hydrostatic pressure at 25.0 °C and −195.8 °C", *Journal of Applied Physics*, Vol. 35, no. 7, pp. 2161–2165, July 1964.
10. S.D. Senturia, *Microsystem design*, Kluwer Academic Publishers, Boston, USA, 2000.
11. S. Timoshenko, *Strength of materials, Part 1*, 3rd edn., Krieger Publishing, USA, 1983.
12. S. Timoshenko and J. Goodier, *Theory of elasticity*, 2nd edn., McGraw-Hill, Tokyo, Japan, 1951.
13. W.C. Young and R.G. Budynas, *Roark's formulas for stress and strain*, 7th edn., McGraw-Hill, New York, USA, 2002.

14. F.P. Beer and E.R. Johnston, *Mechanics of materials*, 2nd edn., McGraw-Hill, New York, USA, 1992.
15. J. Case, L. Chilver and C.T.F. Ross, *Strength of materials and structures*, 4th edn., Arnold Publishers, London, United Kingdom, 1999.
16. S. Diamantis, M. Ahmadi, G.A. Jullien and W.C. Miller, "A programmable MEMS bandpass filter", *Proceedings of the 43rd IEEE midwest symposium on circuits and systems*, Lansing, USA, Vol. 1, August 2000, pp. 522–525.
17. K.Y. Park, C.W. Lee, H.S. Jang, Y.S. Oh and B.J. Ha, "Capacitive sensing type surface micromachined silicon accelerometer with a stiffness tuning capability", *Proceedings of the 11th IEEE micro electro mechanical systems conference, MEMS '98*, Heidelberg, Germany, January 1998, pp. 637–642.
18. M. Elwenspoek and R. Wiegerink, *Mechanical microsensors*, Springer-Verlag, Berlin, Germany, 2001.
19. K.A. Gibbons, J.T. Borenstein, D.S. Nokes, M.S. Weinberg and D.L. Trumper, "The design, fabrication, and testing of a micromechanical silicon oscillating accelerometer", *Proceedings of the AIAA conference on guidance and control*, Boston, USA, August 1998, pp. 1296–1306.
20. L.X. Zhang and Y.P. Zhao, "Electromechanical model of RF MEMS switches", *Journal of Microsystem Technologies*, Vol. 9, no. 6–7, pp. 420–426, September 2003.
21. B. Bahreyni, "Design, modeling, simulation, and testing of resonant micromachined magnetic field sensors", Ph.D. dissertation, Department of Electrical and Computer Engineering, The University of Manitoba, Canada, 2006.
22. C.M. Wang, C.Y. Wang and J.N. Reddy, *Exact solutions for buckling of structural members*, CRC Press, Boca Raton, USA, 2004.
23. L. Landau and E. Lifshitz, in: *Theory of elasticity*, 3rd edn., ser. Course of theoretical physics, Vol. 7, Butterworth Heinemann, Oxford, United Kingdom, 1976. Translated by J.B. Sykes and W.H. Reid.
24. L. Meirovitch, *Analytical methods in vibrations*, MacMillan, New York, USA, 1967.
25. S. Timoshenko and S. Woinowsky-Kreiger, *Theory of plates and shells*, 2nd edn., McGraw-Hill, USA, 1964.
26. C.W. De Silva, *Vibration : fundamentals and practice*, CRC Press LLC, Boca Raton, USA, 2000.

5 Modelling of Dynamics

When analysing the resonance behaviour, it is generally required to estimate the resonant frequency or the sensitivity of a resonant sensor (i.e., the change in the resonant frequency in response to the input). This can be done through studying the dynamic behaviour of resonant devices. The dynamic modelling of even the simplest structures can be tedious and one often needs to make several simplifying assumptions. Depending on the problem, these assumptions may include linearity, simple or no damping effects, rigid supports, etc.

The input force is usually from the transduction of an electrical drive signal to another physical domain (e.g., electrostatic, magnetic, or piezoelectric). This force brings the structure under resonance, which is then sensed at the output port of the device through different mechanisms (e.g., electrostatic, piezoelectric, or piezoresistive). In this chapter, the concentration is on the dynamic modelling of resonators. The transduction mechanisms were covered in Chapter 3 and the interested reader can refer to the literature for more in depth discussion of transduction mechanisms [1–4].

A simple electrostatic mass sensor is used to illustrate the modelling techniques in this chapter. The sensor schematic is shown in Fig. 5.1. The resonant frequency of the sensor changes as a result of the added mass of a particle that settles on the sensor shuttle. The sensor is assumed to be made from single crystalline silicon from the device layer of an SOI wafer. The data required for the analysis of the sensor is summarised in Table 5.1. The area of connections for signals to the input and output ports is also listed as it will be needed when we calculate the parasitics. It is assumed that the sensor operates under vacuum with a quality factor of 15 000 and the handle wafer can be treated as a good, grounded conductor.

5.1 Lumped Systems

In many cases, the resonating system can be modelled as a mass–spring–damper system (see Fig. 5.2). This is the simplest model for a resonator, but often provides valuable insight to the operation of the device. To use a lumped-system model, a system needs to be broken into mass, spring, and damper elements and use a procedure similar to the discussion in Section 1.2. To improve the modelling accuracy, one should use the effective mass, M_{eff}, or spring constant, K_{eff}, of the system which are found from the system energy at resonance:

$$M_{\text{eff}} = 2\frac{\mathcal{K}_{\max}}{v^2} \tag{5.1}$$

$$K_{\text{eff}} = 2\frac{\mathcal{U}_{\max}}{x^2} \tag{5.2}$$

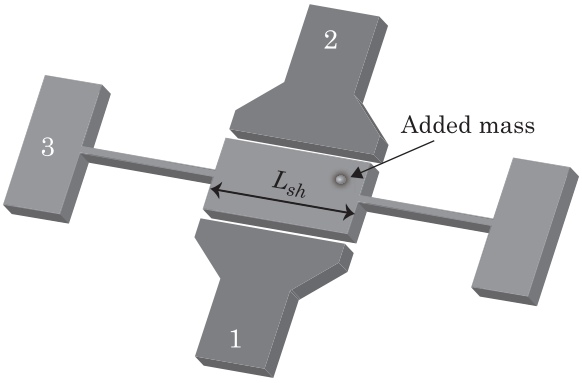

Figure 5.1 Schematic of the mass sensor.

Table 5.1 Parameters for the Analysis of the Mass Sensor

Parameter	Symbol	Value
Young's modulus	E_{si}	140 GPa
Mass density	ρ_{si}	2330 kg m^{-3}
Thickness of the structure	h	10 μm
Buried oxide thickness	t_{ox}	1 μm
Length of the shuttle	$L_{\rm sh}$	100 μm
Width of the shuttle	$W_{\rm sh}$	30 μm
Length of the beam springs	L_b	100 μm
Length of the beam springs	W_b	2 μm
Gap between the electrodes	g	1 μm
Input/output connections area	A_p	15 000 μm^2
Quality factor	Q	15 000

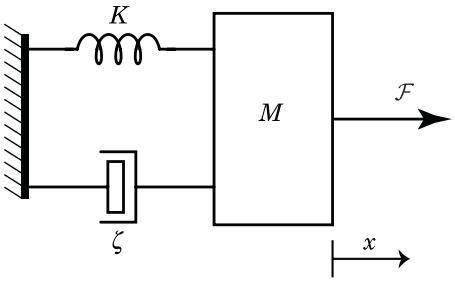

Figure 5.2 A mass–spring–damper system.

where $\mathcal{K}_{\max}$ and $\mathcal{U}_{\max}$ are the maximum kinetic and potential energies of the resonator and v and x are the velocity and displacement of the resonator when the kinetic and potential energies are at their maxima.

5.1.1 Analysis of the Mass Sensor Using a Lumped Model

Using the results in this Section 1.2 and Section 4.2, the resonant frequency of the mass sensor shown in Fig. 5.1 can be calculated. If the shuttle of the sensor is assumed to be a rigid body, the two beam springs attached to it can be regarded as a single clamped–clamped beam of length $2L$. The spring constant of each of the beams for the mass sensor illustrated in Fig. 5.1 is:

$$k_b = \frac{1}{2} \cdot 16 \cdot 140 \times 10^9 \cdot 10 \times 10^{-6} \cdot \left(\frac{2}{2 \times 100} \right)^3 = 11.2 \text{ N/m}. \tag{5.3}$$

Ignoring the mass of the beam springs, the resonant frequency is found to be:

$$\begin{aligned} f_0 = \frac{1}{2\pi} \sqrt{\frac{2k_b}{M_{\text{sh}}}} &= \frac{1}{2\pi} \sqrt{\frac{\frac{16 E_{si} h W_b^3}{L_b^3}}{\rho_{si} h L_{\text{sh}} W_{\text{sh}}}} \\ &= 90\,096.01 \text{ Hz} \end{aligned} \tag{5.4}$$

where M_{sh} is the mass of the shuttle. The sensor sensitivity for measuring a small added mass m is:

$$\begin{aligned} S_m^{f_0} = \frac{df_0}{dm} &\approx -\frac{f_0}{2(M_{\text{sh}} + m)} \\ &= -644.46 \text{ Hz/ng}. \end{aligned} \tag{5.5}$$

5.2 Longitudinal Wave Propagation in Beams

Dynamic analysis of continuous systems is more involved than the modelling of lumped systems. It is sometimes possible to break a continuous system into smaller subsystems and treat the system as a lumped one. For a more thorough analysis, however, the whole system should be treated as a distributed mass–spring system.

The longitudinal resonant behaviour of a thin beam along x-direction can be analysed by solving the wave equation [5,6]:

$$E \frac{\partial^2 \psi}{\partial x^2} = \rho \frac{\partial^2 \psi}{\partial t^2} \tag{5.6}$$

where the longitudinal displacements of the beam are given by $\psi(x, t)$ and ρ is the material density. Eq. (5.6) can also be written as:

$$\frac{\partial^2 \psi}{\partial x^2} = \frac{1}{c_0^2} \frac{\partial^2 \psi}{\partial t^2} \tag{5.7}$$

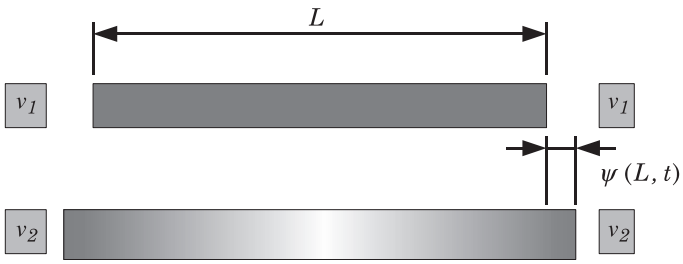

Figure 5.3 A longitudinal beam resonator under symmetric axial electrostatic force at it ends ($v_2 > v_1$).

where $c_0 = \sqrt{E/\rho}$ is the phase velocity of the wave inside the beam. Wavelength of the longitudinal waves along a beam is given by:

$$\lambda_l = \frac{c_0}{f} = \frac{1}{f}\sqrt{\frac{E}{\rho}} \tag{5.8}$$

where f is the frequency. Knowing the acoustic wavelength is important when determining the dimensions of a resonator for a given resonant frequency and also when using beams as anchors in the design of more complicated structures.

5.2.1 A Longitudinal Beam Resonator

Consider the beam resonator shown in Fig. 5.3 which is electrostatically actuated by applying a voltage to the electrodes at its ends.

Method of separation of variables can be employed to solve Eq. (5.7) for free vibrations of the beam. Inserting $\psi(x,t) = \hat{\psi}(x)\, e^{j\omega t}$ into Eq. (5.7), it can be seen:

$$\left(\frac{\partial^2 \hat{\psi}}{\partial x^2} + \frac{\omega^2}{c_0^2}\hat{\psi}\right) \cdot e^{j\omega t} = 0. \tag{5.9}$$

The steady state solution to the above equation is:

$$\hat{\psi}(x) = \mathcal{A}\sin\frac{\omega x}{c_0} + \mathcal{B}\cos\frac{\omega x}{c_0}. \tag{5.10}$$

For a beam of length L, the boundary conditions are $\frac{\partial}{\partial x}\psi(0,t) = 0$ and $\frac{\partial}{\partial x}\psi(L,t) = 0$, yielding $\mathcal{A} = 0$ and $\sin(\omega L/c_0) = 0$ for the characteristic equation. The resonant frequencies of different modes of this resonator are

eigenvalues of the characteristic equation and are given by:

$$f_n = n\frac{c_0}{2L} \quad n = 1, 2, 3, \ldots. \tag{5.11}$$

From the above result, it seems that the resonant frequencies of the longitudinal modes of a beam do not depend on its cross section. A more rigorous analysis of this structure should account for the cross-sectional deformations due to the tension/compression in the beam through incorporating the Poisson's ratio in calculations [7].

5.3 Flexural Waves in Beams

In the absence of axial loads and damping, the dynamic flexural response of a thin beam with constant cross section can be modelled using the well known Euler–Bernoulli beam equation [5,6,8]:

$$\frac{\partial^2}{\partial x^2}\left(E\mathcal{I}\frac{\partial^2 \psi}{\partial x^2}\right) + \rho A_b \frac{\partial^2 \psi}{\partial t^2} = \mathcal{F}(x,t) \tag{5.12}$$

where ρ is the material mass density, A_b is the cross sectional area of the beam (assumed constant along its length), and $\mathcal{F}(x,t)$ is the distributed input force.

Propagation of harmonic waves along infinitely long beams is governed by Eq. (5.12). It can be shown that the wavelength and phase velocity of of the wave are given by:

$$\lambda_f = \sqrt[4]{\frac{\rho A_b}{E\mathcal{I}}}\sqrt{\frac{2\pi}{f}} \tag{5.13}$$

$$c_f = f \cdot \lambda_f = \sqrt[4]{\frac{\rho A_b}{E\mathcal{I}}}\sqrt{2\pi f}. \tag{5.14}$$

Interestingly, the phase velocity of the wave depends on the frequency.

The effects of damping and axial forces on the dynamics of the beam can be accounted for by adding two additional terms to the Euler–Bernoulli beam equation:

$$E\mathcal{I}\frac{\partial^4 \psi}{\partial x^4} - \mathcal{P}\frac{\partial^2 \psi}{\partial x^2} + \rho A_b \frac{\partial^2 \psi}{\partial t^2} + \zeta\frac{\partial \psi}{\partial t} = \mathcal{F}(x,t) \tag{5.15}$$

where the beam is assumed to have a constant cross section and be homogeneous (i.e., uniform mass distribution inside the beam), $\mathcal{P}$ is the applied axial force and ζ is the damping coefficient.

5.3.1 Flexural Beam Resonators

The problem is solved for a clamped–clamped beam (i.e., a bridge) under assumptions that the vibrations are undamped and there is no axial force. The boundary conditions can be looked up from Table 4.2. Method of separation of variables can be employed to solve Eq. (5.12) for free vibrations of the beam:

$$\begin{aligned} &\psi(x,t) = \psi(x) \cdot e^{j\omega t} \\ &\rightarrow \left(E\mathcal{I} \overset{\cdots\cdot}{\psi}(x) - \rho A_b \omega^2 \psi(x) \right) \cdot e^{j\omega t} = 0. \end{aligned} \tag{5.16}$$

Taking the Laplace transform of the time-independent part and applying boundary conditions $\psi(0) = 0$ and $\dot{\psi}(0) = 0$, the homogeneous equation is given by [2,9,10]:

$$\left(E\mathcal{I}s^4 - \rho A_b \omega^2 \right) \Psi(s) - sE\mathcal{I}\ddot{\psi}(0) - E\mathcal{I}\dddot{\psi}(0) = 0 \tag{5.17}$$

where $\Psi(s)$ is the Laplace transform of $\psi(x)$. Defining $\xi^4 = \rho A_b \omega^2 / E\mathcal{I}$ and taking the inverse Laplace transform of the above equation results in:

$$\psi(x) = \mathcal{A}\frac{\cosh(\xi x) - \cos(\xi x)}{\xi^2} + \mathcal{B}\frac{\sinh(\xi x) - \sin(\xi x)}{\xi^3}. \tag{5.18}$$

Constants $\mathcal{A}$ and $\mathcal{B}$ are found by applying the remaining boundary conditions (i.e., $\psi(L) = 0$ and $\dot{\psi}(L) = 0$):

$$\mathcal{A}\xi \left(\cosh(\xi L) - \cos(\xi L)\right) + \mathcal{B}\left(\sinh(\xi L) - \sin(\xi L)\right) = 0 \tag{5.19}$$

$$\mathcal{A}\xi \left(\sinh(\xi L) + \sin(\xi L)\right) + \mathcal{B}\left(\cosh(\xi L) - \cos(\xi L)\right) = 0. \tag{5.20}$$

To find out the non-trivial solution (i.e., $\mathcal{A} = \mathcal{B} = 0$), the determinant of the above system of equation has to be zero, and therefore, the following criterion has to be satisfied:

$$\begin{aligned} &\left(\cosh(\xi L) - \cos(\xi L)\right) \cdot \left(\cosh(\xi L) - \cos(\xi L)\right) \\ &\quad - \left(\sinh(\xi L) - \sin(\xi L)\right) \cdot \left(\sinh(\xi L) + \sin(\xi L)\right) = 0 \end{aligned} \tag{5.21}$$

which reduces to:

$$\cos(\xi L) \cdot \cosh(\xi L) = 1. \tag{5.22}$$

The roots of the above equation can be found numerically or graphically. Each of these roots corresponds to a mode shape (eigenvector) for the beam which has its own resonant frequency:

Table 5.2 List of the Eigenvalues for the First Five Modes of Clamped–Clamped, Clamped–Free, and Pinned–Pinned Beams. The value of $\mathcal{K}_n$ is given for a beam with a rectangular cross section of $A_b = hW$.

	Bridge		Cantilever		Pinned–pinned	
n	ξL	$\mathcal{K}_n$	ξL	$\mathcal{K}_n$	ξL	$\mathcal{K}_n$
1	4.730 04	1.027 92	1.875 10	0.161 54	π	0.453 45
2	7.853 20	2.833 50	4.694 09	1.012 35	2π	1.813 80
3	10.995 61	5.554 79	7.854 76	2.834 62	3π	4.081 04
4	14.137 17	9.182 36	10.995 54	5.554 73	4π	7.255 20
5	17.278 76	13.716 86	14.137 17	9.182 36	5π	11.336 24

$$f_n = \mathcal{K}_n \frac{W}{L^2}\sqrt{\frac{E}{\rho}}. \tag{5.23}$$

Table 5.2 summarises the roots of Eq. (5.22) and the corresponding constant $\mathcal{K}_n$ for each eigenvalue. It is noteworthy that even in this simple one dimensional case the beam has an unlimited number of modes.

The mode shapes (i.e., eigenvectors) are found by inserting the results from Eq. (5.20) into Eq. (5.18):

$$\psi(x) = \mathcal{C}_1 \left(\cosh(\xi x) - \cos(\xi x) - \frac{\sinh(\xi L) + \sin(\xi L)}{\cosh(\xi L) - \cos(\xi L)} \left(\sinh(\xi x) - \sin(\xi x)\right) \right). \tag{5.24}$$

The coefficient $\mathcal{C}_1$ can be found by equating the kinetic and potential energies of the beam under resonance conditions. The first four modes corresponding to the eigenvalues from Eq. (5.22) are illustrated in Fig. 5.4.

Had we solved the beam equation with boundary conditions for a cantilever (i.e., clamped-free), the characteristic equation would be:

$$\cos(\xi L) \cdot \cosh(\xi L) + 1 = 0. \tag{5.25}$$

The characteristic equation for a beam pinned at both ends would be:

$$\sin(\xi L) = 0 \tag{5.26}$$

while a free-free beam would have the same characteristic equation as a clamped–clamped beam although with different mode shapes.

The resonant frequencies of a cantilever and a pinned–pinned beam can be calculated from Eq. (5.23) using the eigenvalues of the Eqs. (5.25) and

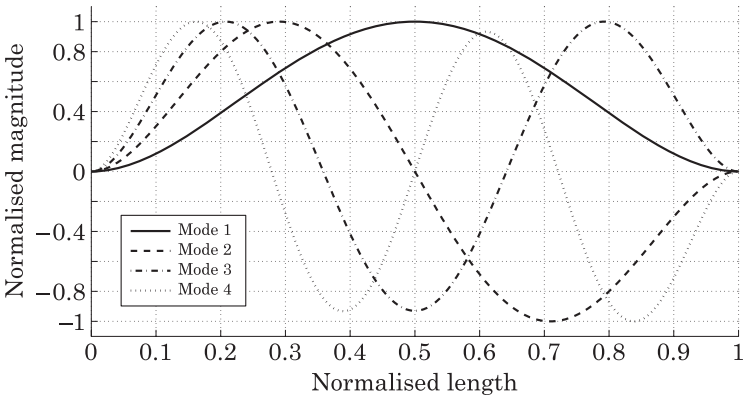

Figure 5.4 The first (normalised) four modes of a bridge (clamped–clamped beam) structure.

(5.26), respectively. Eigenvalues and the required coefficients for calculating the resonant frequencies for these cases are also listed in Table 5.2.

5.4 Dynamics of Plates and Membranes

One can investigate the three dimensional behaviour of a relatively wide beam using plate dynamics and more accurately predict modes and even study those which cannot be resolved using the two dimensional analysis. Furthermore, the dynamic analysis of plates and membranes and estimation of their resonant frequencies is important to prevent unwanted resonance in applications such as micromachined microphones.

Dynamic deflections of a membrane under internal force $\mathcal{F}$ is given by [6,11]:

$$\mathcal{F}\nabla^2\psi + p(x,y,t) = \rho_a \frac{\partial^2\psi}{\partial t^2} \tag{5.27}$$

where $p(x,y,t)$ is the applied pressure on the membrane, ρ_a is the mass per unit area of the membrane, ∇^2 is the Laplace operator defined as:

$$\nabla^2 = \left(\frac{\partial^2}{\partial x^2} + \frac{\partial^2}{\partial y^2}\right).$$

Dynamic deflections of a plate of thickness h are given by [5,6,11–13]:

$$-\mathcal{D}\nabla^4\psi + p(x,y,t) = \rho \frac{\partial^2\psi}{\partial t^2} \tag{5.28}$$

where $p(x, y, t)$ is the pressure on the surface of the plate, $\mathcal{D}$ is the plate flexural rigidity, and ∇^4 is the biharmonic operator.

5.5 Estimation of Resonant Frequency

In this section, two methods for calculation of the resonant frequency of a continuous structure are described. Rayleigh's method is an energy-based method and is well known among the micromachining researchers [1,14]. Rayleigh's method produces accurate results if the mode shapes of the structure are known. However, even relatively poor approximations to mode shapes generally yield results with acceptable accuracies [1,15].

Dunkerley's method was originally developed for estimating the shift in the resonant frequency of rotating shafts under different loads. This method provides a lower bound to the resonant frequency of a structure [15,16]. Depending on the problem, using Dunkerley's method can be simpler than Rayleigh's method for a similar level of accuracy.

5.5.1 Rayleigh's Method

Rayleigh's method is based on the fact that, at resonance, the maximum kinetic energy and the maximum potential energy are equal for linear lossless systems. If $[M]$ and $[K]$ are the mass and stiffness matrices for a system, respectively, and $[\vec{x}]$ is the corresponding displacement vector for the amplitude of vibration, the maximum potential energy, $\mathcal{U}_{\max}$, and the maximum kinetic energy, $\mathcal{K}_{\max}$, are found from:

$$\mathcal{U}_{\max} = \frac{1}{2}[\vec{x}]'[K][\vec{x}] \tag{5.29}$$

$$\mathcal{K}_{\max} = \frac{1}{2}[\dot{\vec{x}}]'[M][\dot{\vec{x}}] = -\frac{1}{2}\omega^2[\vec{x}]'[M][\vec{x}] \tag{5.30}$$

where $[\vec{x}]'$ is the transpose of $[\vec{x}]$. Equating maximum potential and kinetic energies, it can be seen:

$$\omega^2 = -\frac{[\vec{x}]'[K][\vec{x}]}{[\vec{x}]'[M][\vec{x}]}. \tag{5.31}$$

Calculating the kinetic energy of a vibrating structure requires knowledge of the mode shapes. However, since usually a finite number of the mechanical modes are accounted for when computing the kinetic energy of the system [15]. Consequently, the calculated kinetic energy is less than the actual value and the estimated resonant frequency is larger than the actual value.

Vector $[\vec{x}]$ is obtained from superposition of different mechanical modes of the structure, which may not be easy to calculate. A good way of estimating the kinetic energy is to assume that under sinusoidal excitation, the system motion is equal to a static trial function multiplied by sinusoidal time dependence [1]. If the static deflection of a structure is given by the function $\psi(x)$, the trial function under sinusoidal excitation will be $\psi(x,t) = \psi(x)e^{j\omega t}$. The maximum velocity of the points on the beam is then given by:

$$\left.\frac{\partial \psi(x,t)}{\partial t}\right|_{t=\frac{\pi}{2\omega}} = -\omega\psi(x) \tag{5.32}$$

which can now be inserted in Eqs. (5.31) and (5.32) to calculate the resonant frequency of the structure.

The resonant frequency of a clamped–clamped beam using Rayleigh's method is found from:

$$\omega_0^2 = \frac{\int_0^L E\mathcal{I}\left(\frac{d^2\psi}{dx^2}\right)^2 dx}{\int_0^L \psi^2\, dm} \tag{5.33}$$

where the numerator in the above equation is the bending energy of the beam [2,15]. The symmetric structure of the beam allows us to simplify the problem. We choose a trial function of the form $\psi_1(x) = \mathcal{F}x^2(4x - 3L)/48E\mathcal{I}L^3$ for $x < L/2$, where L is the length of the bridge and $\mathcal{F}$ is the force applied to the centre of the bridge. This trial function is in fact for the static deflections of a bridge under a point load, and therefore, satisfies the boundary conditions.

$$\begin{aligned} f_{bR} &= \frac{1}{2\pi}\sqrt{\frac{2\int_0^{\frac{L}{2}} E\mathcal{I}\left(\frac{\mathcal{F}(4x-L)}{8E\mathcal{I}}\right)^2}{2\int_0^{\frac{L}{2}}\left(\frac{\mathcal{F}x^2(4x-3L)}{48E\mathcal{I}L^3}\right)^2 dm}} \\ &= \frac{1}{2\pi}\sqrt{\frac{k_b}{0.37143M_b}} = 1.04458\frac{W}{L^2}\sqrt{\frac{E}{\rho}}. \end{aligned} \tag{5.34}$$

Comparing the results from the Rayleigh's method and the exact solution from Table 5.2, it can be seen that there is a 1.6% of error in the calculated value for the resonant frequency. As expected, the estimated resonant frequency from Rayleigh's method is higher than the actual resonant frequency of the structure. If the resonant frequencies of higher modes are required, trial functions for each of those mode shapes should be found and a procedure similar to the above should be followed [15].

5.5.1.1 Analysis of the mass sensor using Rayleigh's method

Rayleigh's method allows us to take into account the kinetic energy of the springs, which was ignored in our lumped system analysis. The total kinetic and potential energies of the system for a vibration amplitude of $\mathcal{Y}$ are:

$$\mathcal{U}_{\max} = \frac{1}{2} k_b \mathcal{Y}^2 \tag{5.35}$$

$$\mathcal{K}_{\max} = -\omega_{0R}^2 \left(\frac{1}{2} M_{\text{sh}} \mathcal{Y}^2 + \frac{1}{2} 0.37143 M_b \mathcal{Y}^2 \right). \tag{5.36}$$

Therefore,

$$f_{0R} = \frac{1}{2\pi} \sqrt{\frac{k_b}{M_{\text{sh}} + 0.37143 M_b}} \tag{5.37}$$

where k_b is the spring constant of the bridge[1]. The term $M_{\text{sh}} + 0.37143 M_b$ is called the *effective mass* of the sensor, M_{eff}, which accounts for the contributions from all parts of a system to its kinetic energy. The resonant frequency and sensitivity of the sensor are then given by:

$$f_{0R} = 87944.64 \text{ Hz} \tag{5.38}$$

$$S_m^{f_{0R}} = -599.39 \text{ Hz/ng}. \tag{5.39}$$

5.5.2 Dunkerley's Method

The equation of motion for free vibrations of a lossless mass–spring system with r masses and s springs ($s \geq r$) can be written as:

$$[M][\ddot{\vec{x}}] + [A]^{-1}[\vec{x}] = 0 \tag{5.40}$$

where $[M]_{r\times r}$ and $[A]_{r\times r}$ are the mass and flexibility matrices, respectively[2]. Vector $[\vec{x}]_{r\times 1}$ is the displacement vector; i.e., x_i is the displacement of mass m_i. Vector $[\ddot{\vec{x}}]_{r\times 1}$ is the second derivative of the displacement vector with respect to time and represents the acceleration of the masses. To calculate element a_{ij} of the flexibility matrix, the amount of displacement of mass i is calculated when a unit force is applied to mass j when all other force components are zero [15]. If $[A]$ and $[\vec{x}]$ are constructed this way, matrix $[M]$ will be diagonal and $m_{ii} = m_i$.

[1] Notice that we treat the combined effect of the two guided beams on either side of the shuttle as that of a clamped–clamped beam of twice the length of each beam. This is a valid assumption as long as the shuttle can be assumed rigid.

[2] The flexibility matrix is the inverse of the more familiar stiffness matrix; i.e., $[A] = [K]^{-1}$.

For harmonic oscillations at frequency ω we have $[\ddot{\vec{x}}] = -\omega^2[\vec{x}]$. From Eq. (5.40), it follows that:

$$-\omega^2[M][\vec{x}] + [A]^{-1}[\vec{x}] = 0 \tag{5.41}$$

$$([A][M] - \lambda[I])\,[\vec{x}] = 0 \tag{5.42}$$

where $[I]$ is the unity matrix and $\lambda = \omega^{-2}$. The resonant frequencies of the system can be found by finding the roots, λ_i, of the characteristic equation:

$$|[A]\,[M] - \lambda[I]| = 0 \tag{5.43}$$

$$\begin{vmatrix} a_{11}m_1 - \lambda & a_{12}m_1 & \cdots & a_{1r}m_1 \\ a_{21}m_2 & a_{22}m_2 - \lambda & \cdots & a_{2r}m_2 \\ \vdots & \vdots & \vdots & \vdots \\ a_{r1}m_r & a_{r2}m_r & \cdots & a_{rr}m_r - \lambda \end{vmatrix} = 0. \tag{5.44}$$

The left side of the Eq. (5.44) is a polynomial of degree r, and therefore, has r roots. This equation can be rewritten as:

$$\lambda^r - (a_{11}m_1 + a_{22}m_2 + \cdots + a_{rr}m_r)\lambda^{r-1} + \cdots = 0. \tag{5.45}$$

It is well known from algebra that the sum of the roots of an equation is equal to the negative of the coefficient of the second highest power in that equation [15]. For Eq. (5.45), we will have:

$$\sum_{i=1}^{r} \lambda_i = \sum_{i=1}^{r} a_{ii}m_i. \tag{5.46}$$

From Eq. (5.46) and knowing that $\lambda_i = \omega_i^{-2}$ we can write:

$$\frac{1}{\omega_0^2} < \sum_{i=1}^{r} a_{ii}m_i. \tag{5.47}$$

The value of a_{ii} is found by applying a unit force to mass i while keeping all other forces equal to zero, which effectively translates into removing all other masses from the system. If the resonant frequencies of higher modes of the system are much larger than that of the first mode, we will have:

$$\frac{1}{\omega_0^2} \approx \sum_{i=1}^{r} a_{ii}m_i. \tag{5.48}$$

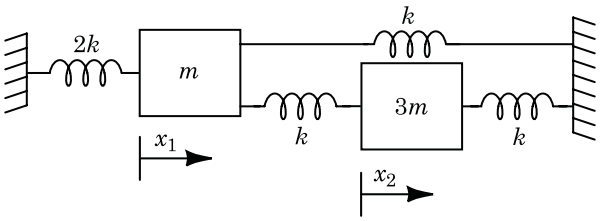

Figure 5.5 A discrete mass–spring system.

Eq. (5.48) is known as *Dunkerley's equation*. As it is obvious from Eq. (5.47), Dunkerley's equation will give a lower bound for the resonant frequency of the first mode of the system.

5.5.2.1 Discrete mass–spring systems

Let us examine the mass–spring system illustrated in Fig. 5.5. In this case, it is easier to calculate the stiffness matrix and then inverse it to find the flexibility matrix. Element k_{ij} of matrix $[K]$ is found by assuming a unit displacement for mass i and calculating the required force to keep mass j in its location. For the system in Fig. 5.5, it can be shown that:

$$[K] = \begin{bmatrix} 4k & -k \\ -k & 2k \end{bmatrix}$$
$$[A] = [K]^{-1} = \frac{1}{7k} \cdot \begin{bmatrix} 2 & 1 \\ 1 & 4 \end{bmatrix}. \tag{5.49}$$

The characteristic equation is:

$$\begin{vmatrix} \frac{2m}{7k} - \lambda & \frac{m}{7k} \\ \frac{3m}{7k} & \frac{12m}{7k} - \lambda \end{vmatrix} = 0. \tag{5.50}$$

Solving Eq. (5.50), we have: $\lambda = \omega^{-2} = mk^{-1}(1 \pm \sqrt{4/7})$. Therefore, the exact resonant frequency of the first mode is:

$$\omega_0 = \frac{1}{1 + \sqrt{\frac{4}{7}}} \sqrt{\frac{k}{m}} \approx 0.755 \sqrt{\frac{k}{m}}. \tag{5.51}$$

Using Dunkerley's method, from Eq. (5.48) the resonant frequency of the first mode is estimated to be:

$$\frac{1}{\omega_0^2} = \frac{2m}{7k} + \frac{12m}{7k} = 2\frac{m}{k}$$
$$\omega_0 \approx 0.707\sqrt{\frac{k}{m}}. \tag{5.52}$$

The estimated resonant frequency has an error of only 6% compared to the exact value.

5.5.2.2 Continuous systems

We analyse a bridge structure as an example of using Dunkerley's method for a continuous system. Referring to Eq. (4.19), the spring constant of the bridge at the point of applying the force is:

$$k_b(x) = \frac{\mathcal{F}}{\psi(x)} = \frac{3E\mathcal{I}L^3}{x^3(L-x)^3}. \tag{5.53}$$

The resonant frequency of the bridge is then given by:

$$\frac{1}{\omega_{bD}^2} = \int_0^{\frac{L}{2}} 2 \times \frac{\rho A_b\, dx}{k_b(x)} =$$
$$\Rightarrow f_{bD} = 0.94157\frac{W}{L^2}\sqrt{\frac{E}{\rho}} = \frac{1}{2\pi}\sqrt{\frac{k_b}{0.45715M_b}} \tag{5.54}$$

where M_b and k_b are the mass and the spring constant for each of the beams, respectively and the summation has been replaced with an integral for this continuous system. It can be seen that the estimated resonant frequency is about 8% lower than the exact value.

5.5.2.3 Analysis of the mass sensor using Dunkerley's method

The shuttle will see an effective spring constant of k_b, where k_b is found from Eq. (4.20). Using the results of (5.54), Dunkerley's method yields:

$$\frac{1}{\omega_{0D}^2} = \frac{M_{\text{sh}}}{k_b} + \frac{1}{\omega_{bD}^2}$$
$$f_{0D} = \frac{1}{2\pi}\sqrt{\frac{k_b}{M_{\text{sh}} + 0.45715M_b}} \tag{5.55}$$

where ω_{0D} is the resonant frequency of the first mechanical mode of the structure and ω_{bD} is the resonant frequency of each of the beam springs.

The analysis results are:

$$f_{0D} = 88753.70 \text{ Hz} \tag{5.56}$$

$$S_m^{f_{0D}} = -616.09 \text{ Hz/ng}. \tag{5.57}$$

5.6 Bulk Resonators

Bulk resonators can be viewed as multi-dimensional expansions of extensional 1-D beam resonators. In these resonators, the bulk of the material fulfils the roles of both the mass and the spring [17,18]. A common example is a quartz crystal where an acoustic wave is initiated and sustained within the crystal through one set of electrodes and the vibrations are picked up by a second set of electrodes. The effective spring constant of bulk resonators is quite large compared to flexural resonators due to the fact that the whole resonator body, which is usually made from a solid slab of a material, has to deform in response to the actuation signals. As a result of the large spring constant to mass ratio for bulk resonators, these devices are frequently used to realise resonators with high resonant frequencies. In general, a bulk resonator has infinite number of vibration modes due to its continuous built. Consequently, excitation of a desired mode requires proper application of the drive signal as the mode frequencies can be close to each other. It is also possible to employ the higher order modes of a bulk resonator. For example, it is common practice to build high frequency oscillators using the higher modes, referred to as *overtone resonance modes*, of quartz crystals [19–22]. A few of the vibration modes of a disk resonator that is anchored at its centre are illustrated in Fig. 5.6.

The mode shapes of bulk resonators can be quite complicated (see Fig. 5.6). To simplify the design process it is important to keep the asymmetries in the device design at a minimum and avoid any fabrication steps which may lead to such phenomena (e.g., fabrication of the resonator body and its anchors in separate lithography steps). To minimise the loss of vibration energy through the supports, and consequently degradation of the resonance quality factor, the anchors to the substrate should be positioned at the resonant nodes [23–26].

Bulk resonators can be analytically modelled with aid of the theory of vibrations of plates [11,27]. Using the method of separation of variables and isolating the time and location dependant functions, the free transverse vibrations of a plate are governed by:

$$\nabla^4 \psi(x, y) - \xi^4 \psi(x, y) = 0 \tag{5.58}$$

where $\xi^4 = \rho\omega^2/\mathcal{D}$. For a rectangular plate, the general solution is:

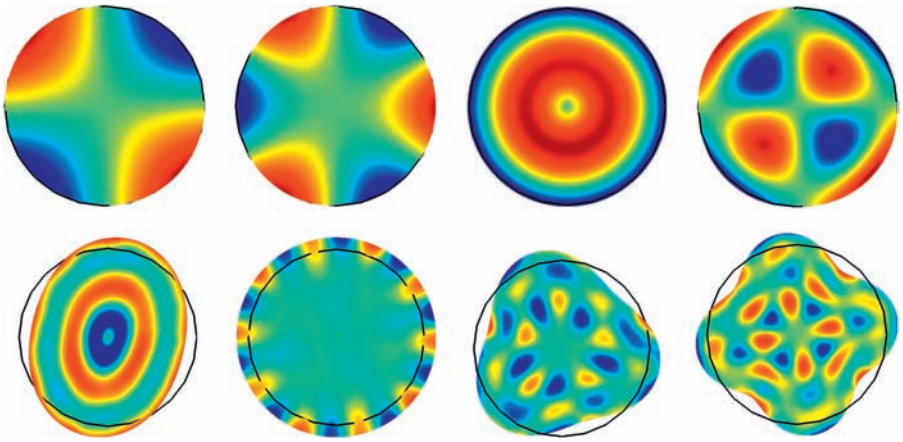

Figure 5.6 Out of plane displacement (from blue for large negative displacement to red for positive displacement) for a few of the vibration modes of a disk resonator anchored at its centre. The mode shapes on top are for transverse oscillations and the ones at the bottom correspond to in-plane (bulk) modes.

$$\begin{aligned}\psi(x,y) = {} & A_1 \sin\alpha x \sin\beta y + A_2 \sin\alpha x \cos\beta y + A_3 \cos\alpha x \sin\beta y \\ & + A_4 \cos\alpha x \cos\beta y + A_5 \sinh\gamma x \sinh\varphi y + A_6 \sinh\gamma x \cosh\varphi y \\ & + A_7 \cosh\gamma x \sinh\varphi y + A_8 \cosh\gamma x \cosh\varphi y \end{aligned} \tag{5.59}$$

where $\xi^2 = \alpha^2 + \beta^2 = \gamma^2 + \varphi^2$. The characteristic equation for the resonator is found from applying the boundary conditions and yields the ratios of A_1 to A_8 as well as relationships between (α, β) and (γ, φ) which can then be used to calculate the resonant frequencies. Solving the plate vibrations equation for a circular plate in polar coordinates leads to the general solution with Bessel functions [11].

The differential equations for calculation of in-plane (i.e., extensional and contour modes) are more complicated compared to the 1D beam extensional resonator and quite often, numerical or approximate techniques are needed to analyse these modes. Nevertheless, analytic solutions have been developed for simple cases such as rectangular or circular plates [50,51].

5.7 Simulation of Resonance

From our discussions so far, it should be clear that the exact modelling of the microsystems can be quite complicated. Even for a structure as simple as our mass sensor, we have had to make several assumptions just to be able to

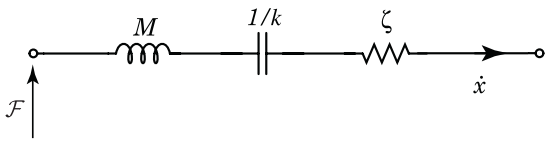

Figure 5.7 Equivalent circuit model of a the mass–spring system in Fig. 5.2.

model the dynamics of the sensor[3]. For these reasons, it is often required to use numerical simulations during the design and testing phase.

We will briefly discuss two of the common methods for simulation of resonant devices. One is to build an equivalent electrical circuit for the resonator which can then be analysed in circuit simulators. This is not a physical model of the device, and quite often, the circuit parameters are derived from measurements on fabricated devices. The other technique which actually allows to predict the device behaviour is the finite element method. Finite element analysis is a very flexible and powerful simulation technique which allows for simulation of any aspect of the device operation that can be described through ordinary or partial differential equations. Finite element simulations can also be employed to investigate critical performance issues which are not easy to measure (e.g., the fringing fields in electrostatic devices).

5.7.1 Electric Circuit Representation

It is common to use the analogy between electrical and mechanical resonators to build an equivalent electrical circuit for a micromachined resonator[1,28,29]. Such a model is often built from a set of experimental measurements and then is used in electric circuit simulators. This approach is particularly useful if the resonator needs to be modelled with the drive or sense electronics. Modelling of a resonator with an electrical circuit requires several steps if the model is based on device design data and not measurements. These modelling steps rely on a number of assumptions which may affect the accuracy of the modelling results. Consequently, finite element simulations are usually performed on the device structure if accurate simulations are needed.

To represent a mechanical device with electrical elements, proper mapping of mechanical to electrical quantities must be carried out. A common set of mapping rules is summarised in Table 5.3. The electrical equivalent model of the mass–spring system in Fig. 5.2 is illustrated in Fig. 5.7.

Mechanical impedance is a useful concept which, much like the electrical impedance, allows simple analysis of vibrating structures under harmonic

[3]Some of our assumptions have been ignoring the damping mechanisms, elasticity of the foundations, and cross-sectional deformations.

Table 5.3 Correspondence between the Mechanical and Electrical Systems

Mechanical parameter	Electrical equivalent
Force, $\mathcal{F}$	Voltage, v
Velocity, $\dot{x}$	Current, i
Displacement, x	Charge, q
Momentum, p	Magnetic flux linkage, λ
Mass, M	Inductance, L
Compliance, $\frac{1}{k}$	Capacitance, C
Viscous resistance, ζ	Resistance, R

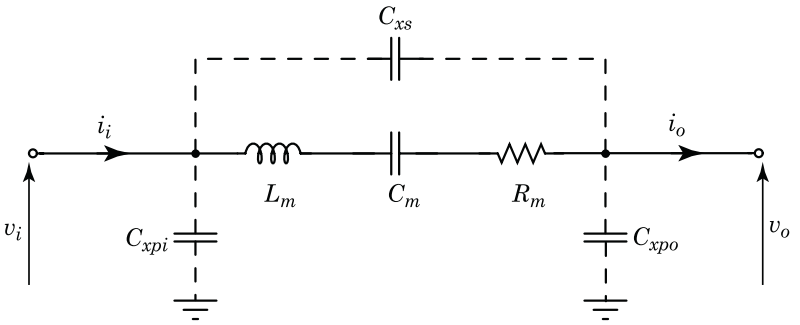

Figure 5.8 Equivalent circuit model of a resonator.

excitations. The value of mechanical impedance of a structure can be derived using the mechanical-to-electrical conversion of quantities as given in Table 5.3:

$$Z_m = \frac{\mathcal{F}}{\dot{x}} \tag{5.60}$$

where $\dot{x}$ is the velocity. As an example, the impedance of a semi-infinite thin beam with cross sectional area of A can be shown to be $Z_m = A\sqrt{\rho E}$ [5]. Using mechanical impedances can especially be useful when studying the wave transmission and reflection at connecting points between mechanical elements.

In most cases, a resonant device is modelled as a series RLC circuit as shown in Fig. 5.8, but in some situations a parallel RLC circuit should be used. Other elements, especially parasitic capacitors, may be added to the circuit to produce more realistic modelling results.

5.7.1.1 Equivalent circuit model of the mass sensor

In this section, we derive the model parameters for the mass sensor. Let us assume that the shuttle is biased with a DC voltage V_{sh}, the input port is driven with an AC voltage $v_a \sin \omega_a t$, and the output port is grounded (or connected to a virtual ground). We assume that lumped modelling produces

accurate enough results. However, we use the effective mass (from Rayleigh's or Dunkerley's methods) for the shuttle of the sensor to improve the accuracy of the model. The equation of motion for the mass spring system is:

$$M_{\text{eff}}\ddot{x} + \frac{M_{\text{eff}}\omega_0}{Q}\dot{x} + Kx = \mathcal{F}_{\text{in}} \tag{5.61}$$

where M_{eff} is the effective mass of the shuttle, Q is the quality factor of the resonator, K is the effective total spring constant, and F_{in} is the force applied to the structure, while $\ddot{x}$, $\dot{x}$, and x are the acceleration, velocity, and displacement of the shuttle, respectively. We use parameter Q instead of damping factor ζ as it can be more easily extracted from measurements.

The force on the shuttle of the sensor, $\mathcal{F}_{\text{in}}$, is given by:

$$\mathcal{F}_{\text{in}} = \frac{1}{2}\left(\frac{\partial C_i}{\partial x}\right)\left(\frac{v_a^2}{2} - 2v_a V_{\text{sh}} \sin\omega_a t - \frac{v_a^2}{2}\cos 2\omega_a t\right) \tag{5.62}$$

where $\partial C_i/\partial x$ is the rate of change in the capacitance of the output port.

If the resonator behaves linearly during its operation, superposition theorem can be employed to solve Eq. (5.61) using the the results of Eq. (5.62) . The current at the output port of the resonator, i_{out}, is given by:

$$\begin{aligned} i_{\text{out}} &= \frac{\partial\left(-C_o V_{\text{sh}}\right)}{\partial t} = -V_{\text{sh}}\frac{\partial C_o}{\partial x}\frac{\partial x}{\partial t} \\ &= \frac{V_{\text{sh}}}{2}\left(\frac{\partial C_i}{\partial x}\right)\left(\frac{\partial C_o}{\partial x}\right)\left(\frac{2v_a V_{\text{sh}}\omega_a \cos(\omega_a t - \phi_a)}{\sqrt{(K - M_{\text{eff}}\omega_a^2)^2 + (\frac{M_{\text{eff}}\omega_0}{Q}\omega_a)^2}}\right. \\ &\quad \left. - \frac{v_a^2\omega_a \sin(2\omega_a t - \phi_{2a})}{\sqrt{(K - 4M_{\text{eff}}\omega_a^2)^2 + (2\frac{M_{\text{eff}}\omega_0}{Q}\omega_a)^2}}\right) \end{aligned} \tag{5.63}$$

where

$$\phi_a = \arctan\left(\frac{\zeta\omega_a}{K - M_{\text{eff}}\omega_a^2}\right), \quad \phi_{2a} = \arctan\left(\frac{2\zeta\omega_a}{K - 4M_{\text{eff}}\omega_a^2}\right).$$

Parameter $\partial C_o/\partial x$ is the rate of change in the capacitance of the output port. Due to the symmetric structure of the mass sensor, we can see that:

$$\frac{\partial C_i}{\partial x} = -\frac{\partial C_o}{\partial x} = -\varepsilon_0\frac{hW_{\text{sh}}}{g^2}. \tag{5.64}$$

Either of the frequency components in Eq. (5.63) can be used to extract information about the behaviour of the resonator. Assuming the DC bias

voltage is much larger than the AC drive voltage (i.e., $V_{\text{sh}} \gg v_a$), the output signal at $2\omega_a$ can be ignored and the output current is written as:

$$i_{\text{out}} \approx V_{\text{sh}}^2 \left(\frac{\partial C}{\partial x}\right)^2 \frac{v_a \omega_a \cos(\omega_a t - \phi_a)}{\sqrt{(K - M_{\text{eff}}\omega_a^2)^2 + (\frac{M_{\text{eff}}\omega_0}{Q}\omega_a)^2}}. \tag{5.65}$$

The parameters of the resonator have to be scaled properly to make the transfer function similar to that of a mass–spring system. Defining $\eta = V_{\text{sh}}\,(\partial C/\partial x)$, we have:

$$i_{\text{out}} = \frac{v_a \omega_a \cos(\omega_a t - \phi_a)}{\sqrt{(k_s - m_s\omega_a^2)^2 + (\frac{m_s\omega_0}{Q}\omega_a)^2}} \tag{5.66}$$

where $m_s = M_{\text{eff}}/\eta^2$ and $k_s = K/\eta^2$.

Parasitic capacitors C_{xpi} and C_{xpo} can be calculated knowing the total area of the electrical connections and the thickness of the buried oxide layer (see Table 5.1):

$$C_{xp} = \varepsilon_0 \varepsilon_{ox} \frac{A_p}{t_{ox}} \tag{5.67}$$

where $\varepsilon_{ox} = 3.9$ is the relative permittivity of the oxide layer [1].

For this simple model, C_{xs} is assumed to stem from direct signal feedthrough from the input port to the output port through capacitive coupling. Its value can be found from:

$$C_{xs} = \frac{1}{2}\varepsilon_0 \frac{hW_{\text{sh}}}{g} \tag{5.68}$$

where the factor 1/2 is included to account for the two equal capacitors in series[4]. It must be noted, however, that signal feedthrough through the substrate and also cables and bond wires can cause the actual value of this capacitor to be significantly larger than the value estimated in here.

The model parameters are summarised in Table 5.4 assuming $V_{\text{sh}} = 20$ V and $v_a = 1$ V.

5.7.2 Numerical Methods

Complexity of micromachined devices and their multi-physics domain operation make their analytic modelling quite challenging. In most cases,

[4]This calculation assumes that the resonator shuttle is not connected to an AC ground.

Table 5.4 Mass Sensor Model Parameters Assuming $V_{sh} = 20$ V and $v_a = 1$ V

Parameter	Value	Units
$\frac{\partial C}{\partial x}$	−26.562	fF/μm
η	−531.240	fF · V/μm
M_{eff}	71.794	ng
K	22.4	N/m
C_m	12.599	fF
L_m	254.392	H
R_m	9.473	kΩ
C_{xp}	517.959	fF
C_{xs}	4.427	fF

the derived analytic model represents the device behaviour under certain circumstances and simplifying assumptions, which may jeopardise the model accuracy. Consequently, one usually needs to resort to numerical simulations to investigate the device behaviour or even to verify the analytic modelling results. This is especially the case when an analytic model cannot be obtained or is too complicated to provide designing insight.

The most commonly used technique for numerical simulation of microsystems is the finite element analysis (FEA) [30,31]. Finite element method is a variational technique which is used to find the solution to the forces, deformations, etc., by minimising the potential energy of the system under the applied loads. In this technique, the structure is divided (*meshed*) into several small segments (*elements*) and a trial function is used to estimate the quantity of interest between the corners of the elements (*nodes*). This trial function is often a first or second order polynomial but higher order polynomials may also be used. The coefficients for the polynomial are found by minimising the potential energy of the system as described above. At the end of the simulations, these polynomials provide a piecewise approximation to the actual function that would satisfy the requirements of the problem. It can be readily seen that the accuracy of the FE simulations should improve if a finer mesh, or in some cases, higher order polynomials are used.

Different analyses can be performed to investigate the static, modal, harmonic, or transient responses of the system. In many cases, it is possible to include nonlinearities in simulations such as those from the material properties. Almost any phenomena that can be described with ordinary or partial differential equations can be programmed and simulated with FE method including statics, electrostatics, magnetostatics, electromagnetics, fluidics, thermal, piezoelectric, ferroelectric, and optics.

A technique, which is particularly useful for microsystem design, is the simultaneous simulation of multiple physical domains such as electrostatics and statics or thermal and fluidics. This allows for a more inclusive analysis of the structure but usually adds substantially to the simulation time and the

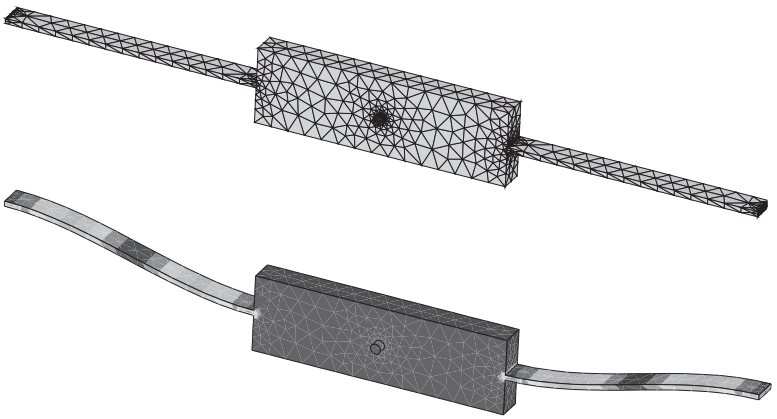

Figure 5.9 The meshed (top) and deflected (bottom) structures of the mass sensor with a 0.1ng mass at the centre of the shuttle. Note that the mesh is considerably denser around sharp corners.

memory requirements for the simulations. There are two main techniques for multiphysics simulations. One is to set up the simulations based on the coupled equations which relate the involving physical domains and then solving the whole system of equations simultaneously. The other technique is to perform the simulations in one physical domain and then pass the results to the other domains. For instance, simulation of an electrostatic device (e.g., the mass sensor) can be broken into two parts: (1) calculation of the electrostatic fields and forces; and (2) calculation of the structural deflections and deformations. However, after transferring the calculated forces to the statical simulator, the structures may move from the positions which were assumed for electrostatic simulations. Therefore, several cycles of electrostatic and static simulations may be required before the simulation error is reduced to acceptable values. Based on the structure and the involved physical domains, each of the two simulations strategies may be adopted. While the simulating the structure in one domain and passing the results to the subsequent physical domains is a more flexible technique, it can, and usually does, take longer for the results to converge.

Meshing is probably the most critical step in FEA. The shape of elements should be chosen such that the structure is properly broken into elements even if it has segments with irregular shapes (e.g., with curvatures). It is common to use triangular elements for 2-D and tetrahedral elements for 3-D structures as it is relatively easy to fill the structure with them. It should be noted that increasing the number of elements does not necessarily improve the accuracy of the results as the numerical errors may become comparable or even larger than the expected improvement in the accuracy of the results. Moreover, increasing the mesh density will require more computational resources (e.g., memory and CPU time) which are limited.

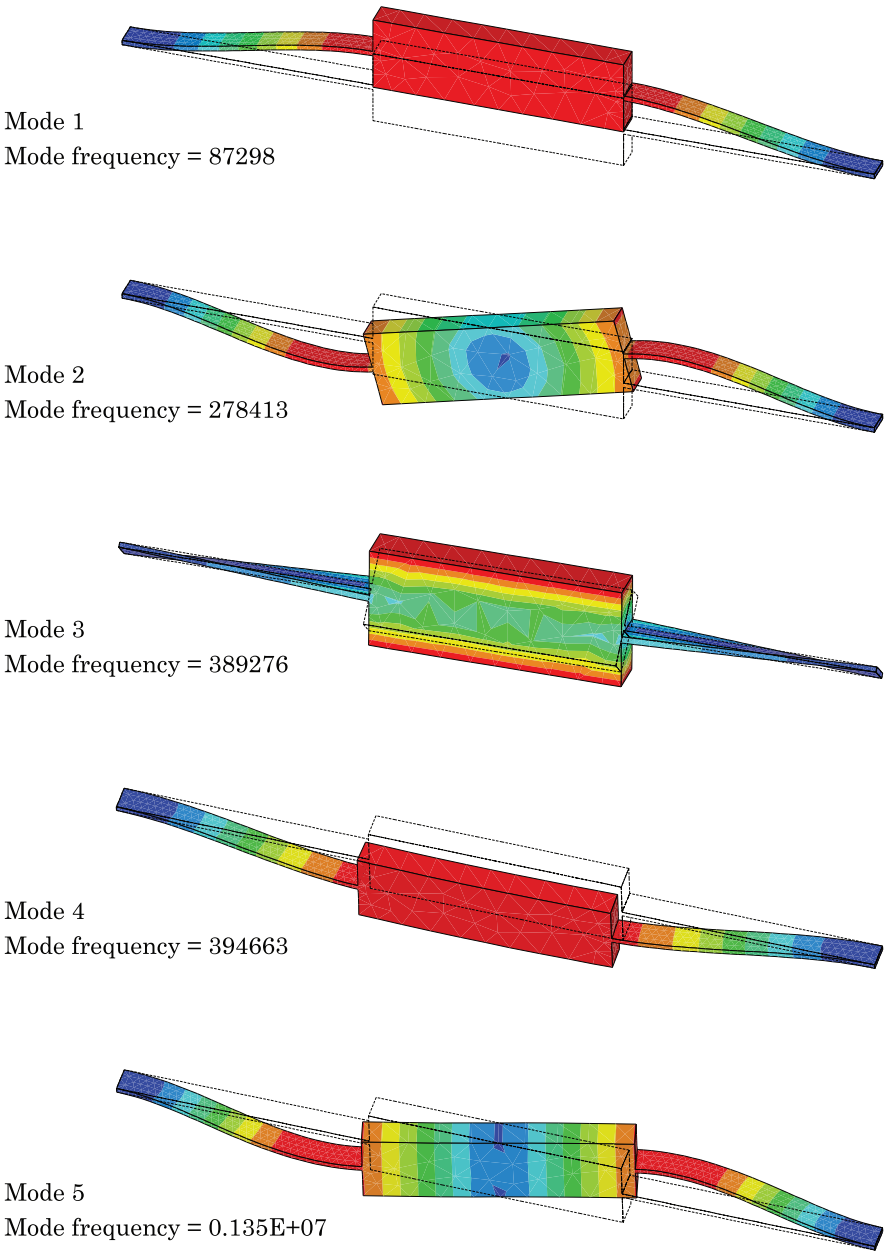

Figure 5.10 The mode shapes for the 1st to 5th vibration modes of the unloaded structure. The edge of the deformed structure is also plotted to aid the 3-D visualisation.

Fig. 5.9 illustrates sample output plots for the simulations of the mass sensor. The sensor was simulated in a commercially available FEM software [32,33]. A modal analysis was run on both unloaded and loaded structure to estimate the shift in the resonant frequency of the first mode of the structure due to adding

Table 5.5 Comparison of the Results for the Analysis of the Mass Sensor Using Different Modelling Techniques

Modelling technique	f_r (Hz)	$S_m^{f_0}$ (Hz/ng)	Error in estimated f_r	Error in estimated $S_m^{f_0}$
Lumped system	90 096	−644	3.21%	−12.97%
Rayleigh's	87 944	−599	1%	−19%
Dunkerley's	87 470	−590	1.67%	−16.75%
FEM	87 298	−740	–	–

a 0.1 ng particle at the centre of the shuttle of the sensor. A modal analysis was performed on the unloaded structure to find out the resonant frequencies of the first five modes which are: 87 298 Hz, 278.150 kHz, 393.72 kHz, 393.99 kHz, and 1.3471 MHz. These mechanical modes are illustrated in Fig. 5.10. It can be seen that the resonant frequencies of higher modes are at least 3 times larger than that of the first mode and one expects the Dunkerley's method to yield a good approximation to the resonant frequency of the first mode.

The simulation results were taken as the measure to evaluate the accuracy of the modelling results. These results are compared in Table 5.5. This simple example illustrates the value of a quick analysis with lumped model parameters. The choice between Rayleigh's and Dunkerley's method depends on the problem and complexity of the structure. Dunkerley's method is often easier to use provided that the conditions for using the Dunkerley's method are met. On the other hand, Rayleigh's method can be expanded to estimate the resonant frequencies of the higher modes [15].

5.8 Nonlinear Behaviour

In many cases, such as for electrostatic or thermal actuators, the actuation mechanism is inherently nonlinear even for small actuation signals. However, even for linear actuation mechanisms, the resonator can still exhibit nonlinear behaviour due to large displacements which contribute to either mechanical or material nonlinearities. As a result, a common feature among resonators is the dependence of the resonant frequency of the structure on the excitation signal or vibration amplitude [15,34–39]. Large displacements contribute to developing internal stresses inside the body of the resonator, which can alter the effective spring constant of the resonator. For a beam spring, it was shown that the effective spring constant increases under large axial forces (see Eq. (4.23)). Since the resonant frequency of a device is proportional to the square root of the effective spring constant, it too will be affected under large signal operations.

The dependence of the resonant frequency on signal amplitude leads to hysteresis in the frequency response of the device as the signal amplitude now

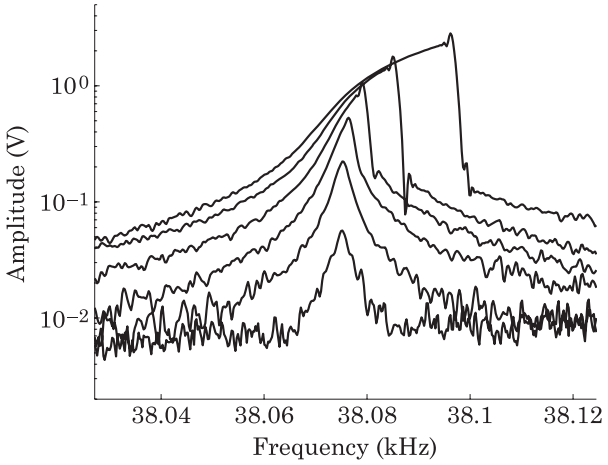

Figure 5.11 Measured output spectrum of an electrostatic resonator when input signal amplitudes was varied in steps whilst the frequency swept from low to high.

depends on he direction of the frequency sweep; i.e., whether the frequency of the input signal is swept from low-to-high or high-to-low. Consider for example the case that is illustrated in Fig. 5.11, where the resonant frequency increased as the signal amplitude became larger due to mechanical nonlinearities [40]. The reason for the positive shift in the resonant frequency of the device is that when the signal frequency approaches the resonant frequency of the structure, the amplitude of vibrations increases dramatically due to the high Q of the micromachined device. As the signal amplitude increases, the effective spring constant of the structure become larger (i.e., *spring stiffening*). This in turn results in an increase in the resonant frequency of the structure. However, if the frequency of the drive signal was swept from high-to-low, the amplitude of the vibrations would not have increased until the frequency of the resonator became close to the small signal resonant frequency of the system, which is smaller than the resonant frequency of the device when the frequency was swept from low-to-high. This hysteresis behaviour is known as *bifurcation*, as the function describing the resonator response versus frequency is no longer single-valued.

The resonator nonlinearities are modelled by adding higher order terms to the effective spring constant of a structure and solving the resulting nonlinear equation of motions. Perturbation analysis can be employed to analyse the behaviour of the systems with small nonlinearities [37,41]. For simplicity, let us assume that the resonator is actuated with a point force. The equation of motion of a resonator is:

$$M_{\text{eff}}\ddot{y} + \zeta\dot{y} + K_{\text{eff}}y = \mathcal{F}_{\text{in}}\cos\omega t \tag{5.69}$$

where K_{eff} and M_{eff} are the effective spring constant and mass of the device, respectively, ζ is the damping factor, $\mathcal{F}_{\text{in}}$ is the applied force to the resonator,

and y is the displacements at the point where the input force is applied. To account for the nonlinearities in the spring constant, the effective spring constant is assumed to be described by:

$$K_{\text{eff}} = K_0(1 + \kappa_1 y + \kappa_2 y^2 + O(y^3)) \tag{5.70}$$

where K_0 is the linear spring constant. Assuming that

$$y(t) = y_0 + y_1 \cos \omega t + y_2 \cos 2\omega t + y_3 \cos 3\omega t + \cdots \tag{5.71}$$

and ignoring damping, it can be shown that:

$$y_2 = \frac{\kappa_1}{6} y_1^2 \tag{5.72}$$

$$y_3 = \left(\frac{\kappa_1^2}{48} + \frac{\kappa_2}{32}\right) y_1^3. \tag{5.73}$$

The resonant frequency is then given by:

$$\omega_0' = \omega_0(1 + \Gamma y_1^2) \tag{5.74}$$

where y_1 is the displacement amplitude at the first harmonic of the drive signal and

$$\Gamma = \frac{3}{8}\kappa_2 - \frac{5}{12}\kappa_1^2. \tag{5.75}$$

Depending on the values of κ_1 and κ_2, the resonant frequency may increase or decrease. A measure for approximating the maximum signal level for linear operation is to find out the displacement amplitude just before bifurcation happens. This point corresponds to a position on the resonator response where the slope of the amplitude versus frequency curve approaches infinity (point y_b in Fig. 5.12). If the applied signal to the resonator becomes any larger, the resonator exhibits hysteresis in its frequency response. The bifurcation amplitude is given by:

$$y_b = \frac{1}{\sqrt{\sqrt{3}Q|\Gamma|}} \tag{5.76}$$

and the maximum displacement amplitude before bifurcation (point y_c in Fig. 5.12) is found from:

$$y_c = \frac{2}{\sqrt{3\sqrt{3}Q|\Gamma|}}. \tag{5.77}$$

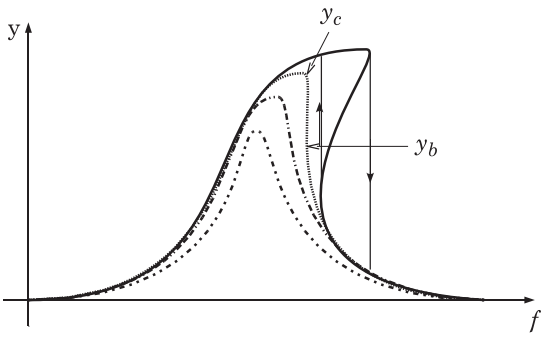

Figure 5.12 Measured output spectrum of an electrostatic resonator when input signal amplitudes was varied from 0.5 V to 3 V in 0.5 V steps with the frequency swept from low to high.

5.8.1 Mechanical Nonlinearity

Mechanical nonlinearity is a result of the stresses that develop inside a structure under large displacements. Generally, a structure becomes stiffer as the amplitude of vibrations increases and consequently the resonant frequency becomes larger. This phenomenon can be demonstrated by analysing a simple clamped–clamped beam resonator as illustrated in Fig. 5.13. For small vibration amplitudes, the displacements of the beam under a point force applied to its centre can be found using the Euler's beam theory (Eq. (4.15)) and is given by:

$$\psi(x) = \frac{F}{48E\mathcal{I}}\left((L-2x)^3 u\left(x-\frac{L}{2}\right) - 3Lx^2 + 4x^3\right) \tag{5.78}$$

where the term $u(x-L/2)$ illustrates the fact that the force was applied to the centre of the beam. The elongation of the beam due to its deflections is found from [5,42]:

$$\Delta L = \frac{1}{2}\int_0^L \left(\frac{\partial\psi}{\partial x}\right)^2 dx. \tag{5.79}$$

Noting that the internal stress is found from $\sigma_i = E\epsilon = E\Delta L/L$ and the corresponding strain energy is [42]:

$$\mathcal{U}_i = \frac{EA}{4L}\left(\int_0^L \left(\frac{\partial\psi}{\partial x}\right)^2 dx\right)^2 \tag{5.80}$$

where A is the cross-sectional area of the beam. The effective spring constant can now be found by considering the total potential energy in the system:

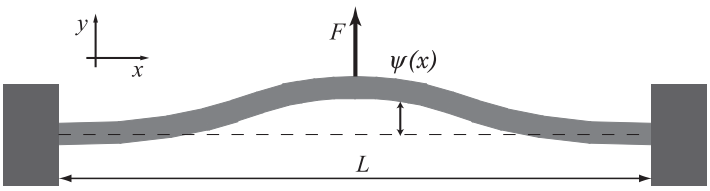

Figure 5.13 Bending of a clamped–clamped beam under a point force.

$$\begin{aligned}\mathcal{U}_{\text{total}} &= \frac{1}{2}k_{\text{eq}}y_0^2 = \mathcal{U}_b + \mathcal{U}_i \\ &= \frac{E\mathcal{I}}{2}\int_0^L \left(\frac{\partial^2\psi}{\partial x^2}\right)^2 dx + \frac{EA}{4L}\left(\int_0^L \left(\frac{\partial\psi}{\partial x}\right)^2 dx\right)^2 \end{aligned} \tag{5.81}$$

where $\mathcal{U}_b$ is the bending energy and y_0 is the deflection of the beam at its centre. The equivalent spring constant of the beam is then given by:

$$\begin{aligned} k_{\text{eq}} &= \frac{192E\mathcal{I}}{L^3} + \frac{AL^3}{3200E\mathcal{I}^2}\mathcal{F}^2 \\ &= \frac{16Ehb^3}{L^3} + \frac{288}{25}\frac{Ebh}{L^3}y_0^2 \end{aligned} \tag{5.82}$$

resulting in (from Eqs. (5.72), (5.73) and (5.75)):

$$\begin{aligned} \kappa_{1m} = 0, \quad \kappa_{2m} &= \frac{16}{25}\frac{1}{b^2} \\ \Rightarrow \Gamma_m &= \frac{27}{100}\frac{1}{b^2}. \end{aligned} \tag{5.83}$$

Since Γ_m is positive, the resonant frequency increases under large amplitude vibrations according to Eq. (5.75). The maximum resonance amplitude before bifurcation is:

$$\begin{aligned} y_{cm} &= \frac{20}{9\sqrt[4]{3}}\frac{b}{\sqrt{Q}} \\ &= 1.69\frac{b}{\sqrt{Q}}. \end{aligned} \tag{5.84}$$

5.8.2 Material Nonlinearity

Most properties of materials exhibit nonlinearity if the physical parameters are outside a certain range. The effective spring constant of typical micromachined devices is directly proportional to the Young's modulus, and

therefore, the nonlinearity in Young's modulus of the structural material is of particular importance to the analysis of resonators [7,43–45]. As an example, for internal strains above 500 micro-strains, the Young's modulus of single crystalline silicon as a function of the applied strain, ϵ, is:

$$E(\epsilon) = E_0 + E_1\epsilon + E_2\epsilon^2 \tag{5.85}$$

where $E_0 = 130$ GPa, $E_1 = 84.5$ GPa, and $E_2 = -598$ GPa for a beam oriented along the [100] direction [7,46,47].

For a clamped–clamped beam resonator made of silicon, the strain inside the beam is found from:

$$\epsilon = \frac{1}{2L}\int_0^L \left(\frac{\partial\psi}{\partial x}\right)^2 dx = \frac{12}{5}\frac{y_0^2}{L^2} \tag{5.86}$$

and since the spring constant is directly proportional to the Young's modulus:

$$\begin{aligned} \kappa_{1M} = 0, \quad \kappa_{2M} &= \frac{12}{5}\frac{E_{1b}}{L^2} \\ \Rightarrow \Gamma_M &= \frac{9}{10}\frac{E_{1b}}{L^2} \end{aligned} \tag{5.87}$$

and:

$$y_{cM} = 1.15\frac{L}{\sqrt{Q}}. \tag{5.88}$$

5.8.3 Electrostatic Nonlinearity

Due to their widespread applications, the nonlinearities in electrostatic resonators are of particular importance. This nonlinearity is a consequence of using parallel plate capacitors where the gap between the pates changes during the device operation [7,37,48,49]. The electrostatic force on the resonator is given by:

$$\mathcal{F}_{es} = \frac{1}{2}\frac{\varepsilon_0 LhV^2}{(g-y)^2} \tag{5.89}$$

where V is the applied voltage to the actuator, h and L are the height and length of the actuator electrode, g is the initial gap between the fixed and moving segments, and y is the displacement of the moving segment towards the fixed plate due to the applied potential. The Taylor series expansion of this

force yields:

$$\mathcal{F}_{es} = \frac{\varepsilon_0 LhV^2}{2g^2}\left(1 + \frac{2}{g}y + \frac{3}{g^2}y^2 + \frac{4}{g^3}y^3 + O(y^4)\right). \tag{5.90}$$

Ignoring the terms of order $O(y^4)$ and higher and inserting the above expression for force in the equation of motion and rearranging the equation results in:

$$M_{\text{eff}}\ddot{y} + \zeta\dot{y} + (k_m + k_e)y = \frac{\varepsilon_0 LhV^2}{2g^2} \tag{5.91}$$

where k_m is the mechanical spring constant and k_e is the electrical spring constant, given by:

$$k_e = -\frac{\varepsilon_0 LhV^2}{g^3}\left(1 + \frac{3}{2g}y + \frac{2}{g^2}y^2\right). \tag{5.92}$$

Defining $k_{e0} = \varepsilon_0 LhV^2/g^3$,

$$\kappa_{1e} = -\frac{3k_{e0}}{2g(k_m - k_{e0})}, \quad \kappa_{2e} = -\frac{2k_{e0}}{g^2(k_m - k_{e0})}$$
$$\Rightarrow \Gamma_e = -\frac{3}{16}\frac{k_{e0}(4k_m + k_{e0})}{g^2(k_m - k_{e0})^2}. \tag{5.93}$$

Since Γ_e is always negative, the electrostatic nonlinearity leads to the reduction of the resonant frequency. This could be anticipated by noting that the electrical spring constant is negative for physical systems and, when added to the mechanical spring constant, reduces the effective spring constant of the structure and hence, its resonant frequency.

References

1. S.D. Senturia, *Microsystem design*, Kluwer Academic Publishers, Boston, USA, 2000.
2. M. Elwenspoek and R. Wiegerink, *Mechanical microsensors*, Springer-Verlag, Berlin, Germany, 2001.
3. J.G. Korvink and O. Paul, Eds., *MEMS: A practical guide to design, analysis, and applications*, William Andrew Publishing, Norwich, USA, 2006.
4. W. Göpel, J. Hesse and J. Zemel, Eds., *Sensors: a comprehensive survey*, Wiley-VCH, Weinheim, Germany, 1997. 8 volumes.
5. K.F. Graff, *Wave motion in elastic solids*, Oxford University Press, Oxford, United Kingdom, 1975.
6. C.W. De Silva, *Vibration : fundamentals and practice*, CRC Press LLC, Boca Raton, USA, 2000.

7. V. Kaajakari, T. Mattila, A. Lipsanen and A. Oja, "Nonlinear mechanical effects in silicon longitudinal mode beam resonators", *Sensors and Actuators A: Physical*, Vol. 120, no. 1, pp. 64–70, April 2004.
8. S. Timoshenko, D. Young and W. Weaver, *Vibration problems in engineering*, John Wiley & Sons, New York, USA, 1974.
9. J.W. Harris and H. Stocker, *Handbook of mathematics and computational science*, Springer-Verlag, New York, USA, 1998.
10. E. Kreyszig, *Advanced engineering mathematics*, 8th edn., John Wiley & Sons Inc, New York, USA, 1999.
11. L. Meirovitch, *Analytical methods in vibrations*, MacMillan, New York, USA, 1967.
12. L. Landau and E. Lifshitz, in: *Theory of elasticity*, 3rd edn., ser. Course of theoretical physics., Vol. 7, Butterworth Heinemann, Oxford, United Kingdom, 1976. Translated by J.B. Sykes and W.H. Reid.
13. S. Timoshenko and S. Woinowsky-Kreiger, *Theory of plates and shells*, 2nd edn., McGraw-Hill, USA, 1964.
14. W.C. Tang, "Electrostatic comb drive for resonant sensor and actuator applications", Ph.D. dissertation, Department of Electrical Engineering and Computer Sciences, University of California, Berkeley, USA, 1992.
15. W.T. Thomson, *Theory of vibration with applications*, 2nd edn., Prentice-Hall, Englewood Cliffs, USA, 1981.
16. S. Dunkerley, "On the whirling and vibrations of shafts", *Philosophical Transactions of Royal Society of London*, Vol. 185, pp. 279–360, 1894.
17. T. Leblois and C. Tellier, "Some investigations on doubly-rotated quartz resonant temperature sensors", *Sensors and Actuators A: Physical*, Vol. 99, no. 3, pp. 256–269, June 2002.
18. J. Soderkvist, "Similarities between piezoelectric, thermal and other internal means of exciting vibrations", *Journal of Micromechanics and Microengineering*, Vol. 3, no. 1, pp. 24–31, March 1993.
19. A. Warner, "High-frequency crystal units for primary frequency standards", *Proceedings of the IRE*, Vol. 40, no. 9, pp. 1030–1033, September 1952.
20. H.-W. Jeong, T. Aoki and T. Hatsuzawa, "Frequency responses of spherically contoured rectangular AT-cut quartz crystal resonators fabricated by fixed abrasive method", *International Journal of Machine Tools and Manufacture*, Vol. 44, no. 11, pp. 1143–1149, September 2004.
21. Y. Nagaura and S. Yokomizo, "Manufacturing method of high frequency quartz oscillators over 1 GHz", *Proceedings of the IEEE International Frequency Control Symposium and Exposition*, vol. 1, Besancon, France, 1999, pp. 425–428.
22. Y. Watanabe, T. Okabayashi, S. Goka and H. Sekimoto, "Phase noise measurements in dual-mode SC-cut crystal oscillators", *IEEE Transactions on Ultrasonics, Ferroelectrics and Frequency Control*, Vol. 47, no. 2, pp. 374–378, April 1999.
23. C. Nguyen, "MEMS technology for timing and frequency control", in: *Proceedings of the 2005 IEEE international frequency control symposium and exposition*, Vancouver, Canada, pp. 1–11, August 2005.
24. Z. Hao, S. Pourkamali and F. Ayazi, "VHF single-crystal silicon elliptic bulk-mode capacitive disk resonators; part I: Design and modeling", *IEEE Journal of Microelectromechanical Systems*, Vol. 13, no. 6, pp. 1043–1053, December 2004.
25. B.L. Bircumshaw, A.P. Pisano and O.M. O'Reilly, "Radial bulk annular resonator using MEMS technology", US Patent 6 894 586 B2, 2005.
26. J. Wang, Z. Ren and C.-C. Nguyen, "1.156-GHz self-aligned vibrating micromechanical disk resonator", *IEEE Transactions on Ultrasonics, Ferroelectrics and Frequency Control*, Vol. 51, no. 12, pp. 1607–1628, December 2004.

27. T. Irie, G. Yamada and K. Umesato, "Free vibration of regular polygonal plates with simply supported edges", *The Journal of the Acoustical Society of America*, Vol. 69, no. 5, pp. 1330–1336, May 1981.
28. H.A. Tilmans, "Equivalent circuit representation of electromechanical transducers: I. lumped-parameter systems", *Journal of Micromechanics and Microengineering*, Vol. 6, no. 1, pp. 157–176, March 1996.
29. H.A. Tilmans, "Equivalent circuit representation of electromechanical transducers: II. distributed-parameter systems", *Journal of Micromechanics and Microengineering*, Vol. 7, no. 4, pp. 285–309, December 1997.
30. K.-J. Bathe, *Finite element procedures*, 2nd edn., Prentice Hall, Englewood Cliffs, USA, 1996.
31. O. Zienkiewicz and R. Taylor, *The finite element method*, 5th edn., Butterworth-Heinemann, Oxford, United Kingdom, 2000. 3 volumes.
32. *ANSYS version 8.1*, ANSYS Inc., Southpointe, 275 Technology Drive, Canonsburg, PA 15317, USA, 2004. [Online]. Available: http://ansys.com.
33. S. Moaveni, *Finite element analysis: theory and application with ANSYS*, Prentice Hall, Upper Saddle River, USA, 1999.
34. J. Zhao, "Experimental characterization of dynamic behavior of micromachined resonators", Master's thesis, Department of Electrical and Computer Engineering, University of Manitoba, Winnipeg, Manitoba, Canada, 2005.
35. H.B. Chan, V.A. Aksyuk, R.N. Kleiman, D.J. Bishop and F. Capasso, "Nonlinear micromechanical Casimir oscillator", *Physical Review Letters*, Vol. 87, no. 21, pp. 211 801–1–211 801–4, November 2001.
36. C. Gui, R. Legtenberg, H.A.C. Tilmans, J.H.J. Fluitman and M. Elwenspoek, "Nonlinearity and hysteresis of resonant strain gauges", *IEEE Journal of Microelectromechanical Systems*, Vol. 7, no. 1, pp. 122–127, March 1998.
37. V. Kaajakari, T. Mattila, A. Oja and H. Sepp, "Nonlinear limits for single-crystal silicon microresonators", *IEEE Journal of Microelectromechanical Systems*, Vol. 13, pp. 715–724, October 2004.
38. T.A.W. Roessig, "Integrated MEMS tuning fork oscillators for sensor applications", Ph.D. dissertation, Department of Mechanical Engineering, University of California, Berkeley, USA, 1998.
39. T. Bourouina, A. Garnier, H. Fujita, T. Masuzawa and J.-C. Peuzin, "Mechanical nonlinearities in a magnetically actuated resonator", *Journal of Micromechanics and Microengineering*, Vol. 10, no. 2, pp. 265–270, 2000.
40. B. Bahreyni, "Design, modeling, simulation, and testing of resonant micromachined magnetic field sensors", Ph.D. dissertation, Department of Electrical and Computer Engineering, The University of Manitoba, Canada, 2006.
41. L. Landau and E. Lifshitz, in: *Mechanics*, 3rd edn., ser. Course of theoretical physics, Vol. 1, Butterworth Heinemann, Oxford, United Kingdom, 1976. Translated by J.B. Sykes and J.S. Bell.
42. S. Timoshenko and J. Goodier, *Theory of elasticity*, 2nd edn., McGraw-Hill, Tokyo, Japan, 1951.
43. H.J. McSkimin and J.P. Andreatch, "Measurement of third-order moduli of silicon and germanium", *Journal of Applied Physics*, Vol. 35, no. 11, pp. 3312–3319, November 1964.
44. H. Igarashi, K. Ishii, N. Akimoto and S. Tashiro, "Nonlinear behavior of piezoelectric ceramics under high power vibration", *Journal of the Korean Physical Society*, Vol. 32, no. 3, pp. S1245–S1247, February 1998.
45. J.-Y. Duquesne, "Measurement of a third-order elastic constant in silicon by a comparison method", *The Journal of the Acoustical Society of America*, Vol. 108, no. 3, pp. 946–948, September 2000.
46. R. Hull, Ed., *Properties of crystalline silicon*, Institution of Electrical Engineers, London, United Kingdom, 1999.

47. J.J. Hall, "Electronic effects in the elastic constants of n-type silicon", *Physical Review*, Vol. 161, no. 3, pp. 756–761, September 1967.
48. M.I. Younis and A. Nayfeh, "A study of the nonlinear response of a resonant microbeam to an electric actuation", *Nonlinear Dynamics*, Vol. 31, no. 1, pp. 91–117, January 2003.
49. M. Agarwal, K. Park, R. Candler, M. Hopcroft, C. Jha, R. Melamud, B. Kim, B. Murmann and T. Kenny, "Non-linearity cancellation in MEMS resonators for improved power-handling", *Technical Digest of the IEEE International Electron Devices Meeting*, Washington, USA, December 2005.
50. R. Holland, "Contour extensional resonant properties of rectangular piezoelectric plates", *IEEE Transactions on Sonics and Ultrasonics*, Vol. 15, no. 2, pp. 97–104, 1968. April.
51. M. Onoe, "Contour vibrations of isotropic circular plates", *The Journal of the Acoustical Society of America*, Vol. 28, no. 6, pp. 1158–1162, 1956. November.

6 Damping Mechanisms

Numerous damping mechanisms can contribute to energy loss in micromachined resonators. In almost all cases, air damping is the major source of energy loss for a properly designed micromachined resonator. Flexural resonators are more susceptible to energy loss from friction with gas molecules than bulk-mode resonators, mainly due to the larger displacements of these devices. The coupling of resonator energy to the substrate through anchors is another damping source as is thermoelastic damping; i.e., the irreversible conversion of elastic energy to heat. The transfer of energy between a resonating structure and phonons or the photons impinging on the surface of a micromachined structures also contribute to the total losses in the system.

Study of damping in resonators is important because: (1) the quality factor of the resonators is a function of the amount of energy loss in the system; and (2) the amount of damping determines the amount of noise at the output of the device. In almost all cases, it is desired to have a high-Q resonance and minimum noise in the system for optimum performance. This chapter overviews the dominant sources of damping in micromachined resonators.

6.1 Viscous Damping

The source of viscous damping is the energy that is dissipated by the resonator to shape the fluid profile around it. Various methods have been employed to model the viscous damping mechanisms in micromachined devices. Most of these models assume that the fluid in which the structure moves is a *Newtonian fluid*. For Newtonian fluids, the exerted shear stress on a plate moving inside the fluid is linearly proportional to the velocity profile inside the fluid:

$$\tau = -\mu \frac{du_x}{dy} \tag{6.1}$$

where τ is the shear stress, μ is the viscosity coefficient (in Kg m^{-1} s^{-1}), u_x is the fluid velocity in x-direction at distance y from the plate (assuming that $\vec{U} = u_x\vec{a}_x + u_y\vec{a}_y + u_z\vec{a}_z$), and the negative sign implies that the exerted stress opposes the movements of the structure. The viscosity coefficient, μ usually ranges from 10^{-5} Kg m^{-1} s^{-1} for gases to about 10^{-3} Kg m^{-1} s^{-1} for liquids. As expected, μ depends on pressure for gases. Solving the gas dynamic equations and using experimental data, it has been shown that [1]:

$$\mu = \frac{\mu_0}{1 + 2K_n + 0.2K_n^{0.788}e^{-0.1K_n}} \tag{6.2}$$

where μ_0 is the viscosity coefficient at atmospheric pressure and K_n is the *Knudsen number* which is a measure of rarefaction effect and is the ratio of the mean free path of the ambient gas molecules, λ, and the gap between the structures: $K_n = \lambda/h$. The value of the mean free path can be calculated from [2]:

$$\lambda = \frac{K_{\mathrm{B}} T}{\sqrt{2}\pi d^2 P_{env}} \tag{6.3}$$

where K_{B} is Boltzmann's constant, T is the ambient temperature in kelvin, P_{env} is the pressure, and d is the diameter of gas molecules.

The Navier–Stokes equation relates the velocity and pressure inside a fluid to each other through a nonlinear partial differential equation[1]:

$$\rho\left(\frac{\partial \vec{U}}{\partial t} + (\vec{U}\cdot\nabla)\vec{U}\right) = -\nabla\vec{P} + \rho\vec{g}_g + \mu\nabla^2\vec{U} + \frac{\mu}{3}\nabla\left(\nabla\cdot\vec{U}\right) \tag{6.4}$$

where $\vec{g}_g$ is the acceleration due to gravity, ρ is the density of the media, and $\vec{P}$ is pressure vector [3]. For the Navier–Stokes equation to be valid, the temperature across the plates should be uniform, velocity of the moving plate should be low enough to prevent the heating of the gas, and the amplitude of the oscillation needs to be small compared to the length of the surface in order to ignore the edge effects.

The continuity equation assures the conservation of mass and continuity of the fluid density:

$$\frac{\partial \rho}{\partial t} + \nabla\cdot(\rho\vec{U}) = 0. \tag{6.5}$$

Navier–Stokes and continuity equations should simultaneously be solved to find the velocity profile inside the fluid. If the liquid is incompressible, the continuity equation yields $\nabla\vec{U} = 0$. Further assumption of negligible pressure gradients within the fluid (i.e., $\nabla\vec{P} = 0$) results in the simplified form of Navier–Stokes equations:

$$\rho\frac{\partial \vec{U}}{\partial t} + (\vec{U}\cdot\nabla)\vec{U} = \rho\vec{g}_g + \mu\nabla^2\vec{U}. \tag{6.6}$$

Often, the term $\rho\vec{g}_g$ can also be ignored at micro- and nano-scales, further simplifying the equation.

[1]The operator ∇ is defined as $\nabla = \vec{a}_x(\partial/\partial x) + \vec{a}_y(\partial/\partial y) + \vec{a}_z(\partial/\partial z)$, where $\vec{a}_x$, $\vec{a}_y$, and $\vec{a}_z$ are the unit vectors along each of the axes in Cartesian coordinates. Operator ∇^2 is defined as $\nabla^2 = \nabla\cdot\nabla = \partial^2/\partial x^2 + \partial^2/\partial y^2 + \partial^2/\partial z^2$.

A parameter that is often used when discussing different flow mechanisms of a fluid is Reynold's number which is defined as:

$$R_e = \frac{L\mathcal{V}}{\nu} \tag{6.7}$$

where L and $\mathcal{V}$ are the characteristic length and velocity for the fluid in a given environment, respectively, and $\nu$is the kinematic viscosity of the fluid: $\nu = \mu/\rho$ [3]. Several flow regimes can be identified using Reynold's number:

- $R_e \ll 1$: the inertial forces are much smaller than viscous forces and can be ignored;
- $R_e < 2000$: the fluid flow is laminar;
- $R_e > 4000$: the flow is turbulent (i.e., the flow and velocity patterns are relatively complicated).

For $2000 < R_e < 4000$, the flow regime is transitional between laminar and turbulent. Due to the small dimension of MEMS, the fluid flow around them is usually laminar.

The amount of viscous damping depends on the type of fluid flow around the structure. We study the three types of viscous damping mechanisms that are usually considered when computing the energy loss through viscous damping for moving microstructures, namely: *Couette*, *Stokes*, and *squeezed-film* damping. The analytic damping models are derived from solving the Navier–Stokes equations under different boundary conditions [1,4–10].

6.1.1 Couette Damping

For one-dimensional movements of an infinite plate (i.e., $\vec{U} = u_x(y)\vec{a}_x$) inside a fluid at micro-scales, the nonlinear term in Eq. (6.6) vanishes and the Navier–Stokes equation can be written as [1,6,11]:

$$\rho\frac{\partial u_x}{\partial t} = \mu\frac{\partial^2 u_x}{\partial y^2}. \tag{6.8}$$

If the plate moves with velocity u_0 in parallel with a stationary plate at distance h from it (see Fig. 6.1), the *no-slip boundary conditions* imply that:

$$u_x\big|_{y=0} = 0 \tag{6.9}$$

$$u_x\big|_{y=h} = u_0 \tag{6.10}$$

$$u_x\big|_{y=\infty} = 0. \tag{6.11}$$

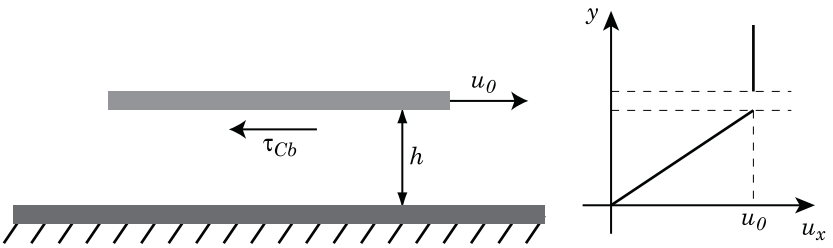

Figure 6.1 Fluid velocity profile between a moving plate at constant velocity u_0 and a fixed one.

Furthermore, since the plate moves at a constant speed, velocity profile should be independent of time; i.e., $\partial u_x/\partial t = 0$. The velocity profile between the plates is found from solving Eq. (6.8) with boundary conditions (6.9) and (6.10):

$$u_x(y) = u_0 \frac{y}{h}. \tag{6.12}$$

The shear stress on the bottom of the moving plate can be calculated using Eq. (6.1):

$$\tau_{Cb} = \mu \frac{u_0}{h}. \tag{6.13}$$

The solution to Eq. (6.8) for the fluid on top of the moving plate with boundary conditions (6.10) and (6.11) shows that the liquid moves with the plate, and therefore, does not cause any drag on the plate (i.e., $\tau_{Ct} = 0$). The total drag force on the moving plate is found from multiplying the shear stress by the area of the plate:

$$\begin{aligned} \mathcal{N} &= A \cdot (\tau_{Cb} + \tau_{Ct}) \\ &= \mu \frac{u_0}{h} A \end{aligned} \tag{6.14}$$

where A is the area of the moving plate.

6.1.2 Stokes Damping

When the moving plate has an oscillatory motion, boundary condition (6.10) changes to $u_x|_{_{y=h}} = u_0\, e^{j\omega t}$, where ω is the frequency of the plate oscillations [1,6,11]. Solving the Navier–Stokes equation between the plates results in:

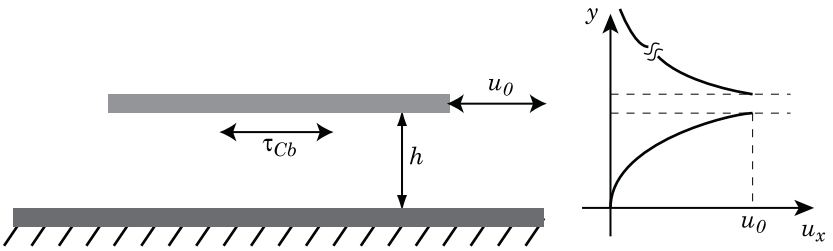

Figure 6.2 Fluid velocity profile between a moving plate at constant velocity u_0 and a fixed one.

$$u_x(y,t) = u_0 \frac{\sinh \sqrt{\frac{j\omega}{\nu}} y}{\sinh \sqrt{\frac{j\omega}{\nu}} h} e^{j\omega t} \tag{6.15}$$

which can be written as:

$$u_x(y,t) = u_0 \frac{\sinh(1+j)\beta y}{\sinh(1+j)\beta h} e^{j\omega t} \tag{6.16}$$

where $y < h$ and $\beta = \sqrt{\omega/2\nu}$ is the momentum propagation velocity. Since the density of structural materials is much larger than that of the surrounding gas, the out-of-phase components of the force can be ignored, leading to:

$$\tau_{Sb} = -\mu\beta \frac{\sinh(2\beta h) + \sin(2\beta h)}{\cosh(2\beta h) - \cos(2\beta h)} u_x \tag{6.17}$$

where τ_{Sb} is the shear stress on the bottom surface of the moving plate, as illustrated in Fig. 6.2.

The fluid velocity profile above the moving plate (i.e., $y > h$) can also be found from Eq. (6.17) by assuming $h \to \infty$, which leads to:

$$\tau_{St} = -\mu\beta u_x \tag{6.18}$$

where τ_{St} is the shear stress on the top surfaces of the moving plate. The total drag force on the moving plate is finally given by:

$$\mathcal{N} = \mu\beta A \left(1 + \frac{\sinh(2\beta h) + \sin(2\beta h)}{\cosh(2\beta h) - \cos(2\beta h)}\right) u_x. \tag{6.19}$$

A more rigorous analysis of this problem would indicate that the damping is frequency dependant [1]. The cut-off frequency for Stokes damping is given by:

$$f_{cs} = \frac{\mu}{2\pi\rho h^2}. \tag{6.20}$$

At frequencies higher that f_{cs}, the damping coefficient increases linearly with frequency.

6.1.3 Squeezed-film Damping

If the gap between the moving structures changes during their movement, another damping mechanism known as *squeezed-film damping* will occur [5,12–15]. The source of this damping mechanism is the required energy to push the ambient gas out of the gap between two structures when they move toward each other or pull it back in when they move away from each other (see Fig. 6.3). While the gas movement results in energy dissipation, the compression of the gas will also introduce a spring-like behaviour, leading to the frequency dependence of this type of damping. Navier–Stokes and continuity equations can be solved to calculate both frequency-independent and frequency-dependent components of the opposing force on the moving structure. However, in order to derive a simple analytic model for this phenomena, additional simplifying assumptions must be made:

- the gas is assumed to follow the ideal gas law;
- the gap should be small compared to the size of the plate;
- the system is isothermal.

With the above assumptions, the gas kinetics are described by:

$$12\mu_{\text{eff}}\frac{\partial(Ph)}{\partial t} = \nabla\cdot\left((1+6K_n)h^3P\nabla P\right) \tag{6.21}$$

where h is the gap between the two plates, K_n is the Knudsen number, and P and h both are functions of location and time. Eq. (6.21) is known as *Reynolds equation*[5,15,16]. This nonlinear equation can be linearised with the aid of perturbation analysis. Assuming that $h = h_0 + \delta h$ and $P = P_0 + \delta p$, where P_0 and h_0 are the pressure and the gap between the structures at their rest positions, it follows from Eq. (6.21) that:

$$\frac{P_0h_0^2}{12\mu_{\text{eff}}}\nabla^2\left(\frac{\delta p}{P_0}\right) - \frac{\partial}{\partial t}\left(\frac{\delta p}{P_0}\right) = \frac{\partial}{\partial t}\left(\frac{\delta h}{h_0}\right) \tag{6.22}$$

where we have also assumed that the gap between the plates is much larger than the mean free path of gas molecules (i.e., $K_n \ll 1$).

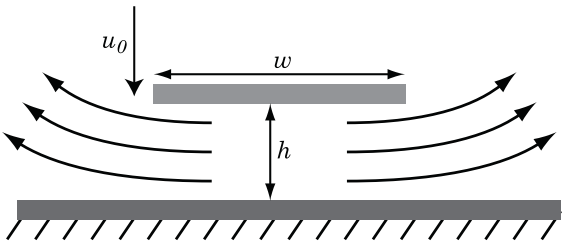

Figure 6.3 Fluid velocity profile when a plate moves towards a fixed one.

The linearised Reynold's equation can be solved for a rectangular beam of length L and width W ($L > W$) moving normal to a fixed plate at distance h_0 from it. For this case, the squeezed-film damping coefficient is given by:

$$\zeta_{sf} = \frac{96}{\pi^4} \times \frac{\mu_{\text{eff}} L W^3}{h^3} \tag{6.23}$$

where it is assumed that the pressure is the same as that of the surroundings at the edges of the beam (i.e., $\delta p = 0$ along the sides of the beam).

At low frequencies and for small displacements, there is enough time for the pressure around the structure to change and the gas has enough time to respond to the movements of the structure. At higher frequencies, however, the movements of the plates simply compresses and decompresses the gas and the fluid essentially behaves as a spring. The cut-off frequency is given by [17]:

$$f_{cs} = \frac{\pi h_0^2 P_0}{24 \mu W^2}. \tag{6.24}$$

The squeezed-film damping coefficient drops with frequency for frequencies higher than f_{cs}.

6.2 Anchor Loss

The main body of the resonator needs to remain connected to the substrate for mechanical stability. Some resonators, like bulk acoustic wave (BAW) or surface acoustic wave (SAW), can be directly fabricated on the substrate. Most micromachined resonators, however, are released structures and need to be mechanically anchored to the substrate or to the films that are fixed to the substrate. A released structure can be anchored to the substrate using straight or curved beams and in some cases, membranes. For many flexural mode resonators, the anchoring beams also serve as the restoring springs as shown in Fig. 6.4. In such cases, the resonant frequency of the structure is directly set by the mechanical properties of the beams. *Anchor loss*, or support loss, refers to the vibration energy that is lost to the substrate as a result of

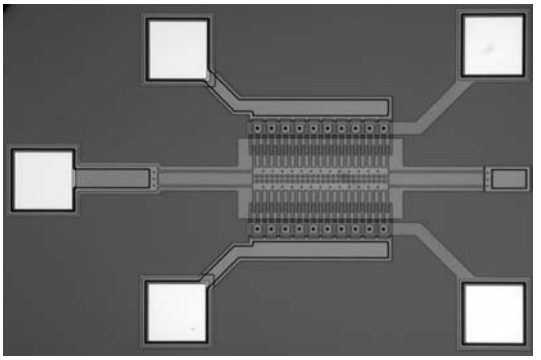

Figure 6.4 A flexural mode resonator fabricated in MUMPS technology. The four anchoring beams for this device also act as the restoring springs.

anchors deflecting with the resonator, or more accurately, due to the work that is done by the resonator vibrations at the anchoring points [18–25].

In many cases, especially for bulk mode resonators, the sole purpose of the anchor is mechanical stability while the resonant frequency is set by a separate segment of the device structure. For these resonators, proper engineering of the anchors is imperative in order to avoid the loss of vibration energy to the substrate. The most important aspect of anchor design is the placement of the anchor points. The anchors are usually placed at the resonant *nodes*. The resonant nodes are locations with the minimum amount of displacement (theoretically zero displacement) during the resonator operation. The location of resonant nodes depends on the desired operating mode of the resonator. As a simple example, the middle of a clamped–clamped beam is a resonant node for the even flexural in-plane modes (check Fig. 5.4 for the shapes of modes 2 and 4). As another example, for a disk resonator like the one illustrated in Fig. 5.6, one can identify a number of resonant nodes on the perimeter of the disk depending on the mode shape [26].

Based on the design requirements, a certain resonant mode is chosen and the locations of anchoring points are determined. In practice, however, an anchor has some width, whose minimum is usually set by lithography. Consequently, the anchor location cannot be a mathematical point as one finds from investigating the mode shapes. On the other hand, in-plane motions of a resonator are converted to normal displacements and vice versa and correspond to each other through Poisson's ratio. Therefore, even when a resonator is operated at one of its in-plane modes of vibration, there will be normal shear forces and moments at the anchoring points which pump a fraction of the resonator energy into the substrate [27–29]. One needs to minimise the coupling of these vibrations through the anchors to the substrate which can be achieved by proper choosing of mechanical properties of the anchor beam. If the anchor is designed such that it resonates with the main resonator while its connecting point to the substrate is a resonant node of the beam, a minimum of the

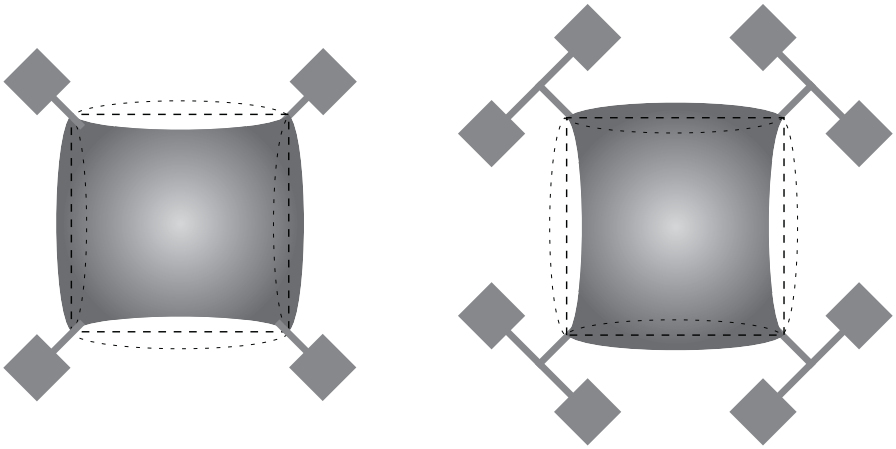

Figure 6.5 The Lamé mode of a square plate resonator with straight (left) and T (right) anchors.

vibrations at the other end of the beam are transferred to the substrate. It should be noted the anchoring beam does not necessarily have to resonate at its fundamental mode [30,31].

Let us go through the anchor design steps for a square plate bulk mode resonator that is excited in its Lamé mode. While resonating at its Lamé mode, the neighbour sides of the resonator move antiphase with respect to each other; i.e., two of the sides facing each other bend away from the centre of the resonator while the other two bend toward the centre [32–34]. This mode shape is illustrated in Fig. 6.5 with two possible anchoring options. As can be seen, the four corners of the resonator are resonant nodes, and therefore, the anchors should be placed at the corners. In the simple case, a straight beam can be used to anchor a node to the substrate. This beam needs to resonate at its longitudinal resonant frequency during the main resonator operation. Following a procedure similar to Section 5.2, the resonant frequency of the longitudinal modes of the beam is found from:

$$f_n = \frac{2n-1}{4}\frac{c_0}{L_a} \tag{6.25}$$

where L_a is the length of the anchoring beam and c_0 is the acoustic velocity of longitudinal waves in the solid. Knowing the resonant frequency of the main resonator, the length of the anchor beam can be set such that the resonant frequency of its first mode matches that of the main resonator:

$$L_a = \frac{c_0}{4f_0} = \frac{\lambda_l}{4} \tag{6.26}$$

where λ_l is the wavelength for the longitudinal waves (see Section 5.2). This is an important result as it shows that to isolate the vibrations at one end of the

beam from the anchor, its length should be a quarter of the acoustic wavelength at the frequency of operation.

The same result can be obtained if the continuous mechanical system is modelled as a distributed electrical equivalent circuit (using the conversion as described in Section 5.7.1). The analysis in this case will be similar to the transmission line calculations in electromagnetics. The mechanical impedance is defined as the ratio of the force to velocity at a point along the beam [35]. If there are no reflections in the beam, the mechanical impedance for longitudinal modes is given by:

$$Z_0 = A\sqrt{\rho E} \tag{6.27}$$

where A is the cross sectional area of the beam. If a beam of length l is terminated with a mechanical impedance of Z_T at one end, the mechanical impedance at its other end is given by:

$$Z_{in} = Z_0 \frac{Z_T + jZ_0 \tan \frac{\omega}{c_0} l}{Z_0 + jZ_T \tan \frac{\omega}{c_0} l}. \tag{6.28}$$

The impedance seen from the end of a beam of length $l = \lambda_l/4 = c_0/4f$ is:

$$Z_{in}|_{L=\frac{\lambda_l}{4}} = \frac{Z_0^2}{Z_T}. \tag{6.29}$$

If the beam is clamped at one end (i.e., $Z_T = \infty$), the impedance seen from the other end will be $Z_{in} = 0$; i.e., it does not load the structure. Therefore, if one wants to minimise the energy loss through the beam to the anchor, the length of the beam must be equal to a quarter of the vibration wavelength. As expected, this result agrees with our earlier discussion on the having the beam resonate with the structure.

The longitudinal acoustic velocity of silicon is between 8.4–9.1 km/sec depending on the crystal orientation [36]. Knowing that $\lambda_l = c_0/f_0$ and considering that the resonant frequency of typical MEMS is typically in the 1 kHz to 1 GHz range, it can be seen that the length of the quarter wavelength transformer beam falls between 2 μm and 2 m. The length of the anchoring beam is obviously too long at low frequencies. In such cases, one can employ the flexural modes of beams. An example is illustrated in Fig. 6.5 where a short beam connects the corner of the resonator to the centre of a clamped–clamped beam. The design requirement is to make the clamped–clamped beam have the same resonant frequency as the main structure. However, the flexural wavelength of a resonator is a function of the width of the beam (see Eq. (5.13)), which is an added degree of freedom when designing a beam for a given resonant frequency.

6.3 Thermoelastic Damping

Thermoelastic damping was first analysed in detail by Zener who also developed analytic models for simple cases [37–39]. Thermoelastic damping refers to the irreversible conversion of vibration energy into thermal energy. These two physical domains are coupled through the linear thermal expansion coefficient of the material[2]. The temperature of the material increases under compression and decreases under tension for a material with a positive thermal expansion coefficient[3]. When a beam is bent, heat transfers from the regions under compression to parts under tension, leading to the dissipation of energy, and consequently, reduction in Q.

Thermoelastic damping is often the ultimate limiting factor in achieving a higher Q for a resonator. While anchor losses can be minimised through proper mechanical design and viscous damping can be reduced by operating the device under vacuum, thermoelastic damping happens internally to the structure of the device. Although the operating mode of the resonator (i.e., flexural, torsional, or longitudinal) and the characteristics of the material do affect the level of thermoelastic damping, the main technique to reduce thermoelastic damping for a device resonating at a given mode is to operate it at low temperatures [40–45].

If thermoelastic damping is the dominant cause of energy loss, the quality factor for flexural in-plane vibrations of a beam is given by [24,37,40]:

$$Q_{TED} = \frac{\rho \mathcal{C}_p}{\alpha^2 E T} \left(\frac{\varpi}{\omega_0} + \frac{\omega_0}{\varpi} \right) \tag{6.30}$$

where ρ is the material density, $\mathcal{C}_p$ is the heat capacity (in J K^{-1} kg^{-1}), α is the linear thermal expansion coefficient, T is the average temperature, and ω_0 is the resonant frequency of the beam. Parameter ϖ is the inverse of the characteristic thermal relaxation time of the beam:

$$\varpi = \frac{1}{\tau_f} = \mathcal{D}_t \frac{\pi^2}{W^2} \tag{6.31}$$

where W is the beam width and $\mathcal{D}_t = \kappa / \rho \mathcal{C}_p$ is the thermal diffusion constant (κ is the thermal conductivity in W m^{-1} K^{-1}). As shown in Fig. 6.6, there is a minimum for the quality factor of a flexural resonator if thermoelastic dissipation is the only damping mechanism. From Eqs. (5.23) and (6.30), the maximum amount of thermoelastic dissipation happens when $\omega_0 = \varpi$:

[2]The thermal expansion coefficient is defined as $\alpha = (1/L)\partial L/\partial T$, where L is the initial length of the beam.

[3]A similar behaviour is observed in gases which can be quantified using the ideal gas law: $PV = nRT$.

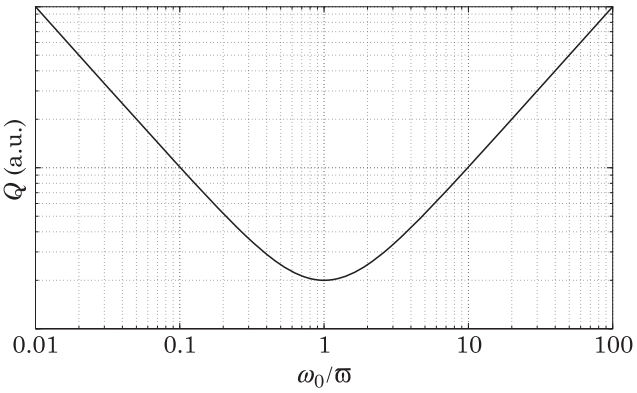

Figure 6.6 Change in the quality factor of a flexural beam resonator due to thermoelastic dissipation versus the resonant frequency of the beam normalised to the frequency of heat transport, ϖ.

$$\mathcal{K}_n \frac{W}{L^2}\sqrt{\frac{E}{\rho}} = \mathcal{D}_t \frac{\pi}{2W^2}$$
$$\rightarrow \frac{W^3}{L^2} = \frac{\pi\kappa}{2\mathcal{K}_n \mathcal{C}_p \sqrt{\rho E}}. \tag{6.32}$$

This equation can be used to choose proper dimensions for the beam resonators in order to reduce thermoelastic damping in them. It can be shown that for a longitudinal mode beam resonator, the thermal relaxation time is given by [24]:

$$\tau_{_l} = \frac{\lambda_{l1}^2}{4\pi^2 \mathcal{D}_t} \tag{6.33}$$

where λ_{l1} is the wavelength of the first longitudinal mode of the resonator:

$$\lambda_{l1} = \frac{c_0}{f_0} = 2L \tag{6.34}$$

where L is the length of the beam.

Comparing $\tau_{_l}$ and $\tau_{_f}$, it can be seen that thermoelastic damping has a smaller effect on longitudinal resonators compared to flexural resonators for typical resonant frequencies of MEMS resonators.

6.4 Surface Losses

There are other sources of energy loss in resonators that become more dominant as the dimensions of the devices are shrunk. An important class of

these losses are *surface losses* which are attributed to the surface stresses that are caused by the adsorption and desorption of molecules to the surface of the resonator. As a direct consequence, this source of damping is proportional to the surface area of the resonator and becomes more dominant as the surface to volume ratio of a resonator increases. It has been verified that surface treatment and replacing the gas in the immediate ambient around the resonator affect its quality factor [44,46–48]. Surface losses are modelled by adding an imaginary term to the Young's modulus of the material. It can be shown that for a beam of width W and thickness h the quality factor due to surface losses is found from [49]:

$$Q_{sl} = \frac{Wh}{2\delta(3W+h)} \frac{E}{E_{ds}} \tag{6.35}$$

where E_{ds} is a property of the surface layer with thickness δ.

References

1. T. Veijola and M. Turowski, "Compact damping models for laterally moving microstructures with gas-rarefaction effects", *IEEE Journal of Microelectromechanical Systems*, Vol. 10, no. 2, pp. 263–273, June 2001.
2. S.A. Campbell, *The science and engineering of microelectronic fabrication*, Oxford University Press, New York, USA, 1996.
3. F.M. White, *Fluid mechanics*, 4th edn., WCB McGraw Hill, New York, USA, 2000.
4. A.H. Nayfeh and M.I. Younis, "A new approach to the modeling and simulation of flexible microstructures under the effect of squeeze-film damping", *Journal of Micromechanics and Microengineering*, Vol. 14, no. 2, pp. 170–181, February 2004.
5. R. Darling and J. Yang, "Compact analytical models for squeeze film damping with arbitrary venting conditions", *Digest of technical papers of the international conference on solid state sensors and actuators, transducers '97*, Chicago, USA, Vol. 2, June 1997, pp. 1113–1116.
6. Y. Cho, A.P. Pisano and R.T. Howe, "Viscous damping model for laterally oscillating microstructures", *IEEE Journal of Microelectromechanical Systems*, Vol. 3, no. 2, pp. 81–87, June 1994.
7. C. Bourgeois, F. Porret and A. Hoogerwerf, "Analytical modeling of squeeze film damping in accelerometers", *Digest of technical papers of the international conference on solid state sensors and actuators, transducers '97*, Vol. 2, Chicago, USA, June 1997, pp. 1117–1120.
8. Z. Xia and W.C. Tang, "Viscous air damping in laterally driven microresonators", in *Proceedings of the 7th IEEE micro electro mechanical systems conference, MEMS '94*, Oiso, Japan, January 1994, pp. 199–204.
9. A. Duwel, M. Weinstein, J. Gorman, J. Borenstein and P. Ward, "Quality factors of MEMS gyros and the role of thermoelastic damping", *Proceedings of the 15th IEEE micro electro mechanical systems conference, MEMS '02*, Las Vegas, USA, January 2002, pp. 214–219.
10. T. Veijola and P. Råback, "Methods for solving gas damping problems in perforated microstructures using a 2D finite-element solver", *Sensors*, Vol. 7, no. 7, pp. 1069–1090, July 2007.
11. W. Ye, W. Hemmert, D. Freeman and J. White, "Air damping in laterally oscillating microresonators: a numerical and experimental study", *IEEE Journal of Microelectromechanical Systems*, Vol. 12, no. 5, pp. 557–566, October 2003.

12. M.I. Younis, "Modeling and simulation of microelectromechanical systems in multi-physics fields", Ph.D. dissertation, Virginia Polytechnic Institute and State University, Blacksburg, Virginia, June 2004.
13. K. Chang, S. Lee and S. Li, "Squeeze film damping effect on a MEMS torsion mirror", *Journal of Micromechanics and Microengineering*, Vol. 12, no. 5, pp. 556–561, September 2002.
14. G. Wong, "Behavioral modeling and simulation of MEMS electrostatic and thermomechanical effects", Master's thesis, Department of Electrical Engineering and Computer Engineering, Carnegie Mellon University, USA, 2004.
15. T. Veijola, K. Ruokonen and I. Tittonen, "Compact model for the squeezed-film damping including the open border effects", *Technical proceedings of the 2001 international conference on modeling and simulation of microsystems, MSM 2001*, South Carolina, U.S.A., March 2001, pp. 76–79.
16. M. Gad-el-Hak, Ed., *The MEMS handbook*, CRC Press, Boca Raton, USA, 2002.
17. J. Brotz, "Damping in CMOS-MEMS resonators", Master's thesis, Department of Electrical Engineering and Computer Engineering, Carnegie Mellon University, USA, 2004.
18. K. Wang, A.-C. Wong and C.T.-C. Nguyen, "VHF free-free beam high-Q micromechanical resonators", *IEEE Journal of Microelectromechanical Systems*, Vol. 9, no. 3, pp. 347–360, September 2000.
19. D.S. Bindel, E. Quévy, T. Koyamat, S. Govindjeet, J.W. Demmel and R.T. Howe, "Anchor loss simulation in resonators", *IEEE Micro electro mechanical systems conference*, Miami, USA, February 2005, pp. 133–136.
20. M. Cross and R. Lifshitz, "Elastic wave transmission at an abrupt junction in a thin plate with application to heat transport and vibrations in mesoscopic systems", *Physical Review B*, Vol. 64, no. 8, August 2001. pp. 085 324:1–085 324:22.
21. J.R. Clark, W.-T. Hsu, M.A. Abdelmoneum and C.T.-C. Nguyen, "High-Q UHF micromechanical radial-contour mode disk resonators", *IEEE Journal of Microelectromechanical Systems*, Vol. 14, no. 6, pp. 1298–1310, December 2005.
22. E.P. Papdakis, "Improvements in a broadband electromechanical bandpass filter in the voice band", *IEEE Transactions on Sonics and Ultrasonics*, Vol. 22, no. 6, pp. 406–414, November 1975.
23. B. Le Foulgoc, T. Bourouina, O. Le Traon, A. Bosseboeuf, F. Marty, C. Breluzeau, J.-P. Grandchamp and S. Masson, "Highly decoupled single-crystal silicon resonators: an approach for the intrinsic quality factor", *Journal of Micromechanics and Microengineering*, Vol. 16, no. 6, pp. S45–S53, June 2006.
24. J. Yan, "Micro/nano-electro-mechanical resonators for signal processing", Ph.D. dissertation, Engineering Department, Cambridge University, Cambridge, UK, July 2007.
25. J.A. Judge, D.M. Photiadis, J.F. Vignola, B.H. Houston and J. Jarzynski, "Attachment loss of micromechanical and nanomechanical resonators in the limits of thick and thin support structures", *Journal of Applied Physics*, Vol. 101, no. 1, pp. 013 521:1–11, January 2007.
26. J. Wang, Z. Ren and C.-C. Nguyen, "1.156-GHz self-aligned vibrating micromechanical disk resonator", *IEEE Transactions on Ultrasonics, Ferroelectrics and Frequency Control*, Vol. 51, no. 12, pp. 1607–1628, December 2004.
27. Y.-H. Park and K. Park, "High-fidelity modeling of MEMS resonators. Part I. anchor loss mechanisms through substrate", *IEEE Journal of Microelectromechanical Systems*, Vol. 13, no. 2, pp. 238–247, April 2004.
28. Z. Hao, A. Erbil and F. Ayazi, "An analytical model for support loss in micromachined beam resonators with in-plane flexural vibrations", *Sensors and Actuators A: Physical*, Vol. 109, no. 1–2, pp. 156–164, December 2003.

29. Z. Hao and F. Ayazi, "Support loss in the radial bulk-mode vibrations of center-supported micromechanical disk resonators", *Sensors and Actuators A: Physical*, Vol. 134, no. 2, pp. 582–593, March 2006.
30. M.U. Demirci and C.T.-C. Nguyen, "Higher-mode free-free beam micromechanical resonators", *Proceedings of the IEEE international frequency control symposium and exposition*, Tampa, USA, May 2003, pp. 810–818.
31. W.-T. Hsu, J.R. Clark and C.T.-C. Nguyen, "Q-optimized lateral free-free beam micromechanical resonators", *Digest of technical papers of the international conference on solid state sensors and actuators, transducers '01*, Munich, Germany, June 2001, pp. 1110–1113.
32. O. Holmgren, K. Kokkonen, V. Kaajakari, A. Oja and J.V. Knuuttila, "Direct optical measurement of the Q values of RF-MEMS resonators", *Proceedings of the IEEE ultrasonics symposium*, Rotterdam, Netherlands, Vol. 4, September 2005, pp. 2112–2115.
33. S.A. Bhave, D. Gao, R. Maboudian and R.T. Howe, "Fully differential SiC Lamé mode resonator and checkerboard filter", in *IEEE Micro Electro Mechanical Systems Conference*, Miami, USA, February 2005, pp. 223–226.
34. H. Kanie and H. Kawashima, "Lamé-mode miniaturized quartz temperature sensors", *IEEE Transactions on Ultrasonics, Ferroelectrics and Frequency Control*, Vol. 47, no. 2, pp. 341–345, March 2000.
35. K.F. Graff, *Wave motion in elastic solids*, Oxford University Press, Oxford, United Kingdom, 1975.
36. H.J. McSkimin and J.P. Andreatch, "Elastic moduli of silicon vs hydrostatic pressure at 25.0 °C and −195.8 °C", *Journal of Applied Physics*, Vol. 35, no. 7, pp. 2161–2165, July 1964.
37. C. Zener, "Internal friction in solids. I. theory of internal friction in reeds", *Physical Review*, Vol. 52, no. 3, pp. 230–235, August 1937.
38. C. Zener, "Internal friction in solids II. general theory of thermoelastic internal friction", *Physical Review*, Vol. 53, no. 1, pp. 90–99, January 1938.
39. C. Zener, W. Otis and R. Nuckolls, "Internal friction in solids III. experimental demonstration of thermoelastic internal friction", *Physical Review*, Vol. 53, no. 1, pp. 100–101, January 1938.
40. R. Lifshitz and M.L. Roukes, "Thermoelastic damping in micro- and nanomechanical systems", *Physical Review B*, Vol. 61, no. 8, pp. 5600–5609, February 2000.
41. S. Pourkamali, A. Hashimura, R. Abdolvand, G.K. Ho, A. Erbil and F. Ayazi, "High-Q single crystal silicon HARPSS capacitive beam resonators with self-aligned sub-100-nm transduction gaps", *IEEE Journal of Microelectromechanical Systems*, Vol. 12, no. 4, pp. 487–496, August 2003.
42. S. Vengallatore, "Analysis of thermoelastic damping in laminated composite micromechanical beam resonators", *Journal of Micromechanics and Microengineering*, Vol. 15, pp. 2398–2404, 2005.
43. B. Houston, D. Photiadis, M. Marcus, J. Bucaro, X. Liu and J. Vignola, "Thermoelastic loss in microscale oscillators", *Applied Physics Letters*, Vol. 80, no. 7, pp. 1300–1302, February 2002.
44. R. Candler, A. Duwel, M. Varghese, S. Chandorkar, M. Hopcroft, W.-T. Park, B. Kim, G. Yama, A. Partridge, M. Lutz and T. Kenny, "Impact of geometry on thermoelastic dissipation in micromechanical resonant beams", *IEEE Journal of Microelectromechanical Systems*, Vol. 15, no. 2, pp. 927–934, August 2006.
45. V. Srikar and S. Senturia, "Thermoelastic damping in fine-grained polysilicon flexural beam resonators", *IEEE Journal of Microelectromechanical Systems*, Vol. 11, no. 5, pp. 499–504, October 2002.
46. K. Yasumura, T. Stowe, E. Chow, T. Pfafman, T. Kenny, B. Stipe and D. Rugar, "Quality factors in micron- and submicron-thick cantilevers", *IEEE Journal of Microelectromechanical Systems*, Vol. 9, no. 1, pp. 117–125, March 2000.

47. T. Ono and M. Esashi, "Effect of ion attachment on mechanical dissipation of a resonator", *Applied Physics Letters*, Vol. 87, no. 4, pp. 044 105:1–3, July 2005.
48. J. Yang, T. Ono and M. Esashi, "Dominated energy dissipation in ultrathin single crystal silicon cantilever surface loss", *Proceedings of the 13th IEEE micro electro mechanical systems conference, MEMS '00*, Miyazaki, Japan, January 2000, pp. 235–240.
49. J. Yang, T. Ono and M. Esashi, "Energy dissipation in submicrometer thick single-crystal silicon cantilevers", *IEEE Journal of Microelectromechanical Systems*, Vol. 11, no. 6, pp. 775–783, December 2002.

7 Noise

Dissipation of energy in physical systems leads to generation of noise. Operation of microelectromechanical systems often involves interactions of multiple physical domains, which results in addition of new energy and dissipation sources [1,2]. Noise analysis is important from various points of view. In sensory applications, the amount of present noise is the ultimate limiting factor for the resolution of a sensor. Similarly, the noise of an amplifier determines the smallest signals which can be amplified with that amplifier before the signal is buried in noise. For an oscillator, the noise in the system determines the spread of the oscillator signal in the vicinity and far from the main signal, which directly affect the usability of the oscillator.

In general, noise is a random signal whose properties cannot be predicted (otherwise it could be cancelled). It is customary to refer to noise sources based on their frequency spectrum. A familiar example is *white noise* whose amplitude is constant all over the spectrum. This is clearly an ideal case as such a signal would have infinite energy. In practice, even the noise sources which are assumed to be white have limited bandwidth, but their bandwidth usually extends to much higher frequencies than typical electrical and mechanical systems can respond to (e.g., in the terahertz range).

Environmental disturbances and ageing of the equipment also act as noise for long term measurements. This noise is usually called *random walk*. The main difference between random walk and other sources of noise is that its effect cannot be reduced by integration. In particular cases, it is possible to reduce the effects of random walk by proper characterisation of the measurement system and further processing of the signal in software.

Due to the random nature of noise, its statistical behaviour is usually studied rather than its momentous behaviour. Therefore, the noise analysis usually deals with statistical averages and variances [3–5]. It is generally assumed that the noise sources, even those of one device, are independent, which is statically specified by this relationship:

$$\lim_{T\to\infty} \int_T \tilde{z}_1 . \tilde{z}_2 \, dt = 0 \tag{7.1}$$

where $\tilde{z}_1$ and $\tilde{z}_2$ are the two independent signals.

The amount of a noise at the output of a system depends on the effective bandwidth of that system as the noise outside this band is filtered. From the time domain point of view, this can be explained by considering that a narrower bandwidth means longer integration times, which causes the signal level to approach to its noiseless limit as the noise signal is averaged. For this reason, the system bandwidth should be mentioned when reporting its noise performance or the amount of noise power should be normalised to frequency.

For a linear time-invariant system, the output signal is shaped by the system transfer function according to the following relationship:

$$S_o(\omega) = S_i(\omega)|H(\omega)|^2 \tag{7.2}$$

where $S_i(\omega)$ and $S_o(\omega)$ are the power spectral densities (PSD)[1] of the input and output signals, respectively, and $H(\omega)$ is the transfer function of the system.

7.1 Noise Sources

7.1.1 Brownian Noise

A familiar type of noise in micromechanical and electrical systems is *Brownian noise* which is also known as *thermal noise*. The source of this noise is random motion and vibration and impingement of particles (e.g., ambient gas molecules, photons, and phonons). Brownian noise can be considered as white noise for normal operating frequencies of typical mechanical and electrical systems [6–8]. An example of the time and frequency domain representations of an ideal white noise is shown in Fig. 7.1.

The power spectral density (PSD) of the Brownian noise force on a mechanical system is given by:

$$\tilde{f}_B^2 = 4K_{\mathrm{B}}T\zeta \ \ \mathrm{N}^2/\mathrm{Hz} \tag{7.3}$$

where K_{B} is Boltzmann's constant ($1.3806503 \times 10^{-23}$ J K^{-1}), T is the temperature in kelvin, and ζ is the linear damping coefficient in the system[2].

A similar result is obtained for the random movements of electrons in a conductor [9]:

$$\begin{aligned} \tilde{v}_B^2 &= 4K_{\mathrm{B}}TR \ \ \mathrm{V}^2/\mathrm{Hz} \\ \tilde{i}_B^2 &= \frac{4K_{\mathrm{B}}T}{R} \ \ \mathrm{A}^2/\mathrm{Hz} \end{aligned} \tag{7.4}$$

where R is the resistance of the conductor.

[1] Power spectral density describes how the signal power (i.e., its weighted variance) is distributed in frequency domain. The Wiener–Khinchin theorem states that the PSD of a signal is the Fourier transform of the autocorrelation of the signal in time domain:

$$S(\omega) = \frac{1}{2\pi}\int_{-\infty}^{\infty}\left(\int_{-\infty}^{\infty} x(t)x^*(t-\tau)\,dt\right)e^{j\omega\tau}d\tau$$

where * denotes the complex conjugate value of the signal.

[2] Refer to Appendix A for a derivation of the PSD of Brownian noise for mechanical systems.

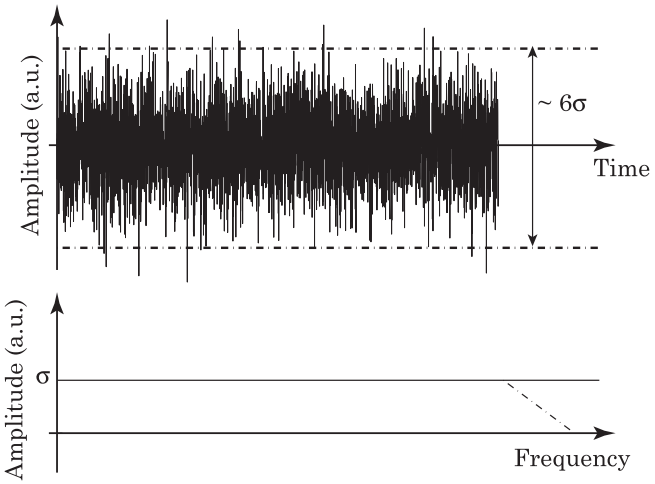

Figure 7.1 Time domain representation (top) and PSD (bottom) of a white noise signal. The width of the stripe which embodies the noise signal amplitude in time domain is about 6σ and can be used to approximate the PSD of the signal.

The effects of Brownian noise on the performance of micromachined structures has been researched extensively [10,11]. Impingement of gas molecules on the surfaces of structures is the main source of Brownian noise force for micromachined devices. A relatively simple method to reduce the Brownian noise force on micromechanical systems is operating the devices at lower pressures. By lowering the operating pressure around the device, it is possible to reduce the effects of gas molecule impingements until other damping mechanisms such as thermoelastic damping or anchor loss become the dominant energy dissipation mechanisms.

Brownian noise is directly proportional to temperature. Therefore, it is possible to reduce this noise by operating the devices (electronic or mechanical) at lower temperatures. However, this requires special arrangements around the system and the devices, which significantly add to the complexity and cost of the system and is often used only as the last resort (e.g., in systems for detection of weak extraterrestrial signals).

7.1.2 Shot Noise

Shot noise is associated with DC currents flowing through a potential barrier (e.g. a *pn* junction). Unlike Brownian noise, the amount of shot noise is independent of temperature as it is produced by random arrival of charge carriers across the potential barrier [9,12]. The amount of this noise is proportional to the number of electrons that pass through the wire at a given time, or in other words, the current. It can be shown that the power spectral

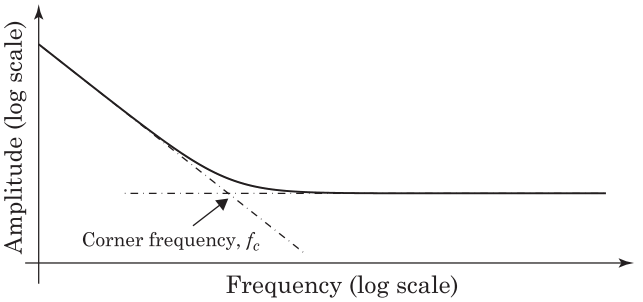

Figure 7.2 A typical PSD for the noise at the output of a system in presence of both Flicker and white noise sources.

density (PSD) of this noise is given by:

$$\tilde{i}_S^2 = 2q_e I_{\mathrm{DC}} \ \mathrm{A}^2/\mathrm{Hz} \tag{7.5}$$

where I_{DC} is the mean value of the current and q_e is the magnitude of electronic charge (1.6×10^{-19} C). Shot noise can be considered as a white noise for most practical applications with operating frequencies of up to several gigahertz.

7.1.3 Flicker Noise

Flicker noise is found in all active electronic components as well as some of the passive devices, and like shot noise, is associated with a DC current flow [9]. A characteristic property of this noise is that its magnitude decreases with frequency, and therefore, is sometimes referred to as $1/f$ *noise*. The PSD of flicker noise is often modelled by:

$$\tilde{i}_F^2 = \mathcal{K}_F \frac{I_{DC}^{\alpha}}{f^{\beta}} \ \mathrm{A}^2/\mathrm{Hz} \tag{7.6}$$

where $\mathcal{K}_F$, α, and β are constants particular to each device and its fabrication technology and I_{DC} is the DC current through the device.

Flicker noise generally dominates at low frequencies for a properly designed system while the white noise sources become dominant at higher frequencies. *Flicker noise corner frequency*, f_c is the frequency where the magnitudes of the white and flicker noises of a device are equal. The PSD of a system output is typically similar to the illustration in Fig. 7.2.

7.1.4 Other Noise Sources

There are other noise sources in addition to the above sources of noise (e.g., *burst* and *avalanche* noises) [9,13,14]. However, these noise sources are usually

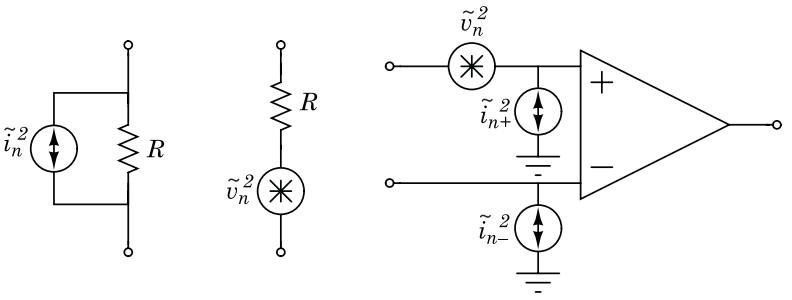

Figure 7.3 Electronic noise source models for resistors and amplifiers.

less important than thermal or flicker noises. The effects of these noises are often studied using empirical models which are beyond the scope of this book.

7.2 System Noise Representation

The noise sources inside electronic systems are generally referred to their inputs for easier comparison of the noise performance between similar devices. Once the system transfer function is known, one can easily find the noise at the output of the system using the equivalent input noise sources. To be able to model the noise behaviour for different configurations, both current and voltage sources are added to the inputs of systems. This form of representation of the noise sources is permissible as long as the correlation between the input voltage and current sources, which may no longer be independent, is taken into account.

Fig. 7.3 illustrates the circuit models of amplifiers and resistors for noise calculations in circuits.

7.3 Interference

Another source of unwanted disturbances, especially with the weak signals from micromachined devices, is *interference*. Unlike the noise sources that we discussed so far, interference is usually a *dependent* variable of an input signal or a strong signal source in proximity of the measurement set-up (e.g., electromagnetic interference from monitors). It is therefore possible to minimise the effects of interference with proper design of the device and its interfacing setup.

A very common source of interference for micromachined devices is the signal feedthrough from the input ports of the device which appear as an offset signal at its output. Depending on the device, the amount of this interfering signal can be large enough to make taking precise measurements of the signal from the device difficult or even impossible. The feedthrough signal is usually capacitively coupled to the output, both through the substrate or through the environment

surrounding the device (e.g., air or vacuum). To reduce the coupling through the environment, the input and output ports of the device should be placed as far from each other as possible while their active surfaces are minimised. An effective technique to reduce feedthrough is to employ differential signals to drive a device and also use differential ports to pick up the sense signal.

The techniques for reducing the feedthrough signal through the substrate mainly depend on the type of the substrate that is used for fabrication of the device. For example, using high-resistivity silicon or glass as the substrate greatly increases the resistance between the capacitors, and therefore, reduces the feedthrough signal amplitude at the output. One should also minimise the feedthrough capacitances by designing small bonding pads and short and narrow signal paths. Using SOI wafers can also help as the relatively thick oxide layer between the substrate and the pads could result in smaller capacitances. If possible, one could also bias a semiconducting substrate with a large DC voltage of proper polarity so that a depletion layer is formed under the pads to reduce the pad capacitance. At high frequencies, the on-chip signal paths should be treated as transmission lines and need to be properly designed to avoid cross coupling of the signals on two different paths.

Another source of interference is the coupling between cables and bond wires that are used for electrical connections to the device. Shielded cables (e.g. coaxial cables) should be used for sending the signals to and from the device. However, it should be noted that these cables often add substantial parasitic capacitance to the device ports (typically about 1 pF/cm). The coupling between the bond wires inside the package does not pose a problem for low frequency devices but their length should be minimised for devices operating at high frequencies and the wires carrying the input and output signals should be placed as far from each other as possible.

Signals from strong sources in the neighbourhood of the device can also appear as disturbance, especially if their frequencies, or their harmonics, are close to the operating frequency of the device. Besides shutting down these sources, the only way to reduce the effect of these signals on the performance of the system is through electromagnetic shielding of the device and electronics.

One may also be able modify the device design and use detection mechanisms which are less susceptible to electromagnetic interference. Optical detection techniques, for example, are very sensitive and offer great robustness against electromagnetic interference. However, the trade-off in this case is the added complexity of the system and integration challenges.

7.4 Quantifying Oscillator Noise

7.4.1 Phase Noise

Micromachined resonators are often used in conjunction with active electronics to form an oscillator. If the resonator is used for timing applications,

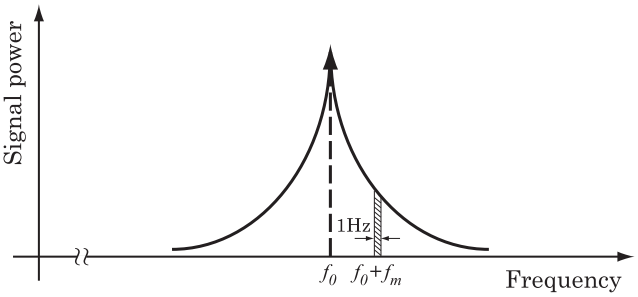

Figure 7.4 Phase noise of the signal from an oscillator.

it provides the required reference signal which is then used in other parts of the system, such as the clock signal for digital circuits. In case of resonant sensors, the oscillator provides a frequency modulated output whose variations correspond to the measurand.

The signal from an ideal oscillator is given by an expression like $v_o(t) = A_0 \cos(2\pi f_0 t)$ and looks like an impulse in the frequency domain. However, both the amplitude and phase of a practical oscillator change with time; i.e., $v_o(t) = (A_0 + a(t)) \cos(2\pi f_0 t + \phi(t))$. Therefore, the oscillator signal in frequency domain has skirts around its centre frequency as shown in Fig. 7.4. In most cases, frequency/phase noise of the oscillator signal is usually the important factor as the amplitude noise can be essentially removed with an amplitude limiting block.

The prevailing method of characterising the noise in oscillators is by specifying their *phase noise*. Phase noise at offset frequency f_m from carrier frequency f_0 is defined as [15,16]:

$$\mathcal{L}(f_m) = \frac{\text{power density in one phase noise modulation sideband, per Hz}}{\text{total signal power}}.$$

Phase noise performance is often represented as decibels below carrier per bandwidth (dBc/Hz):

$$\mathcal{L}(f_m) = 10 \cdot \log \left(\frac{P(f_0 + f_m, 1 \text{ Hz})}{P_{\text{Carrier}}} \right) \tag{7.7}$$

where $P(f_0 + f_m, 1 \text{ Hz})$ represents the single sideband power at a frequency offset of f_m from the carrier with a measurement bandwidth of 1 Hz. Typically phase noise is specified at frequencies close to and far from the carrier signal. For example, the GSM standard requires the phase noise of the local oscillator to be less than -75 dBc/Hz and -121 dBc/Hz at 200 kHz and 6 MHz offset frequencies from the carrier signal at 900 MHz, respectively.

This performance deviation from the ideal scenario is of high significance when choosing an oscillator. Let us assume that the oscillator output is the

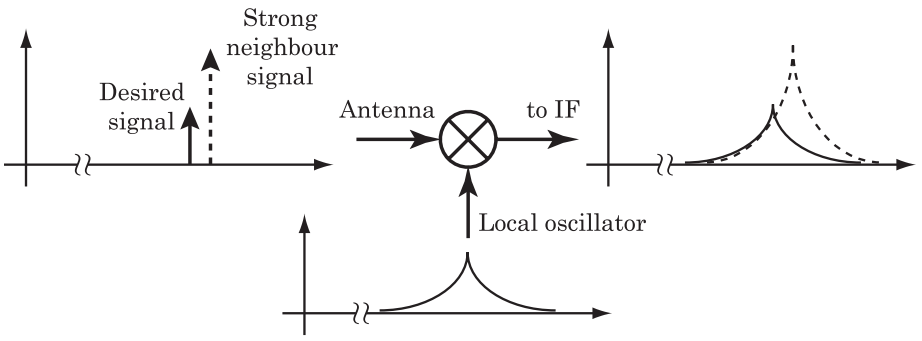

Figure 7.5 Effect of oscillator phase noise on the performance of a superheterodyne receiver.

reference frequency signal for communications to down-convert a high frequency signal using a mixer. As illustrated in Fig. 7.5, using an oscillator with a poor phase noise performance results in loss of data as the signals from the neighbouring channels are mixed with each other. If the oscillator is designed as part of a sensory system, poor phase noise translates into low resolution when reading the signal from the sensor.

Analysis of the phase noise in linear oscillators has been thoroughly investigated due to its importance in communications systems [5,17–23]. The analysis of nonlinearities, however, is usually limited to ring oscillators or to the nonlinear behaviour of the devices in a linear oscillator loop (e.g., the drain current of the transistor in Pierce oscillators) [24–28]. Linear oscillators are usually analysed through linearising the nonlinear elements about their operating point and using transfer functions of the components in the loop. The analysis of linear oscillators is usually performed in the frequency domain. For a simple linear oscillator such as the one shown in Fig. 7.6, it can be shown that:

$$\mathcal{L}(f_m) = 10 \cdot \log \left(\underbrace{\frac{4K_{\mathrm{B}}TR_{\mathrm{gain}}}{\bar{v}_{\mathrm{out}}^2}\left[1 + \left(\frac{f_0}{2Q_l f_m}\right)^2\right]}_{\text{Amplifier noise}} + \underbrace{\frac{4K_{\mathrm{B}}TR_m}{\bar{v}_{\mathrm{out}}^2}\left(\frac{f_0}{2Q_l f_m}\right)^2}_{\text{Resonator noise}} \right) \tag{7.8}$$

where R_m is the motional resistance of the resonator and Q_l is the loaded Q of the resonator [29]. The above equation holds for an amplifier whose bandwidth is much larger than the resonant frequency of the resonator and its noise contribution is much smaller than the noise produced by the gain resistor R_{gain}. The condition for stable oscillations in the ideal case is $R_{\mathrm{gain}} = R_m$, which places the loop poles on the $j\omega$ axis. This simple formula illustrates the

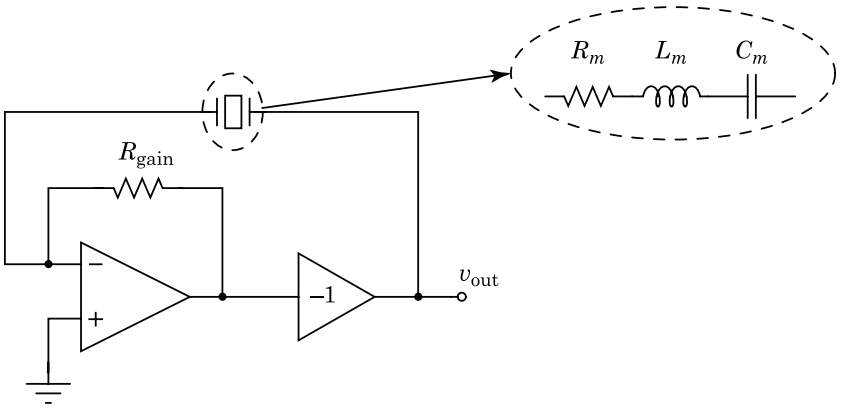

Figure 7.6 Simple oscillator operating at the series resonant frequency of the resonator.

importance of designing resonators with high Q and low motional resistance in order to obtain better phase noise performance.

7.4.2 Jitter

A concept closely related to phase noise is *jitter*. Jitter is the time domain manifestation of oscillator phase noise and is usually used for quantifying the signal from an oscillator with digital output. The signal from an ideal oscillator has a constant period, and therefore, a fixed zero crossing point when subsequent cycles of the waveform are superimposed on top of each other. The period of the signal from an oscillator with jitter, on the other hand, varies around a mean value and the zero crossing points of different cycles are different (see Fig. 7.7). Jitter in one period is the time difference between a measured cycle period and the ideal cycle period: $J_{\text{per}} = T - T_0$, where T and T_0 are the measured and average periods of the waveform, respectively. The jitter for the signal is the expected value of period jitter (i.e., its rms value): $J_{\text{RMS}} = \sqrt{\langle J_{\text{per}}^2 \rangle}$.

7.4.3 Allan Variance

In some cases, it may not be possible to measure the phase noise of an oscillator (e.g., due to high noise floor). The oscillator performance can be quantified by taking long term time-domain frequency stability measurements. Once the dataset of frequency measurements is obtained, the scatter of output frequency values has to be determined as a measure of frequency noise. One could use classical statistics such as standard deviation (or variance, the square of the standard deviation) to quantify the dispersion in signal frequency. However, variance is well defined for stationary data only; i.e., signals whose statistical parameters do not change over time. For stationary data, the mean

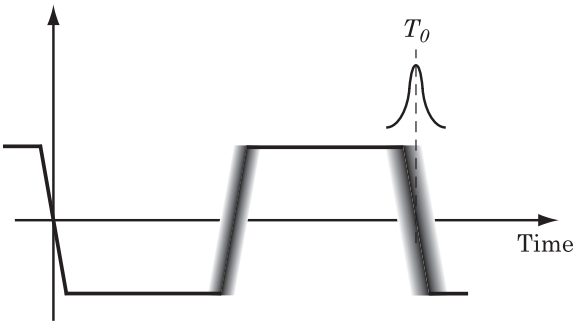

Figure 7.7 Illustration of variation of the period of a signal due to jitter.

and variance will converge to particular values as the number of measurements increases. This is equivalent to assuming that the noise has a white spectral density. With non-stationary data, the mean and variance never converge to any particular values. Oscillator data is usually non-stationary since it contains time-dependent noise contributed by low frequency phenomena such as environmental disturbances and ageing of the components.

For these reasons, non-classical statistics is used to estimate stability in time domain. The statistics which are often employed to analyse the frequency stability of the oscillators is called *Allan variance*, also known as two-sample variance [15,30–33]. Allan variance is defined as:

$$\sigma_y^2(\tau) = \frac{1}{2(N-1)} \sum_{k=1}^{N-1} (\bar{y}_{k+1} - \bar{y}_k)^2 \tag{7.9}$$

where N is the number of data points in the dataset. $\bar{y}_k$ is the fractional frequency deviation averaged over period τ: $\bar{y} = \frac{1}{\tau f_{\text{nom}}} \int_\tau (f - f_{\text{nom}})\, dt$ for f_{nom} being the nominal frequency of the oscillator [5,33,34]. Allan deviation is the square root of Allan variance.

Fig. 7.8 shows the calculated Allan variance for a sample dataset. It can be seen that the stability improves as the measurement (integration) period gets longer. At some point, the oscillator reaches the flicker noise floor limit and increasing the integration period no longer improves the signal quality. Environmental disturbances contribute to random walk and the frequency stability deteriorates for very long integration periods.

It is possible to extract information about the type of noise from the Allan variance graphs. The power spectral density of frequency fluctuations is related to Allan variance data according to the following relationship:

$$\sigma_y^2(\tau) = \int_0^\infty 2 \frac{\sin^4(\pi\tau f)}{(\pi\tau f)^2} S_y(f)\, df. \tag{7.10}$$

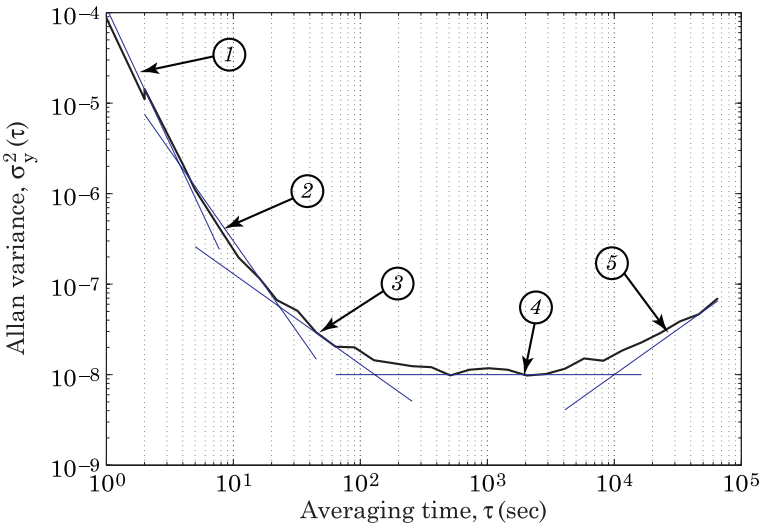

Figure 7.8 Sample Allan variance plot of an oscillator. The asymptotic lines illustrate the different frequency stability regions as presented in Table 7.1.

Table 7.1 The Relationship between Time and Frequency Domain Data. τ_0 is the initial averaging time and $\tau = n\tau_0$, where n is an integer.

Region	Noise source	PSD, $S_y(f)$	Allan variance, $\sigma_y^2(\tau)$
1	White noise PM	$h_2 f^2$	$\left(\frac{1}{2\pi}\right)^2 3 f_h \tau_0 h_2 \tau^{-2}$
2	Flicker noise PM	$h_1 f$	$\left(\frac{1}{2\pi}\right)^2 (1.038 + 3h_1 \ln(2\pi f_h \tau))\tau^{-2}$
3	White noise FM	h_0	$\frac{1}{2} h_0 \tau^{-1}$
4	Flicker noise FM	$h_{-1} f^{-1}$	$2\ln(2) h_{-1} \tau^0$
5	Random walk FM	$h_{-2} f^{-2}$	$\frac{1}{6}(2\pi)^2 h_{-2} \tau$

For white and flicker phase modulation (PM) noises, the upper limit of the integral has to be set to the bandwidth of the measurement system, f_h, to ensure the convergence of the integral. Table 7.1 summarises the relationships between the power spectral densities of common types of noise and the Allan variance of the dataset [34–37].

In special cases, the PSD of phase or frequency fluctuations of the oscillator can be extracted from Allan variance data (see Table 7.1). Knowing the the PSD of the frequency fluctuations, $S_y(f)$, the PSD of phase fluctuations, $S_\phi(f)$, can be calculated from $S_\phi(f) = (f_0^2/f^2)S_y(f)$, where f_0 is the carrier frequency and f is the Fourier frequency. It must be noted, however, that the transformation between Allan variance and frequency domain parameters is generally not a

one-to-one transformation. Therefore, from mathematical point of view, the Allan variance information cannot be mapped into a single set of frequency domain (i.e., phase noise) parameters [38,39].

References

1. T. Kenny, "Nanometer-scale force sensing with MEMS devices", *IEEE Sensors Journal*, Vol. 1, no. 2, pp. 148–157, August 2001.
2. J.R. Vig and Y. Kim, "Noise in microelectromechanical system resonators", *IEEE Transactions on Ultrasonics, Ferroelectrics and Frequency Control*, Vol. 46, no. 6, pp. 1558–1565, November 1999.
3. K. Huang, *Introduction to statistical physics*, Taylor and Francis, London, United Kingdom, 2001.
4. H.L. Pecseli, *Fluctuations in physical systems*, Cambridge University Press, Cambridge, United Kingdom, 2000.
5. W.P. Robins, *Phase noise in signal sources : theory and applications*, Peter Pregrinus, London, United Kingdom, 1982.
6. T.B. Gabrielson, "Mechanical-thermal noise in micromachined acoustic and vibration sensors", *IEEE Transactions on Electron Devices*, Vol. 40, no. 5, pp. 903–909, May 1993.
7. A.N. Cleland and M.L. Roukes, "Noise processes in nanomechanical resonators", *Journal of Applied Physics*, Vol. 92, no. 5, pp. 2758–2769, September 2002.
8. T.H. Lee, *The design of CMOS radio-frequency integrated circuits*, 2nd edn., Cambridge University Press, New York, USA, 2004.
9. P.R. Gray, P.J. Hurst, S.H. Lewis and R.G. Meyer, *Analysis and design of analog integrated circuits*, 4th edn., John Wiley and Sons, New York, USA, 2001.
10. V. Annovazzi-Lodi and S. Merlo, "Mechanical-thermal noise in micromachined gyros", *Microelectronics Journal*, Vol. 30, no. 12, pp. 1227–1230, December 1999.
11. G.M. Rebeiz, "Phase-noise analysis of MEMS-based circuits and phase shifters", *IEEE Transactions on Microwave Theory and Techniques*, Vol. 50, no. 5, pp. 1316–1323, May 2002.
12. M.J. Buckingham, *Noise in electronic devices and systems*, Ellis Harwood, Chichester, United Kingdom, 1983.
13. G. Vasilescu, *Electronic noise and interfering signals: principles and applications*, Springer-Verlag Berlin and Heidelberg GmbH & C., Berlin, Germany, 2004.
14. A. van der Ziel, *Noise in solid state devices and circuits*, Wiley-Interscience, New York, USA, 1986.
15. IEEE Standards Coordinating Committee 27 on Time and Frequency, IEEE Std 1139-1999; IEEE standard definitions of physical quantities for fundamental frequency and time metrology - random instabilities, The Institute of Electrical and Electronics Engineers, 345 East 47th Street, New York, NY 10017, USA, Tech. Rep., 1999.
16. IEEE Standards Board, IEEE Std 1139-1988; IEEE standard definitions of physical quantities for fundamental frequency and time metrology, The Institute of Electrical and Electronics Engineers, Inc, 345 East 47th Street, New York, NY 10017, USA, Tech. Rep., 1988.
17. T.H. Lee and A. Hajimiri, "Oscillator phase noise: A tutorial", *IEEE Journal of Solid-State Circuits*, Vol. 35, no. 3, pp. 326–336, March 2000.
18. B. Razavi, "A study of phase noise in CMOS oscillators", *IEEE Journal of Solid-State Circuits*, Vol. 31, no. 3, pp. 331–343, March 1996.
19. K.A. Kouznetsov and R.G. Meyer, "Phase noise in LC oscillators", *IEEE Journal of Solid-State Circuits*, Vol. 35, no. 8, pp. 1244–1248, August 2000.

20. P. Réfrégier, *Noise theory and application to physics : from fluctuations to information*, Springer-Verlag, New York, USA, 2003.
21. M. Planat, Ed., *Noise, oscillators, and algebraic randomness: from noise in communication systems to number theory*, Springer-Verlag, Berlin, Germany, 2000.
22. A. Demir and A.L. Sangiovanni-Vincentelli, "Simulation and modeling of phase noise in open-loop oscillators", *Proceedings of the IEEE custom integrated circuits conference*, San Diego, USA, May 1996.
23. A. Demir, E.W.Y. Liu and A.L. Sangiovanni-Vincentelli, "Time-domain non-Monte Carlo noise simulation for nonlinear dynamic circuits with arbitrary excitations", *IEEE Transactions on Computer-Aided Design of Integrated Circuits and Systems*, Vol. 15, no. 5, pp. 493–505, May 1996.
24. L. Dai and R. Harjani, "Analysis and design of low-phase-noise ring oscillators", in *Proceedings of the 2000 International Symposium on Low Power Electronics and Design, ISLPED '00*, Rapallo, Italy, July 2000, pp. 289–294.
25. G.V. Klimovitch, A nonlinear theory of near-carrier phase noise in free-running oscillators, *Proceedings of the 2000 third IEEE international caracas conference on devices, circuits and systems*, Cancun, Mexico, March 2000, pp. T80/1–T80/6.
26. H.-G. Ryu, Y.S. Li and J.-S. Park, "Nonlinear analysis of the phase noise in the OFDM communication system", *IEEE Transactions on Consumer Electronics*, Vol. 50, no. 1, pp. 54–63, February 2004.
27. M. Regis, O. Llopis and J. Graffeuil, "Nonlinear modeling and design of bipolar transistors ultra-low phase-noise dielectric-resonator oscillators", *IEEE Transactions on Microwave Theory and Techniques*, Vol. 46, no. 10, pp. 1589–1593, October 1998. part 2.
28. A. Abidi, "Phase noise and jitter in CMOS ring oscillators", *IEEE Journal of Solid-State Circuits*, Vol. 41, no. 8, pp. 1803–1816, August 2006.
29. A. Seshia, "A linear model for phase noise in silicon micro-electro-mechanical resonator oscillators", *Proceedings of the 6th conference on MEMS for millimeter-wave communications*, Lausanne, Switzerland, June 2005.
30. F.L. Walls and D.W. Allan, "Measurements of frequency stability", *Proceedings of the IEEE*, Vol. 74, no. 1, pp. 162–168, January 1986.
31. F. Vernotte, J. Groslambert and J.J. Gagnepain, "A new method of measurement of the different types of noise altering the output signal of oscillators", *IEEE Transactions on Instrumentation and Measurement*, Vol. 42, no. 6, pp. 968–975, December 1993.
32. F. Vernotte, E. Lantz, J. Groslambert and J.J. Gagnepain, "Oscillator noise analysis: multivariance measurement", *IEEE Transactions on Instrumentation and Measurement*, Vol. 42, no. 2, pp. 342–350, April 1993.
33. J.G. Webster, Ed., *The measurement, instrumentation and sensors handbook*, ser. Electrical engineering handbook, Vol. 14, CRC Press, Boca Raton, USA, 1999.
34. J. Rutman, "Characterization of phase and frequency instabilities in precision frequency sources: Fifteen years of progress", *Proceedings of the IEEE*, Vol. 66, no. 9, pp. 1048–1075, September 1978.
35. D.W. Allan, "Time and frequency (time-domain) characterization, estimation, and prediction of precision clocks and oscillators", *IEEE Transactions on Ultrasonics, Ferroelectrics and Frequency Control*, Vol. 34, no. 6, pp. 647–654, November 1987.
36. J. Rutman and F.L. Walls, "Characterization of frequency stability in precision frequency sources", *Proceedings of the IEEE*, Vol. 79, no. 6, pp. 952–960, June 1991.
37. W.F. Egan, "An efficient algorithm to compute Allan variance from spectral density", *IEEE Transactions on Instrumentation and Measurement*, Vol. 37, no. 2, pp. 240–244, June 1988.
38. C.A. Greenhall, "Does Allan variance determine the spectrum?" *Proceedings of the 1997 IEEE international frequency control symposium*, Orlando, USA, May 1997, pp. 358–365.
39. C.A. Greenhall, "Spectral ambiguity of Allan variance", *IEEE Transactions on Instrumentation and Measurement*, Vol. 47, no. 3, pp. 623–627, June 1998.

8 Interfacing

Interfacing is often needed to measure or monitor the resonant frequency of a device during its operation. In sensory applications, it is the resonant frequency of the resonator which is directly or indirectly modulated by the measurand. On the other hand, in timing and actuation applications of resonators, it is desired to take advantage of the sharp frequency response of the resonators by keeping the operating frequency of the device close to its resonant frequency. The resonator may be employed in an open or closed loop configuration. In an open loop system, a signal generated externally is applied to the resonator while the signal from the resonator is monitored on a time or frequency based measurement system. A change in the resonant frequency can be detected from either amplitude or phase information. We will discuss a few of such techniques for measurements on resonant devices.

In a closed loop system, however, the resonator output signal is processed and fed back to its input, realising an oscillator and obviating the need for external sources. The operating frequency of such a closed loop system is automatically set by the resonator response and is often the same as its resonant frequency or its harmonics. Such a system can be employed for autonomous sensory or a frequency/timing reference applications. Some of the oscillator topologies suitable for micro-resonators are also introduced in this chapter.

8.1 Frequency Shift Measurement Techniques

8.1.1 Counting

The simplest method of measuring the period or frequency of a signal is to use an external clock as a reference. To measure the frequency of the signal, the number of signal pulses are counted in a predefined time window from a reference signal. The longer the period of the reference signal is, the larger will be the number of pulses from the sense signal in the time window, and therefore, the more accurate are the readings.

Measurement of the signal period can be done similarly by counting the number of clock signal pulses inside a time window set by the signal. These techniques are illustrated in Fig. 8.1. Both of these techniques, however, are slow. For example, it takes 10 s to measure a 0.1 Hz shift in frequency of a signal. Vernier measurement techniques can be employed to enhance the precision and the bandwidth of these techniques, but usually add considerably to the complexity of the system [1,2].

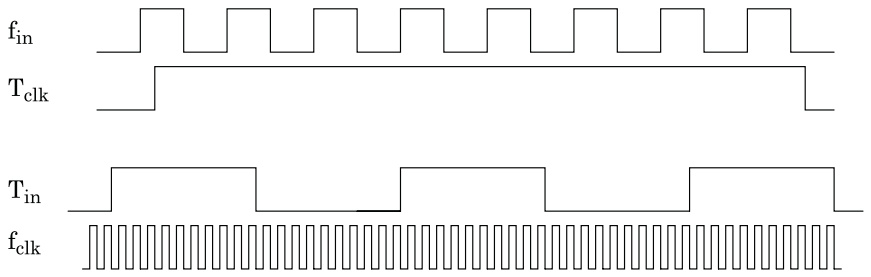

Figure 8.1 Measuring the frequency (top) and the period (bottom) of a waveform.

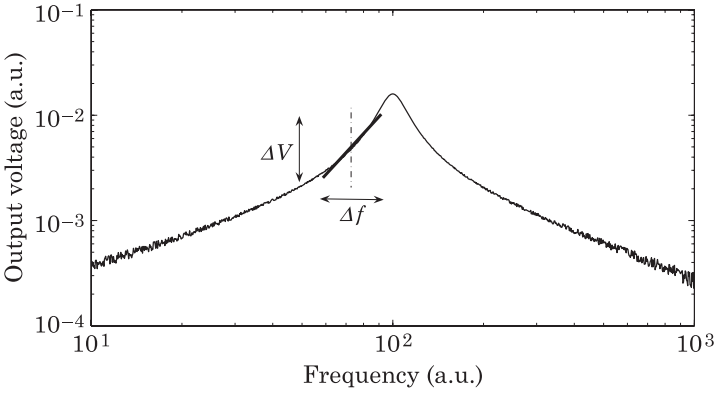

Figure 8.2 FM to AM conversion.

8.1.2 FM to AM Conversion

The variations in the frequency of a signal can be converted to changes in its amplitude by taking advantage of the high Q of the oscillating element that causes a dramatic change in signal amplitude in the vicinity of the resonant frequency. For example, if the sensor is driven at a frequency slightly less that the resonant frequency of the structure, a small increase in the resonant frequency causes a significant drop in the output signal amplitude. Knowing the slope of the frequency response curve, it is possible to estimate the amount of change in the resonant frequency (Fig. 8.2). This technique essentially converts a frequency-modulated (FM) signal to an amplitude-modulated (AM) signal and has been widely used in FM receivers.

Employing this technique for micromachined devices, however, is not a straightforward process. The drive signal must be generated by a stable signal source and its frequency must be carefully set for this technique to work properly. On the other hand, the resonant frequency of many micromachined devices is a function of ambient pressure and temperature. Therefore, manual intervention and tweaking of the equipment are required in most cases. Moreover, the range of the frequencies which can be detected with this method

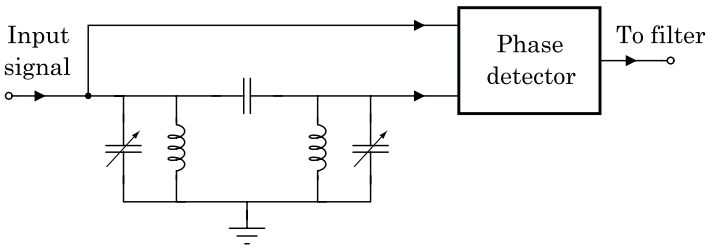

Figure 8.3 Setup for passive frequency-sensitive phase-shift.

strongly depends on the quality factor of the resonator which is not an easy parameter to control. Further, a certain amount of time is needed (depending on Q of the structure) for the signal amplitude to build up to its steady state level after a shift in the resonant frequency of the structure, and thereby, this method may not provide enough bandwidth for some applications.

8.1.3 FM to PM Conversion

By adding a frequency dependent phase-shifter in the signal path, the information embedded in frequency of a signal are converted to a phase difference between the original signal and its delayed version. This can potentially improve the accuracy of measurements by converting small frequency shifts to relatively large phase differences. If the amplitude of the signal is controlled, the shifts in the resonant frequency of the structure are instantaneously converted to phase differences, and hence, the sensitivity and bandwidth of measurements are both enhanced by using this technique.

8.1.3.1 Passive delay networks

Different techniques can be employed to produce a frequency-sensitive phase shift. An LC tank is an example of an element that can be used for this purpose. The resonant frequency of the tank should be tuned to the signal frequency. Deviations in the frequency of the signal cause the phase difference between the input and output of the tank to vary, which can then be measured with a phase detector as shown in Fig. 8.3. The dynamic range and sensitivity of the measurements depend on the quality factor of the elements used in the construction of the tank. For example, it is possible to resolve a 0.01 Hz frequency shift in a 50 kHz signal with a 75 Hz bandwidth when the setup in Fig. 8.3 is used in a closed loop [3].

An alternative to a bulky LC tank is a ceramic resonator. However, the frequency of the input signal must be within a certain range which is specific to the employed ceramic resonator. Therefore, an up or down conversion of the signal in frequency domain may be required.

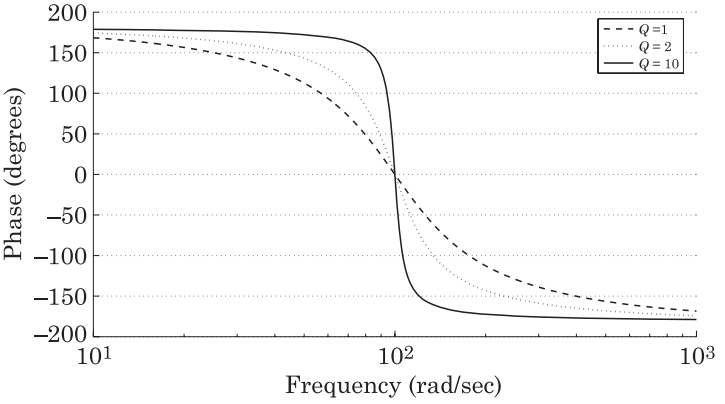

Figure 8.4 Phase response of a 2nd order allpass filter for different values of Q_p.

8.1.3.2 Active delay networks

As discussed in the preceding section, it is often required to tune the phase shift network parameters with the resonator signal. Instead of using passive phase shift networks, one can employ an active alternative which can be an allpass (or delay) filter [4]. Allpass filters do not modify the amplitude of the signal but cause a predetermined phase shift at the designed frequency by properly choosing the locations of poles and zeros of the transfer function of the filter. More specifically, the zeros and poles have the same frequency (to produce a flat amplitude response) but the zeros are placed in the right-half portion of the s-plane to increase the phase difference between high and low frequencies. If allpass networks of orders larger than one are used, it is possible to independently control the centre frequency and phase performance (i.e., Q) of the circuit. An allpass network of order 2 has the following transfer function of the form:

$$T_{ap}(s) = \frac{s^2 - \frac{\omega_p}{Q_p}s + \omega_p^2}{s^2 + \frac{\omega_p}{Q_p}s + \omega_p^2}. \tag{8.1}$$

The effect of the quality factor of the poles and zeros (i.e., Q_p) on the transfer function is illustrated in Fig. 8.4.

It is possible to increase the quality factor of the zeros and poles for enhanced sensitivity. However, the improvement in sensitivity of the electronics comes at the expense of reduced dynamic range, since the full scale phase shift (360° for a 2$^{\text{nd}}$ order allpass filter) happens over a smaller frequency range. If this is undesired, it is possible to cascade multiple allpass stages to obtain a larger phase shift at a given frequency or to use higher order allpass filters. This method does not sacrifice the dynamic range for resolution but special care must be taken when interpreting the output signal as the output might undergo

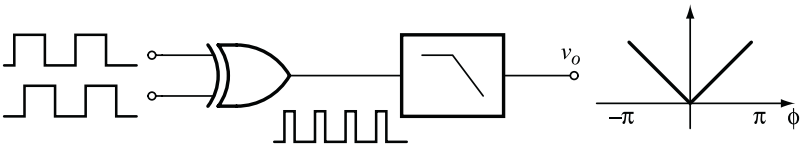

Figure 8.5 A digital phase detector.

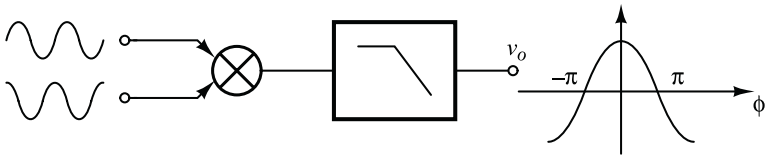

Figure 8.6 An analogue phase detector.

several 360° phase shifts which are not detectable unless the changes of the output signal are tracked.

8.1.3.3 Phase difference detection

The frequency dependent phase difference can be detected using various techniques [5,6]. If the signals are converted to binary format, an Exclusive-OR (XOR) gate can be used to for this purpose (Fig. 8.5). The DC component of the output voltage of the XOR gate is linearly proportional to the phase difference between its two inputs (for $0 \leq \phi < \pi$).

An analogue mixer can also be used for phase difference detection (see Fig. 8.6). If the inputs to the mixer are $A_1 \sin \omega t$ and $A_2 \sin(\omega t + \phi)$, the output is given by:

$$v_{\text{out}} = A_1 A_2 \sin \omega t \sin(\omega t + \phi) = \frac{A_1 A_2}{2}(\cos \phi - \cos(2\omega t + \phi)). \qquad (8.2)$$

The high frequency component can be easily filtered and the output of the filter is a nonlinear function of the phase difference between the two signals.

8.1.3.4 Frequency shift measurement circuitry

In most cases, the amount of frequency shift is small compared to the resonant frequency of the device, some times as small as a few ppm. Therefore, high-Q allpass filters are required if the phase difference detection is to be done at the signal frequency. However, high-Q filters are generally prone to instability and the tuning of high-Q filters is not easy due to their narrow bandwidth. A mixer can be used to bring down the frequency of the resonator signal before

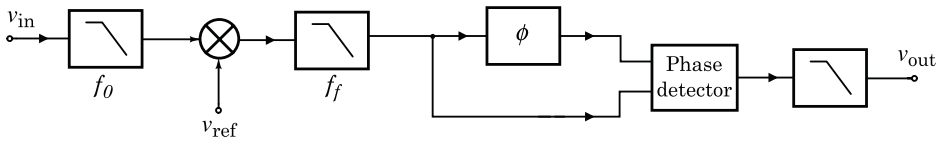

Figure 8.7 Frequency shift measurement circuit.

feeding it to the delay circuitry. This reduction in signal frequency, which is essentially the same as removing the frequency offset that does not convey information, allows for performing sensitive phase difference measurements with relatively low-Q allpass filters. Additionally, if the difference between the mixing signal and the sensor signal is kept constant, a stable and tuned circuit can be designed to produce the delay at the difference frequency, which greatly improves the versatility of the sensing electronics. The complete circuitry to quickly measure frequency shifts by converting them into phase shifts is shown in Fig. 8.7. The input signal is first filtered to remove unwanted high frequency signals. If required, a mixer brings down the frequency of the signal to what the delay network is designed for. The mixer output is then filtered to rid of high frequency components and is applied to the delay network.

8.2 Oscillator Topologies

Stable signal sources and measurement equipment are needed if a resonant sensor is used in an open-loop configuration. Besides requiring extra equipment, such a configuration may not provide the necessary measurement bandwidth for sensory applications, as the frequency of the input signal needs to be swept slowly so that the resonant amplitude has enough time to build up. Therefore, one often needs to place the resonator along with some active elements inside a closed loop and realise an oscillator. For sensory applications, this system produces the frequency-modulated signal which corresponds to the quantity that is being measured. In timing applications (e.g., clock signal in digital systems), this oscillator provides the reference signal.

A linear oscillator, as opposed to relaxing oscillators and such, is generally composed of an amplifier to compensate for the losses in the loop and a bandpass filter to determine the oscillation frequency. To have a stable output frequency, it is needed that the filter provide as narrow a bandwidth as possible. A good candidate for a device to provide the filtering function is a high-Q resonator. Such an oscillator is functionally similar to what is shown in Fig. 8.8. In the steady-state, it can be seen that $x_{\text{out}} = x_{\text{out}}G(j\omega)H(j\omega)$ resulting in $G(j\omega)H(j\omega) = 1$. This is called *Barkhausen–Kurz* criterion to have sustained oscillations in this loop and can be broken into the amplitude

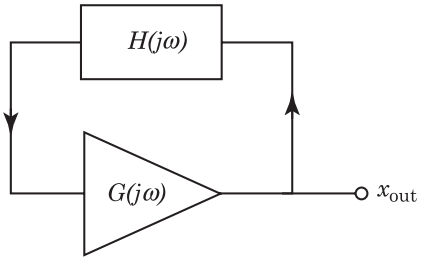

Figure 8.8 Simplified diagram of a linear oscillator.

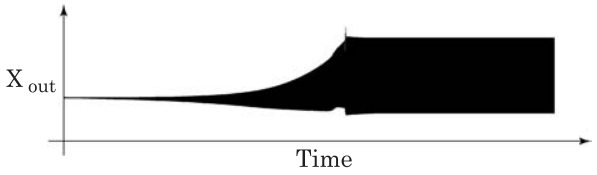

Figure 8.9 Oscillator startup.

and phase requirements:

$$|G(j\omega)H(j\omega)| = 1 \tag{8.3}$$

$$\angle G(j\omega)H(j\omega) = 2n\pi \tag{8.4}$$

where n is an integer. In practice, it is difficult to keep the loop gain exactly one due to the tolerances in device values and various disturbances such as temperature variations and ageing. On the other hand, if the loop gain is exactly one, the signal that goes through the loop can have a very small amplitude which makes its processing difficult for the following stages. For these reasons, the gain of the amplifier in the loop is chosen such that the loop gain is initially larger than one so that the oscillations can start up and a usable signal amplitude is achieved. Thereafter, the amplitude of the signal is kept constant through a nonlinear mechanism, e.g., with an amplitude limiter, to reduce the effective loop gain to around one and sustain the oscillations (see Fig. 8.9). For many linear oscillators, it is the electronic nonlinearity of the sustaining amplifier that limits the signal amplitude. In some cases, it might be necessary to insert phase adjustment elements in the loop to meet the loop phase shift requirement (see Fig. 8.10).

The electrical equivalent circuit of a resonator, as shown in Fig. 8.11, may be used in the design phase or to analyse the performance of an oscillator. This technique is specially advantageous for simulation of linear oscillators where the signal levels in the oscillator loop are chiefly within the linear limits of the resonator and the electronics. The effect of the feedthrough signals is modelled by adding a capacitor, C_{xs}, in parallel with the resonator. Two capacitors, C_{xpi}

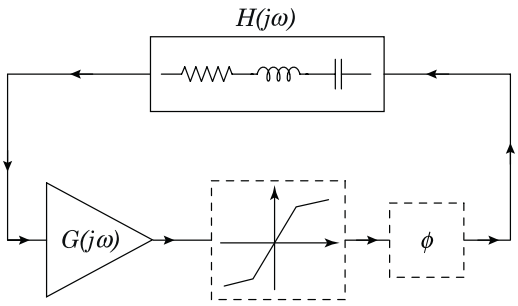

Figure 8.10 A linear oscillator with amplitude limiting and phase adjustment blocks.

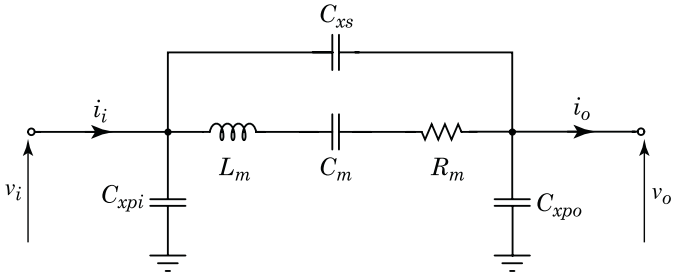

Figure 8.11 The linearised equivalent electrical circuit of a resonator.

and C_{xpo}, in parallel with the input and output ports of the resonator are sometimes added to the model to represent the capacitances of bonding pads and signal lines. It should be noted that unlike the motional elements of the resonator (i.e., R_m, C_m, and L_m) these three capacitors (i.e., C_{xs}, C_{xpi}, and C_{xpo}) are often physical capacitors. In order to have a stable oscillator, one should choose a resonator with high-Q for better signal frequency definition, low motional resistance for simpler amplifier topologies, and small feedthrough capacitance so that the output current from the resonator is mainly from the resonator itself.

8.2.1 Linear Oscillators

The signal inside the loop of a linear oscillator is more or less sinusoidal and the behaviour of these oscillators can be analysed with familiar techniques such as Fourier and Laplace transforms. There are numerous topologies for linear oscillators but we concentrate our discussion to series resonance and Pierce topologies that have been implemented with microresonators more often.

In a series oscillator, the frequency of oscillations is set by the series resonant frequency of the resonator. An amplifier with a much wider bandwidth than the resonant frequency of the resonator is chosen to compensate for the losses in the

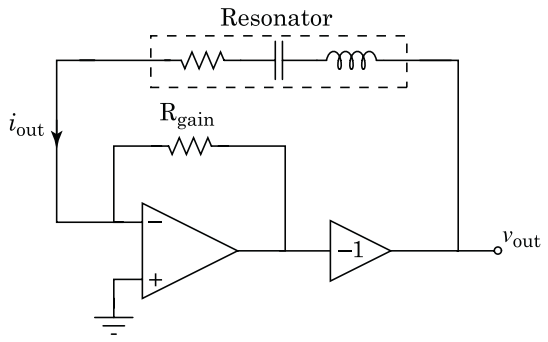

Figure 8.12 A series oscillator employing a transresistance amplifier.

loop. This amplifier typically converts the current through the resonator into an actuation voltage (i.e., a transresistance amplifier) and has small input and output resistances [7–10]. These oscillators have a relatively simple topology as shown in Fig. 8.12.

The oscillations occur at the frequency set by the high-Q block which can be an LC network, a quartz crystal, or a micromachined resonator. If the phase of the input signal to the high-Q network is set properly, a signal with proper frequency is amplified inside the loop. The loop gain in the ideal case has to be unity at desired output frequency. However, in practice the loop gain is designed to be slightly larger than one to assure that the poles of the system are initially in the right half plane. The amplitude of the oscillations is limited by some nonlinear effect in the signal path (e.g., the saturation of the amplifier).

An advantage of using a series oscillator is that the parasitic capacitances at the input and output of the resonator do not play important roles, since one is in parallel with a low resistance source (i.e., the output of the actuation amplifier) and the other is shorted to virtual ground. Moreover, the gain of the amplifier can be easily set by changing R_{gain} as seen in Fig. 8.12. Consequently, this oscillator topology is popular for realising low frequency oscillators. At high frequencies (>10 MHz), however, it can be difficult to design the required wideband amplifier, especially if the motional of resistance of the resonator is large. This topology requires relatively complicated electronic circuitry (e.g., an OpAmp), and therefore, the noise produced by the electronics can be significant which degrades the performance of the oscillator.

Another popular circuit to realise an oscillator with high-Q resonators and simple electronics is Pierce topology which is shown in Fig. 8.13 [11–13]. The amplifier that is used in a Pierce oscillator, which can be as simple as a single transistor in common-emitter or common-source configuration, has non-zero input and output resistances. The Pierce topology relies on utilising these resistances along with the parasitic capacitances of the resonator to gain the required 360° phase shift around the loop. While the amplifier typically provides about 180° of phase shift, the other 180° needs to be provided by the passive

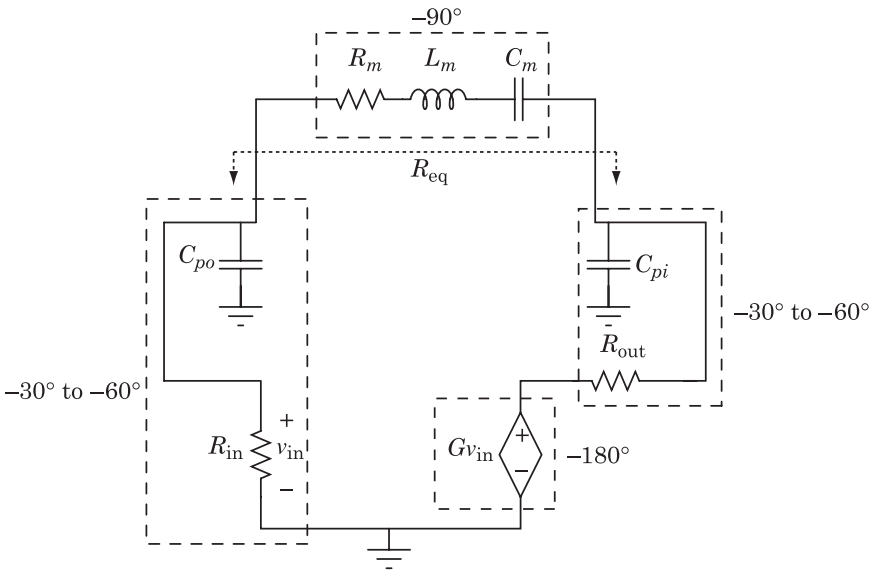

Figure 8.13 A Pierce oscillator illustrating the amount of phase shifts in the loop; note that G is negative.

components in the loop. This forces the oscillation frequency of the loop to be slightly higher than the series resonant frequency of the resonator, meaning that during the operation of the circuit, the resonator acts more like an inductor, in contrast to a series resonator in which the resonator behaves as a resistor. A simple technique to analyse Pierce circuits is to calculate the equivalent resistance seen from the resonator ports (R_{eq} in Fig. 8.13). This resistance should have a negative value at the desired frequency of operation. To ensure that the initial loop gain of the circuit is larger than one, the value of R_{eq} must be larger than the motional resistance of the resonator (i.e., R_m). As an example, R_{eq} for the circuit shown in Fig. 8.13 is:

$$R_{\text{eq}} = -\Re\left(\frac{R_{\text{in}} + R_{\text{out}} - GR_{\text{in}} + jR_{\text{out}}R_{\text{in}}(C_{po} + C_{pi})\omega}{(1 + jR_{\text{in}}C_{po}\omega)(1 + jR_{\text{out}}C_{pi}\omega)}\right). \tag{8.5}$$

Due to its simplicity, Pierce topology is commonly used where a simple low phase noise oscillator is needed to work around a resonator with low motional resistance [13].

8.2.2 Nonlinear Oscillators

Large feedthrough signals can often hamper the operation of linear resonators as the peak of the signal at resonance is not much larger than the feedthrough signal level. This is particularly a problem when the motional resistance of the

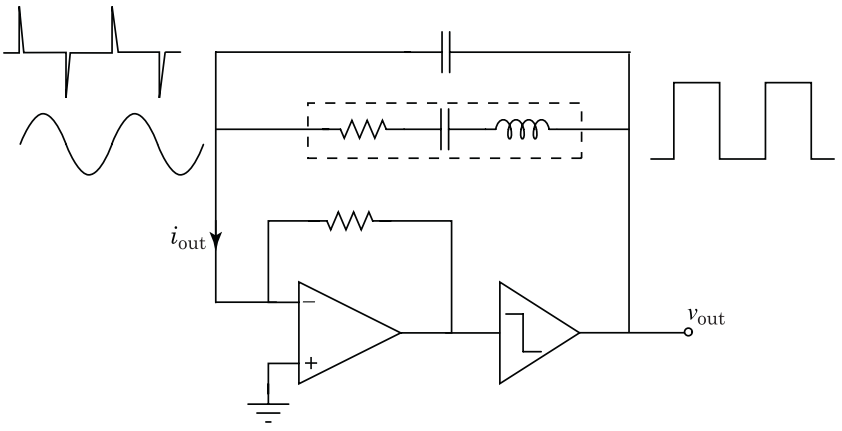

Figure 8.14 Using pulse actuation to reduce the effect of the feedthrough capacitance.

resonator is large, such as the case for typical electrostatic resonators. In such cases, linear oscillator topologies may not be able to function properly and one needs to separate the resonator and feedthrough currents from each other to realise an oscillator.

A techniques to isolate the feedthrough and resonator signals in time domain is to use voltage pulses or impulses to drive the resonator at its resonant frequency [14,15]. In this case, due to the high quality factor of the resonator, the current through the resonator is filtered and will be sinusoidal. The current through the feedthrough capacitor, however, is an impulse, which can relatively easily be discarded, for example with a lowpass filter. A simple oscillator topology based on this technique is shown in Fig. 8.14. In this oscillator, a transresistance amplifier converts the resonator current into a sinusoidal voltage, which is then converted to a pulse train with the aid of a comparator. Other blocks can be added to the loop to convert the pulses to impulses, adjust the phase in the loop, etc.

An advantage of the nonlinear oscillators discussed above over linear oscillators is control over the excitation signal amplitude. Knowing the nonlinear limits of the resonator, one can precisely set the excitation signal amplitude to have a large sense signal at the output of the resonator without degrading the oscillator performance by keeping the resonator away from its nonlinearities [16].

If a nonlinear resonator is used in the loop, one can isolate the feedthrough and resonator signals in frequency domain. For example, since the electrostatic force is proportional to the square of the drive voltage, it is inherently nonlinear. Consequently, higher harmonics of the drive signal can be sensed at the output of the resonator. If the resonator is driven with a sinusoidal signal at half the resonant frequency of the device, $\omega_0/2$, the signal at the resonator output will have the first and the second harmonics of the drive signal (i.e., $\omega_0/2$ and ω_0) while the feedthrough signal will be at the frequency of the drive signal, $\omega_0/2$.

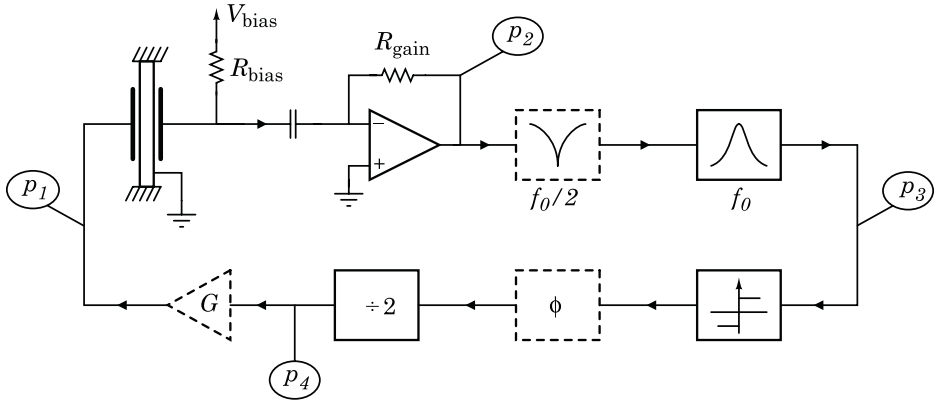

Figure 8.15 Resonator used in a self-oscillating configuration.

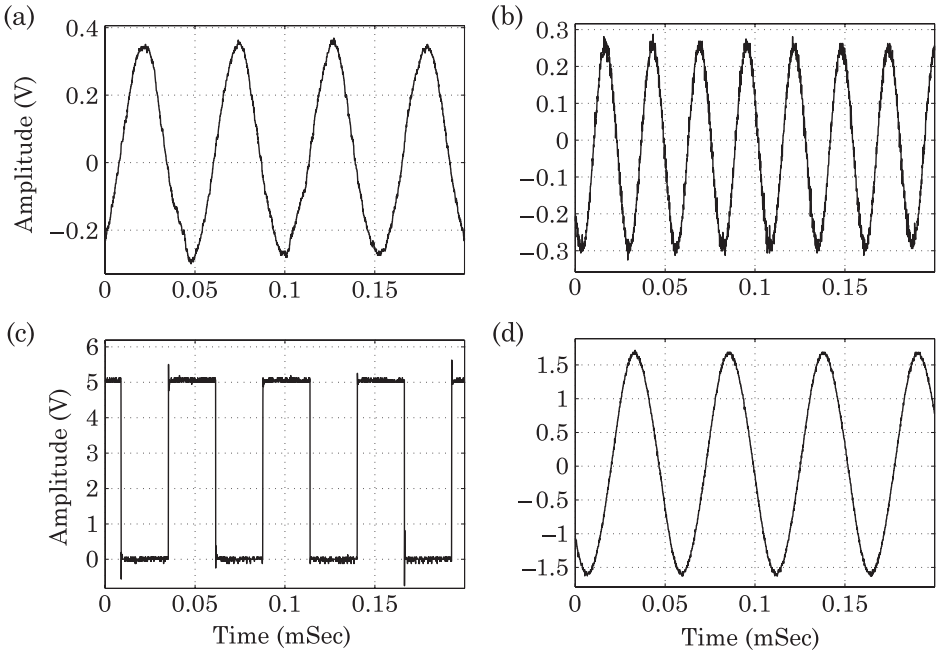

Figure 8.16 Measured signals in the loop taken from: (a) the output of the amplifier (node p_2); (b) the output of the bandpass filter (node p_3); (c) the output of the frequency divider (node p_4); and (d) the input of the resonator (node p_1).

The feedthrough signal is discarded with the aid of a notch filter and the second harmonic of the signal is processed as the actual resonator signal. However, to close the loop, the frequency of this signal needs to be divided by two, which can be simply performed by converting the signal from sinusoidal to binary with a T-flipflop. The schematic of a nonlinear oscillator based on this technique is

shown in Fig. 8.15 [4]. The current through the feedthrough capacitor does not affect the loop performance as long as it is small enough to not cause nonlinear behaviour at the output of the transresistance amplifier. The loop signals are shown in Fig. 8.16.

The amplitude of the signal that is applied to the resonator is set by the logic levels and the gain of the amplifier before the resonator (gain G, which can be less than one). Therefore, the drive signal amplitude is independent of the sense signal amplitude as long as the signal levels at the input of the comparator are large enough to make it switch.

References

1. G.H. McGibney, "Wireless networking with simple terminals", Ph.D. dissertation, Department of Electrical and Computer Engineering, The University of Calgary, Canada, 2000.
2. N.R. Karpov, "Vernier method of measuring time intervals", *Journal of Measurement techniques*, Vol. 23, no. 9, pp. 817–820, September 1980.
3. T.R. Albrecht, P. Grtitter, D. Horne and D. Rugar, "Frequency modulation detection using high-Q cantilevers for enhanced force microscope sensitivity", *Journal of Applied Physics*, Vol. 69, no. 2, pp. 668–673, January 1991.
4. B. Bahreyni and C. Shafai, "Oscillator and frequency-shift measurement circuit topologies for micromachined resonant devices", *Sensors and Actuators A: Physical*, Vol. 137, no. 1, pp. 74–80, June 2007.
5. J.G. Webster, Ed., *The measurement, instrumentation and sensors handbook*, ser. Electrical engineering handbook, Vol. 14, CRC Press, Boca Raton, USA, 1999.
6. W. Rosenkranz, "Phase-locked loops with limiter phase detectors in the presence of noise", *IEEE Transactions on Communications*, Vol. 30, no. 10, pp. 2297–2304, October 1982.
7. C.T.-C. Nguyen and R.T. Howe, "An integrated CMOS micromechanical resonator high-Q oscillator", *IEEE Journal of Solid-State Circuits*, Vol. 34, no. 4, pp. 440–455, April 1999.
8. Y.-W. Lin, S. Lee, S.-S. Li, Y. Xie, Z. Ren and C.T.-C. Nguyen, "Series-resonant VHF micromechanical resonator reference oscillators", *IEEE Journal of Solid-State Circuits*, Vol. 39, no. 12, pp. 2477–2491, December 2004.
9. K. Sundaresan, G. Ho, S. Pourkamali and F. Ayazi, "Electronically temperature compensated silicon bulk acoustic resonator reference oscillators", *IEEE Journal of Solid-State Circuits*, Vol. 42, no. 6, pp. 1425–1434, June 2007.
10. T.A.W. Roessig, "Integrated MEMS tuning fork oscillators for sensor applications", Ph.D. dissertation, Department of Mechanical Engineering, University of California, Berkeley, USA, 1998.
11. T. Mattila, O. Jaakkola, J. Kiihamäki, J. Karttunen, T. Lamminmäki, P. Rantakari, A. Oja, H. Seppä, H. Kattelus and I. Tittonen, "14 MHz micromechanical oscillator", *Sensors and Actuators A: Physical*, Vol. 97–98, pp. 497–502, April 2002.
12. B.P. Otis and J.M. Rabaey, "A 300 μW 1.9 GHz CMOS oscillator utilizing micromachined resonators", *IEEE Journal of Solid-State Circuits*, Vol. 38, pp. 1271–1274, July 2003.
13. R.J. Matthys, *Crystal oscillator circuits*, Krieger Publishing Company, Malabar, USA, April 1991.
14. E. Colinet, J. Juillard, S. Guessab and R. Kielbasa, "Actuation of resonant MEMS using short pulsed forces", *Sensors and Actuators A: Physical*, Vol. 115, no. 1, pp. 118–125, September 2004.

15. K. Wojciechowski, B. Boser and A. Pisano, "A MEMS resonant strain sensor operated in air", *Proceedings of the 17th IEEE micro electro mechanical systems conference, MEMS '04*, Maastricht, The Netherlands, January 2004, pp. 841–845.
16. J.-Y. Lee, B. Bahreyni, Y. Zhu and A. Seshia, "Ultrasensitive mass balance based on a bulk acoustic mode single-crystal silicon resonator", *Applied Physics Letters*, Vol. 91, no. 23, pp. 234 103:1–3, December 2007.

9 Packaging

So far we have discussed how to design resonant devices at the wafer/chip scale. Most applications, however, require packaged devices. Since micromachined devices are made of delicate mechanical elements, their packaging is usually a two-step process. First, the resonator is packaged at the wafer-level or in some cases at the chip level. This step is known as 0-level packaging and, at the very least, is necessary to avoid damaging the resonator through the rest of the processes. The packaged resonator is then wire-bonded inside a plastic or ceramic package (1-level package) which can then be used as an element in system design. An ideal 0-level package should satisfy the following requirements:

- physically and chemically protect the device;
- provide a stable environment around the resonator such as vacuum;
- efficiently couple the measurand to the resonator for sensors;
- exert minimal mechanical stress on the resonator;
- be thermally compatible with the resonator chip;
- minimally affect the electrical connections to the resonator;
- has a compatible fabrication process with that of the resonator;
- allow for a straightforward 1-level packaging.

It can readily be seen that packaging can easily become the commercialisation bottleneck for a resonant micromachined device. This chapter is about the possible solutions to this challenging issue in design of resonant microsystems [1–4].

9.1 Maintaining Vacuum

As seen earlier, a major source of damping for resonant devices is friction with gas molecules. While the resonators may be tested inside a vacuum chamber in a laboratory environment, a suitable packaging technique is required for most applications to maintain a low pressure ambient around the resonator. We will discuss two commonly used techniques for packaging of the resonators: encapsulation by a thin film and bonding a capping wafer. It must be noted, however, that an almost complete isolation of the device from the surroundings is resulted after vacuum packaging. This can lead to very important implications on device design, especially if the resonator is to be used as a sensor. Majority of the commercially available, vacuum packaged resonators do not require a direct coupling to the measurand. For example, being isolated from the environmental disturbances under vacuum is in fact an advantage of a vacuum package for resonators that are used for timing applications, where the resonator response should not depend on such disturbances. Inertial sensors are other devices that

benefit from this isolation since the package is actually their reference frame and they should operated properly the package cavity as long as the package itself is properly mounted. In most other cases, the measured quantity is coupled to the resonator through part of the package. As an example, a resonator can be mounted and packaged on top of a membrane for a resonant pressure sensor, while it is the bottom side of the membrane that is exposed to the environment whose pressure needs to be measured.

A package at the die level can also protect the fragile MEMS from physical, mechanical, and chemical damage. Many of the early MEMS devices were packaged at the die-level; i.e., the wafer was diced and individual devices were put inside packages. However, this requires that the wafer containing the devices to be diced before the final release of the MEMS in order to minimise the risk of damaging the devices during the harsh dicing step. Consequently, the MEMS on each die needs to be released individually, deviating from the batch processing and increasing the overall cost.

An alternative technique to avoid damage to the released devices during the dicing step is to coat them with a protective layer (e.g., photoresist) before dicing. This layer can be removed after the dicing of the chips, for example with an oxygen plasma.

9.1.1 Encapsulation with Thin Films

A seemingly straightforward 0-level capping technology is to encapsulate the released structures with a thin film [5–9]. In a typical thin film encapsulation process, the device is first covered with a sacrificial material. The capping layer is then deposited or grown. This capping layer can be a CVD layer of nitride or polysilicon or an electroplated metal film. Etch holes are patterned to access the sacrificial layer through the capping layer and the sacrificial layer is etched away, often using an isotropic dry etchant. The etch holes are then sealed under relative vacuum in an LPCVD process. These process steps are illustrated in Fig. 9.1.

Thin film encapsulation, however, does suffer from some drawbacks. The thickness of capping layers is often limited to 2–5 μm, and consequently, may not be able to endure the stresses during the subsequent 1-level packaging steps. Moreover, the limited thickness of sacrificial layers leads to a large surface-to-volume ratio inside the cavity which makes maintaining the vacuum level inside the package difficult. On the other hand, the use of an LPCVD process to seal the cavities brings up contamination issues and limits the pressure level inside the cavity to what is required during the final sealing process, typically on the order of several mTorr. On the positive side, this sealing technique does not significantly increase the required real estate on the wafer and provides relatively simple means for electrical connections to the resonator inside the cavity.

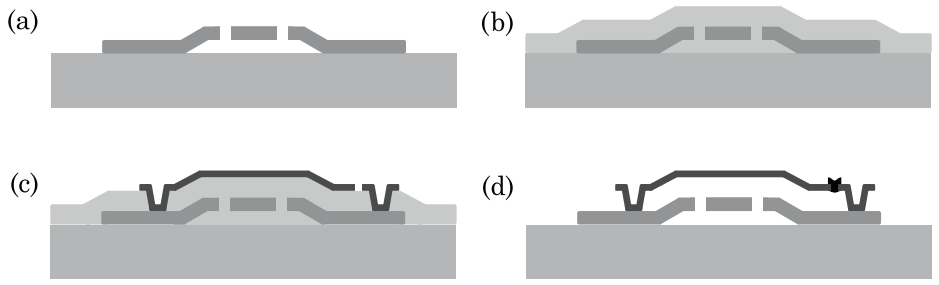

Figure 9.1 Processing steps for thin film encapsulation: (a) the device is fabricated on the substrate; (b) a sacrificial layer is deposited on the device; (c) the patterned sacrificial layer is covered with a capping layer; (d) the sacrificial layer is etched through the etch holes in the capping layer and the holes are sealed.

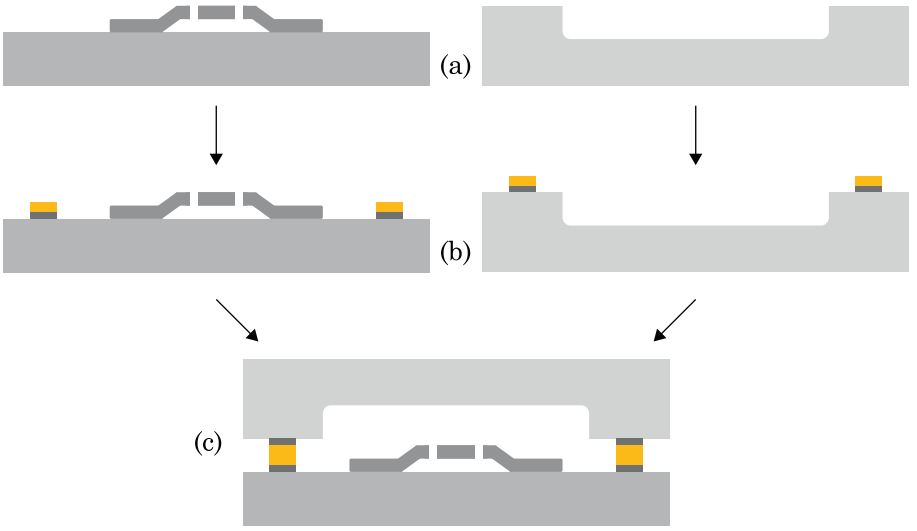

Figure 9.2 Processing steps for encapsulation through wafer bonding: (a) the device is fabricated on a substrate while a cavity is etched in a second wafer; (b) the solder rings are deposited/grown on both wafers; (c) the sealing rings on the wafers are aligned with each other, brought together under the desired environmental pressure, and pressed together while the temperature is raised until the solder forms a bond.

9.1.2 Capping through Bonding

Another technique for hermetic packaging of resonators is to bond a second wafer, typically silicon or glass, to the wafer on which the resonator is fabricated [10–19]. In this technique, a cavity is etched on a capping wafer and is aligned with the resonator on the main wafer. The two wafers are then bonded together to form a sealed cavity. These steps are illustrated in Fig. 9.2.

Eutectic bonding is the preferred bonding technique in order to avoid the high temperatures that are normally required for glass-to-silicon or silicon-to-silicon bonding. This, however, requires that a sealing ring with proper solder metals, such as Sn, to be patterned around the resonator and on the capping wafer to enable bonding of the two wafers at temperatures in the 200–350 °C range. The electrical connections to the resonator inside the cavity need to be covered with an insulating layer in order to avoid short-circuiting them with the metallic ring.

The sealing ring around the device and the space required for electrical feedthroughs results in having a large footprint for the packaged device, and therefore, a smaller density of devices on a wafer. Moreover, the packaging parasitics can be higher for this type of resonator sealing due to the complexity of the package. The overall height of the final device is twice as much as a single wafer, which can restrict the availability of 1-level packages. However, this packaging technique is more flexible than using CVD films for resonator sealing as it has less constraints on the types of materials and films that are used during the device fabrication. This technique is potentially less prone to contamination and the bonding can be performed at pressures in the μTorr range, adding to the degrees of freedom available to the device designer.

9.1.3 Package Level Sealing

The two packaging techniques mentioned above are primarily developed toward wafer-level processing; i.e., 0-level packaging for all of the devices on a wafer. It is also possible to skip the 0-level packaging altogether and use a 1-level package that is capable of maintaining the desired levels of vacuum. In this case, individual devices are packaged after fabrication and testing and can actually be a cost effective method for small volume production or when the process yield is low. The packaging process in this case depends highly on the type of the packaging material (e.g., ceramic or metal) and the vendor.

9.2 Packaging Stress

One of the challenges that one needs to address when designing or selecting a packaging flow, including both 0-level and 1-level packaging steps, is the amount of stress that is induced on the device due to packaging [20–22]. One source of this stress is the *gluing* mechanism that is employed to hold the device chip within the package. This stress manifests itself as a stress offset and can be minimised by using *soft* adhesives or through an initial calibration of the packaged device. The other source of stress is environmental disturbances, which often have a more prominent effect as a result of mismatches between material properties of the package and the device chip. Such disturbances can lead to

strains on the device due to various effects, such as changes in temperature or humidity. The effects of such disturbances should be minimised through proper choice of package materials and, if needed, active monitoring of them and trying to compensate for them dynamically.

References

1. C. Fung, P. Cheung, W. Ko and D. Fleming, Eds., *Micromachining and micropackaging of transducers*, Elsevier Science Publishers B. V., Amsterdam, The Netherlands, 1985.
2. K. Gilleo, *MEMS/MOEM packaging*, McGraw-Hill Professional, USA, 2006.
3. T.-R. Hsu, Ed., *MEMS packaging*, The Institution of Engineering and Technology, London, United Kingdom, 2004.
4. Z. Gan, D. Lin, X. Wang, Chenggang, H. Zhang and S. Liu, "Vacuum measurement on vacuum packaged MEMS devices", *Journal of Physics: Conference Series*, Vol. 48, pp. 1429–1434, 2007.
5. X. Zhu, D.M. Aslam and J.P. Sullivan, "The application of polycrystalline diamond in a thin film packaging process for MEMS resonators", *Journal of Diamond and Related Materials*, Vol. 15, no. 11–12, pp. 2068–2072, November–December 2006.
6. P. Monajemi, P.J. Joseph, P.A. Kohl and F. Ayazi, "Wafer-level MEMS packaging via thermally released metal-organic membranes", *Journal of Micromechanics and Microengineering*, Vol. 16, no. 4, pp. 742–750, April 2006.
7. R. He and C.-J. Kim, "On-wafer monolithic encapsulation by surface micromachining with porous polysilicon shell", *IEEE Journal of Microelectromechanical Systems*, Vol. 16, no. 2, pp. 462–472, April 2007.
8. C. Rusu, S. Sedky, B. Parmentier, A. Verbist, O. Richard, B. Brijs, L. Geenen, A. Witvrouw, F. Larmer, F. Fischer, S. Kronmuller, V. Leca and B. Otter, "New low-stress PECVD poly-SiGe layers for MEMS", *IEEE Journal of Microelectromechanical Systems*, Vol. 12, no. 6, pp. 816–825, December 2003.
9. P. Joseph, P. Monajemi, F. Ayazi and P. Kohl, "Wafer-level packaging of micromechanical resonators", *IEEE Transactions on Advanced Packaging*, Vol. 30, no. 1, pp. 19–26, February 2007.
10. B. Ziaie, J. Von Arx, M. Dokmeci and K. Najafi, "A hermetic glass-silicon micropackage with high-density on-chip feedthroughs for sensors and actuators", *IEEE Journal of Microelectromechanical Systems*, Vol. 5, no. 3, pp. 166–179, September 1996.
11. D. Sparks, R. Smith, R. Schneider, J. Cripe, S. Massoud-Ansari, A. Chimbayo and N. Najafi, "A variable temperature, resonant density sensor made using an improved chip-level vacuum package", *Sensors and Actuators A: Physical*, Vol. 107, no. 2, pp. 119–124, October 2003.
12. D. Sparks, J. Trevino, S. Massoud-Ansari and N. Najafi, "An all-glass chip-scale MEMS package with variable cavity pressure", *Journal of Micromechanics and Microengineering*, Vol. 16, no. 11, pp. 2488–2491, November 2006.
13. Y.-T. Cheng, L. Lin and K. Najafi, "A hermetic glass-silicon package formed using localized aluminum/silicon-glass bonding", *IEEE Journal of Microelectromechanical Systems*, Vol. 10, no. 3, pp. 392–399, September 2001.
14. Z. Li, Y. Hao, D. Zhang, T. Li and G. Wu, "An SOI-MEMS technology using substrate layer and bonded glass as wafer-level package", *Sensors and Actuators A: Physical*, Vol. 96, no. 1, pp. 34–42, January 2002.
15. R.A.M. Receveur, M. Zickar, C. Marxer, V. Larik and N.F. de Rooij, "Wafer level hermetic package and device testing of a SOI-MEMS switch for biomedical applications", *Journal of Micromechanics and Microengineering*, Vol. 16, no. 4, pp. 676–683, April 2006.

16. J.-H. Park, H.-C. Lee, Y.-H. Park, Y.-D. Kim, C.-H. Ji, J. Bu and H.-J. Nam, "A fully wafer-level packaged RF MEMS switch with low actuation voltage using a piezoelectric actuator", *Journal of Micromechanics and Microengineering*, Vol. 16, no. 11, pp. 2281–2286, 2006.
17. H.-A. Yang, M. Wu and W. Fang, "Localized induction heating solder bonding for wafer level MEMS packaging", *Journal of Micromechanics and Microengineering*, Vol. 15, no. 2, pp. 394–399, 2005.
18. Z.-H. Liang, Y.-T. Cheng, W. Hsu and Y.-W. Lee, "A wafer-level hermetic encapsulation for MEMS manufacture application", *IEEE Transactions on Advanced Packaging*, Vol. 29, no. 3, pp. 513–519, August 2006.
19. C. Tsou and H.L.H.-C. Chang, "A novel wafer-level hermetic packaging for MEMS devices", *IEEE Transactions on Advanced Packaging*, Vol. 30, no. 4, pp. 616–621, November 2007.
20. R. Krondorfer and Y. Kim, "Packaging effect on MEMS pressure sensor performance", *IEEE Transactions on Components and Packaging Technologies*, Vol. 30, no. 2, pp. 285–293, June 2007.
21. M. Lishchynska, C. O'Mahony, O. Slattery, O. Wittler and H. Walter, "Evaluation of packaging effect on MEMS performance: Simulation and experimental study", *IEEE Transactions on Advanced Packaging*, Vol. 30, no. 4, pp. 629–635, November 2007.
22. S.F. Bart, S. Zhang, V.L. Rabinovich and S. Cunningham, "Coupled package-device modeling for microelectromechanical systems", *Journal of Microelectronics Reliability*, Vol. 40, no. 7, pp. 1235–1241, July 2000.

10 Survey of Applications

This chapter overviews some examples of resonant microdevices which have been used in different applications. We review resonators for three of their main applications; i.e., sensing, signal processing, and timing references.

10.1 Resonant Microsensors

This is one of the main applications of microresonators. Often, the external physical quantity is converted to a mechanical stress that is transferred to the resonator body through proper support and flexure design. The majority of resonant microsensors can be broken into a strain sensor or a mass sensor and a mechanism to convert the measurand to a strain or a mass alteration. The simplest resonant sensors, therefore, are mass and strain sensors. We will look at a few resonant sensors and briefly discuss their design and fabrication.

10.1.1 Mass Sensors

An example of a straightforward application of MEMS resonators is mass sensing. The resonant frequency of a mechanical resonator depends on its effective mass, and thus, a change in the mass of the resonator leads to a shift in its resonant frequency from which one can estimate the amount of the additional mass. Such sensors may be used to measure the weight of a particle [1] or the density of a film [2].

Cantilevers are among the most widely used resonant elements for resonant mass sensors, partially due to their simple design and fabrication. The cantilever is brought under resonance with different actuation mechanisms such as electrostatic or piezoelectric [3–6]. Resonance detection can be optical, piezoresistive, electrostatic, etc. Micromachined mass sensors are able to detect masses as small as a few femto-grams [2,5,7].

10.1.2 Strain Sensors

A strain sensor is the other resonant device whose design follows from the resonant analysis of mechanical structures. In case of resonant strain sensors, the spring constant of the structure is modified with an external stress, which directly affects the resonant frequency of the device. A strain sensor, in its simplest form, needs to be anchored at two locations which undergo some relative displacement during the device operation [8,9]. The resolution of micromachined resonant strain sensors is on the order of nano-strains [8,10].

10.1.3 Chemical Sensors

The operation of resonant chemical sensors is often a combination of mass and strain sensing. It is often the surface of the resonator which is *activated* such that a certain molecule or particle preferentially binds to or adsorbed at the surface [11,12]. A number of different phenomena contribute to change in the resonator behaviour which can be employed for sensing. For example, the binding of chemicals to the surface of the resonator obviously increases the resonator mass. However, deposited molecules often produce a stress at the surface of the structure, which besides affecting the resonant frequency of the resonator, modifies the surface losses in the structure and alter the quality factor of the resonator. As with mass sensors, cantilevers are a popular family of resonators for chemical sensing applications [3,13,14]. The simple processing steps for cantilever sensors allows for their fabrication in many processes, including standard CMOS processes with additional etch and release steps [15].

10.1.4 Pressure Sensors

An early example of a micromachined resonant pressure sensor is the one proposed by Greenwood in early 1980's [16,17]. The schematic of the sensor is shown in Fig. 10.1. This device used a silicon resonator as the strain sensing element with electrostatic actuation and sensing. An actuation voltage of ∼1 V and a DC bias voltage of 50 V were required for device operation and a JFET amplifier was placed close to the resonator for signal pick-up. The body of the resonator was patterned by doping a silicon wafer with Boron through openings in an SiO_2 mask to 4×10^{19} atoms cm^{-3}. The doped wafer was then etched from the back and front sides in KOH to obtain the final resonator body. The electrodes were patterned separately on a metal-coated piece of glass and were placed about 10–20 μm away from the resonator with the aid of a thin polyester film. The whole assembly was placed in a sealed package under vacuum.

When measuring a pressure, the normal stress on the membrane is converted to a lateral strain on the resonator body (see Fig. 10.2), hence, causing a shift in the resonant frequency of the device. The resonant frequency of the first mode of the device was ∼65 kHz with a sensitivity of ∼200 Hz/kPa and a quality factor of 10 000 under a 1 mTorr vacuum. Later on, Greenwood et al. proposed a sensor topology with a laterally driven electrostatic resonator [18].

Another example of a resonant pressure sensor was proposed by Ikeda in early 1990's [19,20]. This sensor is made of two clamped–clamped beams which are fabricated on a membrane and connected to each other at their centres. As illustrated in Fig. 10.3, an AC current is passed through one of the beams during the sensor operation while the sensor is kept inside a constant magnetic field that is produced externally with a permanent magnet. Lorentz force causes the actuator beam to vibrate and its movements are transferred to the second beam through the connector at the middle of the beams. The vibrations of the sensing

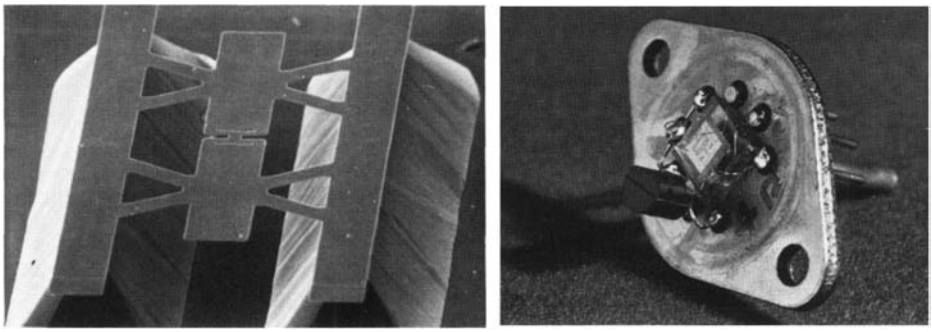

Figure 10.1 Pictures of the resonator (left) and the final packaged sensor by Greenwood [16]. Note the electrodes that were patterned on glass and a discrete JFET that was placed inside the same package to minimise the effects of stray capacitances and interference. *Reproduced by permission of Institute of Physics.*

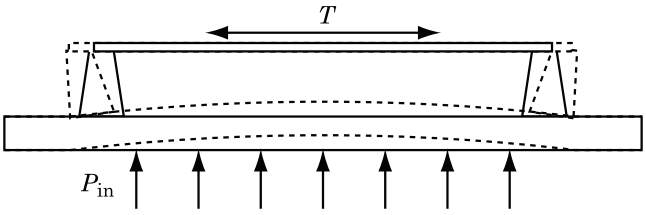

Figure 10.2 Transformation of a pressure normal to the sensing membrane to a lateral stress.

beam inside the present magnetic field lead to generation of a voltage across it, as predicted by Faraday's law. The sensor is placed inside the feedback loop of an amplifier to form an oscillator. External pressure variations deflect the membrane to which the beams are anchored, resulting in an axial stress on the beams and eventually changing their resonant frequencies, which is measured by monitoring the output signal from the oscillator.

The resonator beams are made from an epitaxial $p{+}{+}$ silicon layer surrounded by epitaxial $p+$ silicon. To maintain a high vacuum level around the resonator, the resonators are covered with another $p{+}{+}$ silicon layer. The $p+$ silicon is then selectively etched in a wet process to release the structure. The resonator exhibited a quality factor of about 50 000 inside its vacuum cavity. The sensitivity of the sensor was about 60 Hz/kPa with a resonant frequency of about 46 kHz.

10.2 Signal Processing

Nonlinear properties of certain actuation/sensing mechanisms can be exploited to perform nonlinear operations, such as mixing signals with each

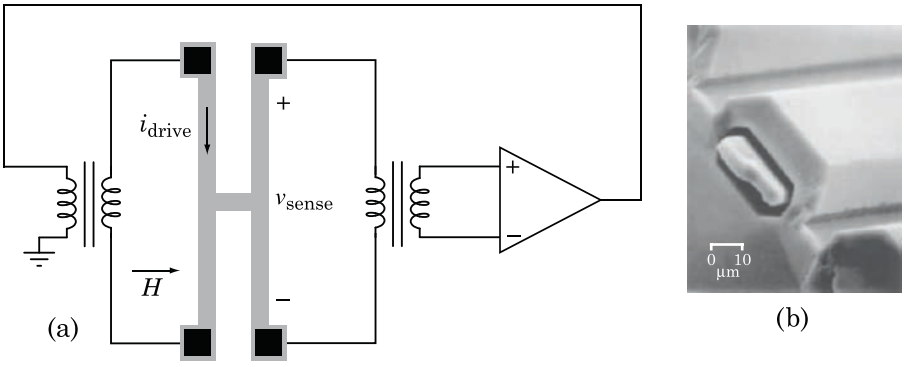

Figure 10.3 The resonant pressure sensor by Ikeda [20]: (a) the schematic of the resonator and circuitry around it and (b) cross-sectional view of one of the beams inside the cavity and the encapsulation film. *Reproduced by permission of IEEE.*

other [21,22]. Furthermore, micromachined resonators can be used as high-Q second order building blocks for analogue signal processing. While it is possible to use capacitors and inductors to make second order resonators, the limited range of quality factors for integrated passive elements does not allow for fabrication of low-order narrowband filters. Quartz crystals, ceramic resonators, and BAW (bulk acoustic wave) and SAW (surface acoustic wave) resonators have been traditionally used to realise bandpass filters with narrow bandwidths [23–26].

Filters made with high-Q resonator are often based on *ladder* or *lattice* topologies as shown in Fig. 10.4 [23,27–30]. For a ladder network, the resonators are chosen such that the resonant frequencies of the series elements matches the anti-resonant frequency of the parallel elements, thereby minimising the signal loss in a narrow band while significantly attenuating the signals outside the passband, thanks to the high quality factor of the resonators.

Micromachined resonators, as second order high-Q elements, can potentially replace the discrete resonators to design bandpass filters. However, the insertion loss through a typical micromachined resonator is larger than a quartz crystal (at low frequencies) or SAW and BAW devices (at high frequencies) [24,26]. On the other hand, while one needs to use several discrete resonators to make a filter, it is possible to fabricate micromachined resonators with different resonant frequencies on the same die and integrate the filter and even multiple filers on the same chip [31,32]. One can also take advantage of sensing and actuation mechanisms to tune the resonant frequency of the individual resonators as an additional degree of freedom, for example by modifying the electrostatic spring constant with a bias or by inducing some stress in the structure [33,34].

A narrow band filter can also be realised by having multiple similar resonators which are actuated in parallel or in series provided that the resonators are coupled to each other properly. A typical resonator has a pair of high-Q poles.

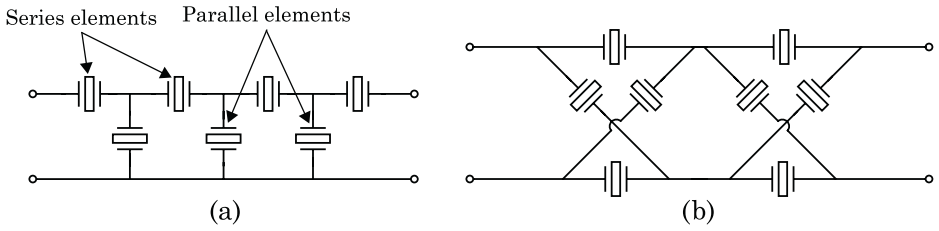

Figure 10.4 Ladder (left) and lattice (right) configurations for narrowband filters based on high-Q resonators.

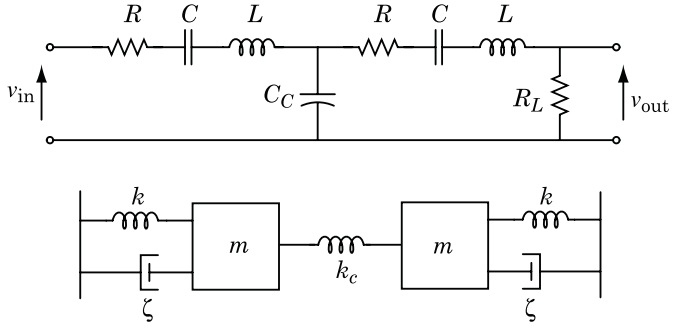

Figure 10.5 Coupling between series resonators with a shunt capacitor in electrical networks, C_c, (top) and between mechanical resonators with a spring, k_c, (bottom).

By coupling the resonators, the location of the poles for each resonator changes slightly, leading to the desired filtering response. In electrical networks, lossless coupling between the resonator elements can be achieved with capacitors or inductors. In mechanical networks, it is usually a spring element that couples the resonators to each other. These cases are schematically illustrated in Fig. 10.5. Fig. 10.6 illustrates the response of a single resonator as well as those of two and three similar weakly coupled resonators.

Resonators that are used in filters can, in theory, use any sensing or actuation mechanism for electromechanical transduction. Electrostatic and piezoelectric resonators have been used most often, in part due to the possibility of realising high frequency integrated filters with them. The resonators can be coupled with beam springs [35–37], through the anchors [38,39], capacitively [40–42], and electrostatically [33] (see Fig. 10.7).

The bias voltage that is needed to operate an electrostatic resonator can also be used as a tuning knob to modify the resonant frequency of the resonators. It is possible to have multiple similar resonators operating in parallel (i.e., the input signal is simultaneously applied to the input port of all of the resonators and their output currents are added to each other by connecting the output ports of resonators to each other) and apply different bias voltages to each of

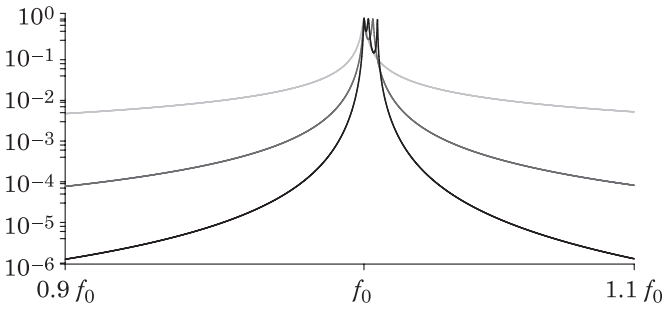

Figure 10.6 Frequency responses of a single high-Q resonator and two and three weakly coupled similar resonators.

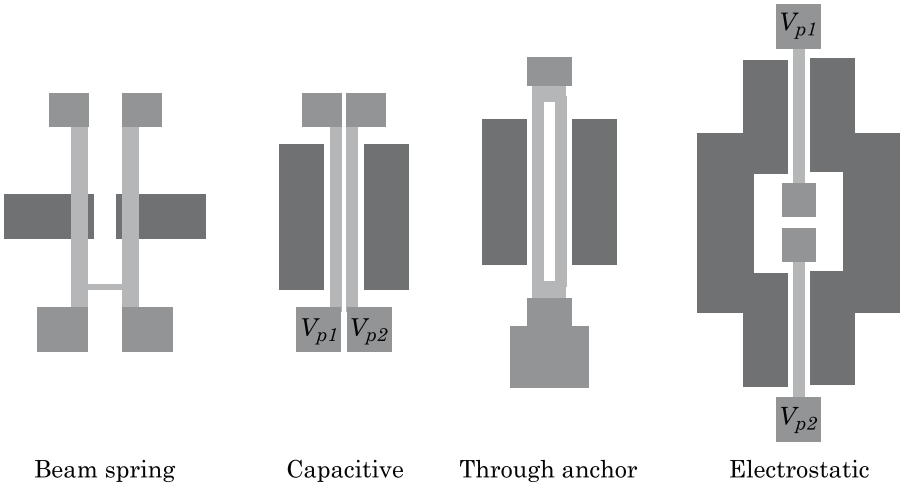

Figure 10.7 Some of the techniques to couple similar resonators. The lighter segments of the resonators are released.

them. This results in having slightly different resonant frequencies among the resonators, leading to the desired filtering response.

Without a trimming/adjustment mechanism (i.e., changing bias voltage for electrostatic resonators, adding mass to the resonator, etc.), it is very difficult, if not impossible, to make isolated resonators behave exactly the same, mainly due to process variations across the wafer and even across a die area. By mechanically coupling the resonators to each other, this issue is alleviated greatly. This performance synchronisation is a well-known property of coupled resonators and has been employed from the earlier days of using mechanical resonators [43,44]. A straight beam is often used to couple the resonators to each other. Due to the complexity of the resultant mechanical structure, the electrical equivalent model of such mechanical filters is derived and used to analyse the system in circuit simulators. In order for the coupling spring to only act as a

spring and not load the resonator with additional mass, its length should be chosen to be a quarter of the wavelength at the frequency of operation [35,45][1].

The use of electrostatic resonators for filtering applications has been studied heavily due to the potential for integration of the passive filters with CMOS electronics and making a complete radio system on a single chip [21,22]. Different resonators have been employed to realise filters, including comb-drives [35,46], clamped–clamped beams [36,41], square plate resonators [47], and disk resonators [37]. While it is possible to obtain the required shapes for the filter response in frequency domain, the insertion loss through typical electrostatic filters is unacceptably large (between −50 to −30 dB). Recall that the motional resistance of an electrostatic resonator is given by:

$$R_m = \frac{g^4\sqrt{KM}}{Q\varepsilon^2 V_B^2 A^2} \tag{10.1}$$

where A is the effective area between the electrodes and g is the gap between them. Typically, the dimensions of a given resonator geometry must be scaled down in order to increase the resonant frequency. Unfortunately, the motional impedance of electrostatic resonators increases dramatically as the dimensions of the resonator are reduced. A relatively straightforward way to reduce the motional resistance of electrostatic resonators is to reduce the gap between the electrodes. However, reducing the gap means that the device will exhibit the nonlinear behaviour at lower signal levels, as discussed in Section 5.8.3. One last resort to reduce the motional resistance of electrostatic resonators is to fill the gap between the electrodes with a high-κ dielectric material [48,49][2]. This, however, might add to the complexity of fabrication process and affect the yield if new materials need to be introduced in the process (e.g., hafnium oxide).

Piezoelectric resonators have significantly smaller motional resistances than electrostatic resonators. Consequently, piezoelectricity has been the chosen sensing/actuation method to realise high frequency narrow-band BAW and SAW filters for the past few decades. However, the resonant frequency of conventional piezoelectric devices is defined by the thickness of the piezoelectric material of which the resonator body is made. Therefore, when designing a conventional piezoelectric filter, it is not possible to have more than one resonant frequency per wafer, which obstructs the integration of multiple filters on the same die. A workaround for this problem is to use resonators whose resonant frequencies are set by their lateral dimensions rather than the film thickness [32,50]. It is also possible to use a thin piezoelectric film merely for sensing and actuation while the main resonator body is made of a different

[1]The procedure for choosing the properties of the coupling beams is similar to the case for designing to minimise the anchor loss.

[2]The value of Q for typical resonators lies in the 10,000–100,000 range and one usually needs to try to maximise the Q through proper device and anchor design. The bias voltage, V_B, is limited to its pull-in value, limits of nonlinearity, and the maximum voltage that is available to the resonator.

material such as silicon [34,51]. In such cases, the electromechanical coupling often happens through the d_{31} coefficient of the piezoelectric film; i.e., a vertical electric field results in a shear strain. Since the thickness of the piezoelectric film is small compared to that of the resonator body, these resonators are often actuated with a moment that can lead to excitation of out-of-plane and even torsional modes. Using piezoelectricity for sensing and actuation, it is possible to design resonators with motional resistance of tens of ohms in the MHz to GHz frequency range.

10.3 Time and Frequency References

Stable, low phase noise oscillators are needed in applications ranging from analogue signal processing to synchronisation of digital data. As discussed in Chapter 8, the phase noise of an oscillator depends on the quality factor and motional resistance of the resonator in the loop. Generally, it is desired to use the simplest possible electronic circuitry to minimise the electronic noise [52].

As with filters, the possibility of integration with electronics makes electrostatic resonators an appealing choice. It is possible to design electrostatic resonators with quality factors as high as 10^6 and motional resistances on the order of kilo-ohms for use in oscillator circuits [2,53]. Unlike filters which often need to be used in systems with specified impedance levels, the closed loop operation of an oscillator allows for using resonators with (almost) arbitrary motional impedances. Various forms of resonators have been employed to realise oscillators, including comb-drives [54,55], clamped–clamped beams [56], free-free beams [57], tuning forks [8,39], disc resonators [56], and square plate resonators [2,58].

To increase the resonator quality factor and improve the stability of its performance over time, most micromachined resonators need to be packaged under vacuum. One, therefore, needs to assure that the package has stable properties over time; e.g., there is no leakage and the packaging stress does not vary significantly with time [59]. A bigger concern, however, is the stability of resonator performance with temperature, which is a major requirement for precision oscillators. Silicon resonators exhibit a typical frequency dependence of -17 to -25 ppm/°C, which is far from acceptable for many applications which might require less than 20 ppm of variation over 100 °C of change in temperature. Quartz oscillators circumvent this problem by making the resonators from certain crystal cuts. As an example, resonators cut from the AT plane of a quartz crystal can have temperature coefficients on the order of 100 ppb/°C.

Several methods have been proposed to compensate for the temperature variations of resonator response. The main cause of frequency drift with temperature for silicon resonators is the temperature dependence of the Young's modulus of silicon. Young's modulus of silicon decreases with temperature, directly affecting the resonant frequency through a corresponding decrease

in effective spring constant, and eventually leading to a decrease in the resonant frequency.

10.3.1 Active Temperature Compensation

It is possible to monitor the temperature continuously and compensate for its variations. For example, if the oscillator output feeds a phase-locked loop (PLL) circuit, one can modify the division ratios of the PLL to keep its output frequency almost independent of temperature. It is also possible to design analogue circuitry to compensate for temperature variations, as has commonly been done in temperature compensated crystal oscillators (TCXOs). A TCXO can easily be 20 times less sensitive to temperature variations compared to an uncompensated crystal oscillator. In case of electrostatic resonators, it is possible to change the biasing voltage on the resonator for temperature compensation. The resonant frequency decreases with both temperature and bias voltage. Therefore, one can modify the bias voltage on the resonator to cancel the effects of temperature variations [60].

Another technique that has been successfully deployed for quartz crystal oscillators is to raise and keep the temperature of the resonators and its immediate ambient to a level above the normal environmental temperatures, giving the name oven controlled crystal oscillator (OCXO) to such oscillators. Since the resonator is operating at a constant temperature, the environmental temperature disturbances do not affect its performance, potentially resulting in better than 1 ppb frequency stability over the whole commercial temperature range. A similar technique can be employed for temperature compensation of micromachined resonators [61]. A drawback with this technique is the extra power that is needed to heat the resonator assembly, which can be as high as several watts for typical OCXOs. To reduce the overall power requirements, the resonator assembly needs to be thermally isolated from the surroundings.

10.3.2 Passive Temperature Compensation

The resonant frequency is a function of internal stresses in the structure. For example, a clamped–clamped beam shows stronger temperature dependence than a clamped-free beam. An increase in temperature would result in expansion in a clamped-free structure, but results in a compressive stress inside a clamped–clamped beam. A compressive stress reduces the resonant frequency of the beam, adding to the effect of temperature on the Young's modulus. It is possible to design a mechanical mechanism such that a temperature dependent stress is applied to the main resonator to oppose the shift in the resonant frequency due to material softening [62,63]. For electrostatic resonators, one may also take advantage of the dependence of the electrical spring constant

on the gap between the structures. Magnitude of the negative electric spring constant increases when the gap between the electrodes of an electrostatic resonator is decreased, leading to a reduction in the resonant frequency of the device [64]. Notice that this technique does not require bias voltage control.

It is possible to compensate for the softening of one material by covering it with another material that becomes stiffer with temperature. Luckily for MEMS designers, Young's modulus of silicon dioxide has a positive temperature coefficient whose absolute value is about three times larger than that of silicon. Covering a silicon structure with an SiO_2 film of proper thickness can potentially result in almost zero first order temperature dependence [65–69].

References

1. A. Ismail, J. Burdess, A. Harris, C. McNeil, J. Hedley, S. Chang and G. Suarez, "The principle of a MEMS circular diaphragm mass sensor", *Journal of Micromechanics and Microengineering*, Vol. 16, no. 8, pp. 1487–1493, August 2006.
2. J.-Y. Lee, B. Bahreyni, Y. Zhu and A. Seshia, "Ultrasensitive mass balance based on a bulk acoustic mode single-crystal silicon resonator", *Applied Physics Letters*, Vol. 91, no. 23, pp. 234 103:1–3, December 2007.
3. N.V. Lavrik, M.J. Sepaniak and P.G. Datskos, "Cantilever transducers as a platform for chemical and biological sensors", *Review of Scientific Instruments*, Vol. 75, no. 7, pp. 2229–2253, June 2004.
4. Z. Shen, W.Y. Shih and W.-H. Shih, "Mass detection sensitivity of piezoelectric cantilevers with a nonpiezoelectric extension", *Review of Scientific Instruments*, Vol. 77, no. 6, pp. 065 101:1–10, June 2006.
5. S.-J. Kim, T. Ono and M. Esashi, "Capacitive resonant mass sensor with frequency demodulation detection based on resonant circuit", *Applied Physics Letters*, Vol. 88, no. 5, pp. 053 116:1–3, February 2006.
6. D. Jin, X. Li, J. Liu, G. Zuo, Y. Wang, M. Liu and H. Yu, "High-mode resonant piezoresistive cantilever sensors for tens-femtogram resoluble mass sensing in air", *Journal of Micromechanics and Microengineering*, Vol. 16, no. 5, pp. 1017–1023, 2006.
7. R. Abdolvand, Z. Hao and F. Ayazi, "A temperature-compensated ZnO-on-diamond resonant mass sensor abdolvand", reza; hao, zhili; ayazi, farrokh; sensors, 2006. 5th IEEE conference on oct. 2007 page(s):1297 – 1300, *Proceedings of the 5th IEEE conference on sensors*, Daegu, Korea, October 2006, pp. 1297–1300.
8. K. Wojciechowski, B. Boser and A. Pisano, "A MEMS resonant strain sensor operated in air", *Proceedings of the 17th IEEE micro electro mechanical systems conference, MEMS '04*, Maastricht, The Netherlands, January 2004, pp. 841–845.
9. R.G. Azevedo, D.G. Jones, A.V. Jog, B. Jamshidi, D.R. Myers, L. Chen, X.-a. Fu, M. Mehregany, M.B.J. Wijesundara and A.P. Pisano, "A SiC MEMS resonant strain sensor for harsh environment applications", *IEEE Sensors Journal*, Vol. 7, no. 4, pp. 568–576, April 2007.
10. B. Bahreyni and C. Shafai, "A resonant micromachined magnetic field sensor", *IEEE Sensors Journal*, Vol. 7, no. 9, pp. 1326–1334, September 2007.
11. R. Howe and R. Muller, "Resonant-microbridge vapor sensor", *IEEE Transactions on Electron Devices*, Vol. 33, no. 4, pp. 499–506, April 1986.
12. T. Ono and M. Esashi, "Stress-induced mass detection with a micromechanical/nanomechanical silicon resonator", *Review of Scientific Instruments*, Vol. 76, no. 9, pp. 093 107:1–5, September 2005.

13. H. Lang, M. Baller, R. Berger, C. Gerber, J. Gimzewski, F. Battiston, P. Fornaro, J. Ramseyer, E. Meyer and H. Guntherodt, "An artificial nose based on a micromechanical cantilever array", *Analytica Chimica Acta*, Vol. 393, no. 1–3, pp. 59–65, June 1999.
14. J. Ransley, M. Watari, D. Sukumaran, R. McKendry and A. Seshia, "SU8 bio-chemical sensor microarrays", *Sensors and Actuators A: Physical*, Vol. 83, no. 4–9, pp. 1621–1625, April–September 2005.
15. I. Voiculescu, M. Zaghloul, R. McGill, E. Houser and G. Fedder, "Electrostatically actuated resonant microcantilever beam in CMOS technology for the detection of chemical weapons", *IEEE Sensors Journal*, Vol. 5, no. 4, pp. 641–647, August 2005.
16. J.C. Greenwood, "Etched silicon vibrating sensor", *Journal of Physics E: Scientific Instruments*, Vol. 17, no. 8, pp. 650–652, August 1984.
17. J.C. Greenwood, "Silicon in mechanical sensors", *Journal of Physics E: Scientific Instruments*, Vol. 21, no. 12, pp. 1114–1128, December 1988.
18. C.J. Welham, J.W. Gardner and J. Greenwood, "A laterally driven micromachined resonant pressure sensor", *Sensors and Actuators A: Physical*, Vol. 52, no. 1–3, pp. 86–91, March–April 1996.
19. K. Ikeda, H. Kuwayama, T. Kobayashi, T. Watanabe, T. Nishikawa, T. Yoshida and K. Harada, "Silicon pressure sensor integrates resonant strain gauge on diaphragm", *Sensors and Actuators A: Physical*, Vol. 21, no. 1–3, pp. 146–150, February 1990.
20. M. Esashi, S. Sugiyama, K. Ikeda, Y. Wang and H. Miyashita, "Vacuum-sealed silicon micromachined pressure sensors", *Proceedings of the IEEE*, Vol. 86, no. 8, pp. 1627–1639, August 1998.
21. A. Wong and C. Nguyen, "Micromechanical mixer-filters (mixlers)", *IEEE Journal of Microelectromechanical Systems*, Vol. 13, no. 1, pp. 100–112, February 2004.
22. C.-C. Nguyen, L. Katehi and G. Rebeiz, "Micromachined devices for wireless communications", *Proceedings of the IEEE*, Vol. 86, no. 8, pp. 1756–1768, August 1998.
23. J. Taylor and Q. Huang, Eds., *CRC handbook of electrical filters*, CRC Press, Boca Raton, USA, 1997.
24. A. Zaki, H. Elsimary and M. Zaghloul, "Miniature SAW device using MEMS technology", *Microelectronics Journal*, Vol. 38, no. 3, pp. 426–429, March 2007.
25. R. Lanz and P. Muralt, "Bandpass filters for 8 GHz using solidly mounted bulk acoustic wave resonators", *IEEE Transactions on Ultrasonics, Ferroelectrics and Frequency Control*, Vol. 52, no. 6, pp. 938–948, June 2005.
26. R. Aigner, "RF-MEMS filters manufactured on silicon: key facts about bulk-acoustic-wave technology", *Digest of papers of topical meeting on silicon monolithic integrated circuits in RF systems*, Garmisch, Germany, April 2003, pp. 157–161.
27. A. Kollias and J. Avaritsiotis, "Analysis and design of thin film resonator ladder filters", *Journal of Microelectronics Reliability*, Vol. 42, no. 7, pp. 1133–1140, July 2002.
28. L. Rohde, "Piezoelectric crystal filter", USA Patent 2 262 966, 1939.
29. C.W. Hansell, "Filter", USA Patent 2 005 083, 1927.
30. K. Lakin, "A review of thin-film resonator technology", *IEEE Microwave Magazine*, Vol. 4, no. 4, pp. 61–67, December 2003.
31. G. Piazza and A.P. Pisano, "Two-port stacked piezoelectric aluminum nitride contour-mode resonant MEMS", *Sensors and Actuators A: Physical*, Vol. 136, no. 2, pp. 638–645, May 2007.
32. G. Piazza, P.J. Stephanou and A. P. Pisano, "Single-chip multiple-frequency ALN MEMS filters based on contour-mode piezoelectric resonators", *IEEE Journal of Microelectromechanical Systems*, Vol. 16, no. 2, pp. 319–328, April 2007.
33. D. Galayko, A. Kaiser, B. Legrand, L. Buchaillot, D. Collard and C. Combi, "Tunable passband T-filter with electrostatically-driven polysilicon micromechanical resonators", *Sensors and Actuators A: Physical*, Vol. 117, no. 1, pp. 115–120, January 2005.

34. G. Piazza, R. Abdolvand, G.K. Ho and F. Ayazi, "Voltage-tunable piezoelectrically-transduced single-crystal silicon micromechanical resonators", *Sensors and Actuators A: Physical*, Vol. 111, no. 1, pp. 71–78, March 2004.
35. K. Wang and C.-C. Nguyen, "High-order medium frequency micromechanical electronic filters", *IEEE Journal of Microelectromechanical Systems*, Vol. 8, no. 4, pp. 534–556, December 1999.
36. F. Bannon, J. Clark and C.-C. Nguyen, "High-Q HF microelectromechanical filters", *IEEE Journal of Solid-State Circuits*, Vol. 35, no. 4, pp. 512–526, April 2000.
37. S. Li, Y. Lin, Z. Ren and C. Nguyen, "An MSI micromechanical differential disk-array filter", *Digest of technical papers of the international conference on solid state sensors and actuators, transducers '07*, Lyon, France, June 2007, pp. 307–311.
38. J. Yan, A.A. Seshia, K.L. Phan, P.G. Steeneken and J.T. van Beek, "Narrow bandwidth single-resonator MEMS tuning fork filter", *Proceedings of the IEEE international frequency control symposium*, Geneva, Switzerland, May 2007, pp. 1366–1369.
39. T.A.W. Roessig, "Integrated MEMS tuning fork oscillators for sensor applications", Ph.D. dissertation, Department of Mechanical Engineering, University of California, Berkeley, USA, 1998.
40. A. Alastalo and V. Kaajakari, "Systematic design approach for capacitively coupled microelectromechanical filters", *UFFCT*, Vol. 53, no. 9, pp. 1662–1670, September 2006.
41. S. Pourkamali and F. Ayazi, "Electrically coupled MEMS bandpass filters: Part I: with coupling element", *Sensors and Actuators A: Physical*, Vol. 122, no. 2, pp. 307–316, August 2005.
42. S. Pourkamali and F. Ayazi, "Electrically coupled MEMS bandpass filters: Part II: without coupling element", *Sensors and Actuators A: Physical*, Vol. 122, no. 2, pp. 317–325, August 2005.
43. E. Papadakis, "Improvements in a broadband electromechanical bandpass filter in the voice band", *IEEE Transactions on Sonics and Ultrasonics*, Vol. 22, no. 6, pp. 406–414, November 1975.
44. M. Demirci and C.-C. Nguyen, "Mechanically corner-coupled square microresonator array for reduced series motional resistance", *IEEE Journal of Microelectromechanical Systems*, Vol. 15, no. 6, pp. 1419–1436, December 2006.
45. M. Konno, S. Oyama and Y. Tomikawa, "Equivalent electrical networks for transversely vibrating bars and their applications", *IEEE Transactions on Sonics and Ultrasonics*, Vol. 26, no. 3, pp. 191–201, May 1979.
46. L. Lin, R.T. Howe and A.P. Pisano, "Microelectromechanical filters for signal processing", *IEEE Journal of Microelectromechanical Systems*, Vol. 7, no. 3, pp. 286–294, September 1998.
47. S.A. Bhave, D. Gao, R. Maboudian and R.T. Howe, "Fully differential SiC Lamé mode resonator and checkerboard filter", *IEEE Micro Electro Mechanical Systems Conference*, Miami, USA, February 2005, pp. 223–226.
48. W.-L. Huang, Z. Ren and C.-C. Nguyen, "Nickel vibrating micromechanical disk resonator with solid dielectric capacitive-transducer gap", *Proceedings of the IEEE international frequency control symposium and exposition*, June 2006, pp. 839–847.
49. H. Chandrahalim, D. Weinstein, L.F. Cheow and S.A. Bhave, "High-κ dielectrically transduced MEMS thickness shear mode resonators and tunable channel-select RF filters", *Sensors and Actuators A: Physical*, Vol. 136, no. 2, pp. 527–539, May 2007.
50. M. Zhu and P.B. Kirby, "Design study of piezoelectric micro-machined mechanically coupled cantilever filters using a combined finite element and microwave circuit analysis", *Sensors and Actuators A: Physical*, Vol. 126, no. 2, pp. 417–424, February 2006.
51. D.L. DeVoe, "Piezoelectric thin film micromechanical beam resonators", *Sensors and Actuators A: Physical*, Vol. 88, no. 3, pp. 263–272, January 2001.
52. R.J. Matthys, *Crystal oscillator circuits*, Krieger Publishing Company, Malabar, USA, April 1991.

53. L. Khine, M. Palaniapan and W.-K. Wong, "6 MHz bulk-mode resonator with Q values exceeding one million", *Digest of technical papers of the international conference on solid state sensors and actuators, transducers '07*, Lyon, France, June 2007, pp. 2445–2448.
54. C.T.-C. Nguyen and R.T. Howe, "An integrated CMOS micromechanical resonator high-Q oscillator", *IEEE Journal of Solid-State Circuits*, Vol. 34, no. 4, pp. 440–455, April 1999.
55. B. Bahreyni and C. Shafai, "Oscillator and frequency-shift measurement circuit topologies for micromachined resonant devices", *Sensors and Actuators A: Physical*, Vol. 137, no. 1, pp. 74–80, June 2007.
56. Y.-W. Lin, S. Lee, S.-S. Li, Y. Xie, Z. Ren and C.T.-C. Nguyen, "Series-resonant VHF micromechanical resonator reference oscillators", *IEEE Journal of Solid-State Circuits*, Vol. 39, no. 12, pp. 2477–2491, December 2004.
57. G. Ho, K. Sundaresan, S. Pourkamali and F. Ayazi, "Low-motional-impedance highly-tunable i^2 resonators for temperature-compensated reference oscillators", *Proceedings of the 18th IEEE micro electro mechanical systems conference, MEMS '05*, Miami, USA, January 2005, pp. 116–120.
58. T. Mattila, O. Jaakkola, J. Kiihamäki, J. Karttunen, T. Lamminmäki, P. Rantakari, A. Oja, H. Seppä, H. Kattelus and I. Tittonen, "14 MHz micromechanical oscillator", *Sensors and Actuators A: Physical*, Vol. 97–98, pp. 497–502, April 2002.
59. B. Kim, R.N. Candlera, M.A. Hopcroft, M. Agarwal, W.-T. Park and T.W. Kenny, "Frequency stability of wafer-scale film encapsulated silicon based MEMS resonators", *Sensors and Actuators A: Physical*, Vol. 136, no. 1, pp. 125–131, May 2007.
60. K. Sundaresan, G. Ho, S. Pourkamali and F. Ayazi, "Electronically temperature compensated silicon bulk acoustic resonator reference oscillators", *IEEE Journal of Solid-State Circuits*, Vol. 42, no. 6, pp. 1425–1434, June 2007.
61. C.M. Jha, M.A. Hopcroft, M. Agarwal, S.A. Chandorkar, R.N. Candler, V. Subramanian, R. Melamud, S. Bhat, B. Kim, K.K. Park and T.W. Kenny, "In-chip device-layer thermal isolation of MEMS resonator for lower power budget", *Proceedings of ASME international mechanical engineering congress and exposition*, Chicago, USA, November 2006.
62. W.-T. Hsu and C.-C. Nguyen, "Geometric stress compensation for enhanced thermal stability in micromechanical resonators", *Proceedings of the IEEE international ultrasonics symposium*, Sendai, Japan, October 1998, pp. 945–948.
63. W.-T. Hsu, J. Clark and C.-C. Nguyen, "Mechanically temperature compensated flexural-mode micromechanical resonators", *Technical digest of the IEEE international electron devices meeting*, San Francisco, USA, December 2000, pp. 493–496.
64. W.-T. Hsu and C.-C. Nguyen, "Stiffness-compensated temperature-insensitive micromechanical resonators", *Proceedings of the 15th IEEE micro electro mechanical systems conference, MEMS '02*, Las Vegas, USA, January 2002, pp. 731–734.
65. R. Abdolvand, H. Mirilavasani and F. Ayazi, "A low-voltage temperature-stable micromechanical piezoelectric oscillator", *Digest of technical papers of the international conference on solid state sensors and actuators, transducers '07*, Lyon, France, June 2007, pp. 53–56.
66. R. Melamud, B. Kim, M.A. Hopcroft, S. Chandorkar, M. Agarwal, C.M. Jha and T.W. Kenny, "Composite flexural-mode resonator with controllable turnover temperature", *Proceedings of the 20th IEEE micro electro mechanical systems conference, MEMS '07*, Kobe, Japan, January 2007, pp. 199–202.
67. B. Kim, R. Melamud, M.A. Hopcroft, S.A. Chandorkar, G. Bahl, M. Messana, R.N. Candler, G. Yama and T. Kenny, "Si-SiO_2 composite MEMS resonators in CMOS compatible wafer-scale thin-film encapsulation", *Proceedings of the international IEEE frequency control symposium*, Geneva, Switzerland, May 2007, pp. 1214–1219.
68. K. Lakin, K. McCarron and J. McDonald, "Temperature compensated bulk acoustic thin film resonators", *Proceedings of the IEEE ultrasonics symposium*, vol. 1, October 2000, pp. 855–858.

69. H. Jianqiang, Z. Changchun, L. Junhua and L. Peng, "A novel temperature-compensating structure for micromechanical bridge resonator", *Journal of Micromechanics and Microengineering*, Vol. 15, no. 4, pp. 702–705, April 2005.

Appendix A. Derivation of the PSD of Brownian Noise

The power spectral density of Brownian noise is derived using the procedure described in [1]. If the noise is represented by a force, $F(t)$, the spectral density of this force, $\mathcal{F}(\omega)$, is found from:

$$\mathcal{F}(\omega) = \int_{-\infty}^{+\infty} \langle F(t)F(t+\tau)\rangle e^{-j\omega\tau}\, d\tau$$
$$\langle F^2\rangle = \langle F(t)F(t)\rangle = \int_{-\infty}^{+\infty} \mathcal{F}(\omega)\, d\omega = \int_{0}^{+\infty} \mathcal{F}^{+}(\omega)\, d\omega \tag{A.1}$$

where $\mathcal{F}^{+}(\omega) \equiv 2\mathcal{F}(\omega)$ so that the last integral is restricted to positive frequencies only. This is permissible since $\mathcal{F}(\omega)$ is a real and even function of frequency [1]. Statistical physics tells us that $\mathcal{F}(\omega)$ is constant for a wide frequency range, and therefore, can be considered as a white noise source [2].

For harmonic motion of a second order mass–spring system, we have:

$$X = \frac{F}{-M\omega^2 + j\omega\zeta + K}. \tag{A.2}$$

Therefore, the mean value of kinetic energy is given by:

$$\begin{aligned}\left\langle \frac{1}{2}M\dot{x}^2 \right\rangle &= \frac{1}{2}M\left\langle \left| \frac{j\omega F}{-M\omega^2 + j\omega\zeta + K} \right|^2 \right\rangle \\ &= \frac{M}{2K^2}\int_{-\infty}^{+\infty} \frac{F^2\omega^2\, d\omega}{(1-\frac{\omega^2}{\omega_0^2})^2 + \frac{\omega^2}{Q^2\omega_0^2}} \\ &= \frac{\mathcal{F}^{+}\omega_0}{2K} \times \frac{Q\pi}{2}\end{aligned} \tag{A.3}$$

where $\omega_0 = \sqrt{K/M}$, $Q = \omega_0 M/\zeta$, and we used the fact that $\mathcal{F}^{+}$ is frequency independent [1,3].

The equipartition theorem states that each independent quadratic term in the total energy of a system has a mean value of $K_{\mathrm{B}}T/2$ where K_{B} is Boltzmann's constant [1,2]. The spectral density of the noise force can now be found from Eq. (A.3) by using equipartition theorem:

$$\begin{aligned}&\frac{\mathcal{F}^{+}\omega_0}{2K} \times \frac{Q\pi}{2} = \frac{1}{2}K_{\mathrm{B}}T \\ &\Longrightarrow \mathcal{F}^{+} = \frac{2}{\pi}K_{\mathrm{B}}T\zeta.\end{aligned} \tag{A.4}$$

If the integral of Eq. (A.3) is taken with respect to frequency f rather than the radian frequency ω, this familiar result is obtained for the mean square value of the spectral density of the noise force:

$$\mathcal{F}^{+} = \tilde{f_B}^{2} = 4K_{\mathrm{B}}T\zeta \ \mathrm{N}^2/\mathrm{Hz}. \tag{A.5}$$

It must be noted that other choices of a system frequency response would result in the same frequency distribution for the spectral density of the noise. Choosing a second degree system in this case merely allowed us to specify different quantities in terms of familiar parameters Q and ω_0. The noise force is shaped by the frequency response of the system under analysis, and therefore, the total amount of noise at the output of a system will depend on its bandwidth.

References

1. T. Hofler and S.L. Garrett, "Thermal noise in a fiber optic sensor", *Journal of Acoustical Society of America*, Vol. 84, no. 2, pp. 471–475, August1988.
2. F. Reif, *Fundamentals of statistical and thermal physics*, McGraw-Hill, New York, USA, 1965.
3. K. Huang, *Introduction to statistical physics*, Taylor and Francis, London, United Kingdom, 2001.

Index

MICRO & NANO TECHNOLOGIES

PUBLISHED 2008

Microdrops and Digital Microfluidics · Jean Berthier · 978-0-8155-1544-9

Micromixers: Fundamentals, Design and Fabrication · Nam-Trung Nguyen · 978-0-8155-1543-2

Fabrication and Design of Resonant Microdevices · Behraad Bahreyni · 978-0-8155-1577-7

FORTHCOMING 2008-2009

Hot Embossing: Theory and Technology of Microreplication · Matthias Worgull · 978-0-8155-1579-1

Introduction to Quantum Information Processing (QIP) · Timothy P. Spiller and William J. Munro · 978-0-8155-1575-3

Nanotechnology Applications: Solutions for Improving Water Quality · Edited by Mamadou Diallo, Jeremiah Duncan, Nora Savage, Anita Street, Richard Sustich · 978-0-8155-1578-4

Micro-machining Using Electrochemical Discharge Phenomenon: Fundamentals and Application of Spark Assisted Chemical Engraving · Rolf Wüthrich · 978-0-8155-1587-6

Industrial Micro and Nano Fabrication · J.G.E. Gardeniers and R. Luttge · 978-0-8155-1582-1

Physics of Carbon Nanotube Devices · François Léonard · 978-0-8155-1573-9

Small Scale Mechanics: Principles and Applications · David Mendels · 978-0-8155-1590-6

Emerging Nanotechnologies for Manufacturing · Edited by Waqar Ahmed and M.J. Jackson · 978-0-8155-1583-8

Risk Governance of Nanotechnology: Environmental, Health and Safety Concerns About Nanotechnology and Their Implication for the Nanotechnology Industry · Edited by Steffi Friedrichs · 978-0-8155-1586-9

Handbook of MEMS Materials and Technologies · Edited by Veikko Lindroos, Markku Tilli, Ari Lehto, and Teruaki Motooka · 978-0-8155-1594-4

Micromanufacturing Engineering and Technology · Edited by Yi Qin · 978-0-8155-1545-6

OF RELATED INTEREST

MEMS: A Practical Guide to Design, Analysis and Applications · Edited by Jan Korvink and Oliver Paul · 978-0-8155-1497-8 · 2006

Nanostructured Materials: Processing, Properties and Applications, 2nd Edition · Edited by Carl C. Koch · 978-0-8155-1534-0 · 2007

Ultrananocrystalline Diamond: Synthesis, Properties, and Applications · Edited by Olga A. Shenderova and Dieter M. Gruen · 978-0-8155-1524-1 · 2006

For the latest information on related titles visit **www.williamandrew.com/MNT/**